

Microstructural Stability and The Kinetics of Textural Evolution

Andrew Lind

Submitted in accordance with the requirements
for the degree of Doctor of Philosophy.

University of Leeds
Department of Earth Sciences

May, 1996

*The candidate confirms that the work submitted is his own
and the appropriate credit has been given where reference
has been made to the work of others.*

Abstract

This thesis is concerned with constraining the processes by which a rock texture may be altered in the geological history after a rock has been deformed and the rates at which that microstructural modification may occur. The area which has been chosen to investigate microstructural change is the Ballachulish aureole in the NW Highlands of Scotland, using samples from the Appin Quartzite. Rocks in this region were deformed during the Caledonian orogeny. Post-dating the deformation was the intrusion of the Ballachulish granite. As a consequence of the thermal perturbation associated with the granite intrusion, deformation microstructures were gradually altered. This process is known as annealing. The Ballachulish aureole is essentially a 'natural laboratory' which preserves an annealing experiment over geological time; rocks are gradually annealed along the traverse towards the intrusive complex where higher temperatures were attained.

Rocks have been sampled along a traverse from outside the igneous aureole towards the contact. A variety of microstructural elements have been characterised using image analysis and crystallographic techniques, some of which have been developed during this study. The changes in rock fabrics along the traverse are used as a basis for developing models of annealing for many microstructural features, including dislocations, subgrains, subgrain walls and grains. The relative stability of each of these microstructures is assessed to show that dislocations are the least stable, then subgrains and grains. An interesting 'mesh' microstructure is identified, preserving evidence of fracturing on a grain scale. These mesh-grains are very stable, surviving annealing in some cases altogether. The presence of impurities on all scales of observation are shown to greatly influence the mechanisms of microstructural change.

The kinetics of microstructural modification are examined using theoretical models based on the processes of annealing which have been identified during this investigation. Again these indicate that impurities can have marked implications on the rates of microstructural change. Kinetic models for rocks undergoing regional prograde and retrograde metamorphism are developed to indicate how this work may be applied on a more regional tectonic scale.

Acknowledgements

This project is the brainchild of Rob Knipe, Geoff Lloyd and Andy Barnicoat, all three of them are thanked for obtaining the grant, giving me the opportunity to carry out the research and their distinctive styles of supervision during my tenure of the studentship. NERC are acknowledged for their lavish funding of the project.

Special thanks for intellectual and technical support go to: Dave Prior, Graeme Potts and John Wheeler for their enthusiasm and good humour during my time at Liverpool; Andy Farmer, for some strange reason (only known to himself) has spent hours, if not days guiding me through the rigours of programming, microstructural geology and of late writing-up - cheers very much for putting yourself through it (I'm blaming you if it all goes wrong). Mark Jessell, Neil-Henrick Schmidt and Dave Mainprice are thanked for managing to show some interest in the work. Closer to home thanks to members of the strucky group some of whom have been a source of inner strength when things are going wrong ("It's never too late.....") - Ned, Jock, Napalm, Slime, Neil, Edd, Lochlann, Will (you're sorely missed), Wibbs, Yen, Louise, Dani, Rob, Helena, Shona, MOOOSE and Steve - no apologies to anybody for my bad temper at the computer. The Keiths did a grand job on the thin section front. Robert Marshall is thanked for his patience at the polisher. Eric Condliffe and Tony Nichols help in electron optics is appreciated.

The Beer Police would like to offer long service medals to Ned, Napalm and Chopper and Sergeant Girth would like to thank Jock for his top tips (and his introduction to t*t cakes). Cheers to the "we're only going for a gallon" crew - those I've already mentioned above know who they are, together with Klaus, Dave, Nigel, Chopper Sue and Clare. Other socialites include: G-Tech (all of them), Tim, Liz&Edd, Kath, Alex H., Quebtin Fisher, Tim Buddin, Ken Baxter, Al (Fat Knacker) Boulton, Slimbo, Karen B, Kathy, Natasha and Anne.

Gold stars will be issued to Andy F, Sue, Ned, Napalm, Neil, Nigel, Wibbs and Clare; Andy and Sue for Otley trips, meals, hols etc.; Ned, Napalm and Neil for destroying my health; Nige, Wibbs (even if your socks are bleached round the toes) and Clare for being good for a laugh .

The family have all been superstars throughout, cheers for your continued support (and money) - Mum, Michael, Stephen and Granddad etc.. In return you now receive a brand new door stop in the form of a thesis.

Table of Contents

Title	
Abstract	i
Acknowledgements	ii
Table of Contents	iv
Table of Figures	xi
CHAPTER 1 INTRODUCTION	
1.1 The Geological Setting	2
1.2 Aims Of Thesis	3
1.3 Thesis Layout	4
CHAPTER 2 DEFORMATION MECHANISMS AND MICROSTRUCTURAL MODIFICATION	
2.1 Introduction	6
2.1.1 Non-Crystal Plastic Mechanisms.....	7
2.1.1.a Diffusive Mass Transfer.....	7
2.1.1.b Cataclasis	7
2.1.2 Crystal Plasticity.....	8

2.2 Rock Rheologies	11
2.3 Processes Affecting Rock Rheologies	12
2.3.1 Hardening	12
2.3.2 Softening.....	13
2.3.2.a Recovery by Dislocation Climb	13
2.3.2.b Recovery by Cross Slip	13
2.3.2.c Annihilation	14
2.3.2.d Polygonization.....	14
2.3.3 Cyclicity of Hardening/Softening	14
2.3.4 Dynamic Recrystallisation.....	15
2.3.4.a Subgrain Rotation	15
2.3.4.b Grain Boundary Migration.....	16
2.3.5 Interaction of Deformation Processes	17
2.4 Static Recovery	18
2.4.1 Static Recovery by Grain Growth	19
2.4.1.a Primary Recrystallisation.....	19
2.4.1.b Normal Grain Growth.....	20
2.4.2 Kinetics of Normal Grain Growth.....	22
2.4.3 Abnormal Grain Growth.....	24
2.5 Geological Implications of Grain Growth	24
2.6 Criteria To Recognise Annealing	26
2.6.1 Microscopic Observations	26
2.6.2 Image Analysis Criteria.....	27
2.6.3 Crystallographic Criteria.....	27
2.7 Conclusions	28
 CHAPTER 3 REGIONAL GEOLOGY	
3.1 Introduction	39
3.2 Lithological Descriptions	40
3.2.1 Metasediments	40

3.2.2 Ballachulish Intrusion	41
3.3 Regional Metamorphism	42
3.4 Caledonian Deformation	43
3.5 The Ballachulish Intrusion	45
3.5.1 Shape Of Intrusion	45
3.5.2 Contact With Country Rocks.....	45
3.5.3 Textures Within The Igneous Complex.....	45
3.5.4 Emplacement of The Ballachulish Complex	46
3.5.5 Deformation of The Country Rocks.....	47
3.5.6 Thermal Conditions of The Ballachulish Complex.....	47
3.6 The Aureole	48
3.6.1 Pressure Estimates.....	49
3.6.2 Temperature Estimates.....	50
3.6.3 Convection Within The Aureole	50
3.7 Thermal Modelling.....	51
3.7.1 Results	51
 CHAPTER 4 METHODOLOGY	
4.1 INTRODUCTION.....	64
4.2 Optical Microscope Techniques.....	65
4.2.1 Substructure Classification	65
4.2.2 Extinction Angle	66
4.3 IMAGE ANALYSIS.....	66
4.3.1 Introduction	66
4.3.2 Image Analysis Methods.....	67
4.3.3 Averaged Grain Size Data Collection Technique.....	70
4.3.4 Data Presentation	71
4.3.5 Grain Data Distribution Analysis	71

4.3.5.a Introduction	71
4.3.5.b Statistical Processing of Data	72
4.4 FRACTAL ANALYSIS - METHODS	73
4.4.1 Introduction	73
4.4.2 What Are Fractals?.....	74
4.4.2.a Introduction.....	74
4.4.2.b Self-Similarity	75
4.4.2.c Monster Curves.....	75
4.4.3 Richardson Plots	77
4.4.3.a Cut-offs	79
4.4.3.b Mixed Fractals.....	79
4.4.4 Computation of Fractal Dimension	80
4.4.4.a Dilation and the Minkowski Sausage	80
4.4.4.b Accuracy of Technique	82
4.4.5 Application To Ballachulish Aureole.....	83
4.5 Crystallographic Analytical Techniques	83
4.5.1 Introduction	83
4.5.2 Data Acquisition.....	84
4.5.3 Data Presentation	85
4.5.3.a Pole Figures.....	85
4.5.3.b Inverse Pole Figures.....	86
4.5.4 Crystallographic Preferred Orientations	87
4.5.5 Misorientation Analysis	87
4.5.6 The Coincident Site Lattice	89
4.5.7 Calculating CSL in Trigonal Minerals	90
CHAPTER 5 MICROSTRUCTURAL DEVELOPMENT	
5.1 OVERVIEW	108
5.1.1 Zone I (>800m from intrusion)	109
5.1.2 Zone II (800-600m).....	109
5.1.3 Zone III.....	110
5.1.4 Crystallographic Controls During Annealing	110
5.2 INTRODUCTION.....	111

5.3 General Microstructural Observations	112
5.3.1 Introduction	112
5.3.2 Deformational Microstructure (Unannealed From Outside Aureole).....	112
5.3.3 Development of Microstructures Through Aureole	115
5.4 Statistical Analysis of Microstructures (Image Analysis)	118
5.4.1.a Deformed samples (non-annealed microstructures):	118
5.4.2 Evolution of Microstructures Through Aureole	119
5.4.2.a Average Data.....	119
5.4.2.b Distribution Data	122
5.4.2.c Fractal Analysis Results	125
5.4.2.d Mixed Fractals.....	126
5.5 Crystallographic Data	128
5.5.1 Introduction	128
5.5.2 Crystallographic Preferred Orientations	129
5.5.3 Grain Boundary Microtexture.....	130
5.5.4 Grain Boundary CSL Analysis	132
5.6 Summary.....	133
5.6.1 Unannealed Samples.....	133
5.6.2 Microstructural Development During Annealing	134
5.6.3 Crystallographic Influences.....	135
5.6.4 Implications.....	135
 CHAPTER 6 MICROSTRUCTURAL PROCESSES AND STABILITY	
6.1 Introduction	178
6.2 Zone 1 (mechanisms of deformation).....	180
6.2.1 Grains/Grain Boundary Processes.....	180
6.2.2 Subgrains	180
6.2.3 Mesh Substructure Visible With CL.....	181
6.2.4 Dislocations	183
6.2.5 Summary of Deformation Processes in Zone I	184

6.3 Zone 2 Primary Recrystallisation	184
6.3.1 Grains/Grain Boundaries	185
6.3.2 Subgrains	186
6.3.3 'Mesh' Grains	188
6.3.4 Dislocations	191
6.4 Zone III (Normal Grain Growth)	191
6.5 Controls on Microstructural Development.....	192
6.5.1 Impurities	193
6.5.1.a Feldspar Impurities/Fluid inclusions	194
6.5.1.b Solute Impurities	195
6.5.1.c Summary	196
6.5.2 Nucleation.....	196
6.6 Crystallographic Control on Growth.....	198
6.6.1 Introduction	198
6.6.2 Crystallographic Preferred Orientation.....	198
6.6.2.a CPOs in Zone I.....	198
6.6.2.b CPO Development in Zones I&II	199
6.6.3 Misorientation Analysis	199
6.7 Initiation of Grain Growth	200
6.8 Summary.....	201
6.8.1 Zone I - Processes of deformation	201
6.8.2 Zone II - Primary Recrystallisation	202
6.8.3 Zone III.....	203
6.8.4 Other Controls on Evolution of Microstructures at Ballachulish.....	203
CHAPTER 7 KINETICS OF MICROSTRUCTURAL MODIFICATION	
7.1 Introduction	217
7.2 Grain Scale Kinetic Models of Annealing in the Ballachulish Aureole.....	220

7.2.1 Introduction	220
7.2.2 Grain Coarsening Kinetic Model.....	220
7.2.3 Monomineralic grain coarsening	222
7.2.3.a Comparison of theoretical model to Ballachulish Data	222
7.2.3.b Microstructural Controls on Grain Sizes at Ballachulish	224
7.2.3.c Zone III - Normal Grain Growth.....	226
7.2.3.d Summary	228
7.2.4 Grain coarsening in Polymineralic Samples	228
7.2.4.a Introduction	228
7.2.4.b The Kinetic Model.....	228
7.3 Kinetics of Subgrain Coarsening	231
7.3.1 Results	232
7.4 Grain Coarsening during Regional Metamorphism/Deformation .	236
7.4.1 Introduction	236
7.4.2 Exhumation of a Deformed Tectonite	237
7.4.2.a Summary Of Exhumation Models	239
7.4.3 Burial of A Fault Rock	240
7.5 Conclusions	242
CHAPTER 8	254
8.1 Introduction	254
8.2 Concerning Quantification of Microstructure.....	255
8.3 Concerning Data from Ballachulish	256
8.4 Concerning Microstructural Stability	256
8.5 Concerning the Kinetics	258
8.6 Future Work	259
APPENDICES	

Appendix A Thermal Modelling	A1
Appendix B Analytical Techniques	B1
Appendix C Kontron Macros	C1
Appendix D Channel - Euler Conversions	D1
Appendix E Program Listings	E1

ENCLOSURE

DISKETTE (thermal modelling and misorientation programs)

Figures

Chapter 2	29-38
Chapter 3	54-63
Chapter 4	94-107
Chapter 5	137-177
Chapter 6	205-216
Chapter 7	245-254

CHAPTER 1

INTRODUCTION

The title “Microstructural evolution and the kinetics of textural change” reflects the two pronged approach to this thesis. Firstly, to quantify microstructures within a well constrained geological environment. Secondly, to use microstructural data to understand the rates of metamorphic/deformational processes.

This investigation essentially brings together aspects from three geological disciplines, microstructure, crystallography and metamorphic petrology, in order to understand processes which are fundamental to each of these large subject areas.

Deformation of natural aggregates has been accurately assessed for numerous temperature and stress regimes in the form of flow laws relating stress to strain. However, there has been relatively little integration of these studies with microstructural investigation to indicate which microstructural processes may be responsible for marked changes in rock rheology. Microstructural studies have indicated that the development of instabilities is an important factor controlling the rheology of an aggregate (Poirier, 1980, Law et al., 1984; Knipe and Wintsch, 1985; Ord and Hobbs, 1989; Knipe 1989; Prior et al., 1990). Investigations of instabilities are usually hampered by unconstrained

stress, strain and strain rate histories. This investigation attempts to understand instabilities within rock indirectly by looking at the '*stability*' of different microstructures (grains, subgrains and dislocation) when rocks are subjected to elevated temperatures.

Microstructural geologists and others investigating the crystallographic influences on rock evolution frequently use rocks which have been deformed at deep levels in the earth's crust to deduce the processes by which aggregates deform. It is fundamental for such studies to conclude that the rock microstructures which are observed truly reflect the environmental conditions during deformation, i.e. the rock microstructures have been stable during exhumation to the earth's surface. Therefore, this investigation intends to assess the stability of microstructures in rocks which have undergone a well constrained temperature history.

The common theme presented thus far is that microstructures evolve and that it is the intention of this investigation to examine the rates at which they evolve, i.e. the kinetics of microstructural evolution. Microstructures in a geological setting with a known temperature history are examined in order to quantify the microstructural change. It is then possible to compare the actual kinetics of microstructural change to theoretical models which predict the rates of change.

1.1 The Geological Setting

Rock microstructures are examined as they evolve under changing temperature conditions. In order to assess these changes it is crucial to constrain a temperature history. One option is to observe microstructural change in a laboratory. However, in such circumstances temperatures have to be elevated to unrealistic levels (in terms of geology) for the experiments to occur on a reasonable timescale (i.e. in a human lifetime). A geological setting with a well constrained temperature history is therefore preferable. An igneous aureole is one such geological setting, where the temperature history may be calculated from mineral reactions and thermal modelling. Thus, a thermal aureole is a 'natural laboratory' to investigate temperature effects on rock microstructures (Joesten 1991).

The aureole which has been chosen is the Ballachulish thermal aureole, which surrounds the Ballachulish granite intrusion, in the NW Highlands of Scotland. This aureole is chosen because of the large amount of work which has been carried out over a number of years in order to constrain the geometry and temperature evolution of the aureole. The culmination of this work was the publication of *Equilibrium and Kinetics in Contact Metamorphism* (Voll et al. 1991), which details the evolution of both the Ballachulish granite and its aureole. This volume serves as the basis from which an in-depth microstructural investigation is undertaken in this investigation.

1.2 Aims Of Thesis

- To quantify the development of microstructures along a traverse from outside the Ballachulish aureole to the contact with the igneous intrusion: a variety of microstructures will be investigated using many different types of analytical tools (Optical, SEM & TEM microscopy, image analysis systems and electron microprobe analysis). New methods for measuring microstructures and microtextures are developed.
- The thesis aims to describe and develop methods of microstructural and microtextural data analysis.
- To interpret the kinematics of microstructural deformation prior to the intrusion of the Ballachulish granite using information gathered from the microstructural analysis.
- To document the changes in microstructures along the traverse towards the igneous intrusion and to assess the processes of microstructural modification as a result of the intrusion. Ultimately, these interpretations are used to discuss the relative stability of different types of microstructural elements.
- To use the microstructural interpretations, together with calculations of the thermal history within the aureole, to produce models which accurately predict the evolution of microstructures within the Ballachulish aureole; these models may be utilised by

workers in other geological settings to predict the evolution of microstructures in a regime with a different thermal/geo-tectonic history.

1.3 Thesis Layout

Chapter 2 reviews the processes by which rocks are deformed, and how deformation-related microstructures may be recognised within natural tectonites. The second section of this chapter indicates how deformational features within an aggregate may be modified once deformation ceases and rocks are subjected to a constant temperature or a non-isothermal temperature time path.

Chapter 3 presents a review of the regional geology of the Ballachulish region, together with a more detailed description of the geology of the Ballachulish granite intrusion and aureole. The data from this chapter is used as input data for *Contact8.pas*, a computer program developed to calculate the temperature history of the aureole.

Chapter 4 presents the methodologies by which microstructures have been quantified during this investigation.

Chapter 5 describes the microstructural data, calculated using the methods reviewed in Chapter 4, for rocks from outside the igneous aureole which display deformational microstructures and from rocks along the traverse which have been modified by the increased temperatures associated with the intrusion.

Chapter 6 interprets the microstructural data from the Ballachulish aureole and presents a number of microstructural models which are responsible for the modification of microstructures. These models provide the basis for the development of theoretical kinetic models to describe the kinetics within the Ballachulish aureole.

Chapter 7 investigates the rates of the microstructural processes within the Ballachulish aureole. The theoretical kinetics of microstructural change are compared to the actual observed rates of change in the Ballachulish setting. The models are developed further to

hypothetical tectonic regimes to examine the effects exhumation rates may exert on microstructures and the effects of burial on fault rocks.

Chapter 8 discusses the main conclusions to be made from this project and highlights suitable topics for future research.

CHAPTER 2

DEFORMATION MECHANISMS AND MICROSTRUCTURAL MODIFICATION

2.1 Introduction

This study examines the effects of annealing on rock microstructures, both during deformation events and during periods of deformation quiescence. In order to achieve this aim it is necessary to have a thorough understanding of dynamic deformation mechanisms and static annealing mechanisms. Both these subjects will be dealt with here, separately. However, during the progression of the thesis it will become apparent that such discrimination is not always clear cut. In this chapter, deformation and annealing mechanisms and the nature of the microstructures produced by these various mechanisms are discussed. The chapter has been divided into dynamic processes (i.e. those which occur during deformation) and static processes (i.e. those which occur between deformation events or when deformation has ceased).

When a stress is imposed upon a rock it responds to that stress by changing its shape. The process by which this motion is undertaken is a deformation mechanism. Deformation mechanisms and their relation to rock rheology has been of increasing interest in recent years (e.g. see reviews of Atkinson and Meredith, 1987; Groshong, 1988; Knipe, 1989; Knipe and Rutter, 1989; Barber, 1990).

Knipe (1989) divides rock deformation mechanisms into three types : 1) diffusive mass transfer; 2) crystal plasticity; and 3) cataclasis. The deformation mechanism at any one moment during a deformation event is dependent on both lithological (e.g. grain size and mineralogy) and environmental controls (stress, temperature, pressure, strain and pore fluid pressure Figure 2.1). Stress magnitudes tend to be both cyclic through time and partitioned within a rock aggregate. Thus, during a single deformation event it is likely that a number of different deformation mechanisms will operate both temporally and spatially. This chapter concentrates upon crystal plasticity and annealing because these processes dominate the microstructural development within the Ballachulish aureole.

2.1.1 Non-Crystal Plastic Mechanisms

2.1.1.a *Diffusive Mass Transfer*

Diffusive mass transfer may be described as the transfer of material from zones of high normal stress to zones of low normal stress by diffusion (Elliot, 1973, and Rutter, 1983). Knipe (1989) envisages a three stage process: 1) source mechanisms are associated with the way which material enters the diffusion path; 2) diffusion mechanisms, involving the transport of material, such as volume diffusion through the lattice (Nabarro-Herring creep - Gordon 1965 and Poirier, 1985), or grain boundary diffusion (Coble creep (Coble, 1963), pressure solution (Rutter, 1976, Etheridge et al. 1984, Poirier, 1985); and 3) sink processes, where material is precipitated from the diffusion path.

2.1.1.b *Cataclasis*

Cataclasis is a term combining two distinct processes, namely frictional sliding and various fracture deformation mechanisms. Knipe (1989) gives a detailed account of both these processes. Frictional sliding involves the sliding of grains past one another within

an aggregate, without the individual grains themselves being deformed. This process is associated most frequently with unlithified sediments. Fracture processes involve nucleation of, and displacement along, new fracture surfaces during deformation (Knipe, 1989). The fracture surfaces are seen at all scales of observation from the tectonic to the grain scale and smaller (Lloyd and Knipe, 1992). Crystal plastic processes have also been inferred to operate at the tips of fractures during cataclasis. (Meredith and Atkinson, 1983; Lloyd and Knipe, 1992 and Knipe and Lloyd, 1995).

2.1.2 Crystal Plasticity

Within the regional setting of Ballachulish, crystal plastic processes will be shown to dominate deformation prior to the Ballachulish intrusion. Thus, the discussion concerning crystal plasticity is presented here in far more detail than that of diffusive mass transfer and cataclasis. Crystal plasticity involves the accommodation of strain by intracrystalline processes such as the movement of lattice defects (dislocations) and twinning (Garofalo et al. 1961, Poirier and Nicolas 1975, White S.H. 1976 and Knipe, 1989). Lattice defects include atom vacancies (involved in diffusional creep mechanisms) and linear arrays of vacancies known as dislocations (Figure 2.2). Intimately associated with crystal plasticity is recovery, although strictly it is not a deformation mechanism. Crystal plastic and recovery processes will therefore be discussed together, and their combined effects upon dislocations, subgrain and grain microstructures assessed. Accumulation of strain without any related increase in stress is direct evidence that a rock is deforming by crystal plasticity. However, in nature perfect crystal plasticity is relatively rare; generally there is a relatively small increase in stress as strain increases.

Dislocations are the fundamental microstructural element which is utilised to accommodate strain during crystal plastic deformation. Two types of dislocation occur, namely edge dislocations and screw dislocations (Figure 2.3). Edge dislocations accommodate an extra half lattice plane within a crystal and have a Burgers vector (defined below) which is normal to this lattice plane (Figure 2.3a). Screw dislocations join two half lattice planes around a dislocation line in a helical fashion and have a Burgers vector parallel to the dislocation line (Figure 2.3b).

an aggregate, without the individual grains themselves being deformed. This process is associated most frequently with unlithified sediments. Fracture processes involve nucleation of, and displacement along, new fracture surfaces during deformation (Knipe, 1989). The fracture surfaces are seen at all scales of observation from the tectonic to the grain scale and smaller (Lloyd and Knipe, 1992). Crystal plastic processes have also been inferred to operate at the tips of fractures during cataclasis. (Meredith and Atkinson, 1983; Lloyd and Knipe, 1992 and Knipe and Lloyd, 1995).

2.1.2 Crystal Plasticity

Within the regional setting of Ballachulish, crystal plastic processes will be shown to dominate deformation prior to the Ballachulish intrusion. Thus, the discussion concerning crystal plasticity is presented here in far more detail than that of diffusive mass transfer and cataclasis. Crystal plasticity involves the accommodation of strain by intracrystalline processes such as the movement of lattice defects (dislocations) and twinning (Garofalo et al. 1961, Poirier and Nicolas 1975, White S.H. 1976 and Knipe, 1989). Lattice defects include atom vacancies (involved in diffusional creep mechanisms) and linear arrays of vacancies known as dislocations (Figure 2.2). Intimately associated with crystal plasticity is recovery, although strictly it is not a deformation mechanism. Crystal plastic and recovery processes will therefore be discussed together, and their combined effects upon dislocations, subgrain and grain microstructures assessed. Accumulation of strain without any related increase in stress is direct evidence that a rock is deforming by crystal plasticity. However, in nature perfect crystal plasticity is relatively rare; generally there is a relatively small increase in stress as strain increases.

Dislocations are the fundamental microstructural element which is utilised to accommodate strain during crystal plastic deformation. Two types of dislocation occur, namely edge dislocations and screw dislocations (Figure 2.3). Edge dislocations accommodate an extra half lattice plane within a crystal and have a Burgers vector (defined below) which is normal to this lattice plane (Figure 2.3a). Screw dislocations join two half lattice planes around a dislocation line in a helical fashion and have a Burgers vector parallel to the dislocation line (Figure 2.3b).

The movement of one dislocation through a crystal offsets the lattice planes above the dislocation from those below to produce an increment of strain equivalent to the lattice spacing (Figure 2.4). It is by movement of dislocations in this manner that strain may be accumulated within a crystal. A dislocation moves through a crystal, leaving in its wake a 'slipped' region whilst ahead is a region of 'unslipped' lattice planes. Thus, lattice planes above and below the slip plane are gradually offset in a 'caterpillar' motion as a dislocation glides along a 'slip plane' (Figure 2.4, Poirier, 1985). The increment of strain produced when the dislocation has passed through to the edge of the crystal (i.e. the lattice spacing) is referred to as the Burgers vector (Figure 2.2). It would seem that the amount a crystal may strain is proportional to the number of dislocations which are contained within that crystal. However, Frank and Read (1950) showed that dislocations may be continuously generated within a crystal at 'Frank-Read' sources (Figure 2.5). These occur when a dislocation is pinned at either end by impurities, or vacancies, i.e. "bound dislocations". The bound dislocations bow out under stress in an expanding dislocation loop until the loop grows to such an extent that two parts of the same dislocation touch. At this moment the dislocation divides into two: a large unbound dislocation loop and a new dislocation segment springs back into the original position pinned by the impurities. The process of continued generation of dislocations and slip along lattice planes may produce large amounts of strain within one crystal. The density of dislocation loops generated at Frank-Read sources within a crystal is proportional to the magnitude of the stress exerted upon that crystal (Friedel, 1964).

Bulk strain within a rock aggregate may be accumulated by continuous production of dislocations together with glide along slip planes within each individual crystal. A number of slip planes within a crystal may operate simultaneously. Furthermore, it has been shown that for an aggregate deforming by crystal slip alone, at least five crystal slip systems must operate simultaneously to prevent gaps appearing between adjacent grains (Figure 2.6 - Ashby, 1973 and Wenk and Christie, 1989). The necessity of five crystal slip systems operating together is known as Von Mises criterion (Ashby 1973). Obviously when other processes are active during deformation (e.g. diffusion and nucleation), Von Mises criterion may not be met. Crystal fabric modelling (Etchecopar 1977) has indicated that single crystals may not actually deform using five slip systems, but that one slip system may dominate the deformation. In these situations, diffusive mass transfer, grain boundary migration, grain boundary sliding and nucleation are

significant processes during microstructure and microtextural development which prevent gaps occurring between adjacent grains within the aggregate. Lloyd and Freeman (1992) present a detailed analysis of subgrain orientations within single crystallites. The data from the analysis suggests that in nature it is relatively common for one crystal slip system to operate during deformation.

During plastic deformation, materials may deform inhomogeneously: i.e. strain and/or strain rate will vary spatially within a sample and at any one point within an aggregate the strain and strain rate will vary through time. Thus, deformation is cyclic with strain rates increasing and decreasing through time and strain being partitioned from area to area within the aggregate (Poirier, 1980, Ord & Hobbs, 1989, Knipe, 1989). An area within a sample where strain rate is relatively high in comparison to the mean strain rate is referred to as a microstructural instability, and the material is locally mechanically soft. The microstructural properties of an instability may change as a result of stress/strain partitioning. For example, it is common to find grain sizes and subgrain sizes to be low in a zone of instability (Prior et al., 1990 and Magennis, 1993). The development of instabilities frequently occurs in a cyclic manner through time, a zone will soften (perhaps as a result of decreasing grain size) and therefore the strain rate increases, but, as stress is partitioned into the zone of instability, dislocations may glide more rapidly and tangle and the material again becomes more difficult to deform, resulting in a strain rate drop.

Superimposed on bulk rock cyclicality and instability evolution is a localised cyclicality on an intracrystalline/intercrystalline scale. In effect, crystals may harden and soften in a periodical manner. The many processes responsible may be grouped together in the "umbrella" terms of 'hardening' and 'softening'. Most hardening and softening processes are active to some extent during deformation. However, some styles may dominate depending upon the temperature and stress conditions. Hardening and softening may occur on a crystal by crystal basis (as is the case during dynamic recrystallisation) or as an instability on the scale of 100s to millions of crystals (i.e. a crustal shear zone).

2.2 Rock Rheologies

A rheological model is a mathematical description of the relationship between the amount a rock will strain and the magnitude of the differential stress imposed on the rock (these equations are commonly termed flow laws). Typically, a rheological model predicts the influence of a microstructural parameter (e.g. grain size) or a deformation mechanism (e.g. diffusive mass transfer) on the strain/strain rates at which a rock may deform. Rheological models, specifically flow laws, have been used to help to explain the geometric complexities of crustal deformation (e.g. Byerlee, 1968; Kirby, 1977; Ord & Hobbs, 1977; Kirby, 1985; Chopra, 1986; Handy, 1989, 1990, 1991). A detailed knowledge of flow laws enables the use of microstructures preserved within deformed tectonites to assess environmental and material controls during a deformation event (e.g. palaeostress magnitudes via palaeopiezometry - White 1979; Nicolas, 1978; Christie and Ord, 1980; Blenkinsop and Drury, 1988; Twiss, 1977; Twiss 1986; Weetmann, 1968; Christie et al., 1980; Hacker et al., 1990, 1992).

Flow laws and palaeopiezometers have been formulated over the past few decades based on the processes outlined above. An underlying assumption to all these equations is that steady state creep (deformation at a constant stress, temperature and strain rate) is attained during a deformation event. The earlier discussion (section 2.1) indicating that a variety of microstructural elements interact simultaneously to accommodate strain would seem to render this assumption unlikely. However, it has been shown that single process may dominate deformation at any one time. For example, Weeterman (1968) developed a theoretical flow law in which strain rate is controlled by dislocation climb. Hardening and other recovery processes do occur and even outpace the rate of dislocation climb. The result is that dislocations become entangled and build up behind obstacles. Further strain can only be attained as dislocations recover by climb, and once a dislocation climbs to another lattice plane, dislocation glide may ensue once again adding increments of strain to the crystal. Steady state deformation is therefore attained, during which the strain rate is controlled by the rate at which dislocations climb.

Application of flow laws and palaeopiezometers to natural tectonites is only possible if the relative contributions of active processes is accounted for. For example Lloyd and

Knipe (1992) and Atkinson and Meredith (1987) discuss the importance of sub-critical plastic flow during fracture of rocks. Any use of a fracture flow law without accounting for plastic flow would be totally inappropriate. The deformation history of a rock aggregate needs to be understood before applying a flow law/piezometer. It is necessary that the preserved microstructure reflects a single event in that history where a specific mechanism was dominating the deformation. Potentially, it is possible to use microstructural evidence from a variety of microstructures to construct a deformation history showing the evolution of stress and deformation mechanisms through time via the use of palaeopiezometry or flow laws. For example, a rock may have reached steady state plastic flow, and later fractured in a steady state manner, and so the resultant microstructure would contain evidence of both events.

When modelling rheological properties of rocks it is important to decide which flow law is appropriate. This involves taking into consideration both environmental and material controls. It is also important to consider these controls when using microstructures as palaeopiezometers. If rocks are deforming at known temperatures, stress flow laws can be applied to predict which microstructures should develop. When microstructures are examined from natural tectonites, it is necessary to understand the effects of temperature on the deformation processes themselves, but also the effects temperature may have on the rock fabric after deformation. Any alteration of a microstructure in a non-deforming system (e.g. post deformation) is a static microstructural change. Static processes generally involve recovery of microstructures and are therefore referred to as static recovery.

2.3 Processes Affecting Rock Rheologies

2.3.1 Hardening

Rheologically, hardening is defined as the decrease in strain rate at a constant stress. Dislocation glide is envisaged as the process responsible for hardening as dislocations (often gliding on different slip planes) interact to produce dislocation tangles or build up behind obstacles in a slip plane (Figure 2.7). Dislocation tangles and obstacles impede dislocation glide and further strain cannot be achieved until the dislocation structures reorganise via recovery, or the stress acting on the system increases. In extreme cases,

stress is able to build up as strain cannot be accommodated, dislocations become more and more entangled and eventually the rock fractures.

2.3.2 Softening

Softening can be demonstrated to be active during deformation when there is an increasing strain rate at constant stress. Mechanistically, softening involves recovery of the material by the processes of dislocation climb, cross slip, dislocation annihilation and polygonization.

2.3.2.a *Recovery by Dislocation Climb*

Dislocation climb is potentially a deformation mechanism in its own right in a situation where shortening is perpendicular to the climb plane. When two edge dislocations, with different Burgers vectors glide on the same slip plane they will become entangled and neither is able to slip any further. However, if one of the dislocations moves normal to its slip plane (Figure 2.8) by one lattice plane both dislocation segments can resume slip unhindered (Friedal, 1964; Poirier & Nicolas, 1985). The movement of a dislocation normal to its slip plane is dislocation climb. In a similar way, dislocations may overcome obstacles by climbing to another lattice plane and bypass the obstacle. Dislocations climb by the diffusion of atoms away from or towards the dislocation line. Dislocation climb is therefore a diffusion process controlled by the kinetics of diffusion and as such is temperature dependent.

2.3.2.b *Recovery by Cross Slip*

A screw dislocation is an imaginary line about which lattice planes are rotated in a helical fashion (Figure 2.3). This contrasts with edge dislocations which occur at the end of a half lattice plane. The helical geometry of screw dislocations does not allow them to climb in the same way as edge dislocations via atom removal. However, screw dislocations may recover by distorting the helix and transferring slip on to another plane whilst retaining the Burgers vector of the dislocation (Figure 2.9, Friedel, 1964).

2.3.2.c Annihilation

Where two dislocations of opposite burgers vector meet they will mutually annihilate each other. Dislocations of opposite sign may encounter one another whilst gliding, climbing or cross slipping. The resultant annihilation event removes the strain fields associated with each dislocation.

2.3.2.d Polygonization

Associated with every dislocation is a stress/strain field. The total energy of a work hardened crystal containing many dislocation tangles may be reduced by re-arranging the dislocations into lower energy configurations. Polygonal arrays of dislocations are a low energy form which may be achieved by mutual annihilation of dislocations, climb and glide (Figure 2.11). An extreme form of polygonization is the formation of dislocation walls, whereby dislocations of one sign collect together to form an array of dislocations separating areas of pristine crystal. It can be seen in Figure 2.10 that the areas of pristine crystal are misoriented by an amount proportional to the burgers vector of the dislocations and the number of dislocations. The resultant microstructure observed is that of subgrains, separated by subgrain walls or boundaries (dislocation walls).

2.3.3 Cyclicity of Hardening/Softening

Deformation generally proceeds through time in a cyclic manner as environmental controls evolve and as lithological controls react to the deformation itself (see Figure 2.1). At low temperatures (or high stresses), recovery by climb, which is rate controlled by diffusion, is relatively slow. The generation of dislocations and subsequent work hardening will far outpace recovery, inhibiting plastic flow as dislocations tangle. Lithological controls during a hardening event may feedback into environmental controls, causing stress to transfer within the aggregate to an area which may be more easily deformed. Therefore, locally, the environmental controls change, perhaps reducing the stress in the work hardened portion of the rock, allowing tangles to recover as the relative rates of recovery and hardening change.

Dislocation climb is rate controlled by diffusion and so increases exponentially with temperature in keeping with diffusion rates. Thus, recovery will dominate crystal behaviour during deformation at high temperatures, whilst at low temperatures (or high stress) the opposite is the case with hardening processes dominating the deformation mechanisms. It is common at low temperatures for crystals to harden to such an extent that stress builds up until fracturing occurs. It can be seen that the style of cyclic deformation within a rock aggregate depends on mutual interaction of temperature, stress, strain rate and rock microstructures all of which may vary during the progression of deformation (e.g. Knipe, 1989).

2.3.4 Dynamic Recrystallization

Dynamic recrystallization is a work softening process, acting on the grain to grain scale within an aggregate. It is not a deformation mechanism in its own right, although the microstructures produced are characteristic of highly strained rocks. Urai et al., 1986 describe dynamic recrystallization as a two phase recovery process, involving subgrain rotation and grain boundary migration.

2.3.4.a Subgrain Rotation

A subgrain is an intracrystalline feature, consisting of pristine material of similar orientation, separated from other areas of pristine material (other subgrains) by arrays of dislocations known as subgrain boundaries (Figure 2.10). The arrays of dislocations within a subgrain boundary cause a misorientation between the two subgrains that it is separating. The magnitude of the misorientation can be calculated from the number of dislocations contained within the boundary and their average Burgers vector.

$$\theta = \frac{b}{d}$$

Equation 2.1

where b is the burger vector and d is the dislocation spacing (Figure 2.10). Essentially, a subgrain is the resultant microstructure of an extreme form of polygonization. Polygonisation is the process by which a subgrain initiates, namely by movement of dislocations into low energy configurations by dislocation climb and glide. Once a

subgrain and its boundary are formed, further misorientation may be attained by subgrain rotation.

The actual processes involved in subgrain rotation are unclear, but they are likely to include the addition of dislocations of one sign to subgrain boundaries and strain accommodation across interfaces (White, 1973 and Poirier, 1985). Adjacent subgrains gradually become misorientated as dislocations enter a subgrain boundary via climb, cross slip or glide. Core and mantle microstructures, with large subgrains developed towards the centre of a grain whilst numerous smaller and equant subgrains are developed towards the edge (Figure 2.12), have been reported as microstructural evidence of subgrain rotation (White, 1976; Lloyd and Freeman, 1992).

Lloyd and Freeman (1992) define subgrains as contained within a host grain until the subgrain boundary is able to migrate. At this moment a subgrain may be treated as a 'new' grain. At low homologous temperatures, activation of grain boundary migration is relatively difficult, allowing more dislocations to enter a subgrain wall before migration occurs. Therefore, high subgrain misorientations are common at low homologous temperatures. At high temperatures, low misorientations are expected. This may not just be a reflection of the rates of dislocation glide versus subgrain boundary migration. It is possible that at high temperatures the misorientation between subgrains are low because mobile grain boundaries consume the subgrains before they are able to become misorientated by continued addition of dislocations to the subgrain wall. The effect of temperature on grain boundary mobility is depicted in Figure 2.13. Thus, at high temperatures grain boundaries are mobile and hence subgrains are eradicated before misorientations are able to become relatively large.

2.3.4.b Grain Boundary Migration

During grain boundary migration, a grain boundary sweeps through a 'highly strained' grain (i.e. a grain with high internal elastic energy) leaving in its wake a relatively unstrained grain. There is a corresponding reduction in the free energy of the system as a migration event occurs because the unstrained grain, with fewer dislocations will have a lower component of internal strain energy. It is this reduction in strain energy that is the driving force for grain boundary migration. The differential elastic strain energy

(proportional to the number of dislocations within a grain) between neighbouring grains controls the rate of boundary migration. Migration controlled by strain energy variations is termed Strain Induced Grain Boundary Migration (S.I.G.B.M).

Grain boundaries bulge away from their centre of curvature towards the grains which are being consumed, producing a distinctive amoeboidal microstructure (Figure 2.14). The migration process involves the movement of atoms from a strained grain across the interface to an unstrained neighbouring grain (Urai, 1986). The rate of migration is therefore diffusion controlled. Because the driving force for migration is the reduction in the internal elastic strain energy within a grain, which in turn is related to the stress, the size of recrystallized grains is also controlled by stress (Twiss, 1986). However, experimental and natural data show that this relationship is not simple, but is adversely affected by environmental controls such as temperature and fluids, although the extent of these controls remains poorly understood. The nature of grain boundaries and the crystallographic orientation of individual grains involved in grain boundary migration exert a second order influence on the kinetics of the migration (Lister et al., 1978; Lister and Hobbs, 1980; Etchecopar, 1977). Urai (1986) suggests that grain orientations which are able to slip on one dominant slip system deform homogeneously in contrast to grains oriented such as to accommodate strain on multi-slip systems (Kamb, 1972). Therefore, multi-slip grains, having a higher internal strain energy, tend to recrystallise more rapidly. Consequently, single slip grains grow at the expense of multi-slip grains. Furthermore, McLaren (1986) indicates that it is not only the orientation of a crystal in relation to the external stress regime which may control recrystallisation, but the orientation of grain boundaries with respect to the neighbouring grains. Stable grain boundaries may potentially influence the rates of grain boundary migration and thereby also control recrystallized crystallographic microtextures (McLaren 1986).

2.3.5 Interaction of Deformation Processes

The dynamic deformation mechanisms and recovery processes outlined above interact with each other both spatially and temporally to produce a composite microstructure. Environmental and lithological conditions vary in a periodic manner on all scales, localising deformation into discrete zones or instabilities through time and in space. Thus, on the scale of an aggregate, microstructures will vary between zones of instability

and, on a tectonic scale, deformation localises into crustal scale shear zones. It is fundamental for our understanding and interpretation of microstructures to consider just how processes interact. In order to achieve this aim an in depth knowledge of the kinetics of the individual processes involved during deformation is required. Figure 2.1 illustrates how deformation mechanisms may interact to produce a microstructure (Knipe, 1989). Feedback between variables within the system is inevitable during one deformation event. Thus, potentially small changes in one variable, or alteration of a microstructural element may have major implications for the style of deformation.

2.4 Static Recovery

Static recovery modifies the microstructure of an aggregate of crystals from a high energy state to a lower energy configuration. Deformed rocks may reside for long periods within the earth's crust not undergoing deformation, during which time they may recover. Intracrystalline recovery processes (previously described) contribute to static recovery, as well as intercrystalline processes on a grain to grain scale (Feltham, 1957; Hillert, 1965; Atkinson, 1988; Joesten, 1983; Bunterbarth and Voll, 1991; Covey-Crump and Rutter, 1989 and Joesten, 1991).

The major mechanism by which intercrystalline recovery is achieved is grain growth, whereby the average grain size of an aggregate increases with a corresponding decrease in the number of grains contained within the aggregate. Grain growth lowers the grain boundary area within an aggregate and hence both the surface energy (which is proportional to grain boundaries) and the Gibbs free energy are reduced. During a PTt (Pressure, Temperature, time) history it is common for a rock to reside for long periods of time at elevated temperatures either between deformation events or after deformation has ceased. During these periods, static recovery processes will control the microstructural rock evolution. Because a rock undergoes deformation for only limited time periods, often in a cyclical manner, it is conceivable that static recovery may affect a rock for over 90% of its PTt history. As is shown later the kinetics of diffusion limits the rates of static recovery. Thus the temperature history of a tectonite is equally as important a consideration as the actual processes of static recovery.

2.4.1 Static Recovery by Grain Growth

Grain growth is the process by which the mean grain size of an aggregate of crystals increases (Feltham, 1957 and review by Atkinson, 1988). The driving force for growth is the reduction in surface energy which accompanies the reduction in grain boundary area within the aggregate. Given sufficient time, an aggregate should evolve to the lowest energy configuration, namely a single crystal. However, in nature, such a state is never attained because opposing grain growth are various forces which inhibit the kinetics of growth to such an extent that the most stable microstructural forms are never reached. Three types of grain growth have been documented: primary recrystallization, normal grain growth and abnormal grain growth (Atkinson, 1988).

2.4.1.a Primary Recrystallization

Primary recrystallisation eradicates any deformation features which may have been inherited from a former deformation event within a rock. The forces driving primary recrystallisation are identical to those driving dynamic recovery, i.e. a reduction in the internal strain energy associated with deformational microstructures. During the cessation of a deformation event, stresses acting upon a rock gradually disappear. However, internal elastic strains and deformation related microstructures within the aggregate remain. Recovery processes continue until internal elastic strains within crystals are at a minimum. Deformation microstructures are replaced with an 'annealed' microstructure which consists of strain-free grains (containing relatively few deformation features such as subgrains, twins and dislocations). The process by which deformation microstructures are removed is commonly grain boundary migration, whereby a grain boundary migrates through a highly strained grain (with a high configurational energy) and leaves in its wake a lower energy 'strain-free' grain. Eventually, a stable grain boundary configuration is produced, with straight grain-boundaries and triple junctions tending towards 120° (Figure 2.15). Normal grain growth (see below) is active during primary recrystallization and enhances recovery rates (Covey-Crump and Rutter, 1989). Because the processes of primary recrystallization are in many ways similar to dynamic recovery processes, they may be used as an experimental analogue for dynamic recovery in a system without the added complexities that may be induced by stress and strain partitioning and/or cyclic deformation. Because primary recrystallisation is in some ways

linked to dynamic recrystallisation it may be possible to apply many of the results acquired from this investigation to zones undergoing dynamic recrystallisation.

2.4.1.b Normal Grain Growth

Kingery et al. (1976) and Brace and Walsh (1962) show that grain boundaries possess a greater energy than a perfect lattice. The additional energy is related to unbonded atoms and dislocations held within the grain boundary and is termed the surface energy. The driving force for normal grain growth is a reduction in the free energy associated with a corresponding reduction in the grain boundary area within an aggregate of crystals. Grain growth results in a texture of uniform appearance; hexagonal grains, 120° dihedral angles and an absence of deformation substructures.

The evolution of 'soap bubble froth' over a half hour time period is a useful analogy to normal grain growth in a crystalline aggregate. A foam may be produced in a container and examined over a number of minutes. During the experiment, the size of the cells of air within the froth increases and the number of cells decreases. The mechanism by which the cells coarsen is diffusion: air diffuses from smaller cells to larger cells (in effect the large cells consume the small cells). Diffusion occurs as a consequence of the curved nature of foam interfaces, an essential topological feature within a three-dimensional network which maintains grain vertex equilibrium. Smith (1952) stated that 'normal grain growth results from the requirements of space filling and the geometrical needs of surface tension'.

Many of the important effects of surfaces arise from the fact that surface energy causes a pressure difference across a curved interface (Kingery et al., 1976, pp.185). This may be seen by considering a capillary inserted into a liquid bath, from which a bubble is blown (Figure 2.17). If there is a negligible density difference, the only resistance to expansion is the increased surface area being formed (i.e. the surface tension). To maintain the bubble the pressure must be greater on the inside than the outside of the bubble. This simple experiment indicates that a force is acting on the bubble causing it to decrease in size. The force is termed surface tension and is a direct result of the surface energy of the bubble interface. The other conclusion from this experiment is that when a curved interface is introduced in any system there is, inherently, a pressure difference across that

interface. In the foam experiment it is the pressure difference across the curved interfaces which drives air to diffuse between cells, causing the mean grain size to increase. The geometry works in a similar way to the bubble experiment, the high pressure side of an interface is the concave side. Thus, air diffuses away from the centre of curvature of the interface (i.e. from the concave side to the convex side), whilst the interface itself will gradually migrate towards its centre of curvature.

Topological constraints require the introduction of curved interfaces into a three dimensional networks of cells. In a two-dimensional system, the energetic need to maintain surface tension equilibrium requires vertices (triple junctions) to have angles of 120° (Hillert 1965). This is possible only if the cells within the array are regular hexagons. If a cell of fewer than six sides is introduced into an array, a cell of more than six sides must also be introduced to maintain the tessellation of the two dimensional surface. The interface between the five and seven sided cells must be curved in order to maintain the 120° vertex angles within the network. As shown above, a curved interface will naturally migrate towards its centre of curvature in order to reduce its own surface tension. Thus the interface between the five-sided and seven-sided cells will migrate, with the seven-sided cell consuming the five-sided cell (Figure 2.18). At the moment a five-sided cell is totally consumed, a further hexagonal cell is reduced to a five sided cell, and another to seven sides. The process of consumption is therefore repeated and the process continues indefinitely, as the cell network gradually coarsens and the total number of cells is reduced.

A three-dimensional network behaves in a similar way to a two dimensional network. The angles at the vertices are kept in equilibrium, which in three dimensions is $109^\circ 28'$ (equivalent to 120° in a two dimensional network - Atkinson, 1988). A three-dimensional network with straight interfaces that tessellates and adheres to the energetic requirement of vertices of $109^\circ 28'$ is actually topologically impossible (see Atkinson, 1988). Thus, in any three-dimensional network which maintains vertex equilibrium, curved interfaces are a geometric necessity. Thus, with the introduction of curved interfaces, grain coarsening occurs in a similar manner to that of a two dimensional network. It can therefore be seen that there is a natural tendency, given sufficient time, for all aggregates to coarsen by normal grain growth.

Coarsening of cells within foam analogues can again provide useful insights into normal grain growth. However, major differences between foam evolution and grain growth in crystalline materials must be taken into consideration. Firstly, grain boundary energy may vary with crystal orientation. Secondly, growth in materials involves diffusion of atoms across grain boundaries and so diffusion kinetics control the rate at which grains grow and also the extent to which equilibrium may be attained, as opposed to the instantaneous diffusion of air in a foam aggregate. Small grains grow at the expense of larger grains and consequently a distinctive grain size distribution will form for rocks which have undergone grain growth. Feltham (1957) suggested that a log normal grain size distribution develops during grain growth and that this distribution then becomes time invariant; the mean grain size increasing as the size distribution is maintained. More recently, Hillert (1965) and Louat (1974) have indicated that distributions may develop that vary from log normal (Figure 2.16). Abbruzzese (1986) suggests that crystal orientation affects the size distribution to such an extent that a log normal distribution is never attained. Results from experimental data are varied, but nevertheless all experiments seem to produce a stable grain size distribution which is time invariant during normal grain growth.

2.4.2 Kinetics of Normal Grain Growth

Experimental investigations (Burke 1951; Feltham 1957 and Coterill and Mould 1976) on a variety of metallic and ceramic systems at isothermal temperatures have revealed a relationship between grain size and time of the form:

$$l_t^n - l_0^n = kt \qquad \text{Equation 2.2}$$

where l_t is mean grain size, l_0 is initial grain size, k is a temperature dependent variable which includes a kinetic coefficient, t is time and n is exponential factor. Turnbull (1951) approached the kinetics of normal grain growth in terms of the velocity of motion of the grain boundary with respect to a reference frame pinned to the centre of the growing grain. In order for a grain to grow atoms are transferred across a grain boundary on to the growing grain, i.e. there is a diffusive flux across the grain boundary. The displacement of a grain boundary by an increment of length dl , in the time interval dt , involves a flux of atoms of component i across the grain boundary:

$$J_i = \frac{dl}{dt} C_i$$

Equation 2.3

C_i is the effective concentration of component i in the grain boundaries. If the grain boundary is a zone of mismatch between ordered structures, then C_i varies with the angle of mismatch. The driving force for diffusion and grain growth is the chemical potential gradient across the curved grain boundary, arising from the pressure difference across the grain boundary (N.B. this pressure difference across curved interfaces is inferred by the capillary bubble experiment). Using the Gibbs-Thompson equations which relate chemical potential to the surface tension, together with absolute reaction rate theory (Turnbell 1951 and Kingery et al. 1976) it is possible to relate dl/dt to:

$$\frac{dl}{dt} = \frac{D_{igb}}{RT\delta} \frac{4\gamma V}{l}$$

Equation 2.4

where D_{igb} is the coefficient for diffusion of i in its own grain boundaries (of width δ), R is the gas constant, T is temperature, γ is the surface energy of a grain boundary and V is the molar volume. The value of D_{igb} varies with temperature in an Arrhenius relationship, so that

$$D_{igb} = D_0 e^{\frac{-Q}{RT}}$$

Equation 2.5

Within an aureole setting the simple relationship of equation 2.2 becomes:

$$\frac{l^n - l_0^n}{n} = \int_{t_0}^t k(T) dt$$

Equation 2.6

The variables unrelated to temperature may be separated out of the time integral and after substitution of equations 2.4 and 2.5 into 2.6 one can derive (Joesten 1983):

$$\frac{l^n - l_0^n}{n} = \frac{4\gamma_i V_i D_0}{R \delta} \int_{t_0}^t \frac{1}{T^{(i)}} e^{\frac{-Q}{RT^{(i)}}} dt$$

Equation 2.7

The pre-integral variables may be grouped together as a material constant k^* . It is this material constant which will be calculated using data from the Ballachulish aureole. Note

that the value of k^* is not the same as k in the equations 2.2 and 2.6, the Arrhenius temperature dependence of diffusion is included in the time integral and not the pre-integral constant k^* in Equation 2.7. Thus the value of k^* is equal to:

$$k^* = \frac{4\gamma_i V_i D_0}{R \delta} \quad \text{Equation 2.8}$$

A great deal of effort has been spent to prove the parabolic relationship between grain size and the diffusion variables with an exponent (n) is equal to two. However, experimental values of n vary between two and four (Figure 2.19). This is attributed to different types of diffusion controlling the grain growth. Martin and Doherty (1975) suggest that n values greater than two can be attributed either to solute drag (Figure 2.19), resulting in non-linear dependence of grain boundary mobility on the driving force, or a lower pressure limit below which grain boundary migration cannot occur.

2.4.3 Abnormal Grain Growth

Abnormal grain growth has been documented in many annealing experiments. Essentially a single grain is observed to grow exceptionally large at the expense of its neighbouring grains. Consequently the grain size distribution typical of normal grain growth is destroyed. The energetic reasoning behind abnormal grain growth of a limited number of grains within an aggregate has been inferred to be a result of minimising surface energy. It has been shown that large grains have a lower surface energy per volume than small grains. Thus, once a grain becomes large in relation to its neighbours, it is possible that surface energy may be most effectively reduced by allowing that grain to grow abnormally, rather than gradually coarsening the whole aggregate.

2.5 Geological Implications of Grain Growth

Grain growth occurs in all rock aggregates as they strive towards equilibrium. The rates of growth depend on the kinetics of atom diffusion within the rock aggregate which are in turn related to temperature (Gilletti, 1984). Many rocks potentially undergo grain

growth at some stage of their geological evolution, depending on their pressure, temperature, stress, and strain rate histories. Grain growth therefore needs to be considered when interpreting microstructural evolution.

The presence/absence of grain growth within a geological specimen reflects the temperature history of that aggregate. The kinetics of diffusion provide a method by which we can theoretically predict the rates of grain growth. Thus, microstructures preserve evidence of a rock's temperature history which we are able to utilise using kinetic theory. In tectonic settings with a poorly constrained temperature history, the microstructures within a rock may be used to help further constrain that history.

When the temperature history of a tectonic regime is known, together with the amount of grain growth (e.g. igneous aureoles), the rocks may yield information about grain growth kinetics. The kinetics of grain growth can therefore be assessed over geological timescales. Diffusion of chemical species is usually measured in laboratories (Giletti 1984). However, normal grain growth within rock aggregates gives us a unique opportunity to quantify diffusion coefficients on geological timescales, and hence provide a useful comparison with these laboratory studies. Examining kinetics over geological timescales is important to structural geologists, geophysicists interpreting structures at depth in the crust and mantle, and obviously for metamorphic geologists.

Grain growth may occur as rocks are being deformed. In such cases, the resultant microstructure will be a reflection of the interaction of deformation and grain growth. Investigations into rocks deforming at high temperatures must take into account the effects grain growth may have both on microstructure and crystal texture. The temperature dependence of grain growth makes such considerations even more crucial in deep crustal and mantle research and also into deformation within internal zones of mountain belts, such as the Ivrea zone of the Alps, or Nanga Parbat in the Himalayas where temperature conditions are relatively high.

2.6 Criteria To Recognise Annealing

During this investigation three methods are employed to distinguish between deformational and annealing microstructures:

- Microscope Techniques.
- Statistical Image Analysis Techniques.
- Crystallographic Techniques.

Below is an outline of some of the features which may be used to assess the extent to which a rock has been annealed within the Ballachulish aureole.

2.6.1 Microscopic Observations

It is necessary to attempt to quantify the degree to which a microstructure is annealed. This may be achieved to a limited degree using direct observations of the microstructure. The characteristics of deformational and annealed microstructures are summarised in the table below.

DEFORMED MICROSTRUCTURE	ANNEALED MICROSTRUCTURE
Elongate grains	Equant grain shapes
Small grain size	Large grain size
Irregular grain boundaries	Straight grain boundaries
Triple junctions dihedral angles deviate from 120°	Triple junctions typically 120°
Substructures within grains (i.e. undulose extinction or subgrains - White 1973a)	Few substructures within grains

High dislocation densities (Twiss 1986), dislocation tangles, subgrain walls	Low dislocation densities and dislocations which are often arranged themselves into hexagonal arrays or long straight rows.
--	---

It is observations such as those mentioned above which help us to assess in a qualitative way the rates of annealing and help improve our understanding of the processes involved in the development and destruction of rock fabrics.

2.6.2 Image Analysis Criteria

Image analysis entails the measurement of structural elements within an image (i.e. grain size or grain shape). Measurements may be relatively simple (e.g. grain areas and perimeters) or complex (e.g. fractal dimensions and fourier dimensions Russ, 1992). Image analysis may be undertaken either manually or computationally. However, with the development of computer technology, once the initial algorithms for measurement have been implemented, computation is less time consuming.

Image analysis is a stringent method of taking quantitative measurements from a rock micrograph. It avoids human error, but more importantly the method of measurement is programmed using an algorithm. Thus, the data produced is reproducible and furthermore the error bars/computational inadequacies can be assessed.

The samples used in this study have been analysed to quantify grain size, grain shape (using aspect ratios and fractal analysis), perimeter length circularity factors and triple junction angles, i.e. all those microstructural elements which may be employed to assess the degree to which a rock is annealed.

2.6.3 Crystallographic Criteria

Crystallographic preferred orientations (CPO) within rock aggregates have received much attention in recent years (Schmid and Casey, 1986; Lister, 1977; Law et al., 1986; Etchecopar, 1977). Our knowledge of the development of CPO's during deformation and their subsequent alteration during annealing is poorly constrained. At present we are

unable to use purely crystallographic evidence to indicate whether rocks have been annealed. This investigation therefore will concentrate on the affects of annealing on CPO within the aureole, and attempt to identify any crystallographic parameters which may affect the annealing process.

2.7 Conclusions

The microstructural processes of deformation outlined within this chapter form the basis by which the rock aggregates at Ballachulish are interpreted. The thesis aims firstly to quantify the degree to which rocks have been annealed in the Ballachulish aureole. This may only be assessed with reference to the microstructural processes discussed in this chapter. Secondly the interpretation of the microstructural processes responsible for the textures seen at Ballachulish are interpreted in chapter 6, using the mechanisms of microstructural modification discussed here. Furthermore the data from Ballachulish will enable a more accurate assessment of the important processes by which a microstructure is modified. Finally the rates of microstructural modification discussed in chapter 2 are estimated using the Ballachulish intrusion as a 'natural experiment' (cf. chapter 7).

Figure 2.1 The inter-relationships between lithological and environmental controls with material processes during rock deformation (from Knipe 1989).

Figure 2.2 Geometry of dislocations: a) edge dislocation as a result of the addition of an extra 'half-lattice plane' of atoms (h-h'). b) i: Cross section perpendicular to dislocation slip plane and burgers vector of a screw dislocation, showing no distortion. ii: Plan view of dislocation showing the helical arrangement of atoms, distorted by the presence of a screw dislocation (from Kelly & Groves 1970)

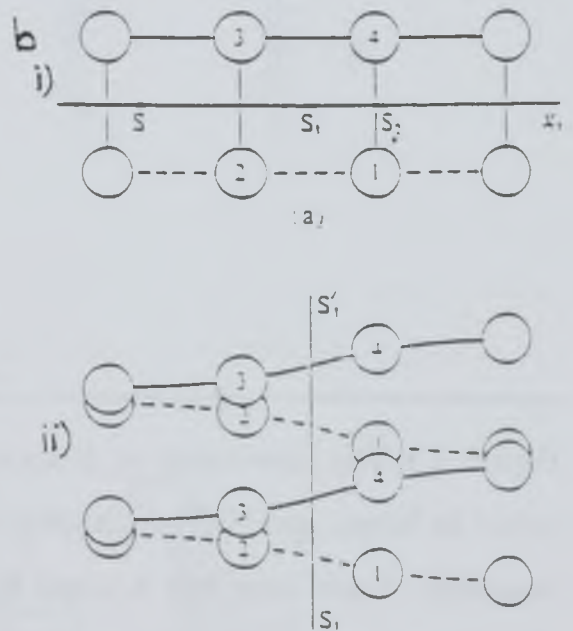
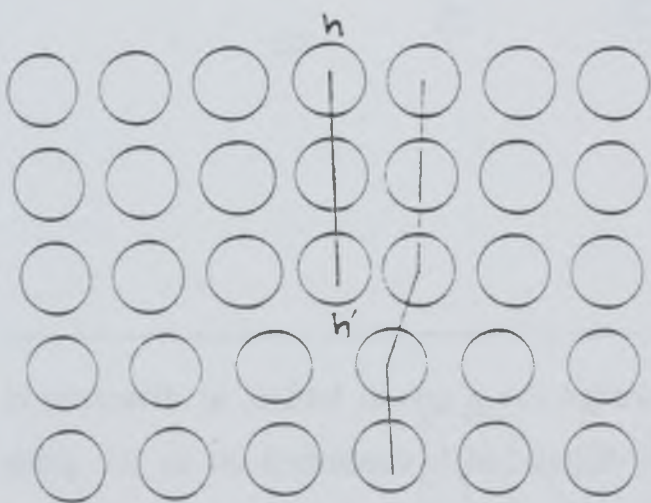
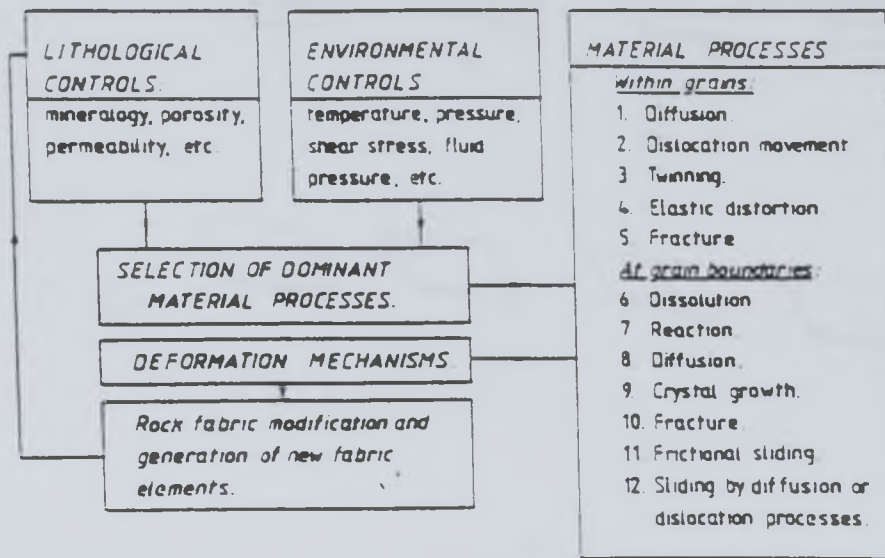
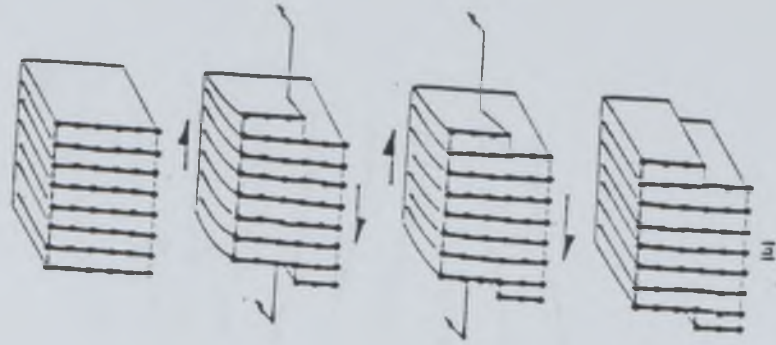
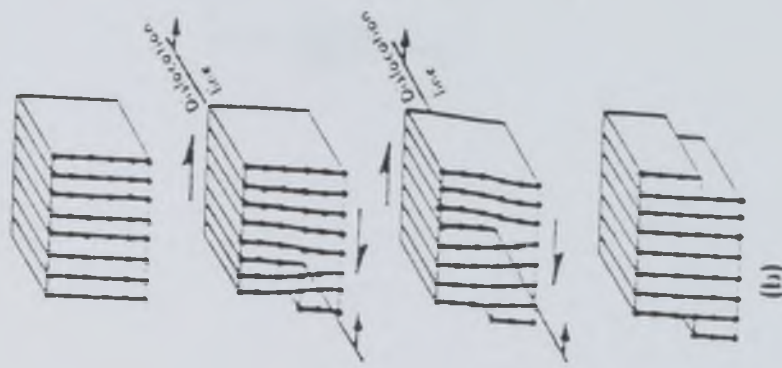
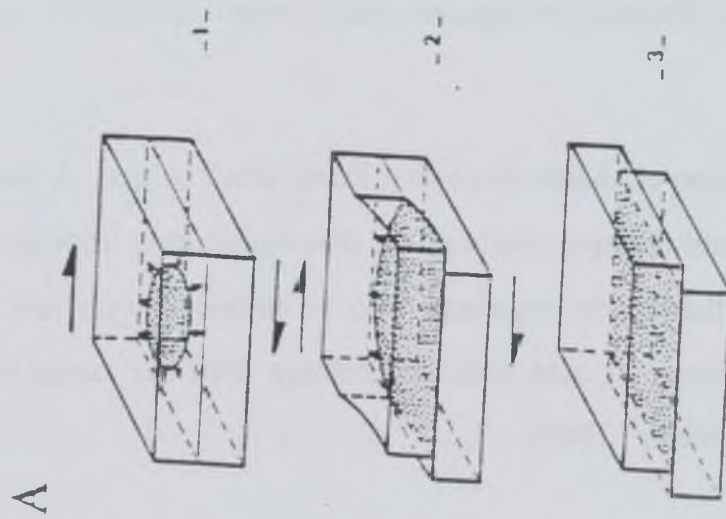




Figure 2.3 The movement of dislocations through the a crystal lattice: a) dislocations occur in loops, gradually enlarging until the dislocation is consumed on to the grain boundary. Each loop has a edge dislocation segment and a screw segment. b) The movement of an edge dislocation by detachment of lattice planes from one side of a dislocation and attachment on the other side. This motion is likened to that of a caterpillar. c) The motion of a screw dislocation is similar to ripping a piece of paper.



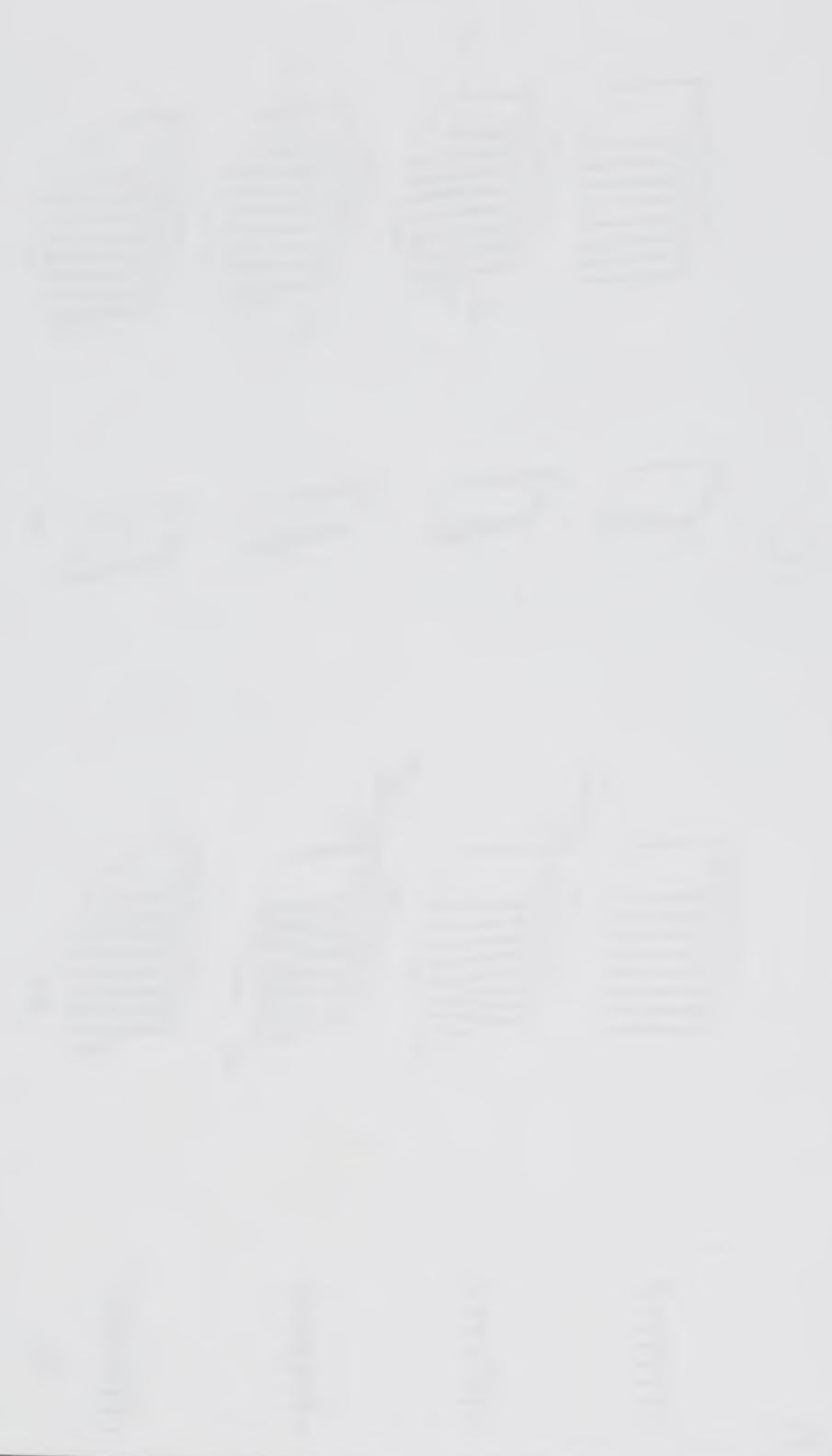


Figure 2.4 The movement of an edge dislocation through a crystal lattice produces a deformation equivalent to one burgers vector. a) Edge dislocation b) Dislocation loop containing an edge dislocation segment and a screw dislocation segment (from Poirier, 1985).

Figure 2.5 Generation of dislocations at a Frank Read source. A pinned dislocation bows out under stress until different parts of the dislocation loop impinge upon one another, at which stage the dislocation separates into an unbound loop and a pinned dislocation segment. The process repeats itself indefinitely until the stress acting upon a crystal diminishes (from Poirier, 1985).

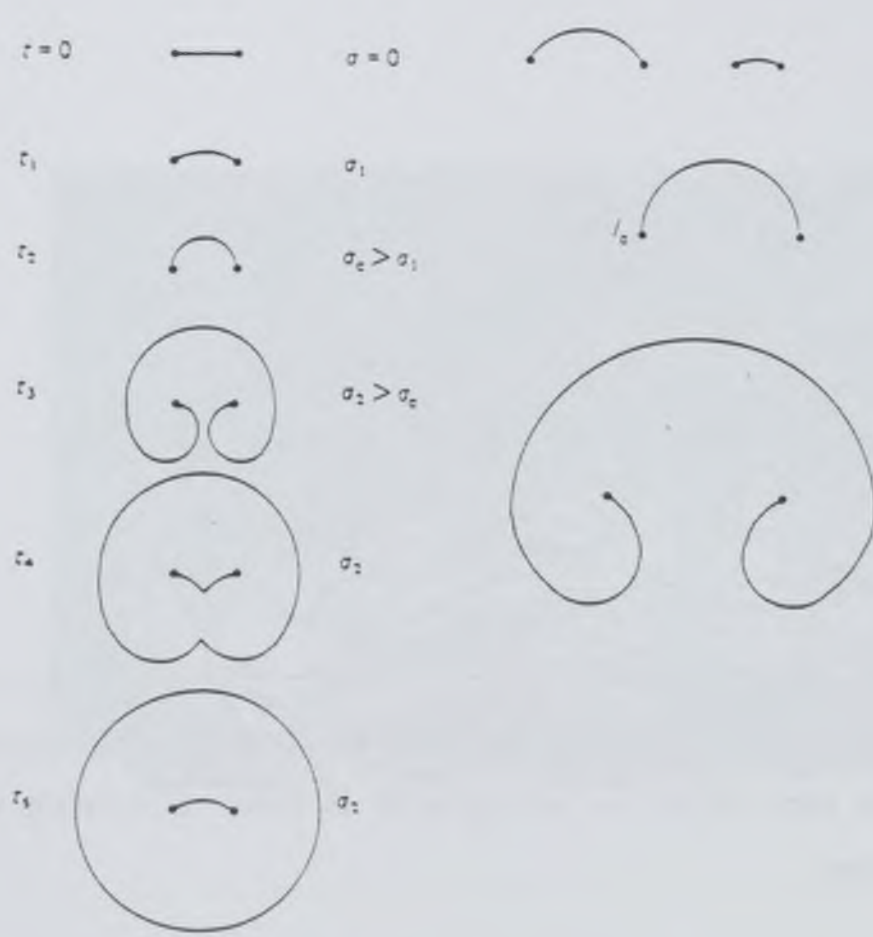
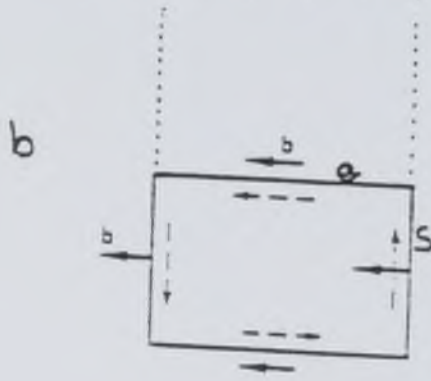
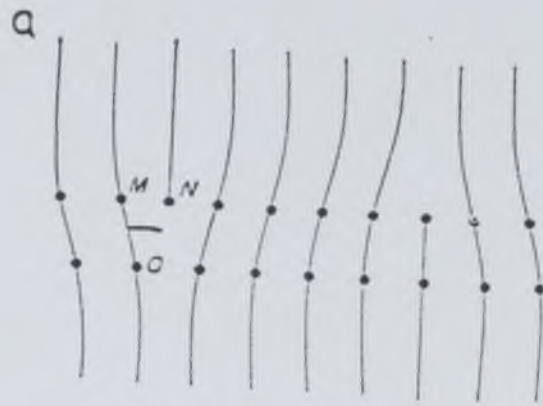




Figure 2.6 Von Mises criterion, demanding the operation of 5 slip systems at any one time within each crystal in an aggregate in order to maintain a coherent grain microstructure.

Figure 2.7 An example of dislocation tangles in silicon. This is indicative of hardening processes, which typically occur during cold working of materials (from Freidal, 1964).



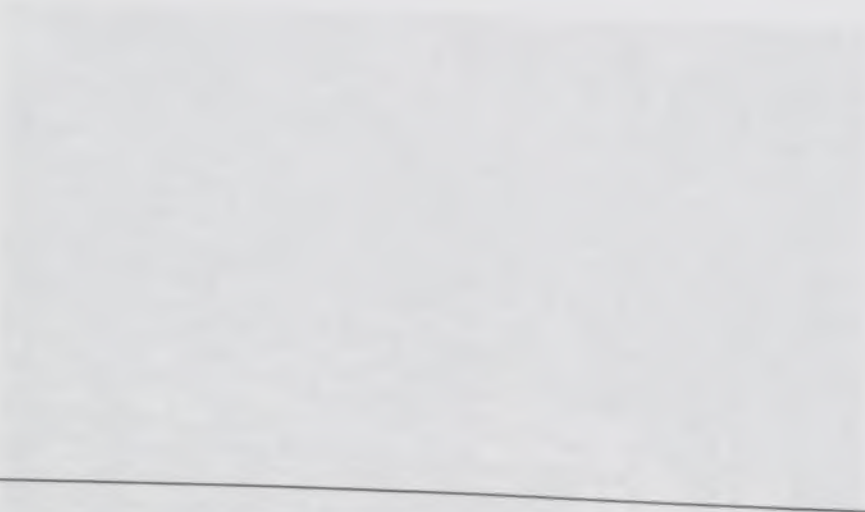


Figure 2.8 a) Climb of an edge dislocation from glide plane by removal of atoms (E) or by addition atoms (A), b is the burgers vector of the dislocation (from Poirier, 1985).

Figure 2.9 Cross slip of an edge dislocation to a different crystal plane, whilst retaining the burgers vector of slip (b). The dislocation loop *initially* expands along the horizontal lattice plane, however, then exchanges slip on to the dipping lattice plain (i.e. 'cross-slips) and the dislocation loop continues to expand (from Freidal, 1965).

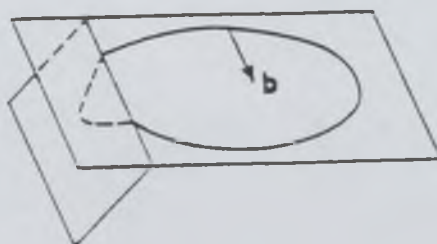
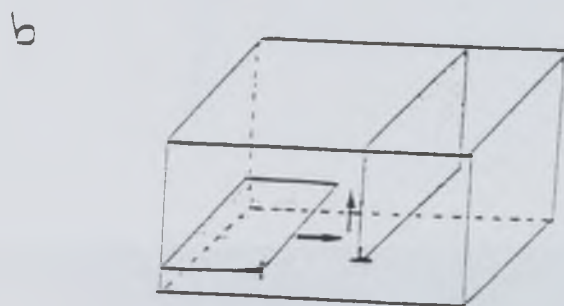
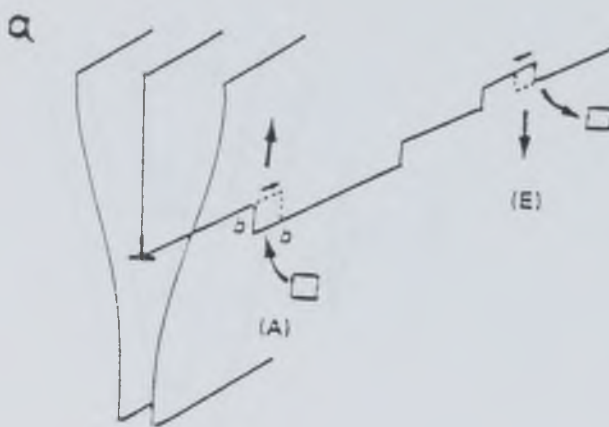
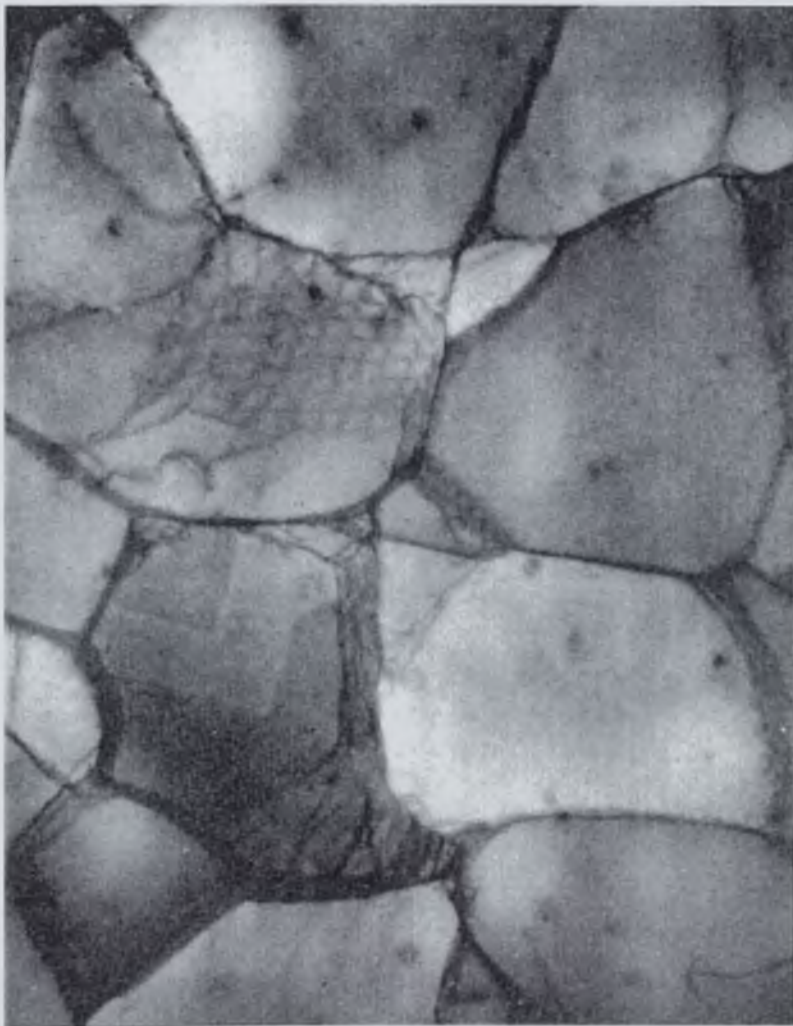
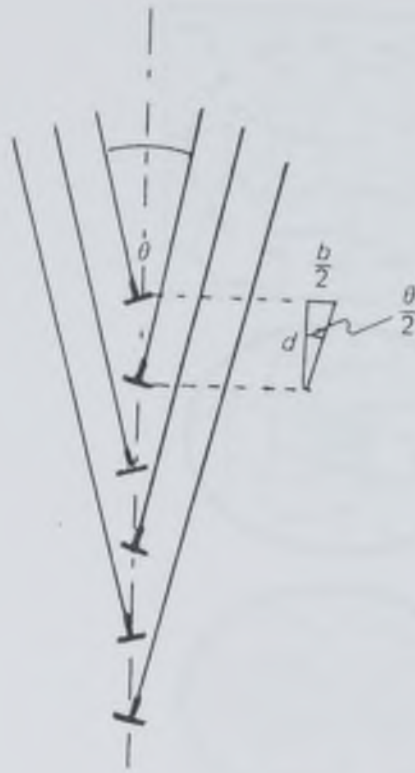




Figure 2.10 Dislocation model of a subgrain boundary (from Kingery et al. 1976). The dislocations have a burgers vector of b and the spacing $= b/\theta$, where θ is the angle of misorientation between the two subgrains.

Figure 2.11 Polygonization in highly strained aluminium (after Whelan, 1958) (35,000 \times).



SCHEMATIC DYNAMIC RECRYSTALLISATION MICROSTRUCTURAL HISTORY BASED ON GRAINS A, B AND C

Mantle
polygonal
subgrains



GRAIN A

GRAIN B

GRAIN C

SUBGRAIN POLYGONISATION

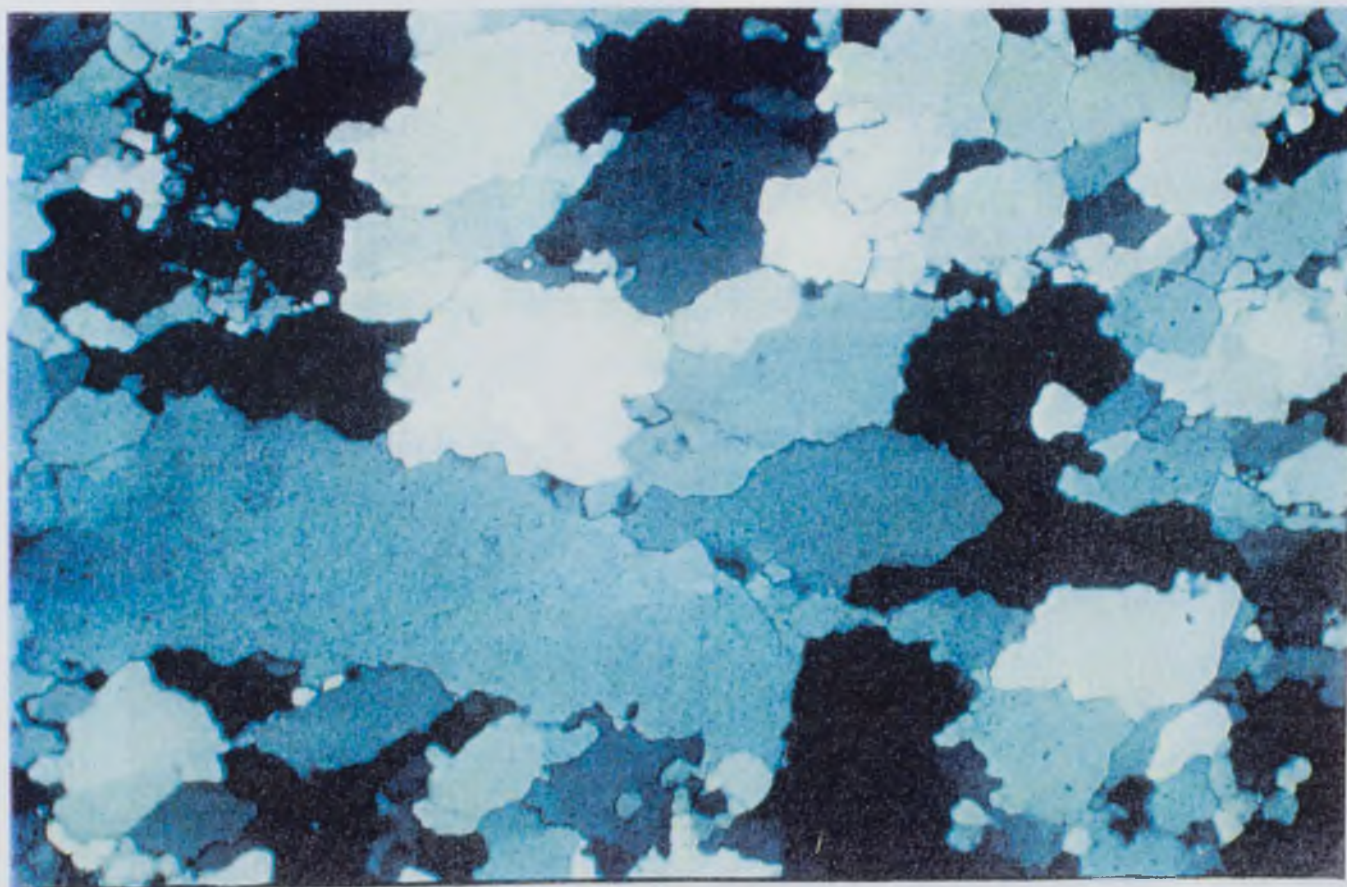
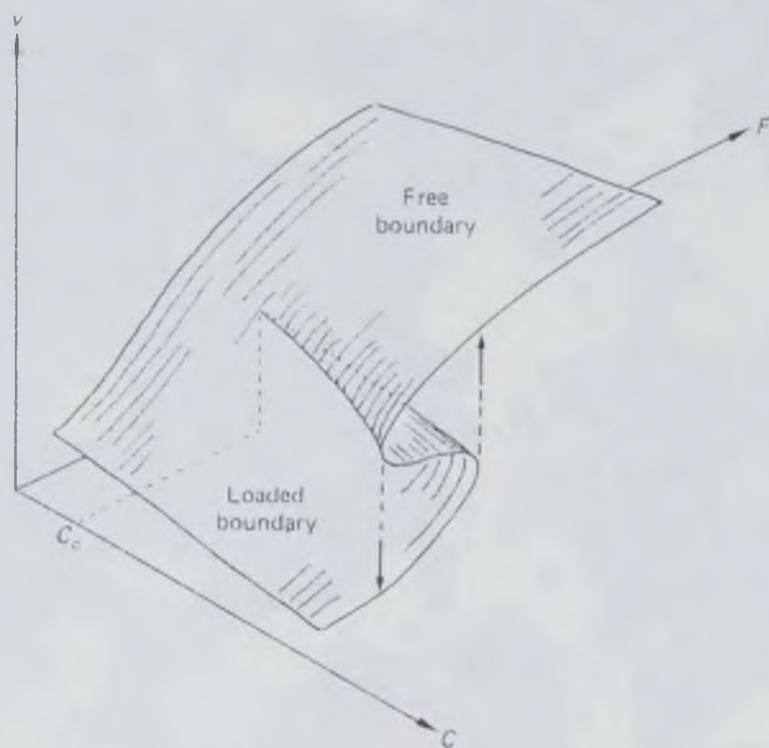
SUBGRAIN/GRAIN ROTATION

GRAIN BOUNDARY MIGRATION

INCREASING DYNAMIC RECRYSTALLISATION

Figure 2.13 Variation of grain boundary mobility (v) with respect to temperature and solute content (from Poirier, 1985). F is the driving force for migration and C is the impurity content.

Figure 2.14 Typical microstructure of a quartzite that has undergone dynamic recrystallization. Note the amoeboidal grain shapes, density of crystal substructures and the elongation of the fabric. Sample 56155, width of view 3mm.



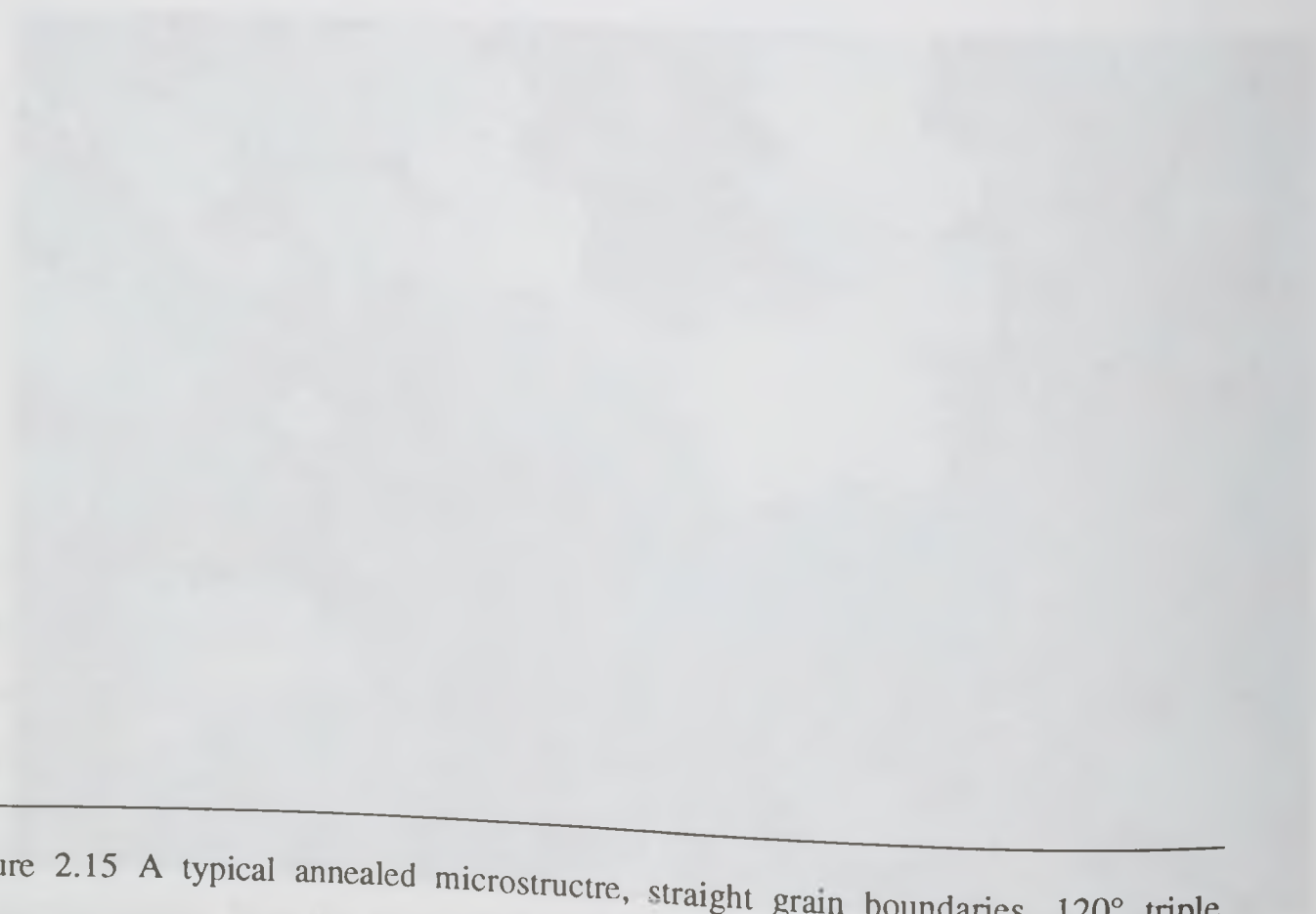
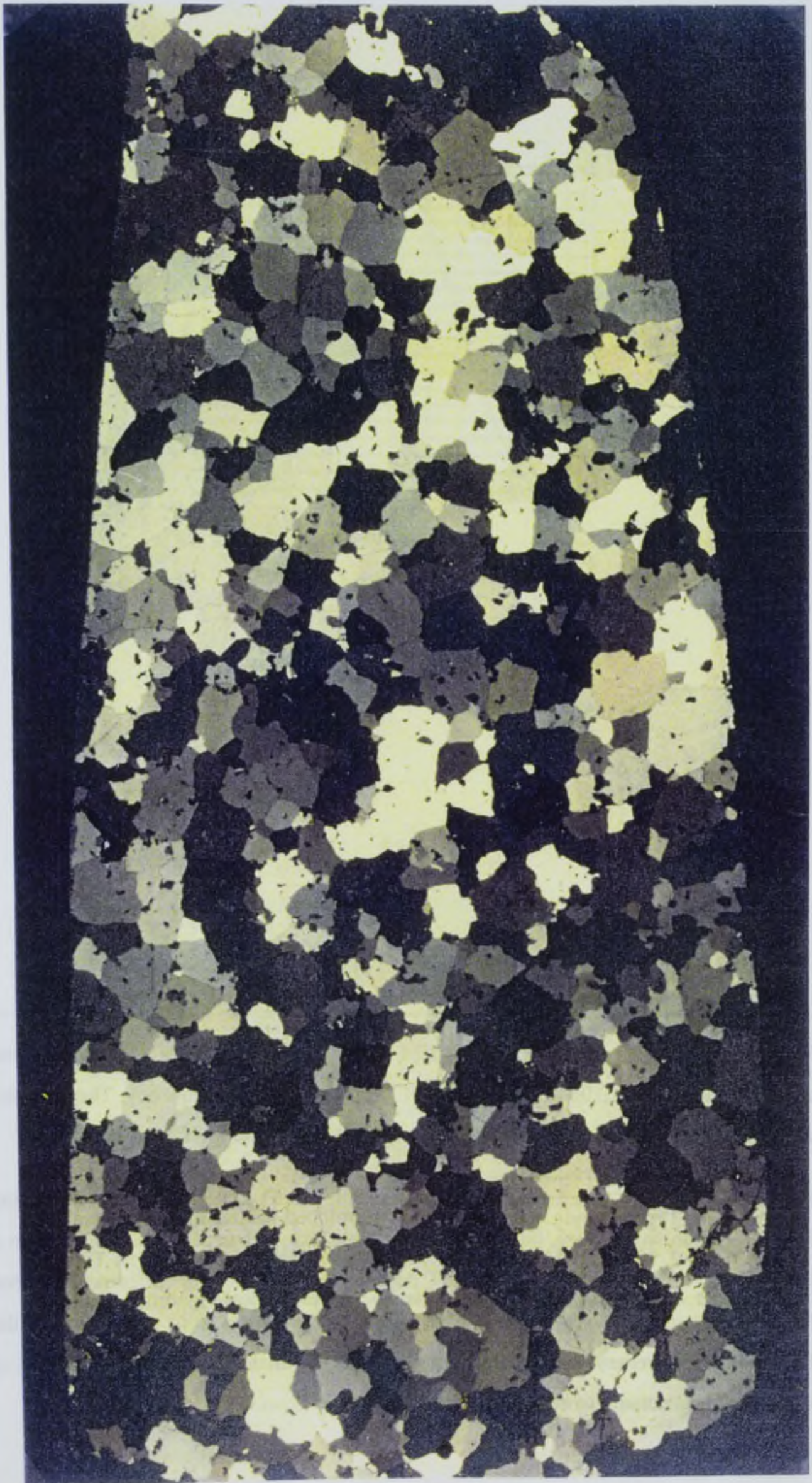


Figure 2.15 A typical annealed microstructure, straight grain boundaries, 120° triple junctions, coarse grain size and limited intracrystalline substructures. Sample 55316, width of view 4.5cm.




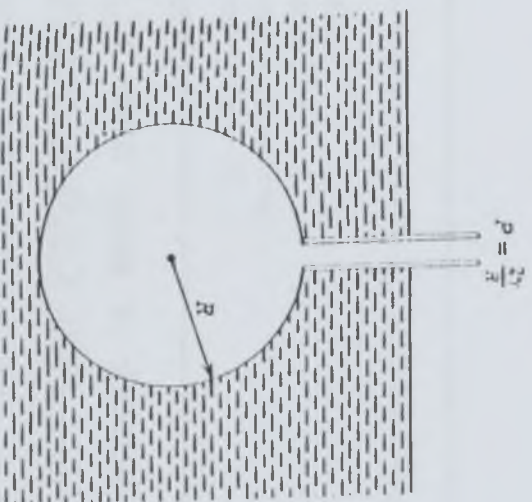
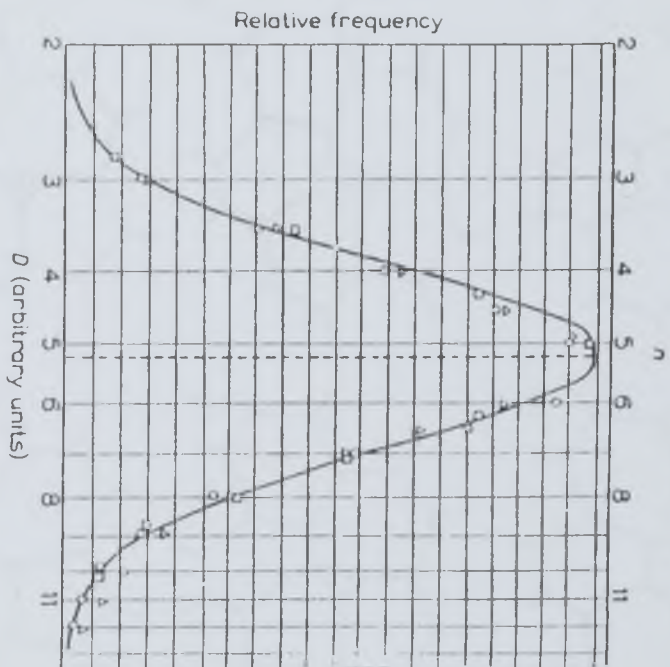


Figure 2.16 Typical grain size distribution developed within annealed ceramics and metals (from Feltham, 1954). Grain size (D) are plotted against frequency. The triangles and squares are data from Beck (1954). The line is a theoretical lognormal distribution

Figure 2.17 Capillary experiment from Kingery et al. (1976) showing that surface tension forces act upon any surface, interface or grain boundary. The capillary is inserted into a liquid, from which a bubble is blown. If there is negligible density difference between (and consequently no gravitational effects), the only resistance to expansion of the bubble is the increased surface area being created. To maintain a spherical surface of radius R it is necessary to keep the pressure at P .



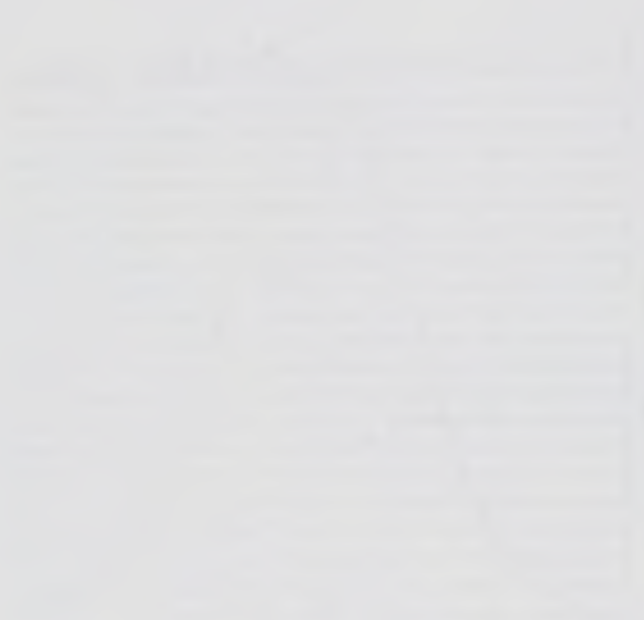
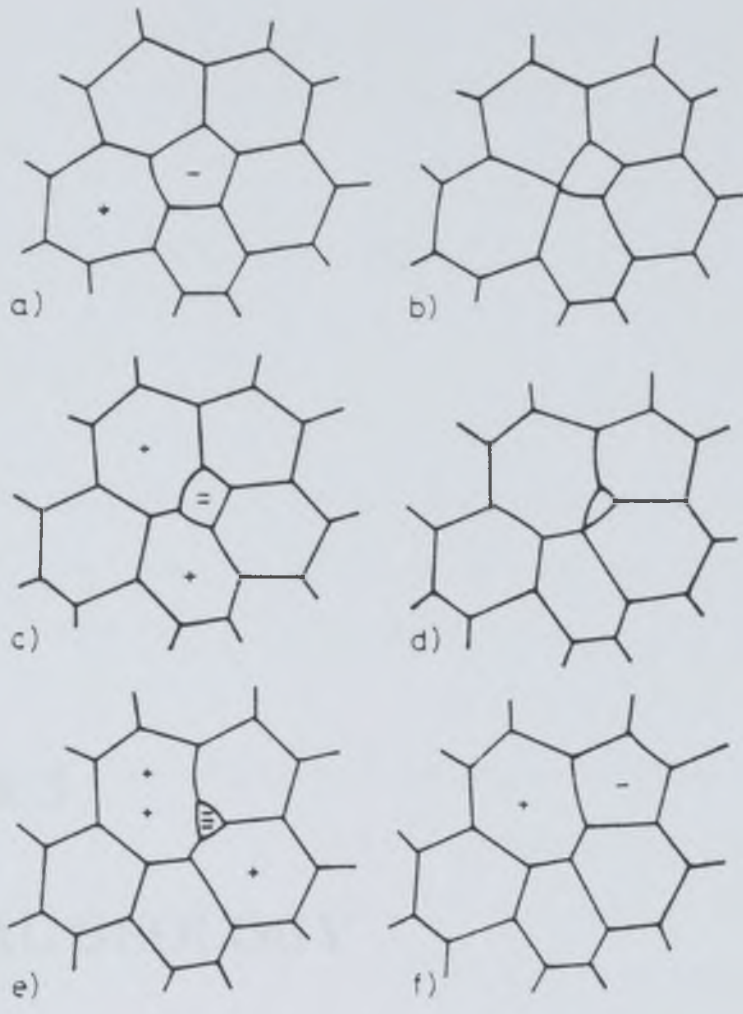


Figure 2.18 Coarsening network of grains driven by grain boundary topology, specifically the presence of curved grain boundaries at the contact between a seven sided crystal (+) and a five sided crystal (-). The five sided grain is consumed at the expense of the surrounding crystals until it is completely eradicated. At that moment another pair of 7-5 sided crystals with a curved interface are generated and the process will therefore repeat. The result of this process is that the number of grains decreases and correspondingly the average grain size increases.

Figure 2.19 Kinetics of grain growth for various mechanisms (from Atkinson 1988).



$$n \ln \frac{V^m - V_0^m}{V_0^m} = kt$$

Pore control:	
Surface diffusion	4
Lattice diffusion	3
Vapour transport ($P = \text{const}$)	3
Vapour transport ($P = 2S r$)	2
Boundary control:	
Pure system	2
Impure system:	
Coalescence of second phase by lattice diffusion	3
Coalescence of second phase by grain boundary diffusion	4
Solution of second phase	1
Diffusion through continuous second phase	3
Impurity drag (low solubility)	3
Impurity drag (high solubility)	2

P = pressure; S = surface energy.

CHAPTER 3

REGIONAL GEOLOGY

3.1 Introduction

The Ballachulish region consists of Dalradian sediments which were deformed and metamorphosed during the Caledonian orogeny. The Dalradian Supergroup is a suite of late Precambrian metasediments situated between the Great Glen Fault to the north and the Highland Boundary Fault to the south (fig. 3.1). The sediments were laid down on the Laurentian margin of the Iapetus Ocean and represent a gradual deepening of the margin as a consequence of syn-depositional extension (Harris, 1975; Harris and Pitcher, 1975; Anderton et al., 1979).

Dalradian sediments are divided into a hierarchy of sedimentary units. There are three main 'supergroups' Appin, Argyll and Southern Highland, which in turn are divided into subgroups (fig. 3.2). Rocks within the Appin Group are exposed in the Ballachulish region (Fig.3.3). A series of igneous bodies, known as the Late Caledonian Intrusives, intruded the Dalradian sediments. Some of the intrusives are coeval to deformation and

others (such as the Ballachulish Granite) post-date deformation. The lithologies exposed in the Ballachulish region are generally contained within the Appin Group.

3.2 Lithological Descriptions

3.2.1 Metasediments

Rock types within the Ballachulish aureole range from Leven schists of the Lochaber subgroup to the Cuil Bay slates of the Blair Atholl subgroup. The sequence is thought to represent a phase of basin deepening (Crane 1993).

The *Leven schists* comprise a lower psammitic schist unit which grades upwards into a grey-green phyllitic unit with intercalations of limestone. The unit often appears as a mottled brownish red colour in outcrop. The limestones in the upper part of the succession indicates a progressive decrease in the amount of terrigenous input. The unit is estimated to have originally been 1500m-3000m thick (Bailey and Maufe, 1960).

The *Ballachulish Limestone* is conformable with the Leven Schist. Typically, it is fine grained and greyish in colour, containing little or no terrigenous material. There is a transition upwards into the Ballachulish Slate.

The *Ballachulish Slates* outcrop as dark grey/black rocks which are well cleaved. Brown Iron staining along cleavage and joint surfaces is a common weathering feature within this unit. Cubic pyrite, up to 5mm in size, occur within some layers. Often the crystals are weathered out, leaving behind holes. Hall (1982) interpreted the Ballachulish Slates as evaporitic sediments, the pyrite crystals representing pseudomorphs of gypsum. Frequently, the Ballachulish Slates are seen to grade upwards into the Appin Quartzite, as the shales become interbedded with quartzose layers. This is known as the *Striped Transition unit* and records distal turbiditic influxes into a black shale environment.

The *Appin Quartzite* gradually replaces the Striped Transition unit. It is well bedded (on the scale of 2cm to 50cm) white in colour, although, it often contain pale pink feldspar impurities (up to 2cm in size). Frequently, the quartzites form positive geomorphological

features, such as cliffs on the coastline and ridges/mountains inland. Ripples, cross beds and pebbly beds occur throughout the unit, suggesting transport of the sediments from the SW. Appin Quartzite beds probably represent a NE prograding tide dominated delta.

The *Appin Limestone* and *Appin Phyllite* are interfingering units that overlie the Appin Quartzite. They reflect influxes of sedimentary material into the deltaic system. The limestone is of variable thickness. It is pale brown in colour and coarse grained. The phyllite consists of psammitic and pelitic layers which give the rock a medium to light grey appearance.

Black Slates of the *Cuil Bay Formation* succeed the open, marine oxidised sediments of the Appin Phyllite. Hickman (1975) considers the Cuil Bay slates to be shallow marine, possibly deposited in a pro-delta setting.

3.2.2 Ballachulish Intrusion

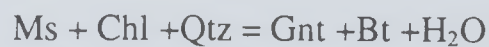
The igneous complex of Ballachulish covers an area of 7.5 by 4.5 km and intrudes the Appin Group metasediments. It is well exposed, with several stream profiles exceeding 600m in height. The pluton consists of an outer grey diorite which surrounds an inner, younger pink granite (fig. 3.3). Radiometric dates for the quartz diorites and granites indicate an age of 412 ± 28 Ma (Miller and Brown, 1965; Harper, 1967; P.E. Brown et al., 1968; Hurford 1977; Haslam and Kimbell, 1981). The intrusion was emplaced at a depth of about 11 Km (equivalent to a pressure of 0.3 GPa) within the Dalradian metasediments (Harte and Voll, 1991).

The *diorite* envelope consists of an inner ring of monzodiorite and an outer ring of quartz diorite. The monzodiorites are dark greenish/grey and contain pyroxenes of medium to coarse grain size, characterised by an adcumulus texture. Andesine, augite, hypersthene and apatite are also present as primocrysts. Intercumulus phases include opaque oxide and alkali feldspar. The quartz diorites have a variable grain size with biotite is the main mafic phase.

The main central *granite* (8 km² in extent) is porphyritic and fairly homogeneous. Euhedral alkali feldspars form reddish megacrystals with an average volume fraction of 5 - 15% (Bailey and Maufe, 1960).

3.3 Regional Metamorphism

Typically, slaty units in the Ballachulish region contain chlorite, muscovite and quartz (fig 3.4a), a mineral assemblage indicative of metamorphism at greenschist facies. The Leven schists outcropping East of Ballachulish Bridge contain chlorite pseudomorphs after garnet (fig.3.4), indicating the regional peak metamorphism reached garnet grade temperatures. Fabric analysis (Roberts and Treagus, 1974) shows that both mica crystallisation and garnet porphyroblasts are coeval with upright folding and related axial-planar fabrics within the area (see below). Pseudomorphed garnet appears in the assemblage muscovite-chlorite-quartz-biotite and a possible Fe-Mg continuous reaction may be responsible for garnet crystallisation.



Pattison (1985) applied garnet biotite geothermometry to fresh garnets within the Ballachulish region to estimate peak temperature of 467°C - 506°C using Hodges and Spear calibration (Hodges and Spear, 1982). Calcite-dolomite thermometry yield an estimate of 500°C for peak temperatures (Masch and Hauss-Aßbichler, 1991). The 470°C - 510°C geothermometry is consistent with transformation of microcline to sanidine near the garnet isograd (Kroll et al., 1989).

Pressure estimates are more difficult to ascertain. Pattison (1985) suggests peak pressures of 0.6 Gpa in the Ballachulish region. The pressure is inferred from regional pressure gradients from Knapdale in the SW to Roy Bridge in the NE (Pattison and Voll, 1991).

The temperatures of the Dalradian rocks in Perthshire at the time of intrusion are estimated ~ 250°C (Dempster, 1985). Pattison and Voll (1991) suggest that this temperature may be representative of the country rocks prior to intrusion at Ballachulish. These temperatures reflect a period of cooling and exhumation between peak metamorphism and intrusion of the Late Caledonian suite of granites at 412 ± 28 Ma (Brown et al., 1965). However, fluids rising immediately prior to the intrusion may have raised temperatures to 300°C (Pattison and Voll, 1991).

3.4 Caledonian Deformation

A variety of fabrics and fold structures are developed within the Ballachulish region. These probably developed during the progressive closure of the Iapetus Ocean (Anderton et al., 1979). Many of the structural relationships in the Ballachulish region may be directly related to the progressive nature of deformation within a similar tectonic framework. Thus, individual structures may be dated relative to one another in a series of 'deformation events' which merely reflect the local interaction of structures during a single major deformation on a regional scale (i.e. the Caledonian Orogeny), rather than several distinct orogenies.

The Appin subgroup forms a series of recumbent fold structures (nappe piles) which are separated by tectonic slides/shear zones (e.g. Fort William Slide, Ballachulish Slide). Associated with the recumbent fold structures is a penetrative cleavage. The folds, slides and penetrative cleavages are the earliest evidence of deformation in the Ballachulish area. The tectonic slides extend the stratigraphy, to the extent that in places some stratigraphic units are omitted. The slides have been interpreted by Anderton (1988) as reactivating listric normal faults within the original sedimentary basin, a model which explains their extensional geometry. Treagus (1987) disputes this, interpreting the slides as lag features during deformation. Although they extend the stratigraphy, the kinematics may relate to compressional tectonics (in a similar way to extensional shear bands within mylonites).

A deformation history has been constructed for the Ballachulish area using structural relationships found by mapping on Ardsheal Peninsula (see enclosure A). Two distinctive

cleavages are observed, with the second cleavage generally crenulating the earlier cleavage (fig. 3.5). However, both cleavages are often rotated into parallelism and cannot be distinguished from one another. The first cleavage has a variable dip as a result of folding during the second phase of deformation. The second cleavage dips consistently at a high angle to the south west.

The first cleavage is a penetrative cleavage on the scale of 0.5mm. The orientation of bedding within the Cuil Bay region is such that this penetrative cleavage is often subparallel to the bedding. It is this cleavage that is related to the large recumbent folds in the region (D1 of Treagus). The D1 cleavage is cross cut by a spaced fabric on the scale of 1-2mm, which crenulates the penetrative S1 cleavage. Associated with this fabric on a regional scale are upright folds which refold the earlier F1 folds into a hook geometry. These upright folds are interpreted by Roberts and Treagus (1977) as being the regional D3 structures. *No regional D2 structures are seen in the Ballachulish area.*

Further deformation refolded earlier structures along an ENE - WSW trend, although no planar fabric such as a cleavage is developed during this event. This deformation is inferred from the plunge of F1 and F3 folds. However, it is also possible that these changes in fold plunges may be related to reorientation of folds which had nucleated at an early stage during the earlier D1 and D3 deformation events.

Kink bands are developed relatively late during the geological history, appearing to post date all other folds and fabrics within the rocks.

A late array of faults (e.g. The Ballachulish Fault) affect both the country rocks and to a differing extent the Ballachulish intrusion. The faulting therefore is interpreted as being synchronous with the intrusion. The NE/SW trend of these faults implies that they may be associated with the movement on the Great Glen Fault.

3.5 The Ballachulish Intrusion

3.5.1 Shape Of Intrusion

Although in detail the form of the igneous intrusion is complex (see Troll and Weiss, 1991), it is necessary to extract the salient features to produce a simplified morphology for the purposes of the thermal modelling presented later (cf. Appendix A). The intrusive complex consists of three rock types: granite, quartz diorite and diorite outcropping in a ring pattern. Outcrop patterns are rarely affected by topography, indicating that the margins of the intrusion are near vertical (except above Lagnaha Farm). The core of the Ballachulish Complex is granite (3400m in diameter at the surface) which is surrounded by rings of monzodiorite and quartz diorite with thicknesses of 550m and 650m respectively. Geophysical gravity data shows that the complex extends from 1 km above sea level to 4 km below sea level (Troll and Weiss, 1991).

3.5.2 Contact With Country Rocks

The Ballachulish cylindrical intrusion has sharp, discordant contacts with the host rocks (fig. 3.6). Troll and Weiss (1991) report in some detail the variation in intrusive style at a number of localities around the intrusion. The style depends on both structural and sedimentary controls of the country rocks. In the North and South the contact truncates the main structural trend using an East-West oriented traverse joint set (fig. 3.6). In the main area of interest (south of Sgorr Dhearg) the contact dips steeply ($>80^\circ$), cross cutting the relatively shallow lying sediments (fig. 3.6). The structure of the western contact is complex (e.g. above Lagnaha Farm) and seems to use the Bein Sglauch antiform in a 'ledge' feature (fig. 3.6).

3.5.3 Textures Within The Igneous Complex

Quartz diorites have been reported to contain a planar fabric defined by elongate plagioclase laths and euhedral pyroxenes 1.5mm long (Troll and Weiss, 1989). Troll and Weiss (1989) interpret these fabrics as forming from flow during convection within the intrusive body. Within the monzodiorites a deformational fabric, produced by crystal plasticity of feldspars, is superimposed upon a convection related fabric. Crystal plasticity

of the feldspars would suggest relatively high temperatures during deformation. This deformation fabric is not developed either within the quartz diorites or the granite core of the intrusion. However, Troll and Weiss (1991) show that these two fabrics form a concentric pattern around the granitic core of the igneous complex (see Figure 3.7). They both therefore are thought to have formed in response to stress related to the intrusion of the quartz diorites or granite core (Troll and Weiss, 1991).

3.5.4 Emplacement of The Ballachulish Complex

Troll and Weiss (1991) consider the Ballachulish intrusion as a two phase sequence. Firstly, a diorite pluton (monzodiorites followed by quartz diorites) intruded in a stoping fashion. Secondly, a granitic pluton intruded diapirically into the diorite.

(a) The Diorite Pluton

The chilled margin of the initial semicircular monzodiorite with its adcumulus texture suggests that it was emplaced in a largely liquid state (Weiss and Troll, 1991). The composition was constantly modified by convective fractionation and assimilation of country rocks towards from the initial monzodiorite composition to a quartz diorite composition. Subsequent to the initial fractionation, regional tensional movements aided enlargement of the pluton, especially to the North and South (Brown, 1979).

(b) The Granite Diapir

The initial mode of emplacement of the granite interior was passive (Troll and Weiss, 1991). However, the ascent of the granite was eventually halted, whilst new material continued to be injected resulting in ballooning of the granite *in situ*. The temperatures of the monzodiorites and quartz diorites was c. 950°C and therefore these rocks behaved in a relatively ductile manner and accommodated the resultant deformation (deformed plagioclase and biotite are found in the monzodiorite). The order of crystallisation is summarised in Figure 3.8 (from Weiss and Troll, 1989). Figure 3.9 illustrates the intrusive models for the Ballachulish intrusion. The granite diapir probably replaced diorites which had previously been intruded during the first stages of igneous activity

(i.e. as part of the diorite) by a stoping process. Marsh (1982) has shown that such large scale stoping would not leave any thermal or chemical traces on the granite diapir, because rafts of country rocks exceeding 50-100m would merely sink to the base of the pluton without chemically mixing with the granite.

3.5.5 Deformation of The Country Rocks

The intrusive mechanisms of the Ballachulish Complex evolved from stoping (involving fracturing and ascent of magma) to a diapiric intrusive style later during emplacement. Deformation of the country rocks associated with stoping is limited to localised contact zones. However, there is evidence of healed fractures emanating from the igneous complex. These healed fractures are now revealed as lines of fluid inclusion trails oriented radially from the contact (fig. 3.10). Fluids driven from the magma during intrusion opened up radial fracture networks, which were subsequently kept open by the pumping of these fluids through the country rocks. Eventually the fluid pressure is reduced and the fractures close, leaving a trail of fluid inclusions (remnants of the migrating fluid) as the only evidence of the original fracture.

Deformation relating to the diapiric emplacement of the central granite core is confined to the diorite pluton (Troll and Weiss, 1991) and the zone of pelite anatexis (Pattison, 1985; Pattison and Harte, 1988). These crystal mushes/melted rocks were rheologically 'weak' and therefore protected the solid country rocks from intrusion related deformation. The lack of deformation within the country rocks makes the Ballachulish aureole ideal for studying the effects of temperature on rocks without the added complexities of intrusive deformation.

3.5.6 Thermal Conditions of The Ballachulish Complex

The crystallisation history and intrusion temperatures of the Ballachulish Complex have been summarised by Weiss and Troll (1991) in figure 3.8. The crystallisation sequence has been ascertained using petrological evidence and was geochemically modelled using pressures of 0.3 GPa and a variety of geochemical techniques. Their conclusions are summarised below.

Initially a dry monzodiorite intruded the host rocks at a temperature of 1100°C (although this temperature may well have varied around the intrusion). Weiss and Troll (1991) argue that the emplacement temperature of the initial monzodiorite varied from 1000°C near the western margin to 1100°C on the Eastern contact. They suggest that an average of 1050°C may serve as an intrusion temperature for computer thermal simulations.

The fractionation stage (i.e. percentage of original melt which had crystallised and fractionated out in terms of differentiation index - D.I.) was 49-53%. The solidus was probably at 760°C, leaving orthopyroxene, clinopyroxene and plagioclase as primocrysts. A quartz diorite melt with D.I. 59-72% and H₂O content of 2-3% evolved from this original magma as fractionation and assimilation of the country rocks ensued. Augite and plagioclase formed at 1050°-900°C, followed by oxides, apatite, biotite and hornblende (at 770°C). The fractionation models predict that fluids would have been released at 700°-690°C. Pattison (1991) calculates that these fluids would have been consumed during melting reactions within the pelitic country rocks (Pattison and Harte, 1988).

The late granitic magma core already contained primocrysts of andesine and alkali feldspar when it was emplaced at 900°-850°C. Again a hydrous phase was released near 700°C before the granitic rock reached its solidus at 680°-670°C.

3.6 The Aureole

Heat diffuses away from an igneous intrusion from the moment of emplacement. Thus, the intrusion itself will gradually cool whilst the surrounding country rocks will heat up. The region around an igneous intrusion where the rocks are heated is termed the metamorphic aureole. It is estimated that the Ballachulish intrusion was emplaced at 1100°C into country rocks of just 250°C (Buntebarth, 1991). The increase in temperatures within the Ballachulish aureole (i.e. up to 850°C at the contact) has driven a series of prograde metamorphic reactions. The principal petrographic features were described by J.S.G. Wilson, J.J.H. Teall, J.S. Flett and E.G. Bailey (reported in Bailey and Maufe, 1960). However the actual reactions involved in the metamorphism have only been established recently (Pattison 1985, 1987, 1989 and 1991).

Pattison (1991), divided the igneous aureole into a series of zones with diagnostic mineral assemblages. A sequence of reactions were established through which the regional mineral assemblages passed to produce their characteristic aureole zonal assemblage. These reactions, and the influence of rock chemistry on the mineral assemblages produced, are summarised in figure 3.11.

Rocks traced from outside the aureole towards the igneous contact record zones of increasing metamorphic grade. At lower grades within the aureole, euhedral biotite porphyroblasts overgrow a regional chlorite, muscovite, quartz, biotite fabric (fig. 3.12). Cordierite is produced at higher grades, initially by breakdown of chlorite and muscovite, and then (fig. 3.12b) with feldspar from muscovite and biotite. At even higher temperatures aluminosilicates (sillimanite/andalusite) form although these reactions are sensitive to bulk rock chemistry and therefore do not occur in all pelites.

Of particular note is the zone of partial melting described by Pattison (1991). This occurs in the Western aureole where the igneous intrusion 'ledges' underneath the country rocks (fig. 3.6). Temperatures near the contact would be elevated in this area compared to other parts of the igneous contact, leading to the partial melting of the country rocks.

3.6.1 Pressure Estimates

Troll and Weiss (1991) argue that owing to the lack of downward or upward drag of the adjacent country rocks to the Ballachulish intrusion the pressure gradient through the aureole during intrusion was isobaric. Furthermore, because uplift rates were far outpaced by heating rates (Dempster, 1985) within the aureole, the prograde pressure/temperature trajectory is also assumed to be isobaric.

Several geobarometers have been published for a number of the high grade rocks within the aureole (e.g. Pattison, 1991). Pattison states the Fe end member geobarometers of Perkins and Chipera (1985) are the most accurate means to calculate pressure. Estimates values range from 0.27 GPa to 0.32 GPa.

3.6.2 Temperature Estimates

The Hodges and Spear (1982) and Ferry and Spear (1978) garnet - biotite; cordierite - biotite, and garnet - orthopyroxene exchange geothermometers (Hartley, 1984) have been applied to a number of pelitic samples throughout the aureole (Pattison, 1991). The garnet - biotite appears to be the most accurate (Pattison and Harte, 1991). In addition, Masch and Heuss Aßichler (1991) used a calibrated T-X (CO₂) reaction grid and calcite - dolomite geothermometry for carbonate rocks, whilst Kroll et al (1991) use the microcline - sanidine transformation to pin-point the 470° - 490°C isograd.

The data from each of these various methods was collated by Pattison (1991) to construct thermal profiles constructed the aureole for a number of transects. Table 3.1 (from Pattison 1991) shows these temperature estimates and the method by which they were calculated.

All the above geothermometers assume the equilibrium of metamorphic assemblages within the aureole. There are a number of lines of evidence to suggest that equilibrium was in fact attained in the Ballachulish aureole. Mineral assemblages fit into the various trivariant and divariant fields with no overlap. Thus, overstepping due to sluggish kinetics did not occur. The variations in Mg/(Mg + Fe) and Al/(Al+Si) between co-existing minerals are consistent with equilibrium (Pattison and Harte, 1991). The pelitic mineral zones also fit very well to the prograde metamorphic reaction path seen on a calibrated reaction grid (fig. 3.27).

3.6.3 Convection Within The Aureole

Hoernes and Voll (1991) measured the $\delta^{18}\text{O}$ SMOW within individual quartz grains from samples throughout the aureole. Their intention was to correlate oxygen composition with the degree of recrystallisation and/or temperature. They concluded that oxygen isotopes did not equilibrate during metamorphism. This surprising result is interpreted as evidence for the absence of any fluid phase derived from the igneous intrusion. Thus, heat transfer within the aureole could only occur by conduction and not convection through a fluid phase.

3.7 Thermal Modelling

Our knowledge of the thermal framework of the Ballachulish aureole is somewhat limited. We are able to constrain the intrusion temperature, the initial country rock temperature and the peak temperatures at a variety of distances from the igneous contact. However, to understand of the kinetics of metamorphic reactions and the evolution of quartz microstructures within the aureole it is crucial to assess the temperature/time trajectory of rocks throughout the entire aureole and not just at a few specific places. This may be achieved by forward thermal modelling using finite element methods to solve heat flow equations (Carslaw and Jaeger, 1954). This approach is described in detail in Appendix A. The thermal models predict the evolution of temperature throughout the igneous aureole from a set of initial temperature conditions. A cylindrical heat source (i.e. the intrusion within low temperature country rocks) is assumed for this purpose.

A number of thermal models have been constructed using starting conditions appropriate for the Ballachulish complex. The basic heat flow equation (Carslaw and Jaeger, 1954) used is:

$$K(\delta^2 T / \delta X^2) = \rho c . (\delta T / \delta t)$$

where K = thermal conductivity; T = temperature; X = distance; ρ = density; c = heat capacity and t = time.

The theoretical basis of the model, together with the intrusion size and initial starting conditions are outlined in Appendix A. The discussion here is limited results obtained from running the thermal model (using a computer program, *Contact8.pas* (Barnicoat, 1982), with modifications for the purposes of this investigation).

3.7.1 Results

Numerous thermal models have been calculated each with different initial conditions and boundary conditions. This investigation is not purely study into the effects of different

variables on thermal evolution of an aureole. The thermal models produced are a means with which kinetics of microstructural evolution are to be examined. Therefore, the numerous models which have been produced will not be presented, but only the model which most closely fits mineral data, and hence is the model used for calculating rates of microstructural change. The starting conditions for the model were as follows: temperature of intrusion 1050°C, country rock temperatures 250°C, size of aureole 30km and an intrusion with a radius of 2900m.

Two graphs are presented, firstly a graph showing the temperature with respect to distance from the intrusion and secondly a graph indicating the peak temperatures attained in the aureole as a function of distance from the intrusion. The temperature history for each node is output to a data file, from which it is possible to construct a graph showing the evolution of temperatures through time at a number of locations within the aureole (Figure 3.13). Peak temperatures are attained more rapidly close to the igneous contact. For example at 100m from the contact peak temperatures are attained within 10,000 years, whereas at 8km the temperatures are still rising even after 500 000 years. This is an important consideration for microstructural development, because not only do peak temperatures vary throughout the aureole, but also the rate of change in temperature with respect to time. It is possible that this may have consequences for microstructural processes. The graph of temperature evolution through time for each node serves as a temperature framework employed to calculate the rates of microstructural change in the Ballachulish aureole.

Figure 3.14 indicates that the fit between the thermal model and mineral equilibrium data is relatively good.

A distinct possibility, that has not been discussed, is that the intrusion was not instantaneous. The flow of magma to the surface to supply volcanic eruptions could potentially pump magma through the intrusion over a period of time. This situation is modelled by resetting the intrusion temperature after each finite element calculation, thereby maintaining the intrusion temperature at 1050°C for a specified number of time steps. These models tended to have a great effect on the country rock close to the intrusion, but relatively little effect further away. Continuous intrusion models do not

compare particularly well with the mineral data. Therefore, non-instantaneous models were discounted.

Summary Statement

The regional setting of the Ballachulish intrusion and aureole has been presented. A well constrained framework of the deformation within the area, the intrusive style and the temperature history of the aureole. This provides an excellent basis for the ensuing microstructural study on the Appin quartzites and modelling of the kinetics of grain growth within single phase and polyphase materials.

Figure 3.1 Major tectonostratigraphic provinces and their bounding lineaments in Scotland, also showing the distribution of late Caledonian granites (from Harte and Voll, 1991).

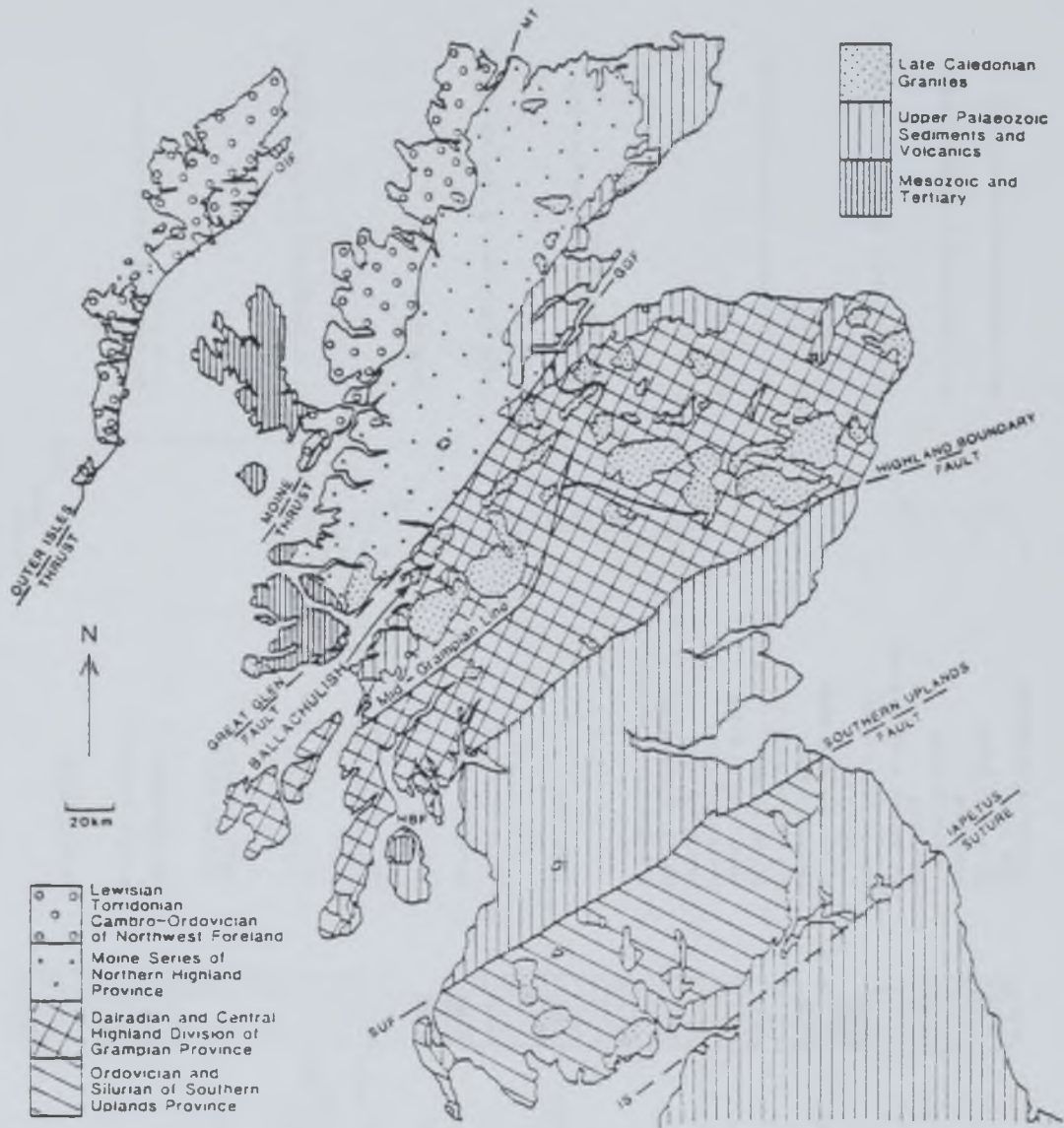


Figure 3.2 Stratigraphic log of the Lochaber-Loch Awe-Islay area (from Crane, 1993).

Composite stratigraphic log for Lochaber-Loch Awe-Islay area

Stratigraphic position of other horizons

Interpretation

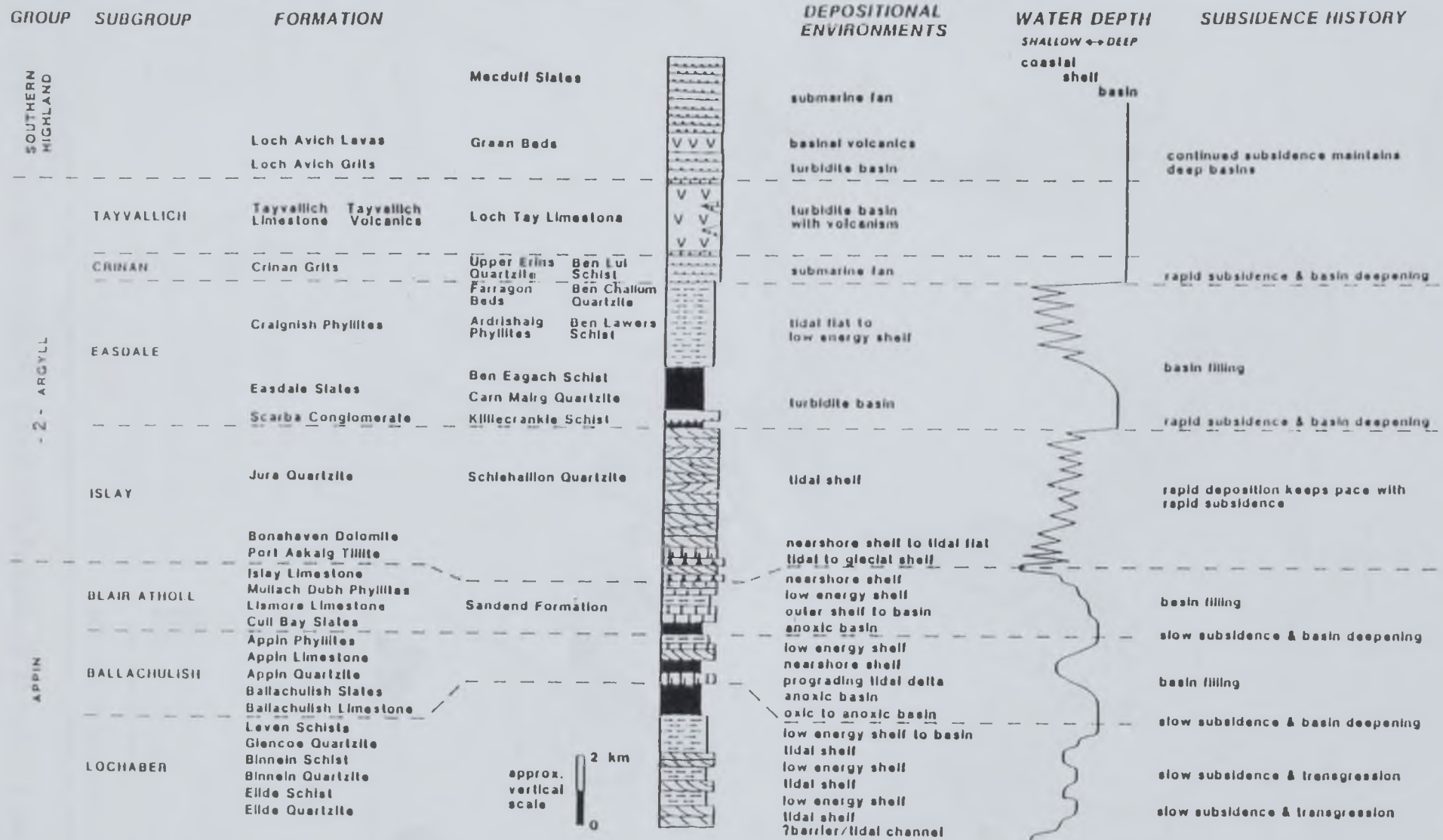
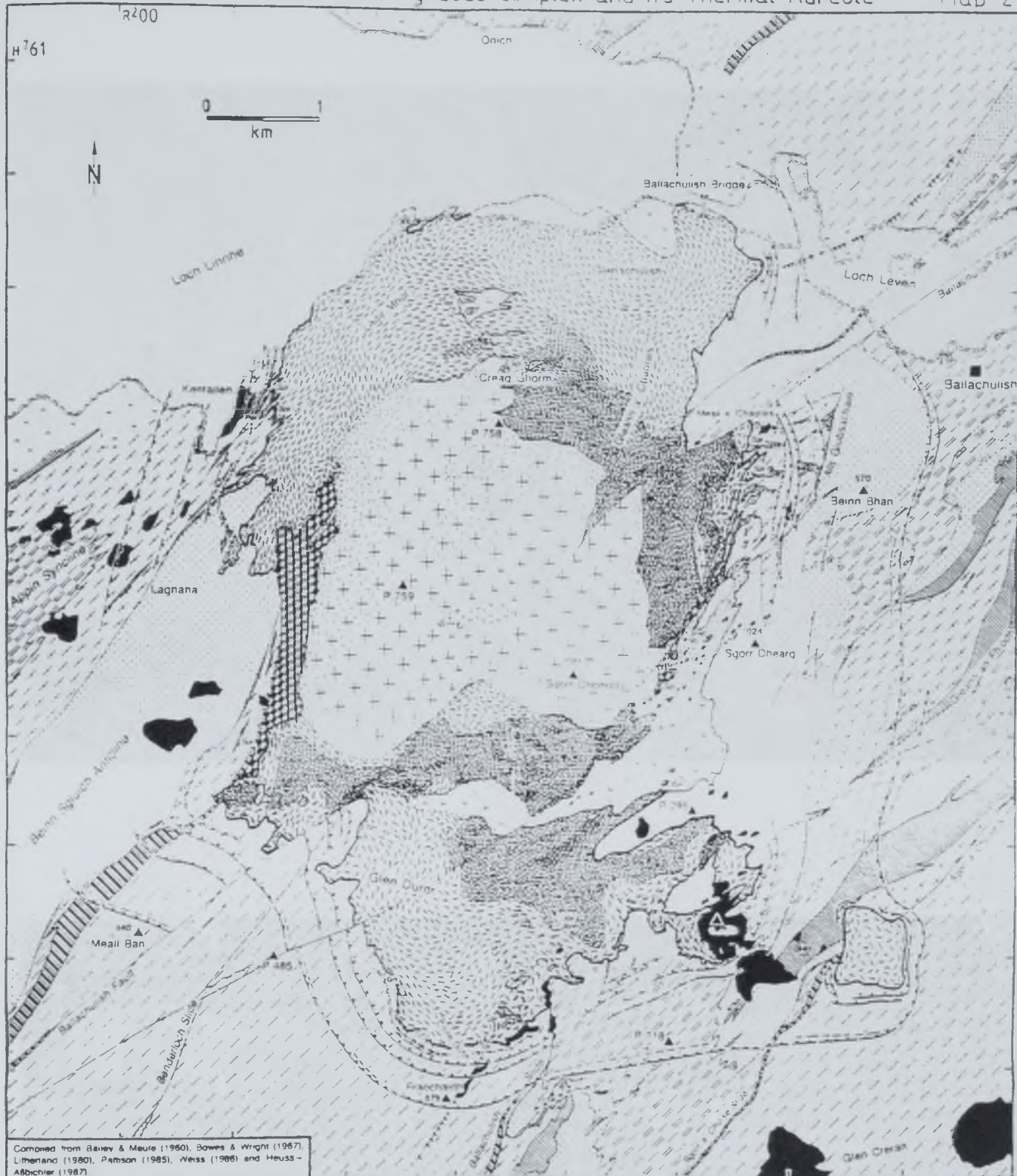


Figure 3.3 Map of the Ballachulish region, compiled by Voll et al. (1991) from Bailey and Maufe (1960), Roberts (1976), Litherland (1982), Pattison (1985) and Weiss (1986).



Compiled from Barnev & Meure (1960), Bowers & Wright (1967), Litherland (1980), Paterson (1985), Weiss (1986) and Heuss & Albrichter (1987)

<ul style="list-style-type: none"> Crean Succession Cuil Bay Slate Appin Phyllite Appin Limestone Appin Quartzite Transition Series Ballachulish Slate Ballachulish Limestone Leven Schist Glen Coe Quartzite Disrupted Pelitic Migmatites Regional garnet isograd 	<p>THERMAL AUREOLE ZONES</p> <p>C1 Dot-Qtz Tic-Cal</p> <p>P1 Ms-Chl-Qtz (550g-560) Crd-Bt Chl-out</p> <p>P2 Ms-Bt-Qtz Ms-Crd (600g-620) Crd-Kfs Qtz-Bt-And Ms-out in sappinites</p> <p>P3 Ms-Qtz (625g-640) And-Kfs</p> <p>P5 Ms (Qtz-absent) (655g-670) Crn-Kfs Kfs-Qtz (Bt-Crd, ALS=1) Liquid (to Crd, ALS)</p> <p> Per Sol Ort Upxi C15 P11 P12 (1750-1900)</p> <p> CIII = Trn + Di + Fo + Grt + Dol (isobaric invariant) (1620) ALS = Al₂SiO₅ polymorph</p>	<p>T-range °C for 0.3GPa (g=granitic pelites)</p> <ul style="list-style-type: none"> Leucogranite Porphyritic Granite Hybrid Granite Quartz diorite (showing igneous lamination and deformation foliation) Monzodiorite Diorite, fine-grained facies Hybrid transition zone/igneous contact Appinite Suite mafic rocks Drift
--	---	--

SW 28


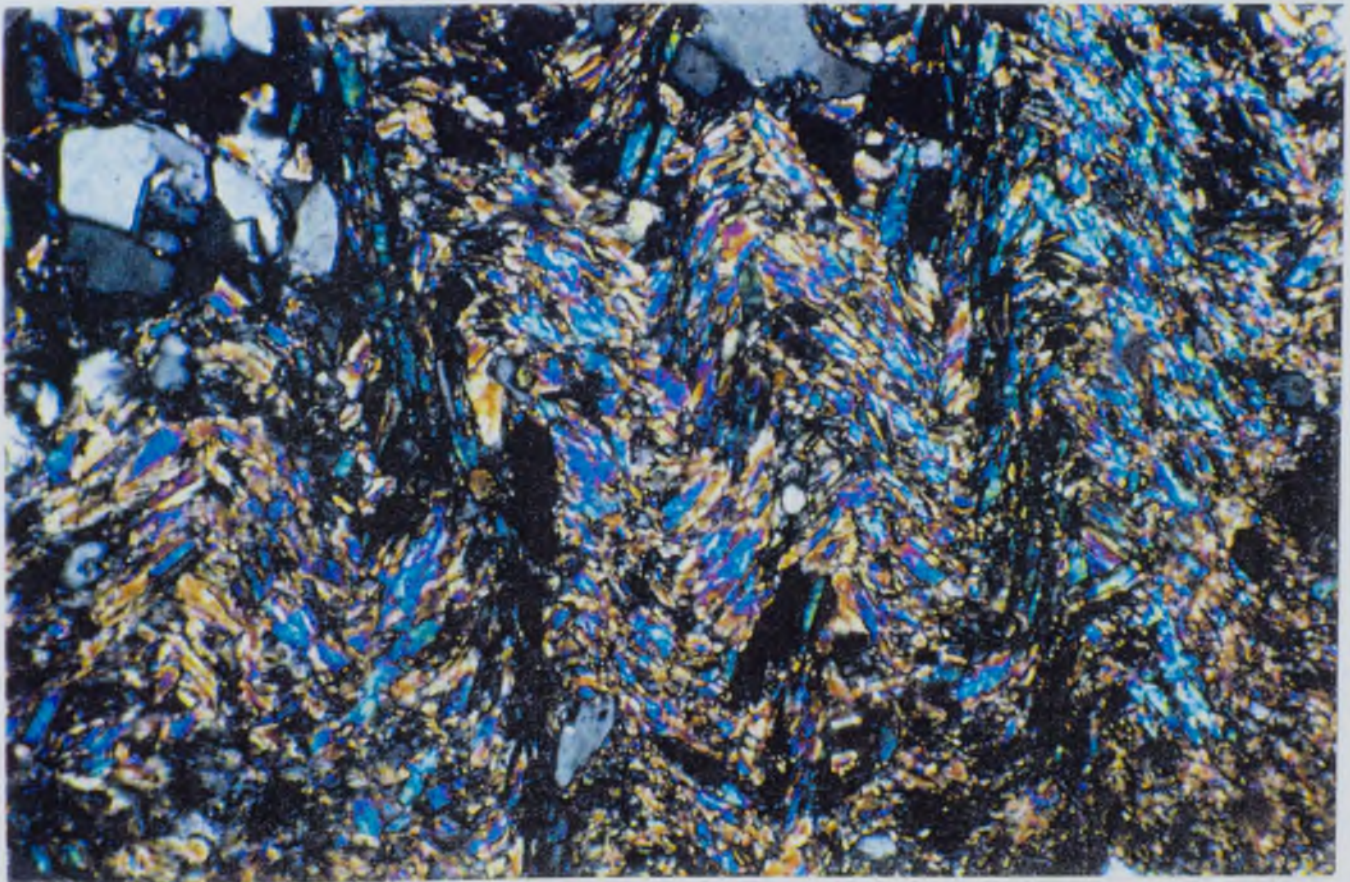
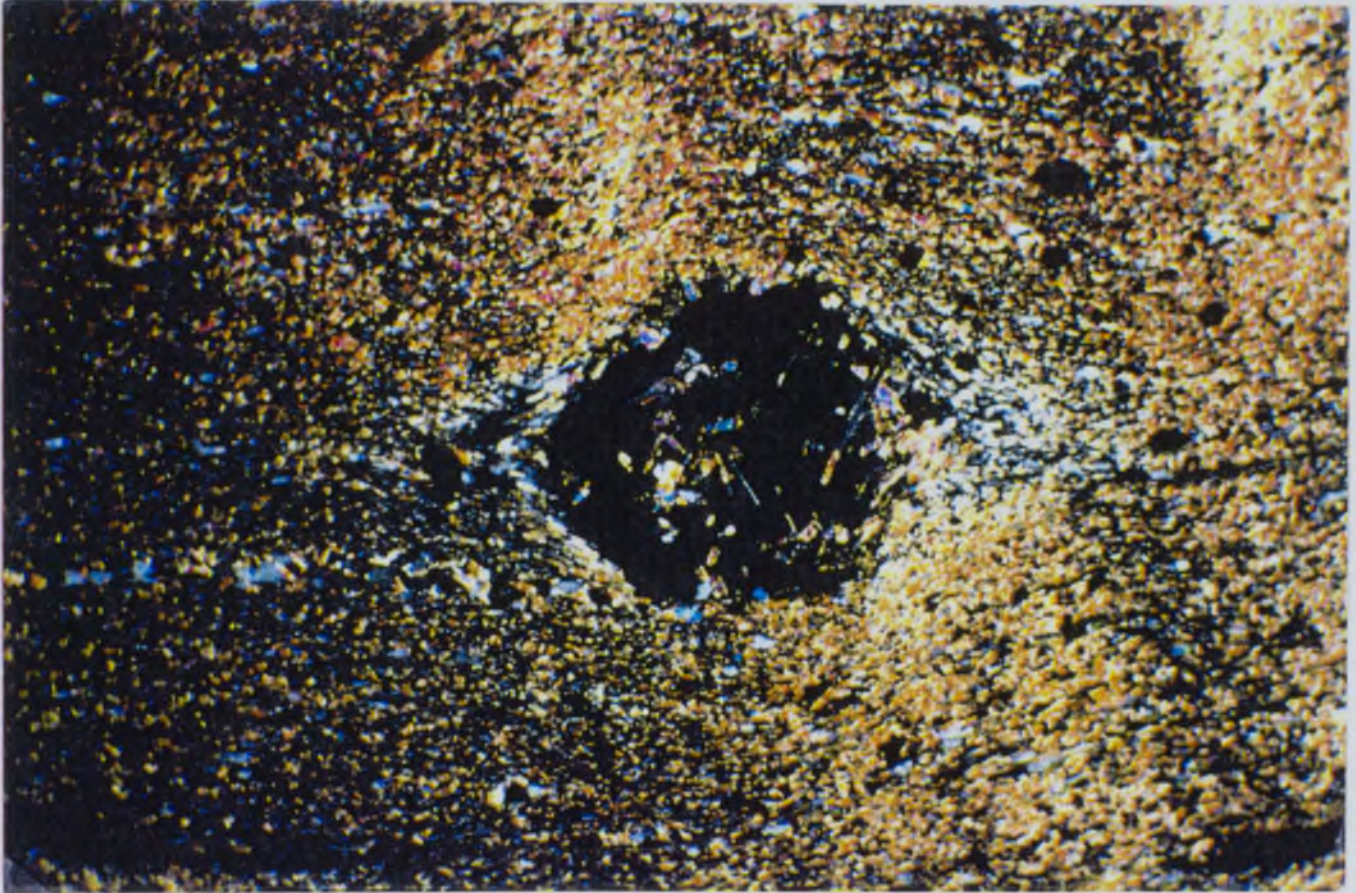


Figure 3.4 Thin section of a pelite from outside the aureole, showing chlorite pseudomorphing garnet. Sample 55888, width of view 4mm

Figure 3.5 An example of a crenulation cleavage developed within a pelite in the Ballachulish area. Sample 55886, width of view 1mm




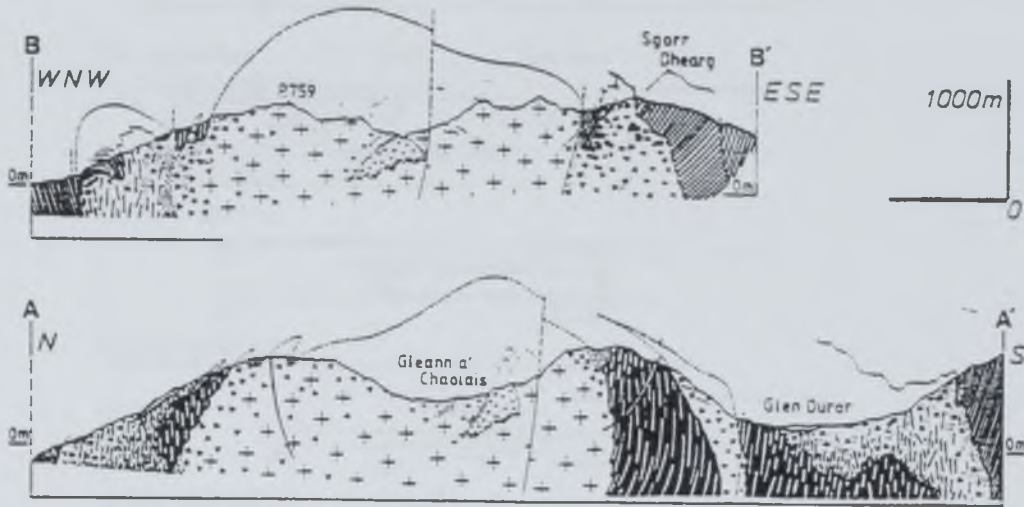
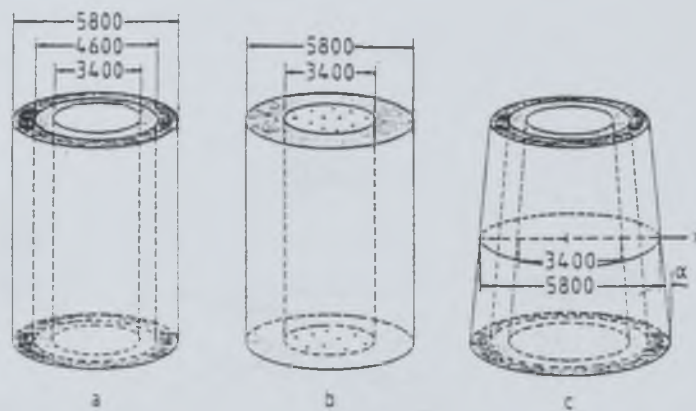
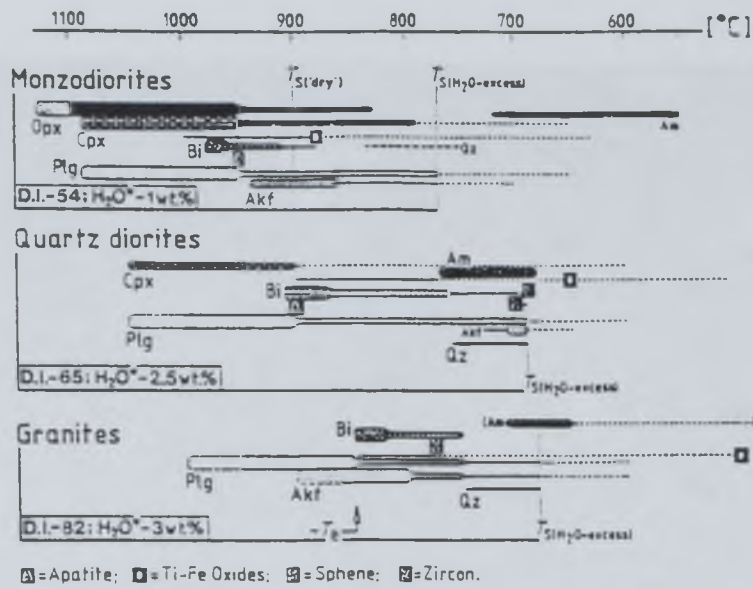


Figure 3.6 Cross sections through the igneous complex and aureole. 1 Metasediments; 2 monzodiorites (with flow and deformation foliation); 3 quartz diorites (with alignment of pelitic xenoliths); fine-grained quartz diorites with xenoliths; 5 granites; 6 transition zones, hybrid granite (from Troll and Weiss, 1991).

Figure 3.7 Linear fabrics developed in the diorite envelope as a consequence of deformation related to the ballooning central granite diapir. The diorite 'mush' accommodated nearly all of the deformation. Thus deformation did not penetrate into the country rocks (from Weiss and Troll, 1991). 1) Trend lines in monzodiorites (line), quartz diorites (long dashes) and granites (short dashes); 2) weak/strong ductile deformation of plagioclase; 3) fine grained granites and marginal facies of the diorites; 4) migmatites (Pattison and Harte, 1988).








Figure 3.10 Fluid inclusion trails within quartz grain (2m from igneous contact) reflecting fracture fill processes. (SEM/orientation contrast image - see Appendix B). Sample 55303.

Figure 3.11 Schematic KMASH petrogenetic grid (not to scale) for reactions in the Ballachulish aureole (from Pattison and Harte, 1991).

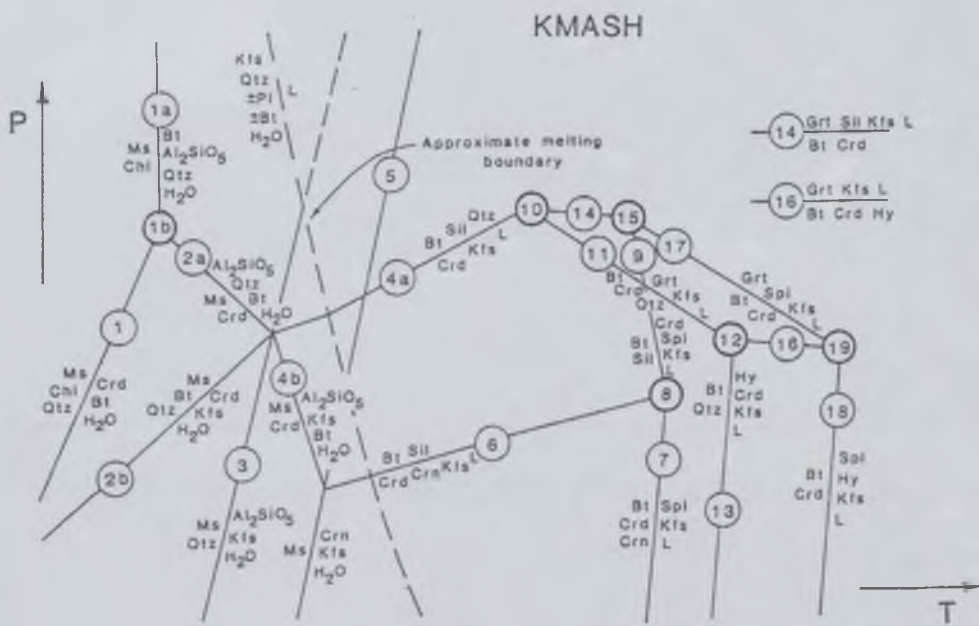
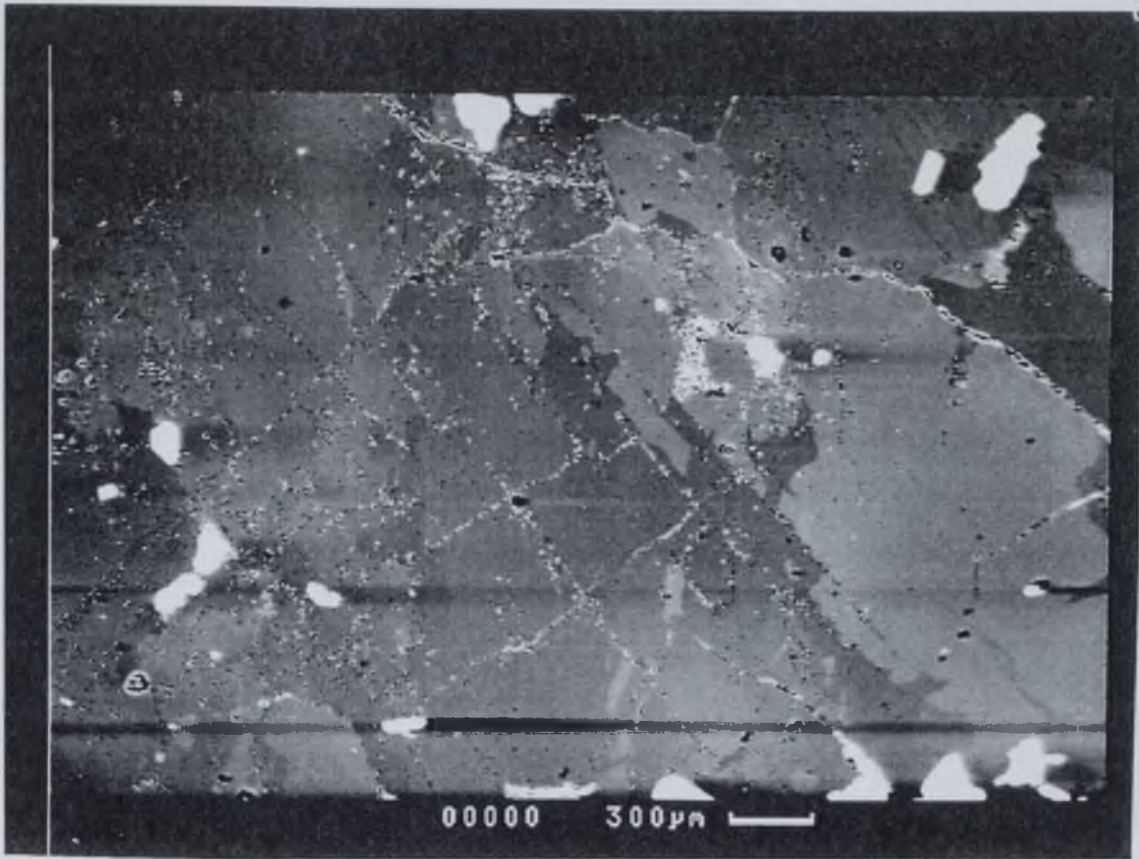
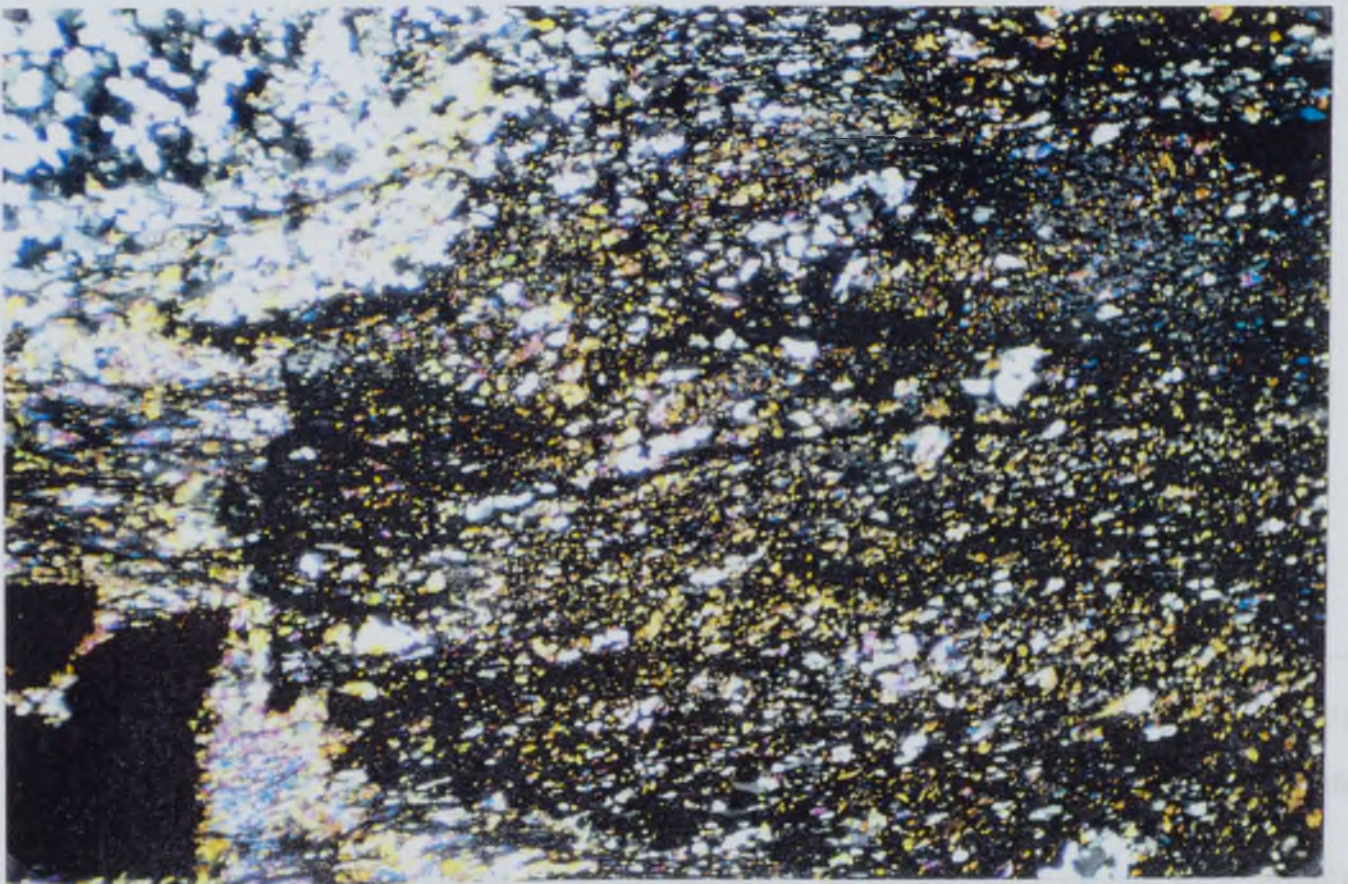
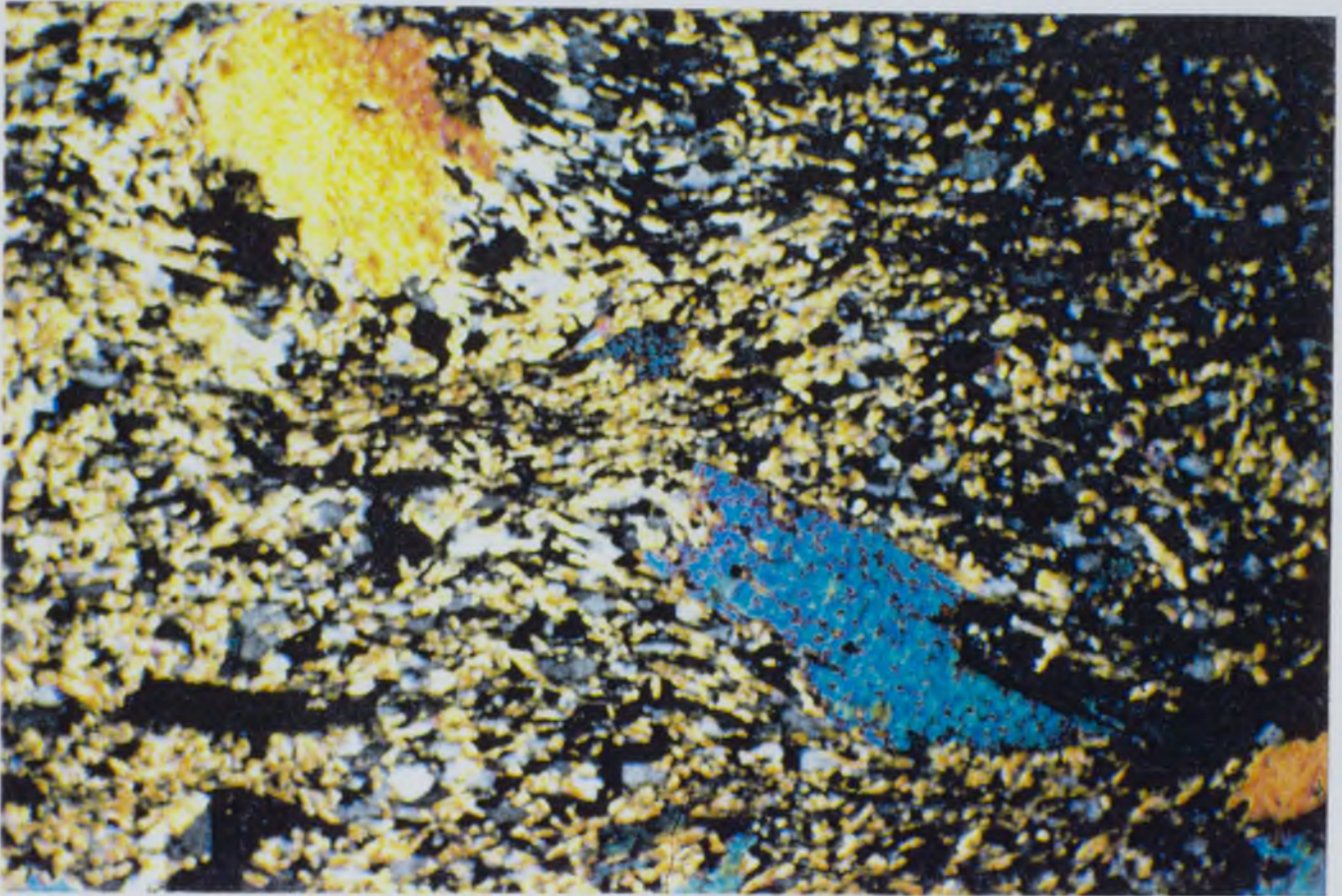




Figure 3.12 a) Biotite poikiloblasts overgrowing deformational fabric. Sample taken from within the aureole. Sample 55892, width of view 1mm

b) Cordierite porphyroblast (large, black mottled mineral) overgrowing muscovite, quartz and biotite. The inclusion rich nature of the cordierite crystal suggests that it has grown rapidly. Sample 55893, width of view 4mm.






Figure 3.13 Temperature of the Appin Quartzite versus time for several distances from the igneous contact.




Figure 3.14 Appin Quartzite peak temperatures as a function of distance from the igneous contact. The superimposed rectangles are geothermometer data for the Ballachulish aureole as summarised by Buntebarth - Fig. 18.16 (1991).

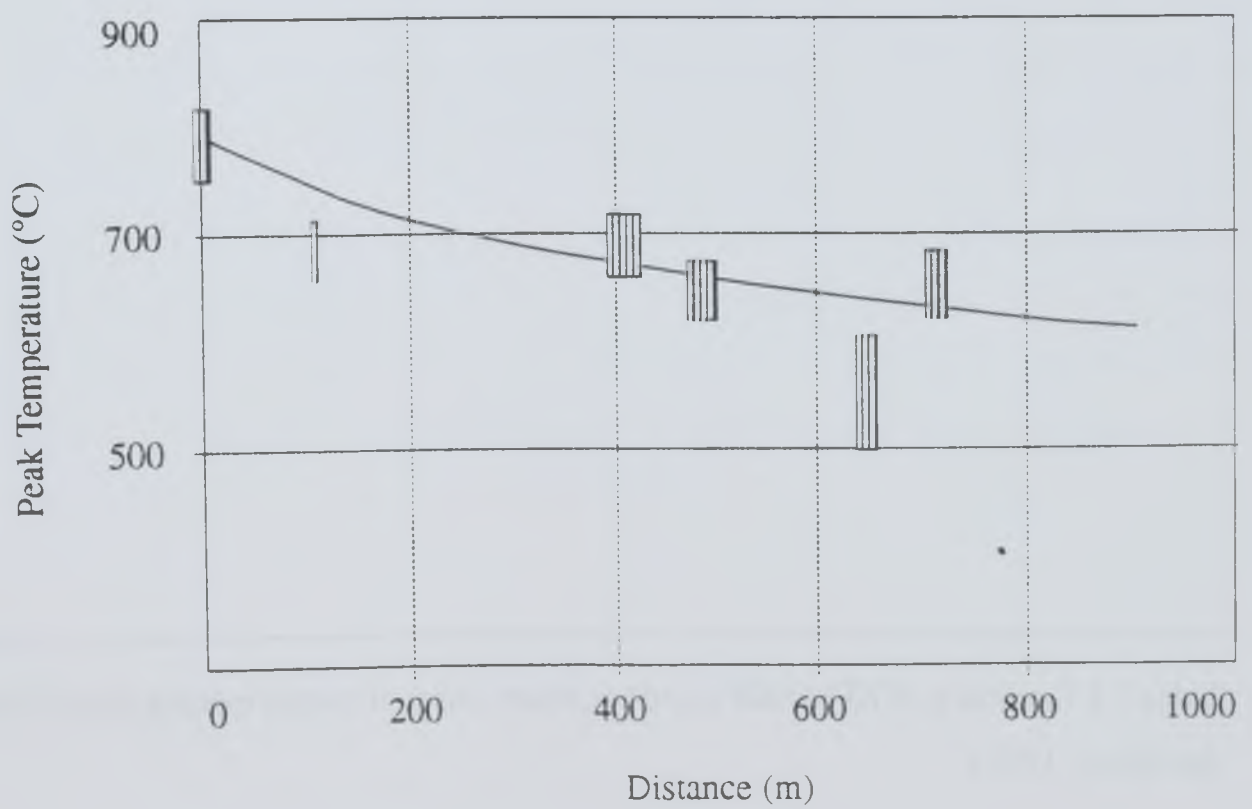
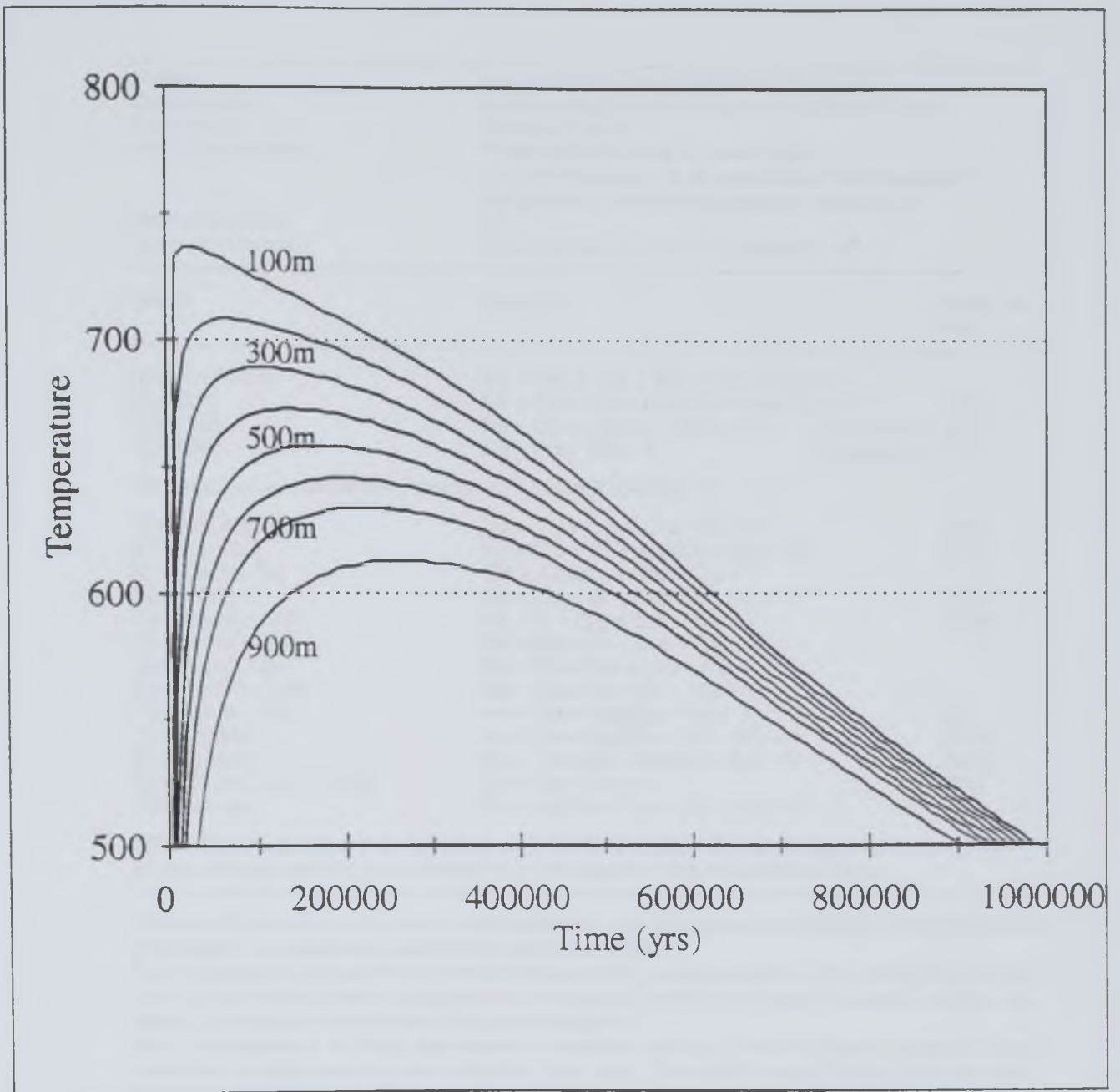




Table 3.1 Summary of KFMASH reactions below onset of partial melting (from Pattison and Harte, 1991).

Phases:	Ms Chl Qtz Bt Crd Crn Al ₂ SiO ₅ Kfs V = 9
Components:	K ₂ O-FeO-MgO-Al ₂ O ₃ -SiO ₂ -H ₂ O (KFMASH) = 6
Exclusions:	Qtz-Crn, Chl-Crn
Other Restrictions:	V assumed present in all assemblages Qtz and Ms present in all assemblages below reaction P3 Kfs present in all assemblages above reaction P3
Invariant Points:	O ^a
Univariant curves:	(Invariant pts in KFASH or KMASH): 4 ^b

Name	Reaction	Reaction No.
[Crn,Al ₂ SiO ₅]	Ms + Chl + Qtz + Kfs = Bt + Crd + V	
[Crn,Kfs]	Ms + Chl + Qtz = Crd + Bt + Al ₂ SiO ₅ + V	(P1b)
[Crn,Chl]	Ms + Qtz = Al ₂ SiO ₅ + Kfs + V	Degenerate (P3)
[Qtz,Chl]	Ms = Crn + Kfs + V	Degenerate (P5)
Divariant curves (univariant curves in KFASH or KMASH): 13 ^c		
[Crn,Kfs,Al ₂ SiO ₅]	Ms + Chl + Qtz = Crd + Bt + V	(P1)
[Crn,Kfs,Chl]	Ms + Crd = Bt + Al ₂ SiO ₅ + Qtz + V	(P2a)
[Crn,Kfs,Ms,Bt]	Chl + Al ₂ SiO ₅ + Qtz = Crd + V	
[Crn,Kfs,Crd]	Ms + Chl = Bt + Al ₂ SiO ₅ + Qtz + V	(P1a)
[Crn,Al ₂ SiO ₅ ,Chl]	Ms + Bt + Qtz = Crd + Kfs + V	(P2b)
[Crn,Al ₂ SiO ₅ ,Ms]	Chl + Kfs = Bt + Crd + Qtz + V	
[Crn,Al ₂ SiO ₅ ,Bt]	Ms + Chl + Qtz = Crd + Kfs + V	
[Crn,Al ₂ SiO ₅ ,Crd]	Chl + Kfs = Ms + Bt + Qtz + V	
[Crn,Chl,Bt,Crd]	Ms + Qtz = Al ₂ SiO ₅ + Kfs + V	(P3)
[Crn,Chl,Ms]	Bt + Qtz + Al ₂ SiO ₅ = Crd + Kfs + V	(P4a)
[Crn,Chl,Qtz]	Ms + Crd = Bt + Al ₂ SiO ₅ + Kfs + V	(P4b)
[Qtz,Chl,Al ₂ SiO ₅ ,Crd,Bt]	Ms = Crn + Kfs + V	(P5)
[Qtz,Chl,Ms]	Bt + Al ₂ SiO ₅ = Crn + Crd + Kfs + V	(P6)

KFMASH univariant curves (invariant pts in KFASH or KMASH) are designated by the phases absent. Reaction curves are numbered as in the figures. V refers to hydrous vapour.

^aGiven only the above exclusions, it is possible that one invariant point is stable, [Crn], but this is presumed to be metastable (see Pattison and Harte 1985).

^bThis assumes that muscovite is pure KAl₃Si₃O₁₀(OH)₂, which makes the [Crn,Crd], [Crn,Bt] and [Crn,Chl] univariant reaction degenerate and identical. The [Crn,Ms] and [Crn,Qtz] reactions are absent for the same reason as the [Crn] invariant point.

^cWith the exception of (P1a), the numbered reactions are seen in the Ballachulish aureole. Only cordierite bearing reactions are considered (see text). Chl-Al₂SiO₅ and Chl-Kfs have not been observed, and cordierite always coexists with biotite.

CHAPTER 4

METHODOLOGY

4.1 INTRODUCTION

This chapter reviews the analytical and practical procedures employed in this investigation to quantify different microstructural elements. The analytical techniques are grouped together under four headings for discussion: microscope techniques, image and statistical analysis, fractal characterisation of grain shapes and crystallographic analysis.

These procedures include the following: average grain size measurements; extinction angle (a measure of strain within individual grains); a substructure classification scheme; image analysis measurement techniques; statistical analysis of image analysis data; fractal characterisation of grain shapes; crystallographic preferred orientation measurements and crystallographic misorientation measurements.

4.2 Optical Microscope Techniques

Various techniques have been used to characterise the microstructures observed using light microscopy. Direct observations (without making quantitative measurements) often provide the greatest insight into the processes which have been active during a rocks evolution. Substructure classification and the measurement of extinction angles (described below), together with direct microscopic observations potentially yield information about the kinematics of deformation and annealing in rocks. It will be shown that an in depth knowledge of the controls on microstructural evolution in the Ballachulish aureole may be obtained by integrating the information.

4.2.1 Substructure Classification

Numerous intracrystalline substructures have been documented within deformed rocks. White (1973) described three types of substructures which are commonly observed under the light microscope: deformation bands, deformation lamellae and undulose extinction. Farmer (1992) subsequently defined the following groups of grain substructures on their extinction characteristics (Figure 4.1).

- *Straight* extinctions are defined by the predominance of a single trend of extinction in deformation bands which are approximately straight and parallel.
- *Lensoid* substructures display anastomosing areas of extinction. This type of extinction is frequently observed, on a small scale, as the subgrain structure associated with deformation bands.
- *Equant* substructures, as the name suggests, are regular extinction patterns defining a network of subgrains.
- *Wobbly* extinction structures are defined when a definite trend of extinction can be discerned, yet the structure cannot be accurately placed in any of the above classes. The extinction often appears like irregular, conical type folds.

- *Indent* extinctions are defined when the pattern can be directly attributed to the impingement of some neighbouring grain. Such structures have been described as ‘flame’ structures by Lloyd and Knipe (1992).
- *Internal extinction tracks* appear as narrow, linear, subgrain like arrays of rectangular rhomb shapes and are always seen to be sub-parallel to straight or lensoid structures
- *Thin fractures* are only identifiable by the manner in which extinction patterns are offset across them. They should not be confused with healed fractures which are frequently seen within individual grains.

Each grain within an aggregate is examined to ascertain which types of substructures are present. Often, one grain may contain more than one type of substructure, in which case the grain is classified according to whichever substructure is dominant. Such a classification scheme is advantageous because it is purely descriptive and not based on interpretations of microstructural process.

4.2.2 Extinction Angle

A qualitative assessment of the degree of deformation within individual grains is attained using the ‘extinction angle’. This is measured by rotating a grain until the whole of the grain has undergone extinction. The angle of rotation between a grain entering extinction to the final part of the grain becoming extinct defines ‘the extinction angle’. The greater the deformation of a grain, the more warped the crystal lattice becomes and hence the greater the extinction angle. Cumulative frequency plots of the different extinction substructures within each sample have been constructed to show the proportion of grains within an aggregate containing a particular extinction angle (cf. chapter 5).

4.3 IMAGE ANALYSIS

4.3.1 Introduction

Image analysis is the direct quantification of measurable parameters (e.g. grain size, area, angles or colours) within an image, be it a photograph, video drawing or tracing (here

the images are rock samples). A computerised system of measurement has considerable advantages over manual image analysis both scientifically and also in reducing the time involved in taking measurements. Scientifically the results from an image analyser are reproducible, because they are in no way prone to human error or bias. The only time consuming aspect to image analysis is programming the algorithm for each specific measurement. Once this step has been achieved, data analysis is relatively simple, merely involving the transfer of data from output files in text format to spreadsheet packages, or programmes specifically designed to process data.

A Vidas 21 Kontron image analyser has been used to perform image analysis on a series of samples from both inside and outside the Ballachulish aureole. The measurement techniques employed in this investigation are outlined below, followed by a review of the statistical tests which have been applied to the data.

4.3.2 Image Analysis Methods

Image analysis involves image collection (e.g. from a microscope), image digitisation and finally image measurement. All three stages are crucial if the data obtained is to be accurate. Geological samples are not particularly easy to analyse, because the images tend to be complex, and the operator may wish to measure very specific microstructural features. Thus, image collection and digitisation techniques are critical in order to obtain rigorous results (Pratt, 1978; Ballard and Brown, 1982; Rosenfield and Kak, 1982; Baxes, 1984; Inoue, 1986; Gonzalez and Wintz, 1987 and Russ, 1988).

Image collection

To measure a microstructural element within an image, it is necessary to distinguish that element from all other microstructural features within the image. Images with each individual grain visible as a different colour (or grey level), or alternatively with the grain boundaries structure highlighted may be utilised to distinguish one grain from another within a rock.

For the quartzite specimens studied in this investigation, three possible techniques may be employed to form useful images: (1) optical microscopy using cross polarised light; (2) scanning electron microscopy (SEM) secondary electron images using etched samples; and (3) SEM backscattered electron (BSE) orientation contrast (OC) images (for details of SEM techniques see Appendix B).

(1) Optical micrographs of quartzites produce images with grain to grain variation in grey level, depending on the crystallographic orientation of each grain's c-axis in relation to the polarisation direction of the light. Grains oriented with their c-axis either vertical, or aligned with the polarisation directions of the light (normally N-S or E-W on the cross hairs of a microscope) will appear black. If a crystal is orientated in any other direction the grain appears as a shade of grey (the shade depends on the crystal orientation of a grain). Because grains within an aggregate have a variety of crystal orientations it is therefore possible to distinguish individual grains using the optical microscope.

(2) Chemical etching preferentially removes soft areas of a sample, such as grain boundaries, thus creating a topographical negative feature which defines the microstructural element removed. The grain boundary structure is readily observed using SEM secondary electrons images (see Appendix B). However, this techniques has not been used during this study for two reasons. Firstly, etching a sample damages the top few microns of the sample surface, which controls the diffraction of Back scattered electrons. This method therefore renders the sample useless for electron channelling (a technique used to study crystallographic orientation). Secondly, etching not only reveals the grain boundary structure, but also other microstructures such as bubble trails and subgrain boundaries (Ball and White 1977; Prior 1988 and Prior et al., 1996).

(3) Image analysis has been performed on samples which have been imaged using SEM orientation contrast (SEM/OC). An example of such an image is shown in Figure 4.2. SEM/OC images are a product of the diffraction of electrons. Thus, the grey level of a grain is influenced by the 3-dimensional crystallographic orientation of a grain (see appendix B) and not just the c-axis as it is in optical microscopy. The grey level of a grain in these images is much more sensitive to crystal orientation and adjacent grains are nearly always distinguishable (although this may not always be true for subgrains - see Prior et al. 1996).

The SEM/OC method is superior to the optical microscopy method because the images are formed by three-dimensional diffraction. There are some circumstances on an optical microscope when two adjacent grains with different orientations are not distinguished. For example, two adjacent grains may have their c-axis oriented parallel vertically, however, in three dimensions, their a-axes are misaligned. In such cases, the optical microscope cannot distinguish neighbouring grains because they appear as one grey level, but SEM/OC will distinguish them as different grey levels.

Image Digitisation

The above discussion indicates that an image can be obtained which can identify each individual grain in an aggregate. However, an image analyser is unable to filter small colour or grey level fluctuations within an image (i.e. "noise" due to impurities, subgrain microstructures, fluid inclusions etc.). Thus, the computer needs a helping hand to filter information. Montages of samples imaged by SEM/OC are traced by hand and the quartz:quartz contacts are coloured black and feldspar:quartz contacts are coloured red. Using the information from the tracings (with the noise filtered manually), the image analyser is able to produce a binary image (black and white) of quartz grains from which grain measurements may be made.

Image Measurements

Once an image has been digitised, individual grains are picked one by one and a number of grain size/shape related parameters are measured. All measurements are automatically scaled into microns. Grain measurement parameters used for this investigation include: area, maximum diameter, diameter of a circle with the equivalent area to the grain, perimeter, aspect ratio and a circularity shape factor. These parameters are measured using macros written for a Kontron image analyser, the definitions of the macros are detailed in Appendix C.

4.3.3 Averaged Grain Size Data Collection Technique

The mean diameter of grains has been measured for some samples on the image analyser (using the DCIRCLE macro - see appendix C), and for other samples using a linear intercept method. The latter approach is based on the fact that the average grain size within an aggregate may be estimated by counting the number of grain boundary intersections along a straight line of known length. The mean grain size is equal to the (length of the line - 1) divided by the number of intersections. Abrams (1971) suggested a technique using three concentric circles with a total perimeter length of 50 cm as the line of measurement. The three circles are placed over an image of a sample (projected on to a shadowmaster), and the number of grain boundary intersections counted. Triple junctions which occur on the line are counted as two (as suggested by Abrams, 1971) to avoid working with non-integer counts, although this may introduce a systematic error (triple junctions technically should count as 1.5).

Linear intercept methods cannot produce true three-dimensional grain size estimates because of the following:

(1) The measurements are taken from a two dimensional section which means the data are affected by the 'stereology' of the grains. Stereology refers to the grain shapes that may be produced on a two dimensional section through a three dimensional aggregate. The main implications of stereology on grain size measurements are that a grain diameter measured from a two-dimensional section is always smaller or equal to the maximum three-dimensional diameter of the grain in question (Figure 4.4). Thus, grain sizes inferred from two-dimensional sections always underestimate the true three dimensional grain size.

(2) The larger a grain, the more likely it is to be cut by the intercept line (Abrams, 1971). Hence, there is an underestimate of the amount of smaller grains. These problems have largely been ignored during this study because it is the relative change in grain size from one sample to another that is of importance and not the absolute grain size. Furthermore, the kinetic equations relating grain size to diffusion are based on experiments which calculate the grain size from two-dimensional sections. Thus, it is not necessary to

account for the three-dimensional structure of grains. Corrections may be applied to grain size analysis to overcome simple stereological problems (e.g. Thompson, 1972).

4.3.4 Data Presentation

The data collected from each specimen involves a large number of measurements (e.g. grain sizes are measured for c. 150 grains within one sample). Such data sets are characterised by the mean and standard deviation for each measurement parameter. However, a more rigorous approach involves defining the form of the entire data distribution for each measurement using histogram statistics. A statistical approach is preferable as it enables the detection of trends within distribution data sets, which may be overlooked if data are merely assessed by their means and observation of a large number of histograms.

The techniques which were applied to produce average grain sizes have been discussed in section 4.3.3. The following section introduces statistical tests which are employed to help define the frequency distributions of data sets.

4.3.5 Grain Data Distribution Analysis

4.3.5.a Introduction

Merely averaging data sets has serious limitations. In particular, that two samples may have the same average, but originate from radically different parental distributions (Figure 4.5). Thus, relying solely on the mean results in a loss of information. In such cases, it is necessary to examine how distributions differ between samples in order to correctly interpret variations in the averaged data. Histogram distributions, which show the spread of data within one sample, contain far more information than one average number which represents the whole sample.

Traditionally, distribution data are presented in the form of histograms, whereby data are divided into a number of cells of equal width (e.g. grain sizes between 1-10 μ , 10-20 μ ,

20-30 etc.). The bands are plotted on the x-axis and the number of measurements which fall within a band are related to the area of each cell on the graph (i.e. the frequency of measurements is plotted on the y-axis). There are an infinite number of possible histogram shapes, but these may be generalised into a small number of common shapes or type-distributions (Harr, 1977), including: bell shapes, J-shapes, bimodal, uniform, Gaussian, exponential and lognormal. It is here that the problem with histograms arises. Firstly, because each sample is represented by one histogram, it is difficult to interpret trends within large data sets that consist of many samples simply because of the quantity of histogram diagrams (as is the case in this study). Secondly, it is difficult to distinguish visually between some of the different histogram shapes. Statistical tests therefore are needed to define histogram distributions.

4.3.5.b Statistical Processing of Data

It has been shown that a histogram presents data whereby the frequency of data within a band is related to the area on the graph. The whole distribution can therefore be described by a continuous frequency function:

$$f(x) \propto \sum_x^0 z dx \quad \text{Equation 4.1}$$

where x is a band width and z is its frequency.

Elderton and Johnson (1969) have shown that any distribution can adequately be described by four coefficients (the first four sample moments), namely the sample mean, variance, skewness and kurtosis. The variance yields information about the spread of data around the mean, the skewness indicates how symmetrical the data is about the mean, and finally the kurtosis describes the degree of clustering within a data set. These moments are defined as follows:

$$\mu_1 = 1/N \sum \{f_i x_i\} = \text{sample mean} \quad \text{Equation 4.2}$$

$$\mu_2 = 1/N \sum \{f_i (x_i - \mu_1)^2\} = \text{sample variance} \quad \text{Equation 4.3}$$

$$\mu_3 = 1/N \sum \{f_i (x_i - \mu_1)^3\} = \text{sample skewness} \quad \text{Equation 4.4}$$

$$\mu_4 = 1/N \sum \{f_i(x_i - \mu_1)^4\} = \text{sample kurtosis} \quad \text{Equation 4.5}$$

Pearson defined a function:

$$K = \beta_1 (\beta_2 + 3)^2 / 4(2(\beta_2 - 3 \times \beta_1 - 6)(4 \times \beta_2 - 3 \times \beta_1)) \quad \text{Equation 4.6}$$

with which he was able to classify the different types of frequency distributions. In this expression β_1 and β_2 are two dimensionless coefficients which are defined as:

$$\beta_1 = \text{skewness}^2 / \text{variance}^3 \quad \text{Equation 4.7}$$

$$\beta_2 = \text{kurtosis} / \text{variance}^2. \quad \text{Equation 4.8}$$

β_1 defines the symmetry of the distribution, whilst β_2 the peakedness of the distribution. β_1 and β_2 coefficients are relatively simple to calculate and interpret, although the justification for adopting these parameters is complex (see Lloyd, 1983). Because the Pearson parameter (K) is purely a function of β_1 and β_2 it is possible to distinguish the different distributions which this parameter defines by plotting a graph of β_1 versus β_2 . This diagram is known as a moment ratio plot (Harr, 1977 and Lloyd, 1983 - e.g. Figure 4.6).

A number of common histogram distributions are shown on a moment ratio plot in Figure 4.6. Moment ratio plots are a powerful tool for quantifying the shapes of histograms, readily discriminating between different distributions and are used to this effect later.

4.4 FRACTAL ANALYSIS - METHODS

4.4.1 Introduction

It will be shown in chapter 5 that small variations in grain shapes may be detected using simplistic shape factors (e.g. Kontron macros FCIRCLE and FSHAPE) which compare perimeters, areas and aspect ratios of grains. However, these analyses are unable to define the precise form of shape changes. A method of grain shape measurement is

therefore required whereby a grain shape is defined in terms of a parameter which may be directly related to the detailed structure of grain shapes. Furthermore, the parameter should contain information about a grain shape at a variety of scales, from the micron scale distortions on the grain boundary to the larger scale (mm) grain boundary irregularities.

Fractal dimension analysis is one such method of relating grain shapes over all scales of observation (within practical limits) to a mathematical function. It is this ability to define shape at a variety of scales that makes fractal analysis a powerful image analysis tool. A fractal analysis of the microstructures developed in the Appin quartzite potentially enables an accurate assessment to be made of the manner in which grain shapes evolve during annealing.

Much of the discussion concerning the methods for calculating fractal dimensions uses examples of fractal shapes which have been characterised by other workers (e.g. Flook 1978; Russ 1992). These works are referred to only to introduce the concepts of fractal dimensions, the actual measurements which have been calculated to measure the shapes of grains at Ballachulish are presented in chapter 5.

4.4.2 What Are Fractals?

4.4.2.a Introduction

Scientists are accustomed to the concept of dimensions to describe shapes of objects; a line has a dimension of one, a surface two and a volume three. The perimeter of a circle or a square is line and hence a one-dimensional object. However, not all shapes can adequately be described in this conventional manner. For example, an outline of the coast of Britain, although a line, is a locus of points, which to a limited extent fill a two-dimensional area (i.e. the paper on which the map is drawn). In this respect, it is a useful concept to think of a line as something between one dimension and two dimension, depending upon the degree to which it fills the two-dimensional surface (or page) on which it is drawn. A line which visits every point on the page is in fact a two-dimensional

surface. A fractal dimension is a rigorous mathematical method used to assign a non-integer value to a line which describes the extent to which that line fills two-dimensional space.

4.4.2.b Self-Similarity

Consider a map of the coastal outline of Wales (Figure 4.7). This map has a natural shape which has been etched by geological processes over a long period of time. To describe this shape mathematically is difficult because it does not seem to conform to regular Newtonian mathematical laws in the same way as, say, a circle or a hexagon. For example, the common relationships between area and perimeter and angles which are frequently found for regular shapes, cannot be expressed for natural landforms or coastlines. Traditionally, these shapes were assumed to be random, but a closer look at the Wales reveals that, although it is not regular, it does not seem to be totally random. For example, if one section of coastline is inspected at a greater magnification, more detail is revealed, yet this 'new' detail often seems 'similar' in appearance to the larger scale features seen at lower magnifications. This is shown by comparing the form of the smaller St. Davids Bay in South Wales to the larger Cardigan Bay (Figure 4.7). The irregularity of the two sections of coastline are alike, yet on completely different scales. In essence, the morphology of the shapes which form coastlines can be seen repeated at smaller and smaller scales as one looks in more and more detail. This behaviour is known as self similarity (Mandelbrot 1982; Kaye 1988; Kaye 1989 and Russ 1992). It was pointed out by Mandelbrot (1982) that self similarity commonly occurs in many natural systems. Furthermore, Mandelbrot was able to describe self similarity mathematically, and was therefore able to investigate the nature of this phenomena. A fractal is a method of expressing mathematically the self similarity of an object.

4.4.2.c Monster Curves

The notion of self similarity may be clarified by studying a set of shapes known to mathematicians for over 100 years as 'monster curves'. These curves are created by an interactive elaboration process, creating more and more detail after each step. Thus, one of the characteristics of these curves is that they have an indeterminate and perhaps infinite perimeter. An example of a monster curve is the Koch curve shown in Figure 4.8.

The basic shape is an equilateral triangle. This is elaborated by an infinite iterative process in which each straight line segment is replaced by a line segment of the shape shown in Figure 4.9, which is one third longer. The process of elaboration is repeated ad finitum and so the boundary length increases without limit (Figure 4.8).

Figure 4.10 shows some examples of other monster curves which have similar properties, (i.e. the perimeter increases with each iteration). The number of sides the Koch triadic curve will possess at any point in the iterative process (Figure 4.8) may be described by the relationship

$$N_{(i)} = \lambda \eta_{(i)}^{-d} \tag{Equation 4.9}$$

where $N_{(i)}$ is number of segments that a line is divided into after i iterations, $\eta_{(i)}$ is the length of one side of the object after i iterations and λ is a scaling constant.

The perimeter of the object may be approximated by,

$$P_{(i)} = \lambda \eta_{(i)}^{1-d} \tag{Equation 4.10}$$

This equation shows that even though the perimeter length increases by a constant factor, the number of sides to the shape increases by an exponential function d . This exponential function is known as the fractal dimension. This parameter contains the information about how an object scales down from a simple Euclidean form (e.g. a triangle) to a complex monster curve form. The parameter d may also be obtained by using equation 4.12, which is a general formula used to describe any object which is self similar:

$$d = \frac{-\log(N_r)}{\log(1/r)} \tag{Equation 4.11}$$

where $N_{(r)}$ is the number of elements of an object of reduction ratio r .

Clearly, the more elements a line is divided into, the more intricate the shape becomes, filling space more effectively. For example, the Koch quadratic curve divides each line

into 8 segments, each one being one quarter of the length of the original square (Figure 4.10). The resultant shape is more complex than the triadic curve and therefore has a higher fractal dimension of 1.5 ($N=8$, $r=4$).

Monster curves are unique examples of fractal shapes that may be generated from a simple Euclidean shape using a fractal relationship. These types of fractal shapes are termed 'structured fractals'. Natural shapes, such as coastlines, cannot be generated by the same process of elaborating a simple shape into a complex curve using a fractal formula. However, coastlines do possess characteristics which may be associated with fractals, namely self similarity. Natural fractals are self similar, but not in the rigorous manner as in the examples of monster curves. A natural fractal cannot be produced by systematic demagnification and repetition of a specified shape, but the shapes which mould the perimeter at one scale are similar in form/roughness to the form of the perimeter at all scales of observation. The fact that natural shapes are self similar enables them to be analysed in a similar way to monster curves, whereby the number of sides at any one magnification is related to a fractal scaling factor (d , *i.e. the fractal dimension*), which depends on the complexity of the perimeter form as it is inspected at greater and greater detail.

The method by which self similarity can be examined is the Richardson plot (Richardson, 1961).

4.4.3 Richardson Plots

Richardson (1961) was one of the first people to study self similarity of natural shapes, although he did not actually use the term self similarity. He was studying the economic and military conflicts between nations and the length of their borders. He noticed that the perimeter lengths varied markedly depending on the scale of the map. He measured the apparent perimeter length of Britain as a function of the unit of measurement by performing a 'structured walk'. During a structured walk compass dividers are used to set a unit of measurement for an object and the perimeter of the coastline measured in compass units, the process is repeated at smaller and smaller divider step sizes.

Richardson observed that the perimeter length of the coastline increased without limit as the stride size decreased. If the perimeter length was plotted against the stride size on a graph with logarithmic axes (a Richardson plot), the result is a straight line (Figure 4.12). Straight frontiers, such as the boundary between Egypt and Libya plot as horizontal lines on these graphs, indicating that for the case of straight national borders the perimeter length does not change as the step size of the dividers is decreased.

The significance of the straight line on a log:log plot is twofold. (1) At higher and higher magnifications the perimeter increases in a self similar fashion, and an object exhibits the same style of irregularities at all scales. (2) The scaling of self similarity is described by the gradient of the slope on the graph. The slope of the line on a Richardson plot is negative because the largest value for the perimeter length is obtained with the shortest stride length (Figure 4.12). Furthermore, the number of sides is related to the step size by:

$$N_{(i)} = \lambda \eta_{(i)}^{-d} \quad \text{Equation 4.12}$$

where η is the step size of the dividers. Again the perimeter length may be approximated to:

$$P_{(i)} = \lambda \eta_{(i)}^{1-d} \quad \text{Equation 4.13}$$

A theoretical fractal dimension is obtained for structured fractals by fixing the divider step size to the size of the reduced object which is used for elaboration of the monster curve. Because the length of the sides after each iteration are known, and the perimeter length is also known, a fractal dimension may be calculated using equation 4.14. When determining fractal dimensions by structured walk techniques, the reduction factors and side lengths of the object etc. are unknown. The step sizes therefore, cannot be designed to correspond with the length of the sides, making a direct comparison between the theoretically defined fractal dimension and the actual measured dimension scientifically unreliable. Usually, the measured fractal dimension and the measured dimension will correspond with each other. However, if measurement inaccuracies occur they will result in an underestimate of the fractal dimension.

4.4.3.a *Cut-offs*

There are resolution limits when using the structured walk technique to measure fractal dimensions of objects (Figure 4.13). The dividers themselves may ‘wobble’, or may create holes in the map causing difficulties in precisely locating the boundary. A map is not designed to be inspected at all scales of observation; there is a limit to the amount of detail which may be represented which depends on the scale of the map. Thus, the resolution of the Richardson plot depends on the resolution of the map itself. At stride lengths smaller than the map resolution there will be no increase in the perimeter length, causing the gradient to tend towards zero. The accuracy of the structured walk also tails off when the stride length becomes too large for the object to be measured. At large step sizes the number of steps to be taken before the boundary is completely traversed is small because the amount of perimeter that is left unmeasured (length a in Figure 4.11) becomes large in comparison with the total perimeter. Techniques to measure fractal dimensions need to avoid using data from beyond either of these limits/cut-offs.

4.4.3.b *Mixed Fractals*

Kaye (1989) describes examples of carbon fleck particles which cannot be described by a unique fractal dimension over all scales. The carbon fleck particles shown in Figure 4.14 have a fractal dimension of 1.13 at low magnifications. However, at higher magnifications the carbon fleck can be seen to be an aggregate of Euclidean spheres. Thus, the perimeter length at high magnifications becomes fixed, resulting in a fractal dimension of 1.0. Shapes which may be more adequately described by more than one fractal dimension, are referred to as mixed fractals. Mixed fractals have frequently been cited as a reason for not undertaking fractal analysis of objects. However, it is absurd to think that all shapes are fractal on all scales; eventually at some scale the fractal nature of an object will breakdown (e.g. on an atomic scale or as in the case of a carbon fleck on the scale of the carbon spheres). It is therefore important to be able to identify shapes which have mixed fractal properties and distinguish them from objects which are genuinely fractal over all scales. Furthermore if a shape is a mixed fractal, over what scale does it behave in a fractal manner and how may that observation be related to process of formation. These considerations will be discussed further in Chapter 5.

4.4.4 Computation of Fractal Dimension

The technique of measuring the perimeter of a grain/object using compass dividers does not lend itself to automation very easily. However, a method for measuring fractal dimensions has been described by Flook (1978) which is in some ways the opposite of the traditional structured walk, but still produces the same results. Instead of increasing the length of the dividers to measure the perimeter of a boundary with less and less accuracy, the detailed morphology of the boundary is gradually removed from the object in an orderly manner, whilst the object is measured using the same stride size (a computer pixel). Therefore, the perimeter decreases as more and more detail of the boundary is destroyed, thereby enabling a Richardson Plot to be constructed relating the scale of the irregularities removed to the perimeter length. The method by which morphology is gradually removed from a line is the Minkowski sausage.

4.4.4.a *Dilation and the Minkowski Sausage*

The Minkowski sausage is a technique for eradicating irregularities on a line at different scales by replacing the original line by a series of overlapping circles (Figure 4.16). The resultant structure is the Minkowski sausage (Minkowski, 1901). Figure 4.16 illustrates that as the diameter of the circle employed in creating the sausage is increased more detail of the original line is lost. The area of the sausage divided by the diameter of the circle which was used to create the sausage is an estimate of the equivalent perimeter of the original shape. If the circles don't overlap this technique is equivalent to the Richardson technique where the size of the circle is equal to the stride length.

Computation of the fractal dimension using this methodology is achieved using the standard image analysis technique of dilation. A line on a computer consists of a series of square picture points known as pixels. These may be thought of as a Minkowski sausage of squares similar to the circular structuring elements in Figure 4.16. It is a relatively simple task to replace every pixel on a line by the octagonal array of pixels. This procedure is known as dilation (Figure 4.17) and produces a Minkowski sausage with a diameter equivalent to the diameter of that octagonal structuring element. A whole series of Minkowski sausages of different sizes may be obtained from the original line or object

boundary. A Richardson plot is constructed by calculating the equivalent perimeter from each sausage (i.e. the area divided by the diameter of the structuring element).

It is obvious that a computer cannot produce circular Minkowski sausages; the octagonal structural element is the closest shape to which a circle may be approximated by a computer. A correction to the structuring element diameter has therefore been suggested by Flook (1978) of the form,

$$A_w = 7w^2 + 4w + 1 \quad \text{Equation 4.14}$$

where A_w is the area of one pixel dilated by w steps.

Because all orientations of boundary are equally probable, it is reasonable to estimate the radius of the structuring element (η) as:

$$\eta = 1/2(A_w/\pi). \quad \text{Equation 4.15}$$

A program has been developed (Appendix E) to automatically perform such an analysis for each grain within an aggregate using a Kontron Vidas21 image analysis system. Grains are picked from the aggregate one at a time, the boundary outline (perimeter) is drawn and a series of dilations are performed to produce Minkowski sausages. After each dilation the area of the Minkowski sausage of the grain boundary is measured and the diameter of the structuring element calculated. The process of dilation is continued until the structuring element has a diameter equivalent to the feret diameter of the object. Using the areas of the Minkowski sausages, together with the diameter of the structuring element (equivalent to the stride size for a structured walk), a Richardson plot may be constructed.

The actual fractal dimension of a grain is calculated from the gradient of a line on a Richardson plot of $\log(\text{perimeter})$ vs. $\log(\text{structuring element diameter})$. A linear regression is performed on the data set from each grain and the gradient of the line itself is calculated using a least squares method,

$$d = \frac{n \sum xy - (\sum x)(\sum y)}{n \sum x^2 - (\sum x)^2}$$

Equation 4.16

where n is the number of measurements, x and y are the values on the horizontal and vertical axes respectively.

4.4.4.b Accuracy of Technique

The automated system of fractal measurement has been tested for both accuracy and its ability to reproduce results using structured fractals. Structured fractals of a known fractal dimension are employed for two reasons. Firstly, they are relatively easy images to construct. Secondly, they have been used by many other authors to examine the validity of their measurement techniques (Flook, 1978; Russ, 1989; Kaye, 1989).

Three objects have been measured and the results compared with theoretical fractal dimensions, together with results from a variety of measurement techniques (e.g. box counting, structured walks and Euclidean distance mapping - see Russ, 1994). The three objects used are a triadic Koch curve, a quadratic Koch curve and a hexagon. The results for the triadic and quadratic Koch curves are close to their theoretical value (1.25 and 1.48 respectively). whilst the hexagon has a fractal dimension of one, which is expected (Figure 4.18). The results indicate that the measurement of fractals using the Minkowski approach is not ideal. This is because there may be small deviations in the gradient in the line on a Richardson plot. However, the results from all the shapes measured using the algorithm which has been developed suffer from the same inadequacies, enabling a comparison to be made between results. Russ (1992) warns of the dangers of comparing numerical values which have been acquired by a variety of techniques (see also Russ, 1994). The same shapes have been measured on several occasions and produced exactly the same results, indicating that the results are indeed reproducible.

Unlike mathematically generated fractals, real data cannot be fractal over all scales. Minor deviations always occur. Bearing this in mind, it is still useful to compare data from grain to grain to determine if there are broad differences from sample to sample, or even within one sample.

4.4.5 Application To Ballachulish Aureole

The method by which a grain is measured to obtain its fractal dimension (i.e. structured walk) is an important procedure for characterising the shape, whether the object is truly fractal or not. If the object that is being measured is fractal, at least over some scales of observation, then a fractal dimension may be assigned to that shape. On the other hand, if it is not clear that the shape is indeed fractal, then the data acquired using the structured walk still contains information about the grain shape, even if this information cannot be expressed as a single numerical value. It is just as important a result if grain shapes are shown not to be fractal.

The philosophy behind the analysis for the rocks through the Ballachulish aureole is to presume that the grains do exhibit fractal characteristics, and so calculate the fractal dimension of each grain. This is a large assumption, and will be justified after the initial fractal analysis is complete. Such an approach is taken because it is necessary to manually inspect Richardson plots for each grain to determine whether that grain has fractal characteristics. Obviously this is time consuming and an absolute waste of time if the grains are fractal anyway. The fractal dimensions therefore are measured for every grain in each of the samples, trends in the data are investigated and a visual examination of the results compared to grain roughness is undertaken. If no trends are found, or the fractal dimensions of grains do not relate to the complexity of the shapes involved, further analysis is needed to determine if the shapes may be mixed fractals.

4.5 Crystallographic Analytical Techniques

4.5.1 Introduction

In this section the methods by which crystallographic data are collected are described, followed by a description of the graphical methods by which these data are presented in this study. Crystallographic data from the rocks at Ballachulish have been examined for the following:

- crystallographic preferred orientations (CPO) of grains in relation to the strain regime at Ballachulish;

- local 'mesotexture' analysis describing the misorientations between neighbouring grains;
- low energy grain boundary orientations (or coincident site lattices - CSLs).

The methods of processing crystallographic data to investigate each of the above are outlined in sections 4.5.4, 4.5.5 and 4.5.6.

4.5.2 Data Acquisition

In order to understand how crystallographic preferred orientations (CPO) may influence a rock microstructure, it is necessary to obtain a complete three-dimensional crystallographic description of each grain within an aggregate, combined with a spatial description of microstructural features (Schmidt and Casey 1986). Due to technical limitations, this is not possible with conventional techniques such as the optical microscope, transmission electron microscopy and X-ray goniometry. In quartz, optical microscopy enables only the orientation of a crystal's c-axis to be determined. X-ray goniometry only provides an analyses of the bulk rock fabric whilst TEM does not adequately describe the spatial variation of a microstructure and its corresponding microtexture because it is limited to small areas of samples. Two SEM techniques do permit full crystallographic and spatial descriptions of rock samples to be derived, via either electron channelling (Booker 1970; Joy and Newbury, 1977; Saimoto et al. 1980; Joy et al. 1982; Lloyd 1987) or electron back-scatter diffraction - EBSD (Randle, 1992).

During this investigation, crystallographic orientations have been measured using the electron channelling technique (see Appendix B for more details). This technique measures the orientation of a crystallite with respect to a specimen reference frame. The specimens have been cut so the specimen reference frame is aligned with the principal strain directions of the regional deformation. The computer program CHANNEL 1.3 has been used to index channelling patterns (the basics of the program are described in N-H. Schmidt and Olesen 1989). Channelling patterns are manually digitised into a computer, which calculates the crystal orientation by comparing the digitised pattern with a theoretically calculated set of electron channelling bands (which together form an ECP

map) stored in a data base. The computer picks the best fit to the calculated bands by comparing the band widths and angles.

The output data from CHANNEL is in the form of a 3x3 matrix describing the angular relationships between a crystals reference frame (a,b,c) and the specimen reference frame (x,y,z). Each element of the matrix is a direction cosine between two reference frame axes (i.e. the direction cosine between the c-axis of a crystal and the x direction of the specimen). For a detailed description of the mathematical treatment of the output and conversion between different versions of the CHANNEL program see Appendix D.

4.5.3 Data Presentation

A number of methods have been routinely used in Material Science and Geology to depict crystallographic textures of materials, specifically: pole figures, inverse pole figures, euler space and Rodrigues-Frank space. The first two methods are stereographic plots relating a crystal vector to an external reference frame or the crystal reference frame for pole figures and inverse pole figures respectively. For the purposes of this investigation pole figures and inverse pole figures are used to present crystallographic preferred orientations as these diagrams are relatively simple to understand and are also the most widely used methods for presenting crystallographic orientations.

4.5.3.a Pole Figures

Pole figures relate directions within a crystal lattice (crystal vectors) to an external reference frame. A stereographic projection is used to display the vector orientations in a similar way that linear structural elements from a field map (e.g. a lineation) are displayed with respect to North, South, East and West on a stereonet. A pole figure plots a crystal direction (usually a major zone axis) in relation to the x,y,z axes of an external reference frame (usually the specimen reference frame). Perhaps the most common pole figures are c-axis pole figures - see Figure 4.19. Many authors have used c-axis distributions with respect to regional strain orientations to infer deformation frameworks (pure shear or simple shear - Etchecopar 1977; Lister 1978; Law 1986; Schmid and Casey 1986 and Law and Potts 1987) and also deformation processes (Law and Knipe 1987).

The orientation of a crystal vector (or Miller index of a crystal vector) in a specimen reference frame may be determined from the orientation matrix [G] by:

$$\begin{bmatrix} U' \\ V' \\ W' \end{bmatrix} = [G] \cdot \begin{bmatrix} U \\ V \\ W \end{bmatrix}$$

Equation 4.17

where UVW is the Miller index of a vector within a crystal related to the external reference frame by [G] and U'V'W' are the new co-ordinates of the vector in the external reference frame.

Thus, the orientation of a crystal vector may be calculated with respect to an external reference frame and represented on a stereonet in the form of a pole figure. A number of pole figures may be constructed for any one sample to display the orientation of any appropriate crystal vector. Crystal vectors in non-cubic materials must be converted to a Cartesian system before they can be rotated into the pole figure space (i.e. an external reference frame). For details of these operations see Bunge (1985).

4.5.3.b Inverse Pole Figures

The inverse pole figure is a very specific form of pole figure relating a vector to a crystallographic reference frame (Boisen and Gibbs, 1985). Any type of vector may be plotted on an inverse pole figure (e.g. zone axes, the specimen normal or the misorientation axis between two grains - see Figure 4.20). In the case of plotting the specimen normal (a vector of 100 in x,y,z space) the normal is rotated around into the crystal reference frame for each grain in turn. For the purposes of this study, inverse pole figures will be used to illustrate features associated with grain boundary misorientations. The reduced area of inverse pole figures is a function of the crystal symmetry. For example, an inverse pole figure for quartz may be constructed using only one third of the stereographic sphere.

The choice of plotting style depends on the information that is required from a sample. Both methods have their advantages and disadvantages. Pole figures are ideal for investigations which consider the controls upon crystal fabrics by the kinematic

framework (e.g. tectonics or flow), whilst inverse pole figures are well suited to studies investigating the controls crystallography may exert on the modification of fabrics (e.g. during deformation or heating) within a sample.

4.5.4 Crystallographic Preferred Orientations

The rocks at Ballachulish are examined in Chapter 5 for crystallographic preferred orientations. The data are presented as a series of pole figures, which for this investigation are limited to comparing the orientation of quartz c-axes to the regional deformational strain. An example of a pole figure is seen in Figure 4.19.

4.5.5 Misorientation Analysis

Normally, grain orientations are described by referencing a grain's axes (a,b,c) to the external specimen reference frame (x,y,z). Alternatively, it is possible to relate one grain to another (neighbouring) grain. This is referred to as a misorientation (Randle 1992; Grimmer et al. 1974 and Pospiech et al. 1986). The relationship of the reference frames of two grains may be described by a misorientation matrix, which is similar to the orientation matrix relating a crystal to the specimen reference frame. Grimmer (1970) has shown that the misorientation matrix $[M]$ for two grains may be calculated by:

$$[M]_{AB} = [G]_A^{-1} [G]_B \quad \text{Equation 4.18}$$

$[M]$ is the matrix which represents a rotation of grain G_A on to G_B . Alternatively, the rotation may be described by Euler angles. Neither Euler angles nor a misorientation matrix are particularly useful as a means of presenting misorientation data. Significantly more useful is the axis/angle pair construction, which provides a means of representing misorientation data in a graphical format.

The axis/angle pair is simply a rotation of angle θ about a specific axis l (where l is a direction common to both grains) which brings both grain orientations into coincidence. The fact that an axis/angle pair is described by a vector (the axis) and an angle makes it an ideal expression of misorientation for plotting on a variety of crystallographic

diagrams (e.g. pole and inverse pole figures). The axis angle pair is derived from the misorientation matrix via,

$$\theta = \cos^{-1}(M_{11} + M_{22} + M_{33} - 1) / 2 = \text{angle} \quad \text{Equation 4.19}$$

$$U:V:W = M_{32} - M_{23}:M_{13} - M_{31}:M_{21} - M_{12} = \text{vector} \quad \text{Equation 4.20}$$

where U:V:W: is the misorientation axis and M_{ij} are elements of the misorientation matrix (after Farmer 1992).

Due to the symmetry inherent in minerals, there are a number of possible solutions for the misorientation axis/angle pair (Haessner et al. 1983; Bunge 1985; Pospiech et al. 1986 and Farmer 1992). For example, a cubic mineral has 24 axes of symmetry, which give rise to a possible $24 \times 24 = 576$ possible rotation axes. However, there will only be 24 different axis/angle pairs (Bunge, 1985, Boisen and Gibbs 1985 and Farmer 1992). It is necessary to decide which of the 24 solutions is the most appropriate to represent the misorientation between two grains. The choice is dependent upon the nature of the investigation. Studies which deal with subgrains with low magnitudes of misorientation from a common parental orientation (e.g. Farmer 1992, McGennis 1993 and Neuman 1995) chose the solution with the smallest angular mismatch. However, this is not the obvious choice for this study because grain:grain misorientations are being examined which do not have a common parental orientation from which they have been misorientated by a small magnitude with respect to each other. Randle and Furley (1991) and Fliervoet and White (1995) both chose the axis/angle pair solution which is closest to a CSL (Coincident Site Lattice) boundary description (see section 4.5.6). The choice of misorientation solution is discussed further in Chapter 5.

A complete inverse pole figure for quartz is shown in Figure 4.21. A vector (e.g. a pole to a plane) may be plotted on the diagram. However, it will have two other vectors which are symmetrically equivalent which plot elsewhere on the diagram. The trigonal symmetry of quartz means that an inverse pole figure may be divided into three sectors. Typically, only one of these sectors is shown, in the knowledge that any vector which is depicted on the diagram is equivalent to a vector in each of the other sectors. Inverse pole figures for quartz misorientations may be further reduced to $1/6^{\text{th}}$ of the stereonet

because the vectors for a misorientation are bi-directional (i.e. the axis/angle of rotation is the same whether the vector is viewed 'down-plunge' or 'up-plunge'). This is shown in Figure 4.21, a rotation around a pole to the z-plane is equivalent to a rotation around the pole to the r-plane and so all misorientation axis angle pairs may be represented within just 60° of inverse pole space (Mainprice, 1992). Because inverse pole figures do not display any information about the angle of misorientation it is necessary to construct a number of figures, each one representing misorientations with angles of misorientations within a fixed range (cf. Chapter 5).

4.5.6 The Coincident Site Lattice

Many studies have shown that crystallographic orientation exerts a major influence upon deformation and annealing processes. More recently, many authors have indicated that grain boundary orientation may also be a relevant control on the evolution of a microstructure/microtexture (Randle, 1992 and Fliervoet and White, 1995). The Coincident Site Lattice (CSL) is a means of investigating the theoretical structure of grain boundaries, the starting point for which is to predict any specific orientations which have a low energy configuration. Once these orientations have been calculated, it is necessary to determine whether these orientations are stable microstructural features during deformation and/or annealing.

Clearly, some grain boundary orientations are relatively common within materials. For example, twin relationships which relate two grains of a mineral species about a fixed twin law (a rotation about a unique crystal axis) are low energy grain boundary configurations which are reported throughout the geological literature in most minerals. What makes twin relationships a low energy configuration is that the crystal lattices related by the twin are able to share a number of their atoms within the twin plane, hence lowering the surface energy of that special grain boundary.

The CSL theory is based on the same premise, that certain grain misorientations form geometries which enable the crystal lattices either side to share atoms within the grain boundary. Three factors control the number of CSL special orientations which may occur within a crystal:

- 1) The crystal lattice parameters (i.e. a, b and c axes lengths) and crystal symmetry.
- 2) Misorientation of one grain to its neighbour.
- 3) The orientation of the grain boundary plane.

An example of a CSL within quartz is shown in Figure 4.22. The atoms from both grain domains which coincide within the grain boundary form a super-lattice that is termed the coincident site lattice. The CSL has a 'multiplicity' proportional to the number of atoms within the superlattice which coincide with the normal crystal lattice. In the example, the super-lattice coincides with the crystal lattice once in seven times, and thus has a multiplicity (Σ) of 7. In cubic minerals the multiplicity may be related to the misorientation matrix by (Randle 1992),

$$[M] = \frac{1}{\Sigma} [G]. \quad \text{Equation 4.21}$$

[G] is the orientation matrix.

In theory, a CSL may be formulated for any value of Σ . However, the CSL description becomes physically less significant the larger the multiplicity because less atoms are coincident within the grain boundary at these values. Shvindlerman and Straumal (1988) suggest that only values of Σ which are less than 49 are significant.

4.5.7 Calculating CSL in Trigonal Minerals

Two approaches for determining CSL within trigonal minerals have been documented, a manual method (McLaren, 1986) and a theoretical method (Grimmer, 1989). McLaren (1986) investigated the occurrence of coincident site lattices between crystals misoriented along common zone axes. The method involves projecting a crystal lattice on to two separate acetate sheets. The two images of the projection are then overlain and rotated with respect to one another until a CSL is produced. The multiplicity is easily

calculated from the number of atoms which coincide between the CSL super-lattice and the crystal lattices.

Grimmer (1989) derived a general solution calculating coincidence orientations in rhombohedral lattices. The orientations and multiplicity of CSL in general depend on the axial ratio. The description of the geometrical model for coincidence site lattices outlined below is based on that from Grimmer 1989.

The calculation is feasible only when c^2/a^2 is rational. It is then possible to write,

$$\frac{c^2}{a^2} = \frac{3\mu}{2\rho} \quad \text{Equation 4.22}$$

where μ and ρ are integers such that $\mu - \rho$ is a multiple of 3 and that μ and $(\mu - \rho)/3$ have no factor in common. Now,

$$\text{gcd}(\mu, (\mu - \rho) / 3) = 1.$$

Thus μ and ρ are variables which reflect the axial ratio of a mineral (gcd = greatest common denominator).

Let m, u, v, w be integers such that $2u + v + w$ is a multiple of 3 and that,

$$\text{gcd}(m, u, v, (2u + v + w) / 3) = 1 \quad \text{Equation 4.23}$$

where u, v, w is a vector denoted in by their Weber indicies $(uv.w)$ in which the dot is a replacement for t in the Weber index and m is a parameter for the definition of the rotation angle (Doni and Bleris 1991).

A rotation axis $[uv.w]$ and angle θ given by,

$$\tan \frac{\theta}{2} = \sqrt{\frac{\mu w^2 + 2\rho(u^2 + uv + v^2)}{3\mu m^2}} \quad \text{Equation 4.24}$$

generates a coincidence lattice with multiplicity,

$$\Sigma = \frac{f}{(3f_1 \cdot f_2 \cdot f_3 \cdot f_4)} \quad \text{Equation 4.25}$$

where $f = \mu(3m^2 + w^2) + 2\rho(u^2 + uv + v^2)$

and $f_1 = \gcd(2, m+w)$

$$f_2 = \gcd(2, m+w, u, v)$$

$$f_3 = \gcd(m, 2f_1^{-1}u, 2f_1^{-1}v)$$

$$f_4 = \gcd(\rho, 2f_2^{-1}m, m+w, 2(\mu w + \rho(v-u))(3f_3)^{-1})$$

It follows that Σ is independent of μ and ρ for rotations with an axis parallel to the three-fold symmetry axis [00.1] of the trigonal lattice and for 180° rotations with axes perpendicular to the triad. Rotations which satisfy either $u=v=0$ or $m=w=0$ are called common rotations and have the same Σ for any axial ratio. If c^2/a^2 is rational, there may also be specific rotations which depend on the value of the axial ratio.

There is a lower bound for multiplicities of specific rotations which varies as a function of μ and ρ :

$$\Sigma \geq \frac{\sqrt{8\mu\rho}}{3} \quad \text{if } \mu \text{ and } \rho \text{ are odd,}$$

otherwise:

$$\Sigma \geq \frac{\sqrt{2\mu\rho}}{3}$$

This bound can be used to compute tables of all specific coincidence rotations with c^2/a^2 in a given interval and multiplicity up to a given value (in this investigation 49). A given misorientation rotation may be described by different rotation vectors due to the trigonal symmetry of quartz. These rotations form an equivalence class. The rotation with the smallest angle in each class is chosen to represent the CSL rotation.

Using the theory outlined above every possible rotation (axis/angle pair) between two crystals may be calculated up to a given Weber index and examined to determine whether it is a CSL within quartz (or any other mineral with a rhombohedral lattice). Thus, a table of coincident site lattice rotations within quartz may readily be constructed and compared to the misorientation data from rock aggregates. A table of CSL generated for rhombohedral lattices with similar parameters of c and a to quartz is presented in Figure 4.23.

The following microstructures are typical of quartz grains in a deformed rock. The first is a typical subgrain structure, where the grain is divided into smaller subgrains by low-angle grain boundaries. The second is a structure with a high density of dislocations, which are small defects in the crystal lattice. The third is a structure with a high density of grain boundaries, indicating a high degree of deformation. The fourth is a structure with a high density of dislocations and grain boundaries, indicating a high degree of deformation and recrystallization.



Figure 4.1 Typical substructures found within deformed quartz grains (from Farmer, 1992).

Figure 4.2 An SEM photomicrograph shows that substructures of deformed grains are complex, a number of grains are imaged within this micrograph.



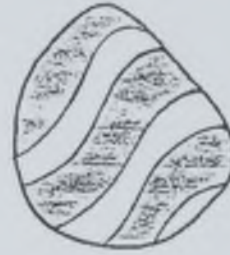
Equant



Straight



Lensoid



Wobbly



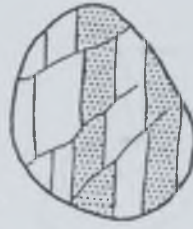
Indents



High contrast



Internal tracks



Thin fractures



Recrystallised fractures

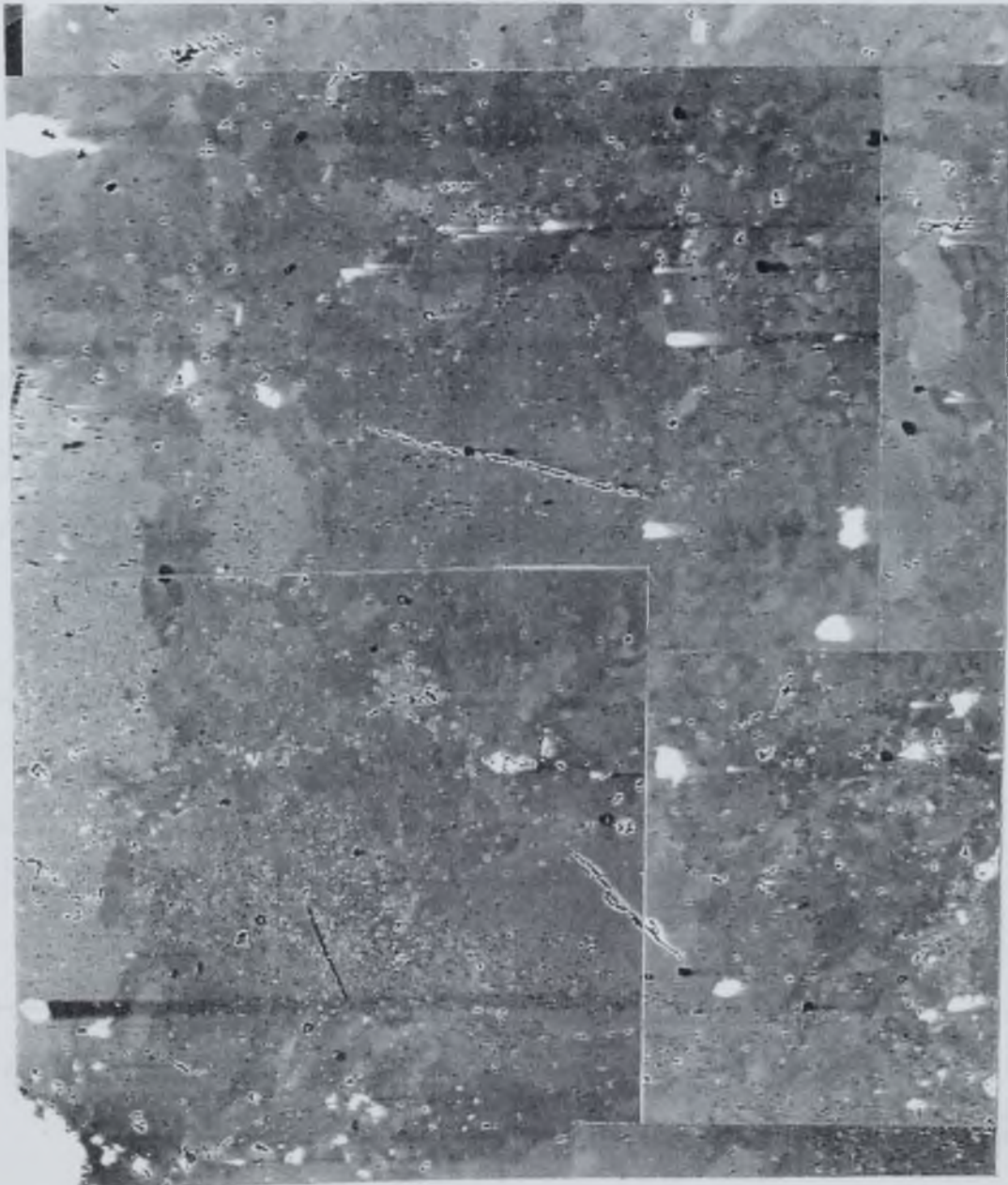




Figure 4.3 A typical binary image which is produced from coloured grain maps (see Appendix F) using macro "Grains" - Appendix E.

file = 48





Figure 4.4 Stereological problems occur even in the simplest case of a sphere. Planes (akin to a thin section through a rock) cut the sphere such that the diameter of the intersection of the sphere and plane is always less than or at best equal to the true 3-D sphere diameter.

Figure 4.5 Examples of two theoretical distributions which have the same average, but a different distribution shape.

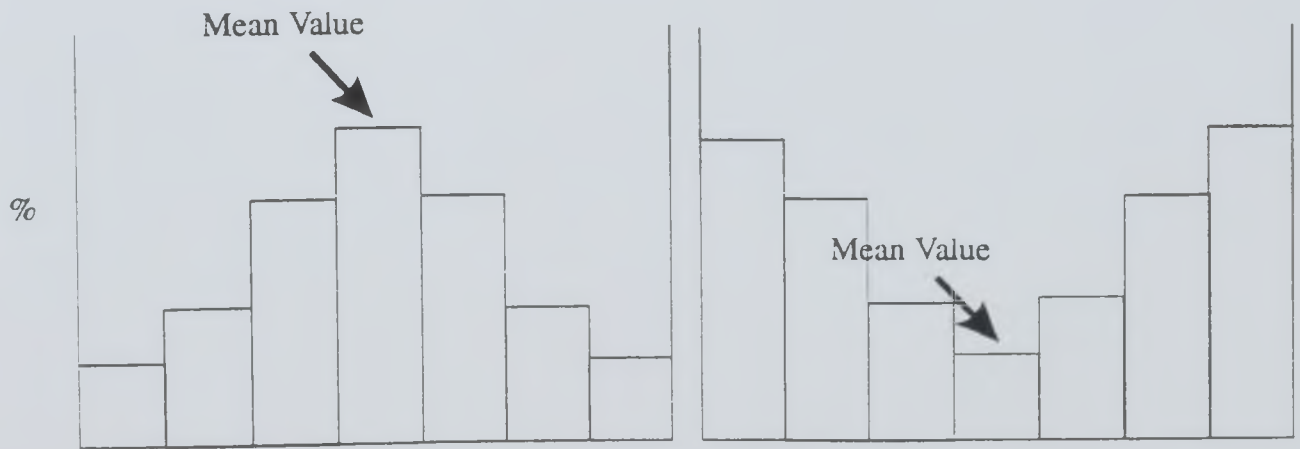
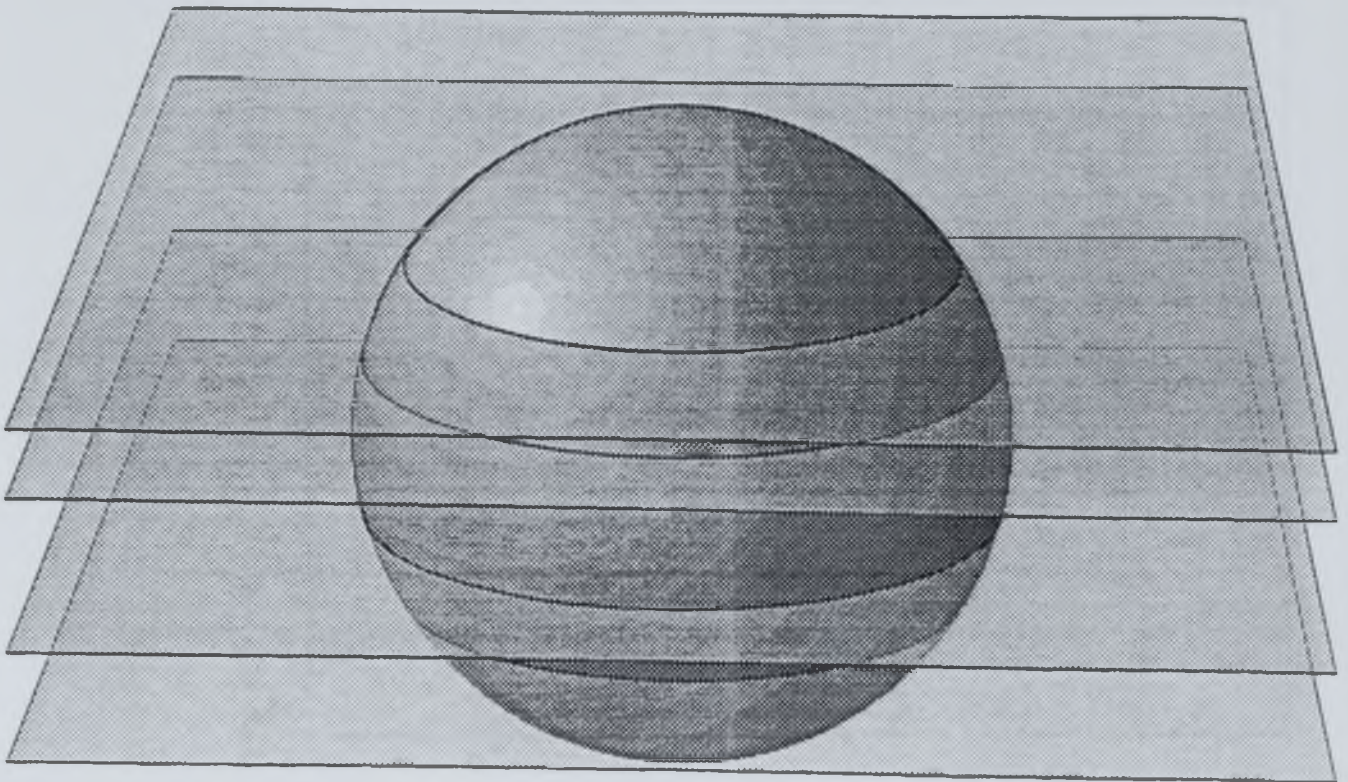


Figure 4.6 A moment ratio diagram showing where common distributions plot (from Lloyd, 1983).

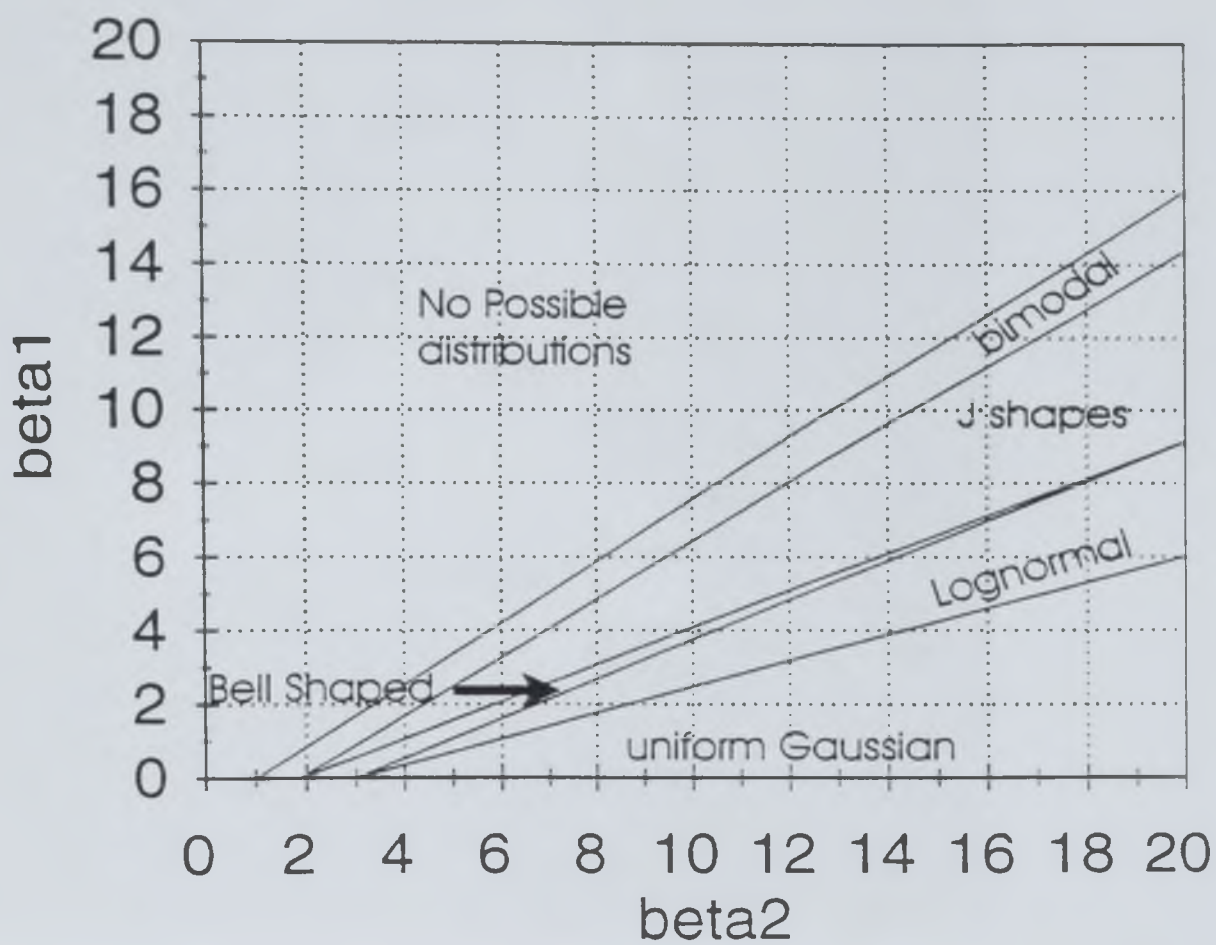
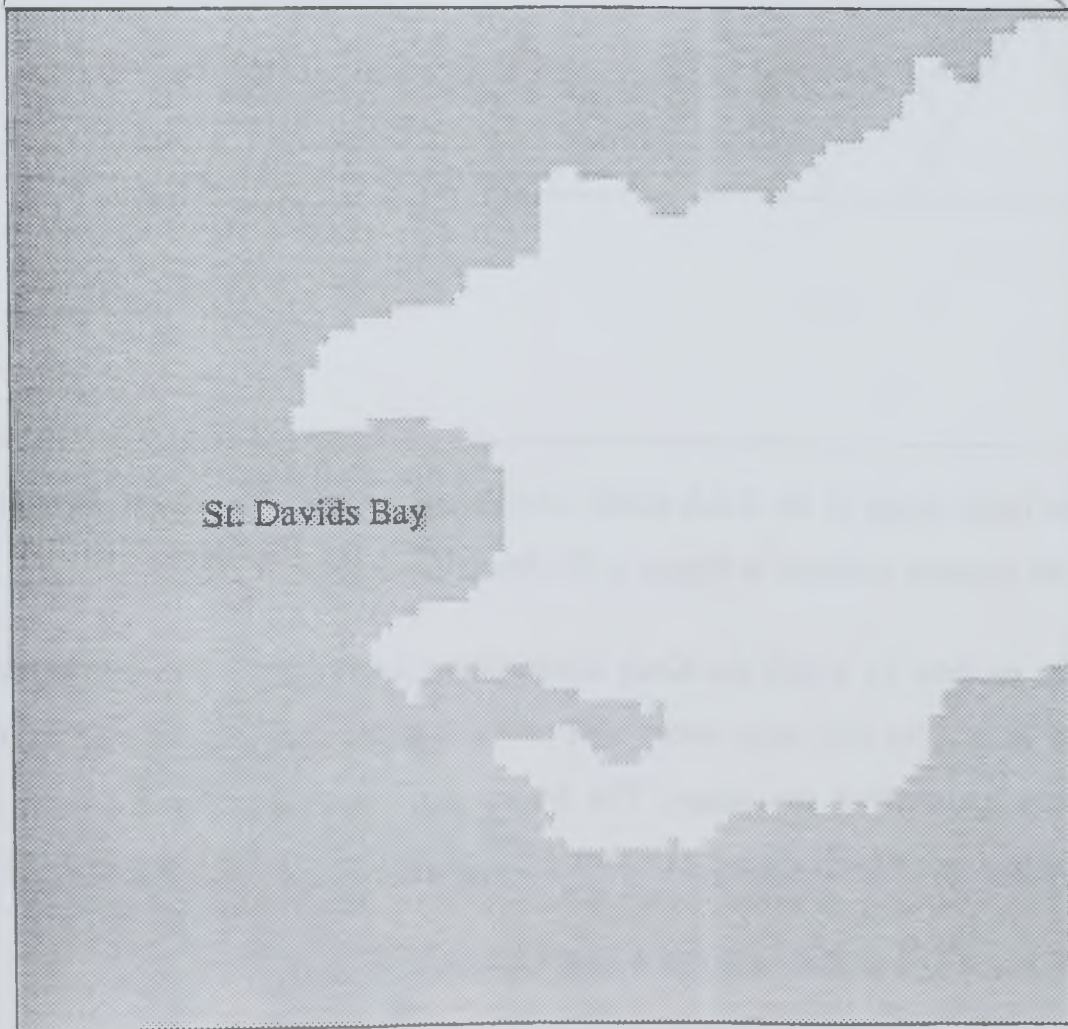
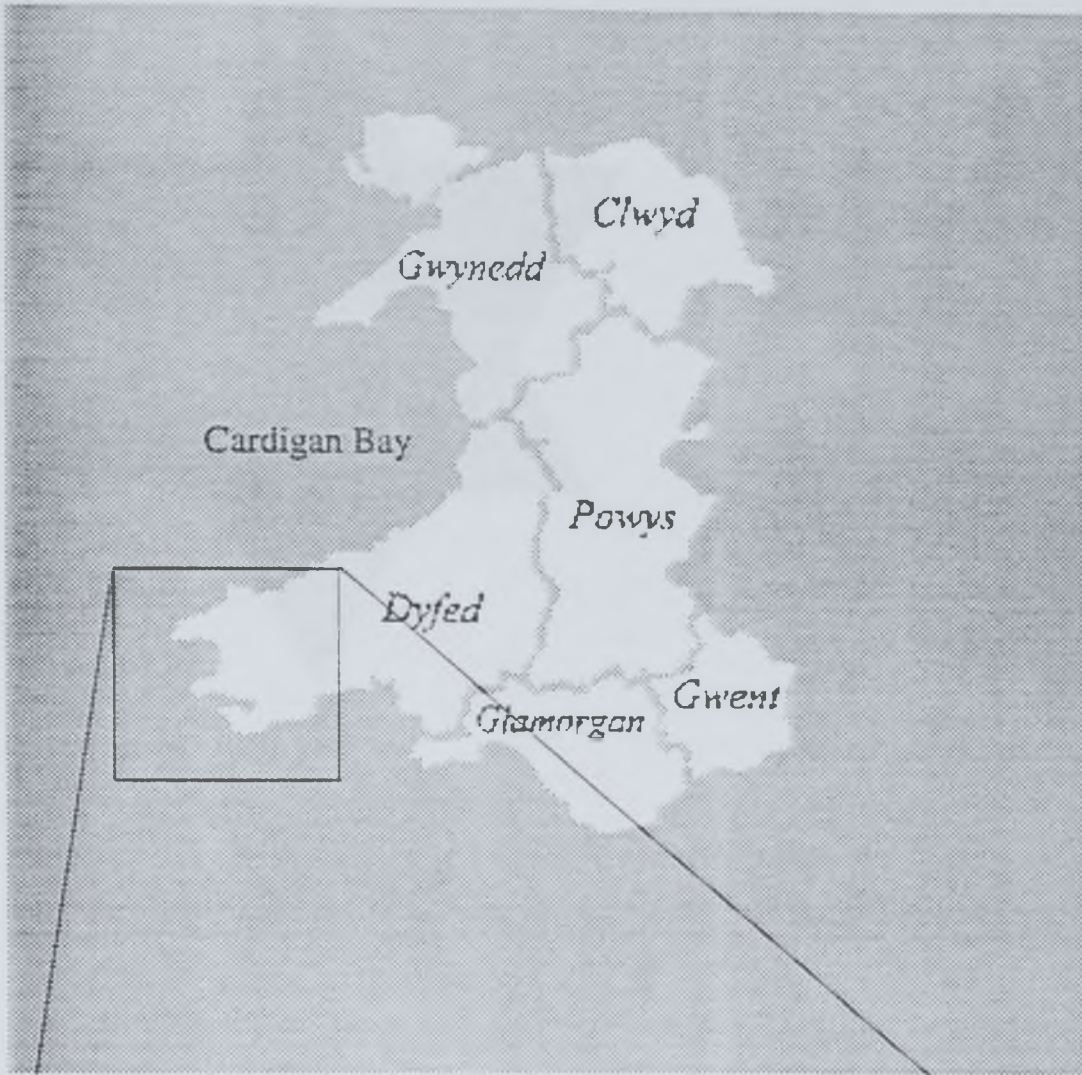




Figure 4.7 Self similarity of the coastline of Britain, at different magnifications, the coastal feature, although not identical but they are similar.






Figure 4.8 The basic shape of the Koch triadic island, together with the shape after three iterations by the process outlined in Figure 4.32 - fractal dimension = 1.262.

Figure 4.9 The method by which the Koch triadic island is produced. The line segment (a) is reduced in size by one third, every side of the original shape is replaced by this feature, thereby elaborating the shape. The fractal dimension is calculated from the $\log(\text{number of features which are reduced})/\log(1/\text{the reduction factor}) = \log(4)/\log(1/3)$.

Figure 4.10 A Koch Quadratic curve has a fractal dimension of 1.5000.

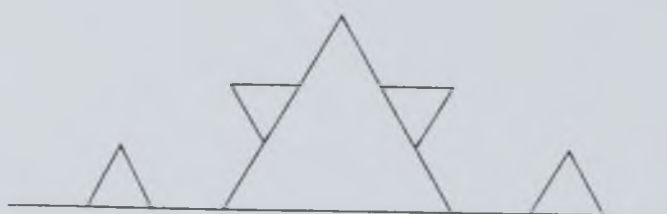


Figure 4.11 The principal of a structured walk. An irregular outline is converted to a polygonal approximation using different step lengths. The total number of sides (including the final partial one) times the length of the stride gives an estimate of the perimeter, which increases as the step size becomes smaller.

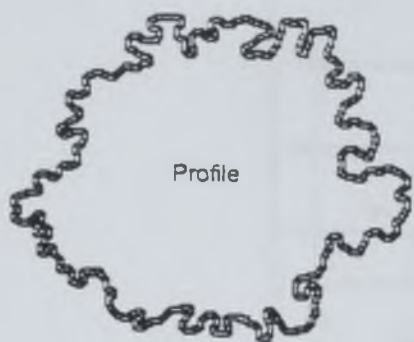
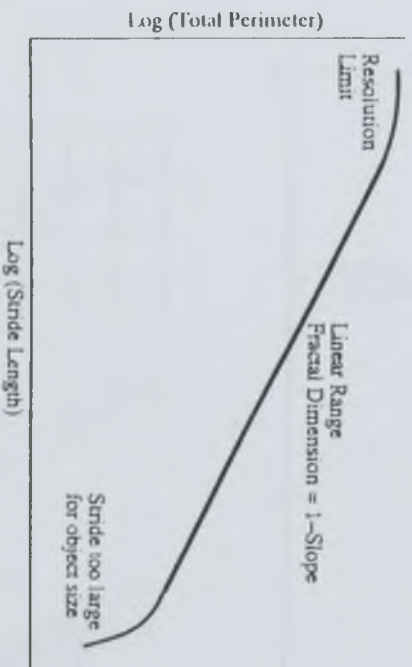
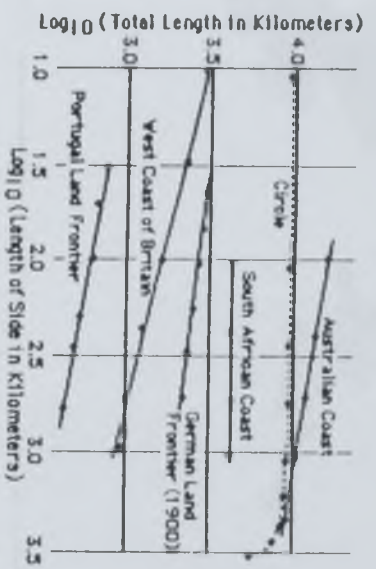




Figure 4.12 A typical Richardson plot. The data for various geographical boundaries (from Richardson 1961).

Figure 4.13 Schematic diagram of a Richardson plot shows that at very small and large step sizes the gradient of the line tends towards 0 and infinity respectively. These are the resolution limits (cut-offs) for measurement of fractal dimensions.



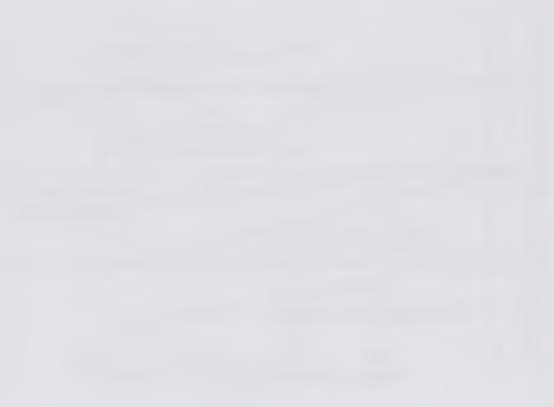
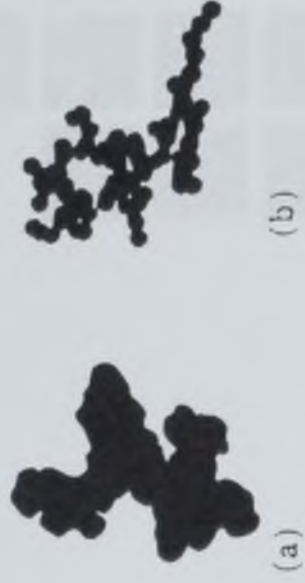


Figure 4.14 Two examples of carbon fleck particles (from Flook 1977).

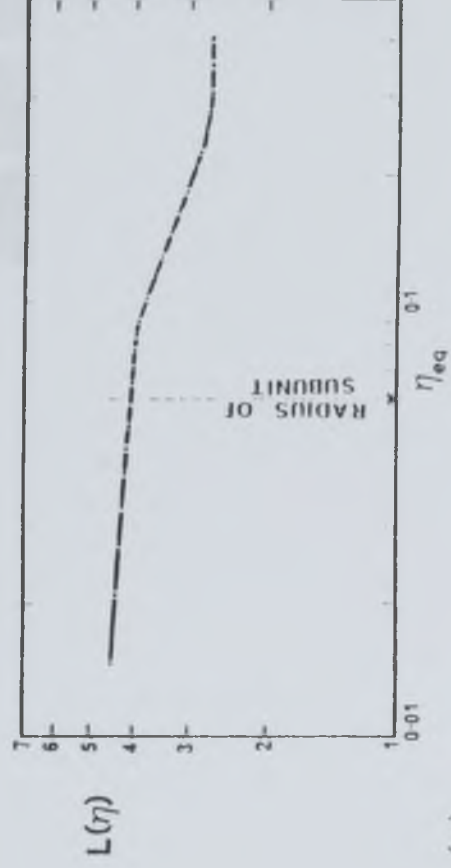


Figure 4.15 Richardson plots for the carbon fleck particles in Figure 4.37 produced from a dilational method (from Flook, 1977).

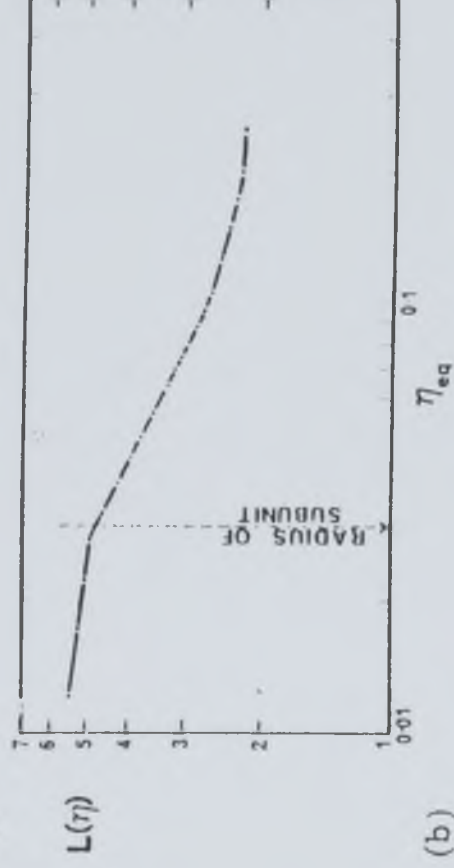
Figure 4.16 A comparison between the Minkowski sausage and the structured walk techniques for measuring fractal dimensions. As the Minkowski sausage becomes larger less detail of the original line is preserved.



(b)



(a)



(b)

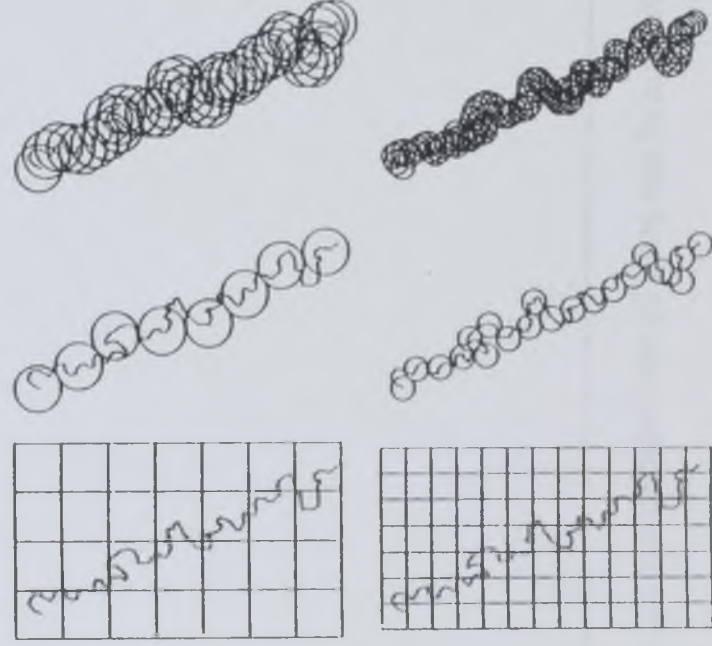




Figure 4.17 Dilation of one pixel by an octagonal structuring element.

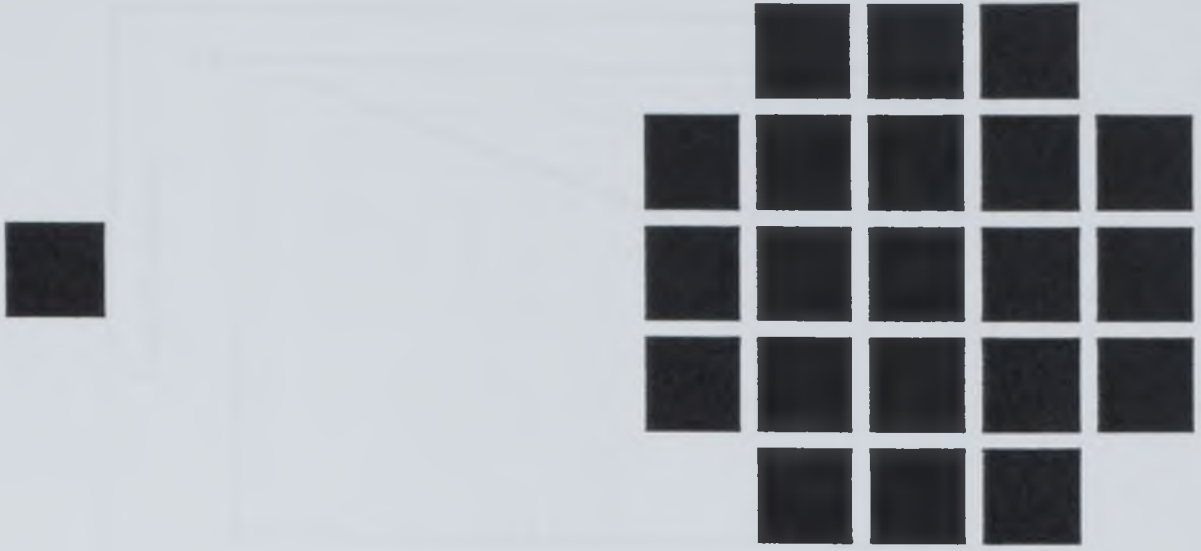




Figure 4.18 Richardson plots for Koch triadic island (Top - fractal dimension=1.26), quadratic island (middle - fractal dimension=1.5) and a hexagon (bottom - fractal dimension of 1.0). The Richardson plots have been calculated using program 3 (Appendix E).

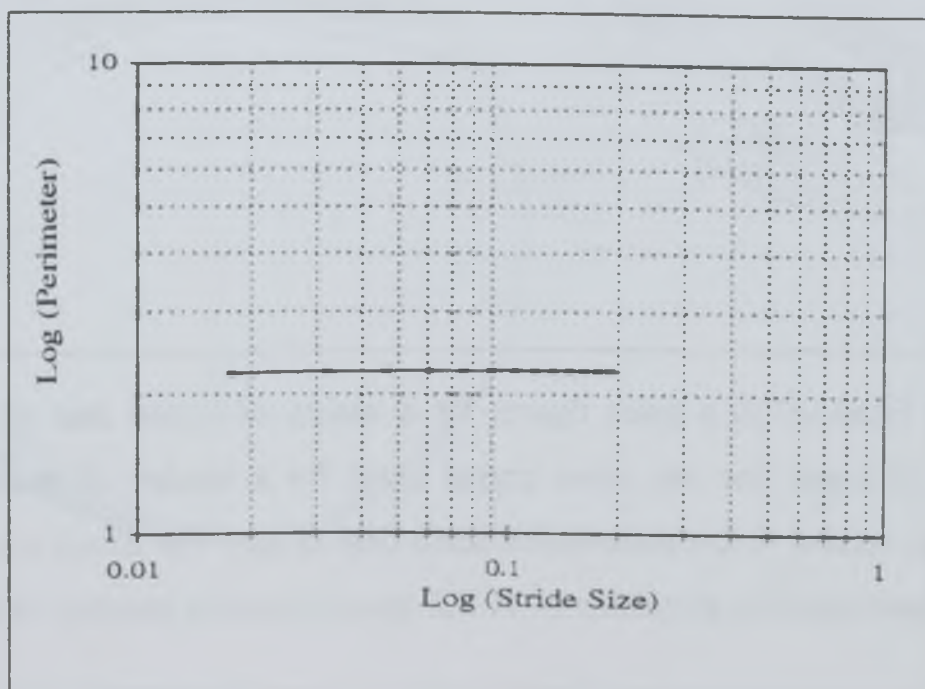
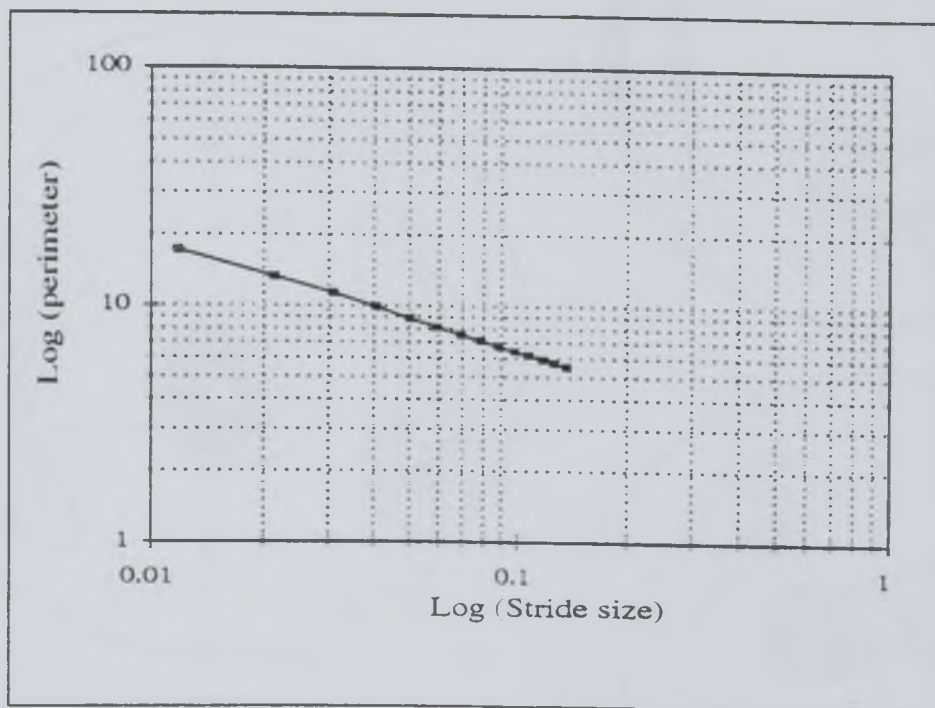
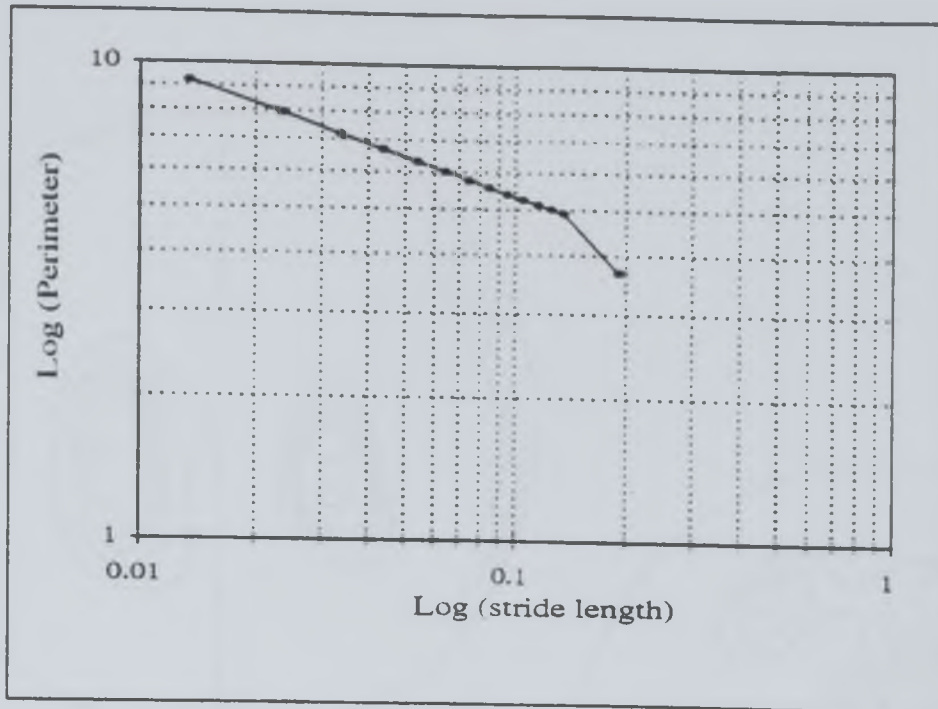


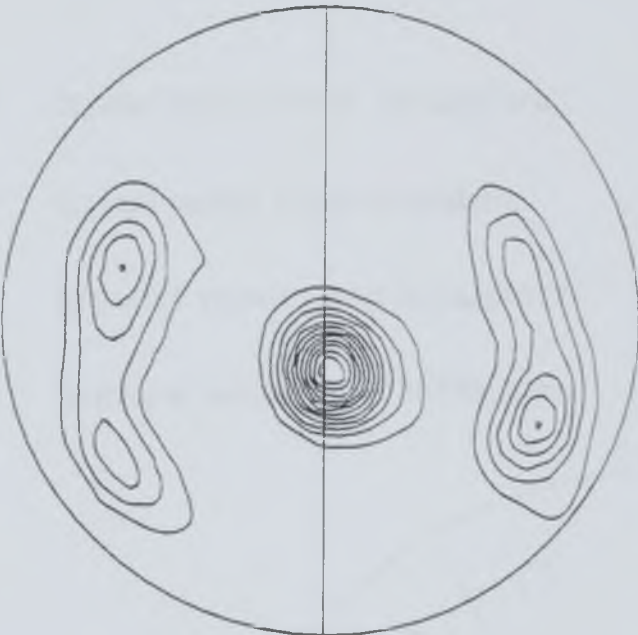


Figure 4.19 Example of a poles figures for a variety of crystal axis of quartz. The distribution of c-axis (or any other crystal axes) for a number of grains within an aggregate are related to the deformation strain field (x,y,z). The c-axis are plotted as a vector on a stereographic projection of X,Y,Z space. (Diagram courtesy of G.E. Lloyd)

a 1.0(1.0)9.0



m 1.0(1.0)13.0



c 1.0(2.0)17.0



z 1.0(0.5)4.5



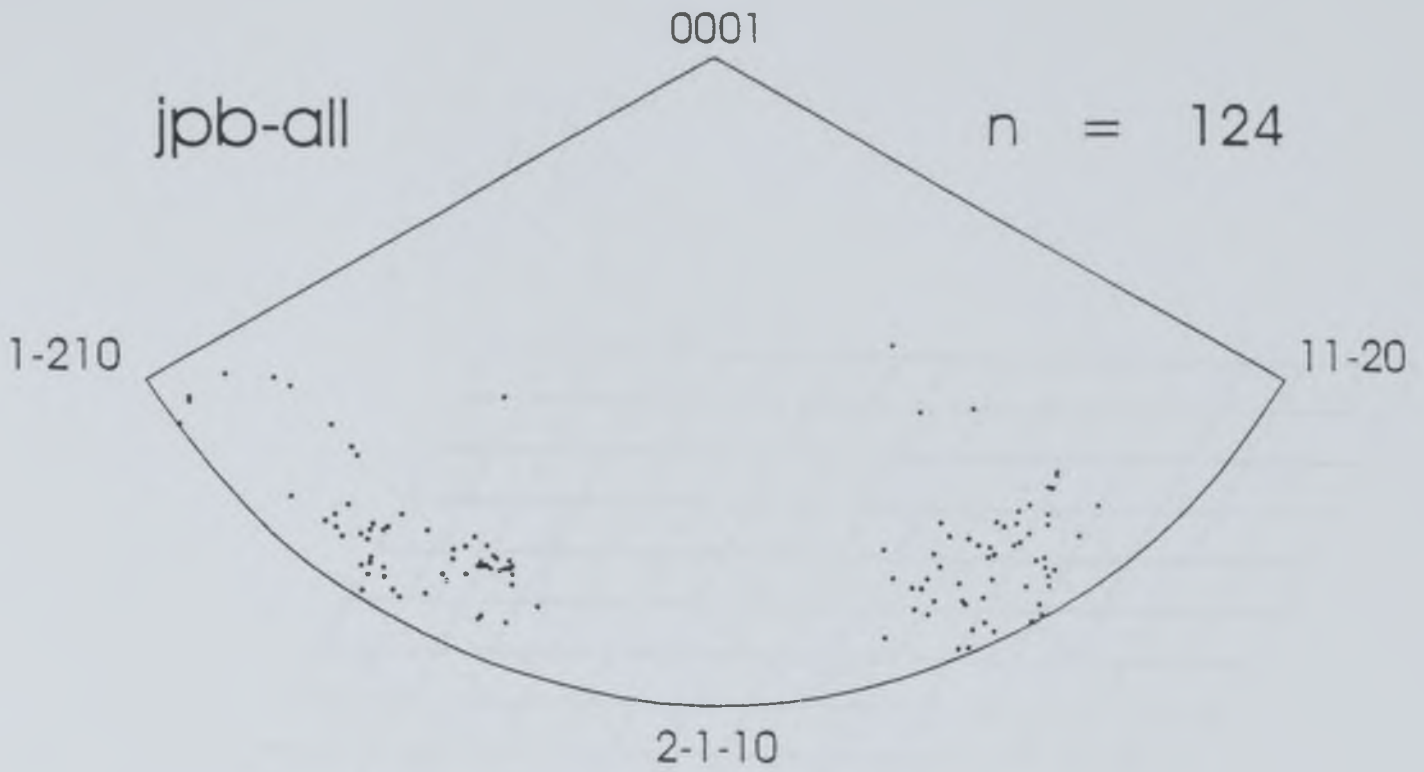
r 1.0(0.5)4.5





Figure 4.20 An example of an inverse pole figure which plots the orientation of the specimen normal for each grain in an aggregate in relation to the crystal reference frame. (Diagram courtesy of G.E. Lloyd)

Figure 4.21 A complete inverse pole figure of quartz indicating the symmetry of the rhombohedral lattice. It is because of the symmetry within quartz that the inverse pole figure may be reduced to $1/3$ of the sphere when plotting the orientation of the specimen normal, or $1/6$ of the sphere for misorientation inverse pole figures.



- crystal vector lower hemisphere
 - crystal vector upper hemisphere
 - negative vector lower hemisphere
 - negative vector upper hemisphere
- a-axis diad
- ▲ c-axis triad

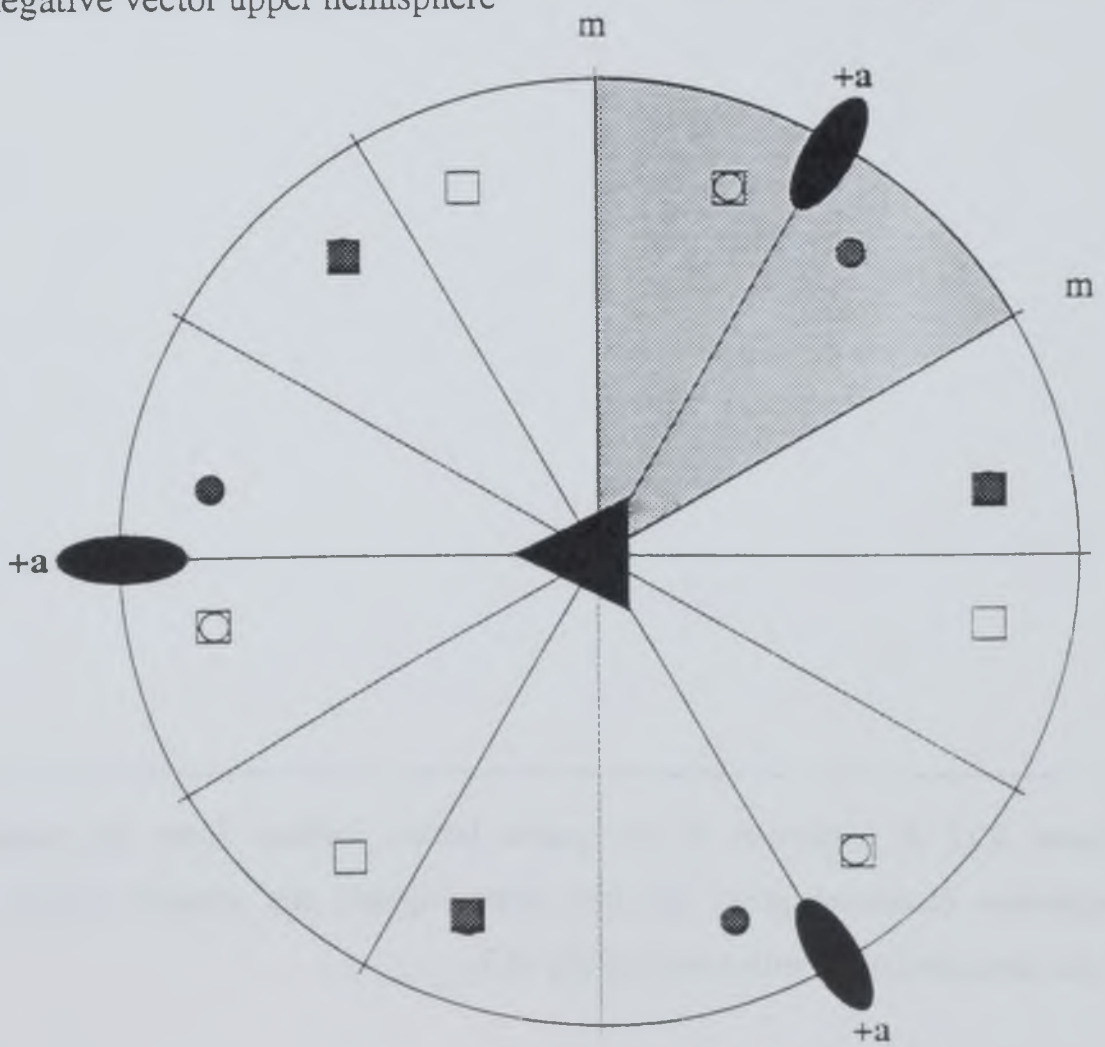


Figure 4.22 A projection of the quartz lattice, looking down the c -axis. Another projection (coloured grey) has been superimposed and rotated around to form a coincident site lattice with a multiplicity of 7.

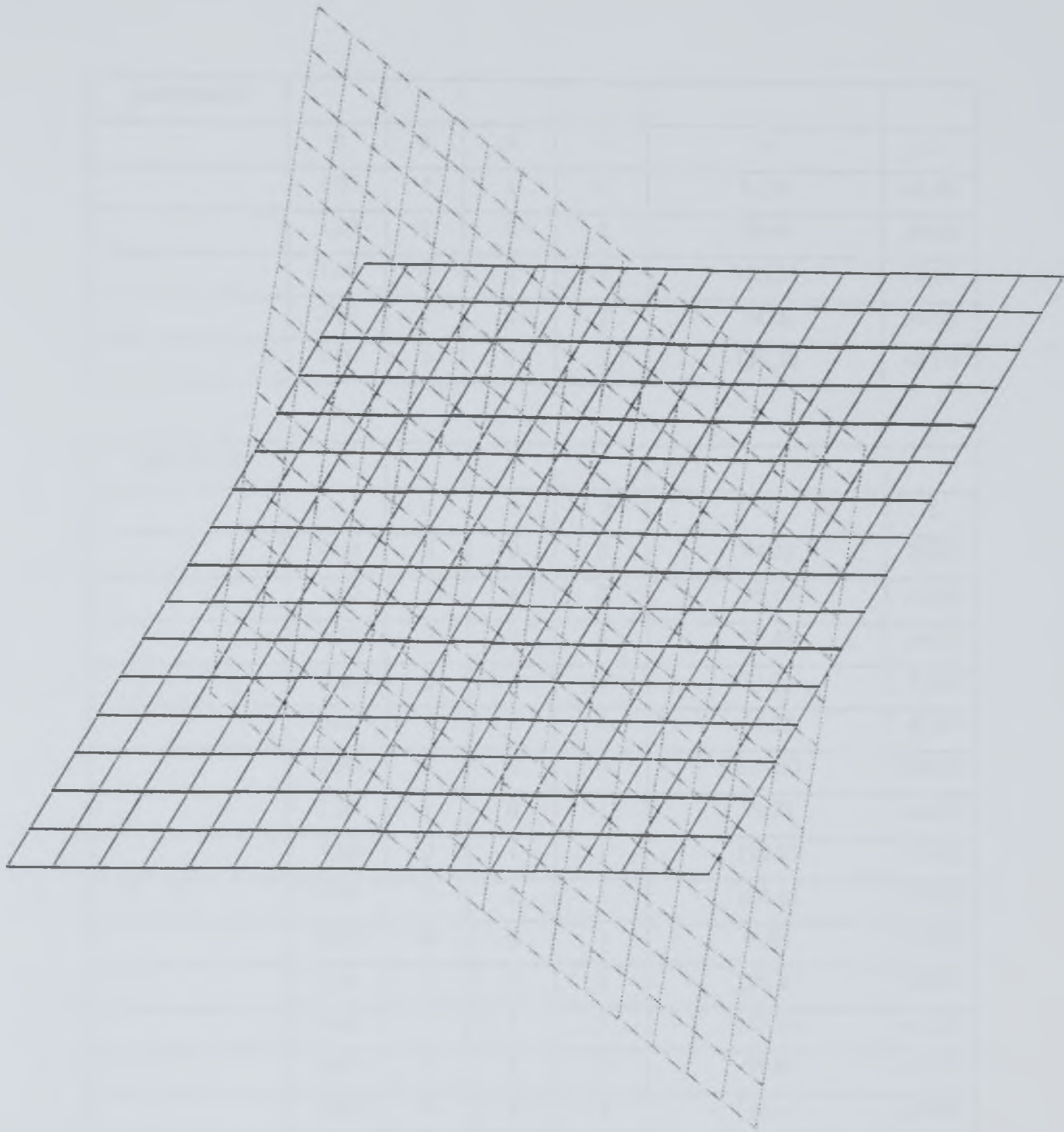


Figure 4.23 A table of special rotations which generate a CSL with a multiplicity <49 within lattices with unit cell parameters similar to that of quartzite. The table has been generated using the computer program listed in Appendix E.

$\mu=46 \rho=25$						
	m	u	v	w	θ	Σ
	1.00	1	1	0	92.39	48.00
	1.00	1	0	1	79.66	39.00
	1.00	0	2	1	106.34	16.00
	2.00	2	0	2	79.66	39.00
	1.00	2	2	3	139.50	48.00

$\mu=33 \rho=18$						
	m	u	v	w	θ	Σ
	2.00	3	0	0	84.26	20.00
	2.00	1	1	0	55.15	42.00
	2.00	2	2	0	92.49	34.50
	2.00	0	3	0	84.26	20.00
	6.00	3	3	0	55.15	42.00
	2.00	3	3	0	114.90	38.00
	1.00	1	0	1	79.71	14.00
	1.00	2	1	1	118.97	32.00
	1.00	0	2	1	106.42	23.00
	21.00	0	0	3	9.43	37.00
	1.00	3	0	3	136.47	20.00
	1.00	1	1	3	127.38	42.00
	3.00	2	2	3	84.26	45.00
	1.00	0	3	3	136.47	20.00
	3.00	3	3	3	100.08	20.00
	1.00	3	3	3	148.79	38.00

$\mu=27 \rho=15$						
	m	u	v	w	θ	Σ
	1.00	3	0	0	122.58	39.00
	1.00	0	3	0	122.58	39.00
	1.00	1	0	1	79.98	23.00
	1.00	0	2	1	106.83	19.00
	21.00	0	0	3	9.43	37.00
	1.00	3	0	3	136.66	33.00

CHAPTER 5

MICROSTRUCTURAL DEVELOPMENT

5.1 OVERVIEW

The microstructures developed throughout the Ballachulish aureole are characterised and quantified within this chapter. The main results are previewed here to provide a brief summary.

The data from a microstructural analysis of the rocks along a traverse through the Ballachulish aureole enables the aureole to be divided into three distinct zones:

Zone I: At distances greater than 800m from the intrusion rocks exhibit microstructures indicative of (Dalradian) deformation.

Zone II: Grain coarsening, and annealing of deformation features dominates this zone between 800m and 600m from the intrusion.

Zone III: Although the form of annealed microstructures remain unaltered, grain size gradually increases towards the intrusion. This is the zone of normal grain growth.

Within each zone microstructures are characterised by direct observations and quantified using image analysis, from which the rates at which different microstructural elements evolve may be assessed.

5.1.1 Zone I (>800m from intrusion)

The microstructures in Zone I represent those which were once developed throughout the aureole before the igneous intrusion. Grains average $196 \pm 20 \mu\text{m}$ in size, often have irregular boundaries and contain a wide variety of intracrystalline, deformation related, substructures. In particular, a 'mesh' microstructure has been identified within a number of grains, using SEM cathodo-luminescence techniques. This texture, hitherto undocumented in geological literature, preserves either evidence of healed fracture patterns and/or outlines the subgrain boundary network within these grains.

5.1.2 Zone II (800-600m)

Within this zone, increased temperatures (due to the proximity of the intrusion) enable deformation microstructures to be destroyed. The driving force for this is the reduction of strain energy via strain induced grain boundary migration, together with the reduction of surface energy by grain growth. There is a gradual increase in grain size towards the igneous intrusion, reducing the grain boundary area per unit volume (a measurement proportional to the surface energy within an aggregate). Grain shapes become more regular, reaching a stable grain shape at 600m from the intrusion. Triple junctions, with equilibrium dihedral angles, form during the initial stages of annealing.

Subgrains rapidly disappear between 700m and 600m either by being consumed during grain boundary migration or by subgrain coalescence during subgrain coarsening. However, the mesh substructures identified in Zone I are stable features, surviving annealing through Zone II and even well into Zone III. Cathodo-Luminescence banding (imaged by SEM/CL) preserves the history of migrating grain boundaries, and provides

evidence for the nucleation of new grains during the initial stages of the annealing process.

5.1.3 Zone III

In Zone III the average grain size of samples increases towards the intrusion. However, the actual grain shapes remain unchanged. Feldspar impurities within samples affect the shapes of grains within the samples. A fractal dimension grain shape analysis shows that grains which do not impinge upon feldspar impurities are more regular in their form. The fractal analysis also indicates that irregularities on the scale of 30μ which occur on boundaries of grains measured from outside the aureole have been removed during the annealing process characteristic of Zone II by the time normal grain growth initiates in Zone III.

5.1.4 Crystallographic Controls During Annealing

Full crystallographic descriptions of specimens through all zones demonstrate that there is no crystallographic control on grain growth in the Ballachulish Aureole (this may not be the case in other geological settings). No preferred crystallographic orientations, misorientations or low energy CSL boundary orientations develop within any samples. Thus, the kinetics of grain growth in the Ballachulish aureole may be investigated in the knowledge that there are no added complications due to crystallographic controls.

5.2 INTRODUCTION

The fundamental aim of this investigation is to quantify the microstructural changes which occur during annealing, using the Ballachulish aureole as a natural annealing experiment, in terms of both the configuration of fabrics and the rates at which fabrics evolve. This information will be used to examine and interpret the processes which are involved in the development of microstructures (cf. Chapter 6) and in doing so help develop microstructural models which investigate the kinetics of fabric change (cf. Chapter 7). It is, therefore, necessary to:

- Identify the range of microstructures present

- Characterise microstructural changes through the aureole
- Construct a microstructural model for texture evolution
- Use such a model as a basis for examining the kinetics of microstructural changes.

Summary of Geological Setting and Sample Collection

Rocks throughout the Ballachulish region were deformed prior to the intrusion of the Ballachulish Granite (Harte and Voll, 1991). The microstructures developed were therefore common to the whole region. The intrusion annealed the surrounding country rocks and the degree to which any one sample is annealed is dependent upon the thermal history that the rock experienced during the evolution of the aureole. Thus, rocks on the edge of the aureole, where temperatures remained constant during the intrusion, remained relatively unchanged. In contrast, rocks at the contact with the igneous body were radically altered by the intrusion.

Rock samples have been collected along a transect from outside the igneous aureole to the igneous contact (Figure 5.1). Two end-member samples are identified: those rocks immediately adjacent to the igneous aureole are the most highly annealed rocks within the section; those samples from outside the igneous aureole have not been affected by annealing and therefore retain microstructures which had developed during deformation.

Presentation of Microstructural analysis

The microstructural analysis is presented in three sections:

- (1) General microstructural observations.
- (2) Statistical and image analysis.
- (3) Crystallographic analysis.

The critical task is to identify microstructural trends along the geological traverse which may be related to the intrusion of the granite. Thus, within each section the original deformed rock microstructures prior to intrusion are described (i.e. those samples from

outside the igneous aureole), followed by a description of the changes in each microstructural element along the transect towards the igneous intrusion as distinguished by each analytical procedure (i.e. Zone I microstructures are analysed followed by Zones II and III).

5.3 General Microstructural Observations

5.3.1 Introduction

The review of microstructural processes in Chapter 2 identified the following microstructural elements as important factors which may control textural evolution: grains, grain boundaries and intragranular substructures (i.e. subgrains, fractures and dislocations). The various rock microstructures which are observed within samples will be discussed firstly for the rocks unaffected by annealing, followed by those samples from within the igneous aureole which are annealed.

5.3.2 Deformational Microstructure (Unannealed From Outside Aureole)

In characterising samples from outside the igneous aureole, we are determining the original microstructural textures before the 'natural annealing experiment' at Ballachulish began. The various microstructures present in these samples are discussed in turn from large scale microstructures (e.g. grains) to smaller scale microstructures such as intracrystalline substructures and dislocations.

Grains/Grain Boundaries

The mean grain size in non-annealed specimens is varies between 180-200 μ . In many samples the grains are arranged into clasts surrounded by feldspar rich regions. This architecture probably reflects the original sedimentary fabric. These sub-conglomeratic samples exhibit a limited amount of flattening (ellipsoid shapes $x:y:z = 1.6:1:0.6$ - Buntebarth and Voll 1991). Individual quartz grains are not flattened with respect to the tectonic stretching lineation (this is investigated further using image analysis in section

5.4.2). The relatively large grain size and absence of flattening suggest that bulk rock deformation in the area was relatively weak, and strain was accommodated by large scale folding and shear zones.

Grain boundaries within deformed samples are irregular, wave-like features, oscillating on a 20-50 μ scale (a statistical analysis of grain boundaries is presented in section 5.4). Triple junctions between neighbouring grains vary markedly from the 120° equilibrium angle configuration (Figure 5.2).

Substructures Within Grains

Intracrystalline substructures have been classified using the scheme described in Chapter 4. Figure 5.5a-f indicate that substructures within grains from samples outside the aureole contain equal proportions of undulose extinctions, equant subgrains, straight subgrains and no deformational substructures (lensoid, wobbly, high contrast and indent substructures are relatively rare). The implications of such a variety of grain substructures are discussed in Chapter 6. Measurements of extinction angles (proportional to the amount of strain within a single crystal) in these samples reveals that 35% of grains have extinction angles of 5° or more (see Figure 5.6).

SEM/OC images exhibit many substructures with a similar form to those outlined above. The sensitivity of SEM/OC means that it may be employed as a useful research tool, a more detailed grain substructure is revealed by SEM/OC than is seen under a light microscope. Further work is needed to relate the substructures seen using light microscopy to those imaged by SEM/OC. The optical classification scheme demonstrates that individual grains within an aggregate do not all react in the same manner during deformation.

Within deformed samples, substructures (which are developed within most grains) exhibit many shapes and forms. Figure 5.7 shows some of the common substructures developed in samples from outside the aureole (complex, equant and straight subgrains and deformation lamellae). Within any one grain, subgrain-boundaries are often complex in form (Figure 5.7a). However, straight subgrain boundaries and equant subgrains

(probably akin to straight and equant extinction patterns observed with the light microscope) do occur (Figure 5.7b&c). Subgrain boundaries vary in form from sharp to diffuse as shown in Figure 5.7b where one grain contains sharp subgrain boundaries whilst its neighbour's subgrains are poorly defined. Figure 5.7d is an example of small scale deformation lamellae, associated with slip planes within a grain. Core Mantle structures (cf. Chapter 2, White (1973) and Lloyd and Freeman (1991 - Figure 5.8) are not well developed within these samples.

In summary, subgrains are present in the majority of grains within samples from outside the igneous aureole. The form of these subgrains varies from grain to grain. However, within any one grain the substructures tend to have similar characteristics. This suggests that individual grains deformed in a homogeneous manner, although, the aggregate as a whole has deformed inhomogeneously.

A 'Mesh' Microstructure

When samples are imaged using SEM/CL (see Appendix B) the majority of the grains within a deformed sample fail to luminesce. However, a distinctive regular luminescent network microstructure is developed in a minor proportion of the grains (an example is shown in Figure 5.9) and is referred to as a 'mesh' structure. Grains with the mesh microstructure look identical to the non-luminescing grains when they are imaged using SEM/OC (see Figure 5.9 for comparison of SEM/OC and SEM/CL of luminescing and non-luminescing grains). The mesh microstructure tends to be developed in grains which are above average size for the sample. To the author's knowledge these 'mesh' microstructures have not been documented elsewhere, although they have now also been recognised in specimens of fault rocks deformed at relatively low temperatures (Lloyd pers. comm. 1996). Interpretations as to the nature of the deformation processes involved in generating such mesh microstructures are discussed in chapter 6. It will be seen that these microstructures have fundamental implications for microstructural stability and potential hydrolytic weakening of dislocations (and thus grain hardness).

Dislocations

Dislocation densities have been shown to vary depending on both the style of deformation and the magnitude of the stresses during deformation (White 1975; Twiss 1986). Dislocation densities are relatively high in deformed samples from the Ballachulish region, averaging $10^9 \text{ m} / \text{m}^3$ in the sample seen in Figure 5.10. Hexagonal arrays of dislocations are common, with the dislocations themselves being straight or slightly curved (Figure 5.10). Dislocations are also often found to be organised into dislocation walls (see B in Figure 5.10).

Summary

The microstructures outlined above detail the typical microstructures developed in the rocks before annealing. These microstructures are the starting microstructures from which all the rocks within the aureole have evolved. Any variations from these characteristic microstructures are considered to be a consequence of the thermal history relating to the intrusion. The microstructural changes from the 'background microstructure' are now discussed as a function of their distance from the igneous contact.

5.3.3 Development of Microstructures Through Aureole

Grains / Grain Boundaries

The average grain size is observed to increase towards the igneous intrusion (compare Figure 5.2 to Figure 5.3). Accompanying this increase in grain size is a gradual straightening of the grain boundaries (compare Figure 5.2 to Figure 5.4). Boundaries are relatively straight at distances between 600m and 300m from the contact, however at distances less than 300m from the intrusion, grain boundaries are seen to become more irregular again (compare Figure 5.3 to Figure 5.4). Triple junctions are organised into configurations with 120° dihedral angles during the incipient stages of annealing at distances between 800m and 600m (again compare Figure 5.2 to Figure 5.3). Note that some of these changes, which are clear observations are not so easily quantified by the statistical shape analyses presented later (see Figures 5.15, 5.22 and 5.23)

Second phase particles such as feldspars, which were originally located at triple junctions and in grain boundaries in samples from outside the aureole, are frequently found to be contained within individual quartz crystals (Figure 5.11). These 'consumption textures' become more common in samples proximal to the igneous intrusion. The presence of feldspars within grains is an interesting feature, because energetically it is more favourable for them to be located on the grain boundaries (Covey-Crump and Rutter 1989).

Subgrains

Intracrystalline substructures are eradicated during annealing. Rocks from less than 600m contain grains with very few substructures when imaged using either the light microscope or SEM. It is the outer 200m of the aureole (i.e. between 600m and 800m) which exhibit most of the changes in intragranular structures (Figure 5.5).

The percentage of grains with large extinction angles gradually decreases in samples from 35% of grains with extinction angles of 10° or more at 800m compared with only 3% at 600m. Thus, substructures are annealed out of existence between 600m-800m. This investigation is very much focused upon this region, where we can observe the relative rates at which different microstructural elements anneal and hence assess the stability of those microstructures.

Subgrain microstructures are annealed out of existence rapidly within the aureole. At distances of 700m they are present within most grains, yet at 600m they have been completely annealed out of existence. The change in subgrain microstructures is not gradual, they are either present within a sample or they are absent. Figure 5.5a-f shows that all types of substructures are annealed between 800 and 600m, resulting in aggregates being dominated by grains with no substructures whatsoever. At 600m, 85% of grains contain no deformation-related substructures. Furthermore, between 800 and 600m there is no major change in the relative proportions of the different types of substructures identified within samples, indicating that the shapes of substructures are unchanged during the initial stages of annealing.

Mesh Microstructure

Grain exhibiting the mesh microstructure observed in SEM/CL (e.g. Figure 5.12) occur throughout the aureole, even at distances from the intrusion where there is no evidence of any other types of substructures. Figure 5.9 is one such example, the 'mesh grain' is surrounded by a number of featureless grains which contain no substructures. 'Mesh-grains' are found in samples at 600m from the contact, and even within a sample from 2m from the igneous contact. The stability of mesh substructures suggests that the substructures themselves are not only unable to reconfigure into a low energy state during annealing, but also that these microstructures prevent grain boundaries from migrating through these grains. The processes affecting these grains are discussed in further detail in chapter 6. Thus, grains which contain this mesh microstructure are very stable throughout the annealing process, effectively unable to alter and at the same time preventing other microstructures from destroying them. Grain boundaries are prevented from migrating through mesh grains because the mesh microstructure pins the migrating boundary.

Cathodo-Luminescence Banding

Annealed samples imaged using SEM/CL contain grains which often luminesce towards their edges. In detail this luminescence is banded. The luminescent bands are interlayered with dark layers which do not luminesce. Figure 5.13 shows a grain containing such a structure bulging into a grain with a mesh microstructure. Generally, the banding is parallel to the grain boundaries. However, as Figure 5.13 shows, this is not always the case. These bands are useful indicators, tracking the history of grain boundary migration (they are discussed further in Chapter 6). Figure 5.13 is an example of banding developed throughout the grain, concentric about a central point. It is possible that these grains may have nucleated during annealing (see Chapter 6).

Dislocations

Dislocation densities are considerably lower within annealed samples from within the igneous aureole. The relatively common dislocation walls seen in deformed samples

become rare and unbound dislocations are linear (Figure 5.10). No examples of hexagonal arrays have been found in annealed samples.

5.4 Statistical Analysis of Microstructures (Image Analysis)

The results of image analysis for those samples outside the igneous aureole are briefly outlined. Subsequently in section 5.4.2 the image analysis results of rocks within the aureole are compared to the non-annealed microstructures detailed below in order to quantify the rates at which microstructures change within the aureole.

5.4.1.a Deformed samples (non-annealed microstructures):

Grain Size

The average grain size for rocks from outside the aureole measured by a linear intercept method vary between 180 μm and 200 μm .

Grain Shapes

Three parameters have been measured for non-annealed samples, FCIRCLE (described in Appendix C), Aspect ratios and the grain boundary area per unit volume (see chapter 4 for descriptions of the measurements). FCIRCLE, which is a measure of the complexity of grain shapes, averages between 0.5 and 0.6, indicating that grain boundaries are fairly irregular (a circle would have a value of 1). Grain boundary area per unit volume is about 0.016. This variable is a function of both the grain size and the complexity of grain boundaries within the aggregate. Aspect ratios tend to range between 0.6 and 0.7, which are lower than regular shapes such as a circle or a hexagon which are common shapes in many annealed/grown geological specimens.

Moment ratio β_1 and β_2 analysis of the distribution of grain size/shape parameters within samples from outside the aureole are somewhat varied. Generally grain size distributions (grain diameter and grain perimeter measurements) plot within the 'bell-shape' region on

a moment ratio plot (Figure 5.18). Results from grain area distributions indicate that they are J-shaped, whilst shape parameters (FCIRCLE and FSHAPE) plot as symmetrical almost ideal uniform Gaussian distributions (i.e. $\beta_1 = 0$ and $\beta_2 = 3$).

The actual values of β_1 and β_2 (see Table 4.2) factors for grain size measurements are somewhat varied for unannealed samples from outside the igneous aureole. The variation is of a similar magnitude for both β_1 and β_2 values. Thus the actual shape of distributions plot within the same field on a moment ratio plot. However, the actual values are widely dispersed within that field (see Figure 5.18).

The average fractal dimension of grain shapes (calculated from Richardson plots) for grains within specimens from outside the aureole is 1.134. Average fractal dimensions calculated for grains which have no feldspar neighbours are considerably lower ($d=1.10$) than the above figure, which is calculated using every quartz grain within a specimen, irrespective of its neighbouring grains. This indicates that feldspar impurities exert a strong influence on quartz grain shapes within a sample.

5.4.2 Evolution of Microstructures Through Aureole

5.4.2.a Average Data

This section presents the evolution of *grain size measurements*, followed by the evolution of *grain shape measurements* along the geological traverse from outside the aureole towards the igneous contact.

Grain Size

Grain size gradually increases from between 180 and 200 μm at 800m to over 400 μm at the igneous contact (Figure 5.14). The increase in grain size is linear between 800m and 300m. However, between 300m and the igneous contact the rate at which grain size increases with respect to distance decreases. Thus, grain growth is inhibited between 300m and the contact.

The graph of grain size versus distance from the intrusion presented in Figure 5.14 is fundamental for calculating the kinetics of annealing. At each position within the aureole it is presumed that the original grain size was similar to grain size in samples from outside the aureole (i.e. 180μ). Thus the amount of coarsening for each sample can be calculated. Using grain coarsening data together with the temperature history it is possible to calculate diffusion rates which would be needed to induce such coarsening (see Chapter 7).

Grain size is obviously an important aspect within this study. However, more information is needed in order to interpret the precise microstructural processes which may be active during the annealing process. For example, if we wish to investigate grain boundary migration processes, it is necessary to examine the shapes of grain boundaries. Thus, a number of other measurements have been acquired which allow the evaluation of the changing microstructural processes involved during annealing. Of specific importance are shape parameters which can detect subtle microstructural changes which cannot be identified by size parameters alone.

Grain Shapes Parameters

FCIRCLE MEASUREMENTS

The FCIRCLE macro (as described in Appendix C) is able to distinguish between objects which are elongate or rough from objects which are circular. Figure 5.15 displays the changes in FCIRCLE with distance from the igneous contact. The values of FCIRCLE are stable as there is little variation in the mean value from aggregates throughout most of the geological transect. There is a slight increase in the value between 800m and 600m. Indeed, such an increase is expected as the deformed microstructure is replaced by a regular annealed microstructure within the aureole. The two samples closest to the intrusion (43m and 2m from the contact) have mean values of FCIRCLE which are again slightly reduced in comparison to many of the other samples. The values of FCIRCLE vary between 0.55 and 0.75, which is really only a limited range. More work is necessary to assess the significance in terms of grain shapes to the minor differences in this variable. The data set is also relatively small. Notwithstanding this, if the variations are significant, two possibilities may explain the shape changes along the transect:

(1) there is an active change in the shape of the quartz grains as aggregates react either to increased temperatures or intrusion related deformation in the aureole;

(2) quartz grains change shape in a passive manner as the effects of second phase feldspar impurities become more dominant during grain growth.

The former process may be caused by slight intrusive deformation resulting in grain boundary migration of the quartz grains. The latter process of grain shape change occurs passively during grain growth. As coarsening proceeds the distances between the feldspars remains constant, whilst the average grain size increases. Consequently, a greater proportion of quartz grains will be impinged upon by feldspars. Thus, the coarsened quartz grains become more irregular, affecting the average value of FCIRCLE within the aggregate in a passive manner.

GRAIN BOUNDARY/UNIT VOLUME

The ratio between total area of the aggregate which is contained within grains and the total grain boundary perimeter within an aggregate changes through the aureole. This measurement is equal to the grain boundary area/unit volume. Figure 5.16 shows the change in total area:total perimeter ratio as a function of distance from the intrusion. There is a gradual increase in the ratio from 60 outside the aureole to between 80 and 100 at the igneous contact. The change in the ratio reflects both the change in grain shapes to a regular morphology and the increase in grain size.

The value of the area:perimeter ratio is proportional to the amount of surface energy within an aggregate and as such is also proportional to the driving forces of grain growth. The significance of a reduction in the surface energy within these aggregates, in relation to the driving forces for microstructural modification and the forces which oppose microstructural change is discussed in Chapter 6.

ASPECT RATIOS

distribution of grain diameters with a maximum grain diameter of 360 μm and a mean of 180 μm has been produced using a sine function, where

$$f(x) \propto \sum_x^{\bar{v}} \sin(z) dx$$

where z is the proportion of grains with grain size in the band dx .

From this function β_1 and β_2 values can be calculated and plotted on a moment ratio plot. The distribution of the areas for this theoretical example has been calculated using the grain diameters and presuming that the grains are circular. The area of each grain is related to the diameter by $\pi \times (\text{diameter}/2)^2$. An initial Gaussian distribution calculated from grain diameters is equivalent to an exponential distribution of the grain areas. Thus, it is shown that the difference between grain diameter and grain area distributions in the Ballachulish data set are similar to theoretical expectations.

Perimeter distributions for all samples (Figure 5.18c) border the bell-shape and J-shape zones of moment ratio plots. Perimeter measurements have the same dimension as grain diameters (i.e. not related by an exponential factor) and also have a similar distribution. This implies that the area and perimeter distributions vary from the grain diameter distributions as a consequence of their mathematical description and not as a result of any direct microstructural reason.

Moment ratio plots are an excellent way of representing histogram distributions graphically because trends within data sets from a number of samples are easily identified. So far the data from the aureole have been discussed in terms of the shapes of the distributions, for example bell-shape or J-shape. However, data in

Figure 5.18a-f are more complex, in so far as the data sets form a linear array of points on the diagrams. Thus, although grain diameters from all the samples are bell-shaped, some samples have data distributions with relatively high values of β_1 and β_2 whilst others have low values. It is therefore crucial firstly to identify linear trends within the data set and secondly to attempt to account for these trends, in terms of the underlying

microstructural feature responsible. For example, do beta factors increase as a function of distance from the intrusion, feldspar content or perhaps grain shape.

Figure 5.18b, a moment ratio plot of DCIRCLE from all the samples measured, indicates that there is a clustering of β_1 and β_2 values around $\beta_1 = 3$ and $\beta_2 = 1$. Samples 54, 57, 60 and 77 define the linear relationship on the diagram. All four of these samples have been obtained from outside of the aureole, or between 800m and 600m (i.e. the zone where deformed microstructures remain, unannealed). This implies that beta values are in some way related to distance from the igneous intrusion, and in turn the degree to which a sample is annealed. Figure 5.18a & b show the relationship of β_1 and β_2 with distance from the intrusion. At distances greater than 650m the values of β_1 and β_2 are varied. However, nearer to the intrusion (<650m) the values stabilise. Although there is a definite relationship between distance and the values of beta factors, uncertainties exist as to the real influence on the beta factors. It is unclear whether it is due to subtle changes in grain shapes or due to grain size alteration during annealing.

Feldspar impurities seem to have little or no effect on the beta values. For example, sample 60 with a feldspar content of 4% has the greatest beta factors, yet sample 77 again with high beta factors has a feldspar content of 20%.

Grain Shape Distributions

A similar moment ratio analysis has been undertaken for grain shape histograms (FSHAPE and FCIRCLE parameters). Both shape factors plot in a tight cluster on their respective diagrams (Figure 5.18 d & e) and have β_1 factors close to 0, showing that the data distribution is symmetrical around the mean whilst β_2 factors tend to have values in the region of 3. Such distributions are in fact close to the ideal Gaussian. Although, the mean may vary from sample to sample, the distribution of data within each sample is unchanged. Thus, the mean of each sample adequately reflects the development of grain shapes within this data set. Consequently, further analysis of the frequency distributions of grain shapes has not been undertaken.

5.4.2.c *Fractal Analysis Results*

In Chapter 4 it has been explained that the fractal dimension of a shape defines the relative complexity of shapes which are self similar. Figure 5.21 are examples of grain maps with the fractal dimension (or 'boundary roughness') of each grain superimposed on to the image. The fractal dimensions in each of the grain maps seems to be a fair reflection of the roughness of the grains. Thus, it is reasonable to suppose that the quartz grains within all the samples exhibit fractal characteristics to some degree. This follows because grains which are not fractal (i.e. exhibit no relationship between length of the perimeter and the size of the measuring stick- see Chapter 4) over the scale of observation would be expected to show random fluctuations in the fractal dimension when compared to the observed roughness of the shapes involved. A fractal dimension therefore adequately defines the grain shapes within the Appin quartzites over a limited number of scales. The grains will be examined for mixed fractal characteristics in section 5.4.2.d.

The extent to which fractal dimensions change from sample to sample through the aureole may be assessed using the average fractal dimension for each sample. A graph of the average fractal dimension versus distance from the aureole (Figure 5.22) reveals that there is little difference throughout the transect. Significantly, the analysis of average fractal dimensions from each sample appear to confirm the results of the earlier shape analyses (Figure 5.15) that it is difficult to statistically quantify some of the shape changes which are relatively clear to see from SEM photomicrographs. However, the mixed fractal analysis (see below) is able to distinguish some of these features we see by eye, the average fractal dimension and FCIRCLE analysis is probably quantifying the more general microstructure of a grain network interacting with second phase particles.

The hypothesis that it is the interaction of the quartz network with the feldspar grain which is the main influence on the value of the fractal dimension has been examined by taking out of the analysis any grains which impinge upon the feldspars. Figure 5.23 shows the variation in the average fractal dimension of samples in the transect using only quartz:quartz neighbours. The results produce fractal dimensions that are far lower than the analysis using all the grains, indicating that when feldspar impurities are present, grain shapes become more complex. A change in grain shape may be a direct result of

feldspar related processes (e.g. Ostwald ripening of the feldspars) or as a result of quartz-feldspar interactions, such as pinning (see chapter 6). It is possible that there is a slight increase in the fractal dimension towards the igneous contact for grains with quartz:quartz contacts only, however, it is necessary to analyse more samples and within each sample measure more grains in order to truly assess the significance of any trends.

5.4.2.d *Mixed Fractals*

The data presented so far reveals general characteristics about the microstructures along the transect ascertained from fractal dimension variation as calculated from a gradient on a Richardson plot. However, the assignment of a fractal dimension conceals subtle variations which occur in a Richardson plot. Minor variations in data away from the average gradient potentially contain detailed information about grain shape which is lost when linear a regression is performed (fig 4.46). Variations in the gradient of a line on a Richardson plot indicate that the shape that is measured is not an ideal fractal over all the scales of observation. It may be possible to determine one fractal dimension for a shape at one scale, yet at another scale a different fractal dimension fits the data more accurately (see Figure 5.24). Grains which exhibit this behaviour are referred to as mixed fractals (Kaye, 1989, Russ, 1992, Mandelbrot, 1982). The examples of mixed fractals from Kaye (1989) show that the point on a line on the Richardson plot where there is a sharp change in gradient corresponds to a major change in the form of the shape on the scale of the step size at that point of inflexion. Thus, sharp changes in gradients on a Richardson plot pinpoint the scale at which a shape may change its characteristics using such plots. Richardson plots provide a tool for establishing the microstructural elements responsible for grain shape variation either within one sample or from sample to sample.

Figure 5.25 shows some examples of Richardson plots for grains which can be seen to be different by the naked eye (grains 1,2 from sample 56157 (780m from the intrusion) and 3 from sample 56149 (395m from the intrusion), the grains are shown on the grain maps in Figure 5.21). The plots have been constructed in order to discover if these grains are mixed fractals, and if so what is the nature of the mixed fractal. Essentially the graphs are examined to see if there are any distinct changes in the gradient and at what scale any inflexions occur.

At lower values of the step size, all the graphs have inflexion points as the gradients decrease to zero. This inflexion would seem to coincide with the resolution of the measurement technique. However, careful examination of the value of the inflexion point on the x-axis shows that the inflexion point is in a slightly different place for each grain. The same measurement technique has been used on all the samples, and so it would be expected that the resolution limit would be the same for all samples. The value of the step size at which an inflexion point occurs therefore reveals that there is a distinct change in the characteristic of a grain on the scale of the step size.

If the control on the inflexion point is the resolution of the technique, then the inflexion would occur in the same position irrespective of the fractal dimension of the object. Figure 5.25a, a plot of grain 1 and grain 2 from sample 57 have an inflexion at -1.45 (on the x-axis) which is equivalent to a step size of 7 pixels. In contrast, grain 3 from sample 49 which is an annealed sample has an inflexion point at the equivalent of 15 pixels (-1.7 on the graph). At step sizes below the inflexion point on both examples, the gradient tends towards 0, indicating that the shape is Euclidean at this scale (i.e. irregularities do not occur on a scale of < 7 pixels for grains 1 and 2, whilst irregularities do not occur at < 15 pixels for grain 3). Thus, grains 1 and 2 have irregularities at a smaller scale than grain 3. In terms of location, grains 1 and 2 are from a sample outside the aureole, which has obvious deformation features, whereas 3 is obtained from an annealed sample (56157). It is obvious to the naked eye that the deformed sample does exhibit irregularities finer scale (compare Figure 5.21, file 49 with file 57). The Richardson plot is a means by which these differences may be quantified.

Summary

Fractal analysis indicates that the main control on the grain shape is the size and distribution of feldspar impurities. As a consequence the average fractal dimension of grains within a sample is similar for all samples because the distribution of the feldspar impurities is similar for most samples used in this study (the sample areas for study were selected because they had relatively few feldspars of a similar size and distribution).

The fractal dimensions of grains which do not impinge upon feldspar impurities are generally smaller than grains in contact with feldspars. These grains are able to form equilibrium shapes, probably via grain boundary migration mechanisms (see later), whereas grains in contact with feldspars become pinned and are therefore unable to reorganise their shapes into more energetically favourable forms.

At small scales of observation (6 - 15 pixels in length), grains are shown to become regular in appearance. However, some of the deformed samples from outside the aureole (especially sample 57) lose their 'jaggedness' at smaller scales compared to annealed samples. Deformed samples become regular at 6 pixels, which is close to the resolution of both the image analyser and the SEM. Grain boundaries are etched slightly during polishing, which unfortunately limits the magnification to which irregularities may be resolved.

5.5 Crystallographic Data

5.5.1 Introduction

Rocks microtextures have been reported by many authors to influence the microstructural processes which occur during both dynamic and static events (e.g. Hobbs 1968; Abaov 1971; White 1976; Lister 1980; Poirier 1985; Abbruzzese 1986; McLaren 1986; Knipe 1989; Jessell 1990; Law 1990 and Fliervoet and White 1995). At each stage in a rocks history the microtexture evolves in a manner that is controlled by the existing crystallographic distribution and the environmental conditions under which the rocks are developing (cf. chapter 2). Therefore, a microtexture is a reflection of present and past processes, thereby containing information about a rocks tectonic history.

Two aspects of microtextures are examined in this investigation, firstly the changes in crystallographic fabrics through the aureole with respect to the regional deformation and secondly more localised studies to determine the relationship between crystallographic orientations of grains with respect to grain boundaries. The former investigation of the development of crystallographic preferred orientations considers whether specific grain orientations are more stable (i.e. survive annealing) than others, whilst the latter considers the stability of low energy grain boundary orientations. If either

crystallographic preferred orientations or grain boundaries are shown to affect the stability of microstructures during annealing we need to understand which microstructures are influenced and how they are influenced because such behaviour will have profound implications for the kinetics of microstructural evolution during annealing.

5.5.2 Crystallographic Preferred Orientations

Two methods are used to display the crystallographic data acquired from the Ballachulish aureole, c-axis pole figures and inverse pole figures. C-axis pole figures are used to examine the data set for the basic trends because they are relatively easy to understand, even if they do not represent a full crystallographic description of crystal orientations. Inverse pole figures are then used to investigate for more subtle variations in crystal orientations which potentially may only be shown on diagrams which depict the full three-dimensional variation of crystallographic orientations.

Sample 56157, from outside the igneous aureole preserves microstructures of deformation prior to the intrusion. The c-axis distribution (Figure 5.26) is not preferentially clustered in specific areas of the stereonet. Thus, this rock did not develop a CPO during deformation. The inverse pole figure (Figure 5.27) indicates that even when the full crystallographic description is presented no CPO can be distinguished. These crystallographic textures are random.

The samples from within the igneous aureole (56154, 56149 and 56148) have similar characteristics to the sample from outside the aureole, i.e. random orientations with no CPO developed in any of the samples (see Figure 5.26 and Figure 5.27).

There are three main conclusions to draw from this data. (1) Crystallographic preferred orientations were not developed during deformation of the Appin Quartzite prior to the intrusion of the Ballachulish intrusion. (2) During annealing all orientations continue to survive, indicating that no one orientation is destroyed preferentially. (3) Thus, crystallographic orientations have no direct influence upon the rates and processes of annealing.

5.5.3 Grain Boundary Microtexture

The randomness of crystallographic preferred orientations described above does not necessarily mean that all aspects of the crystallographic configurations are random. Although the fabric as a whole may be random with respect to an external reference frame it is possible that locally very specific relationships exist between crystallographic orientations and grain boundary orientations. In particular, a strong 'misorientation' fabric may be developed within a specimen with little or no CPO (MacKenzie 1964). The grain boundary orientation may be compared to the crystallographic orientation of the grains on either side to determine whether low energy grain boundaries may dominate a microstructure in the form of CSL configurations (see Chapter 4). In order to investigate these relationships it is necessary to calculate grain misorientations and then the actual orientation of grain boundaries.

In circumstances where one is examining the orientation of microstructural elements with reference to the local crystallographic features it is appropriate to present data on an inverse pole figure. In such a representation, the influence of random crystallographic texture is removed from the analysis and it is possible to concentrate only on the orientation of the misorientation axes of grains with respect to the local crystallography.

There are two aspects which control the characteristics of misorientation plots, (1) the symmetry of the mineral and (2) actual preferred misorientations. The influence of symmetry is examined using diagrams in which the misorientations of each grain is calculated against every other grain in the aggregate. This is merely to generate a mass of data to show more clearly data clustering which occurs as a result of symmetry. The analysis of any preferred misorientation fabrics is calculated only for those grains which are neighbours.

Effects of Quartz Symmetry

Figure 5.28 and Figure 5.29 are sets of misorientation diagrams obtained from the same data set. The difference between the two diagrams are the sizes of the angle bands (the magnitude of misorientation) which are plotted on each pie slice. In Figure 5.28 the bottom right pie slice with the highest misorientations contains data for a broader band of

angles. The significance of this diagram is that the data are more clustered in the pie-slices with the large misorientation angles. In diagrams with misorientations greater than 60° the data is more clustered towards the edge of the stereonet and furthermore in Figure 5.29 the data for misorientations greater than 91° the clustering is confined to an even tighter girdle.

The clustering of data in this manner results from the mathematical solution employed to calculate the misorientation. For each misorientation between two quartz crystals there are a possible 6 axis/angle pairs which describe that misorientation. These are solutions which are symmetrical equivalents. In this investigation the solution with the lowest angle has been used to describe the misorientation (cf. Chapter 4), and it is for this reason that clustering occurs on the misorientation diagrams for angles over 60° . This may be visualised by a misorientation of 61° about a c-axis [0001], such a solution is more adequately described by a misorientation of 1° about the c-axis because of the triad axis of symmetry about [0001]. It is this solution with the smallest angle of rotation which is chosen by the computer as representative of the misorientation. Thus, the highest angle of misorientation possible about the c-axis is 60° . However, greater angles of misorientation are possible for different orientations. For example it is feasible to have 90° misorientation about an a-axis within quartz. There is a 107° limit to the magnitude of misorientation, a direct consequence of quartz symmetry because, irrespective of the orientation of the misorientation axis, if the angle of misorientation is greater than 107° a solution with a lower angular magnitude may be derived.

Preferred Misorientations

Now it has been shown that there will always be a clustering of data on the misorientation diagrams, it is necessary to examine data sets for neighbouring grain misorientations to see if there is any further clustering superimposed as a result of a strong mesotexture. Figure 5.30 presents misorientation diagrams for a number of samples. It can be seen that data are not preferentially grouped any more than would be expected as a result of symmetry influences. However, it should be noted that further statistical analysis is needed in order to confirm this conclusion (time/facilities did not suffice).

5.5.4 Grain Boundary CSL Analysis

An alternative approach to analyse grain boundaries is to pick a misorientation solution which most closely matches a CSL boundary within quartz. Brandon (1966) suggested that grain boundary coincidence may be retained even when a misorientation deviates away from a theoretical CSL orientation. It is estimated (Brandon 1966) that a CSL will be preserved up to an angle of V_m away from a theoretical CSL (Σ is the multiplicity of the CSL) where,

$$v_m = 15^\circ \times \Sigma^{-\frac{1}{2}}$$

Table 5.3 lists a number of CSL orientations which are potentially low energy orientations for neighbouring grains in quartz. The calculation (using program Multiplicity, Appendix E) could not be performed using the actual measurements of the lattice unit cell of α -quartz because the mathematics of CSL demand that the cell parameter c^2/a^2 is a rational number. Unfortunately, this is not the case for α -quartz. Thus, CSLs have been calculated for a number of cell parameters which are similar to the quartz unit cell. A similar approach to investigating CSLs in corundum has been documented by Grimmer (1989). He found that many of the CSLs predicted in materials with similar unit cell parameters to corundum were in fact also found in corundum (albeit associated with dislocation networks along the grain boundary). This example indicates that the CSLs presented in Table 5.3, although they have slightly different cell parameters to α -quartz, may indeed be present in quartz crystals. The CSL boundaries discovered by Grimmer in corundum contained dislocations which he interpreted as geometrically necessary because of the difference in the theoretical value of c^2/a^2 for a coincidence to occur and the actual value of c^2/a^2 in corundum.

The main conclusions to make from the table of CSLs is that there are a very limited number of CSL misorientations in the trigonal lattices. Randle (1992) and McLaren (1986) predict that this is the case, although they did not present any data to confirm such remarks. The data presented here is firm evidence that there are few CSL descriptions within quartz. Many authors have noted that although there are a limited number of possible CSL descriptions within a material, those few 'special boundaries'

occur more frequently than they would be expected in a truly random microtexture. Thus, the frequency of CSLs within the quartzites within the Ballachulish aureole has been calculated and compared to that expected for a random microtexture.

Grimmer (1989) estimates that if grains are orientated randomly in an aggregate the percentage of boundaries with rotations which satisfy the Brandon criteria and $\Sigma < 36$ should be 1.42%. In the Ballachulish samples studied here, CSLs occur even less frequently than 1.42%. This indicates that CSL grain boundary orientations are not preferentially developed outside the aureole, or at any point along the geological traverse.

This conclusion has important implications for the development of rock microstructures within the Ballachulish aureole because it proves that low energy grain boundaries are not developed during annealing. Preferential development of CSL boundaries would have profound, unquantifiable implications on the kinetics of grain growth. The fact that CSLs are not produced during annealing makes a kinetic description of the annealing in the Ballachulish setting more readily predictable (see Chapter 6/7).

5.6 Summary

5.6.1 Unannealed Samples

Microstructures within unannealed samples from outside the igneous aureole, consist of the following microstructural elements:

- An average grain size of 180 μ .
- Various deformation related intracrystalline substructures are developed throughout the aggregate (e.g. subgrains, deformation lamellae and dislocations).
- Grain boundaries are irregular, and triple junctions deviate from 120°.
- Fluid inclusions are relatively common.

- An intracrystalline 'mesh' structure has been identified in many grains, preserving a healed fracture microstructure from an early stage in the rocks evolution
- Grain boundary area/unit volume ratios are relatively low (0.016).
- β_1 and β_2 ratios of grain size measurements (area, diameter and perimeter) are varied and relatively high in comparison with annealed samples.

5.6.2 Microstructural Development During Annealing

As samples are traced into the igneous aureole, microstructural elements react in different ways and at different rates to the increased temperatures. This is depicted on a 'stability' diagram in Figure 5.31.

- Grain size increases gradually towards the igneous contact with an average of 400μ at the contact.
- Grain shapes tend to alter markedly between 800m and 600m at which stage they become relatively stable, remaining unchanged even though grain size continues to increase.
- Subgrains and other intracrystalline substructures disappear between 700m and 650m from the contact.
- dislocation densities diminish rapidly even at distances greater than 800m.
- 'mesh' substructures are found to survive annealing often beyond 600m and in one example even up to 2m from the igneous contact.

The size and frequency of cathodo-luminescence banding gives a unique insight into the rates of grain boundary migration within a sample.

Fractal characterisation of grain shapes indicates that feldspar impurities directly influence the shapes of grains, making them more complex, hence grains in contact with feldspars have higher fractal dimensions. A detailed fractal analysis using Richardson plots shows that deformed grains within samples from outside the aureole have

irregularities on the scale of 30-40m which are not present in samples from within the aureole.

5.6.3 Crystallographic Influences

- Full crystallographic descriptions of specimens through all zones demonstrate that there is no crystallographic control on grain growth in the Ballachulish Aureole (this may not be the case in other geological settings).
- No crystallographic preferred orientations or misorientation preferred orientations are developed in these rocks.
- Low energy CSL are not preferentially developed within any samples.
- Thus, the kinetics of grain growth in the Ballachulish aureole may be investigated in the knowledge that there are no added complications due to crystallographic controls.

5.6.4 Implications

Using these results it is possible to divide the aureole into three zones, each with distinctive microstructural features reflecting the differing processes active in each zone during the thermal evolution of the Ballachulish aureole.

Zone I: Non-annealed regions at distances greater than 800m.

Zone II: Samples between 800m and 600m where deformation microstructures are eradicated (i.e. substructures, dislocations) and grain shapes become more regular.

Zone III: A region of grain growth at distances less than 600m where grain size and distribution of second phase particles are the only controls on the textural evolution.

The data presented in this chapter enables a detailed interpretation of the microstructural processes which occur during annealing (see chapter 6). The rates of changes of different microstructural elements through the aureole have also been quantified. Thus, using both our knowledge of process and rates of textural change along the transect, theoretical kinetic models may be constructed to assess the rates of the metamorphic and microstructural processes which have been observed in the Ballachulish aureoles (see chapter 7).

Faint, illegible text at the top of the page, possibly bleed-through from the reverse side.

Figure 5.1 A geological map of the South side of Sgoor Dhearg showing sample localities. The sample numbers are field numbers, for thin section numbers refer to Table 5.1.

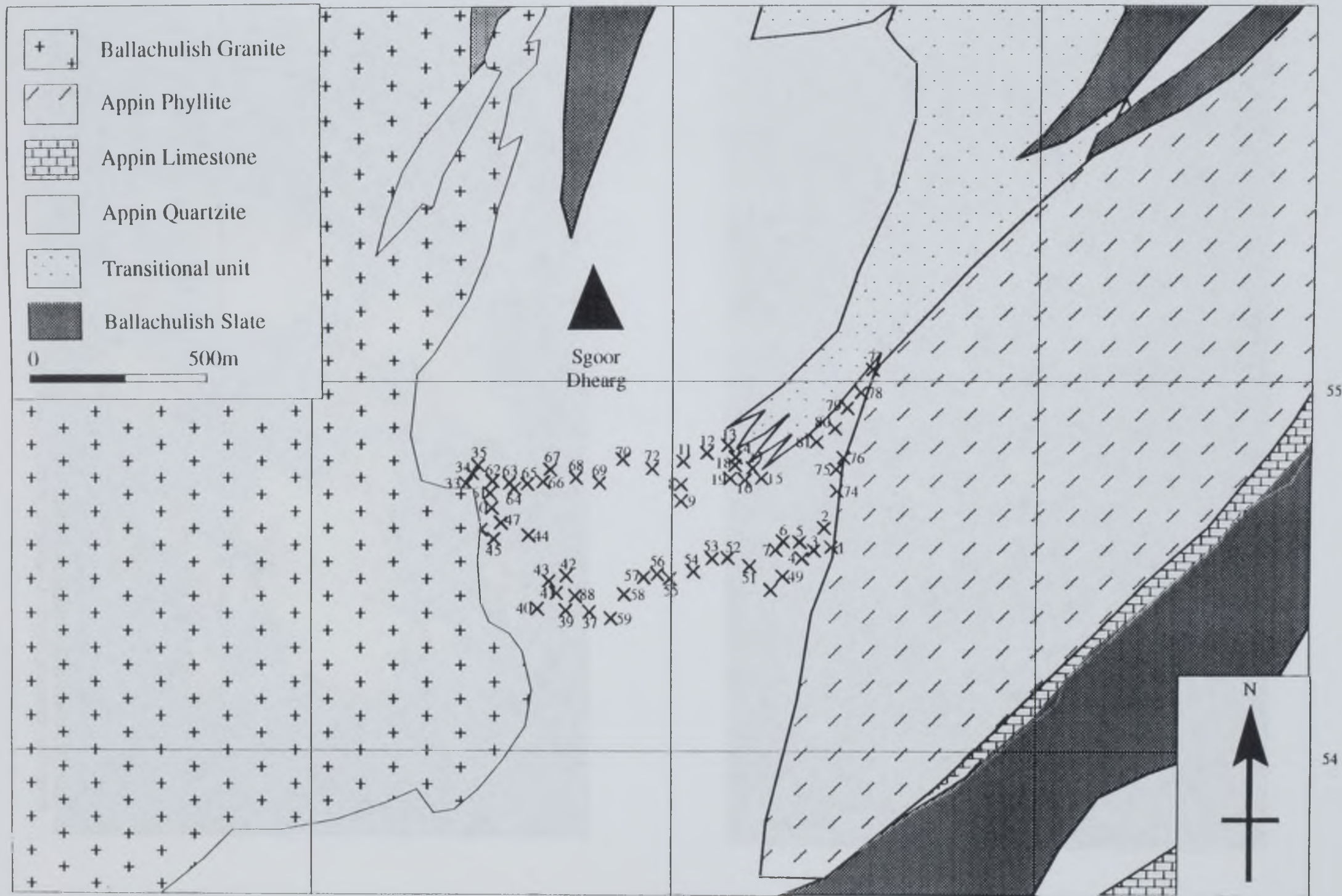
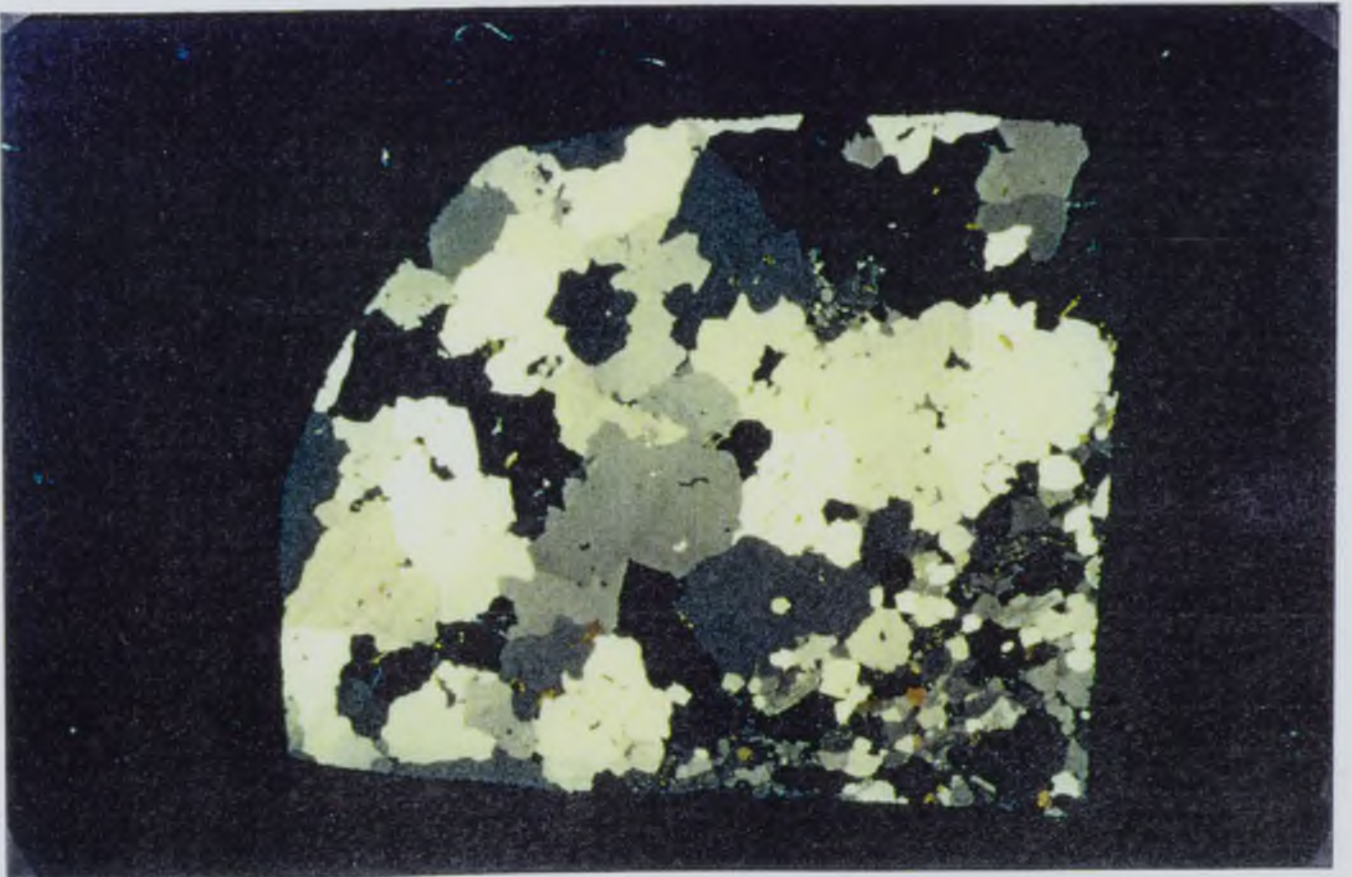
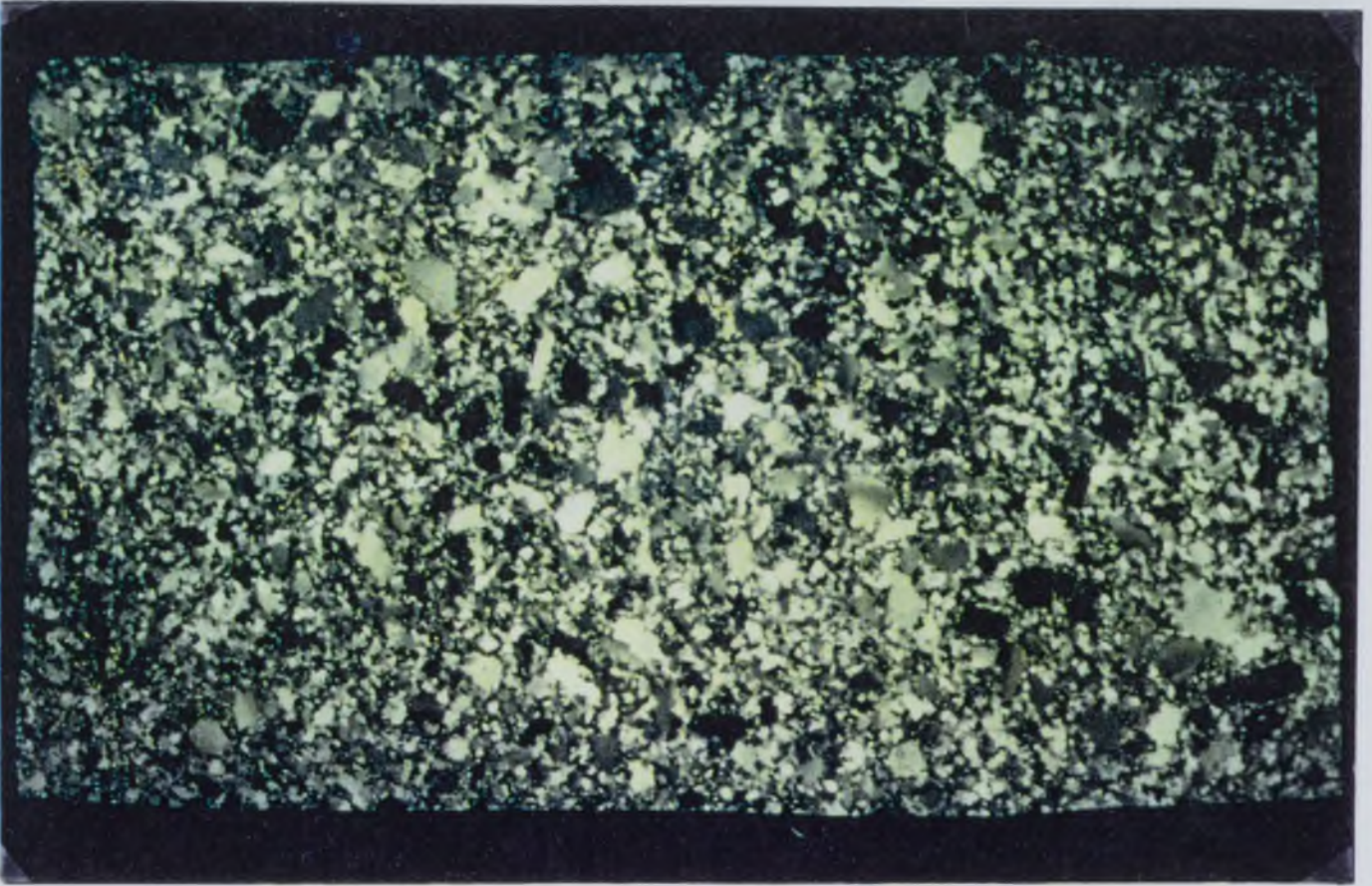




Figure 5.2 An example of a deformed tectonite from the Appin Quartzite (sample taken from outside the igneous aureole). Sample 55325, width of view 4cm.

Figure 5.3 An example of an annealed tectonite from the Appin Quartzite (sample taken from the igneous/Appin Quartzite contact). Sample 55301, width of view 4cm.



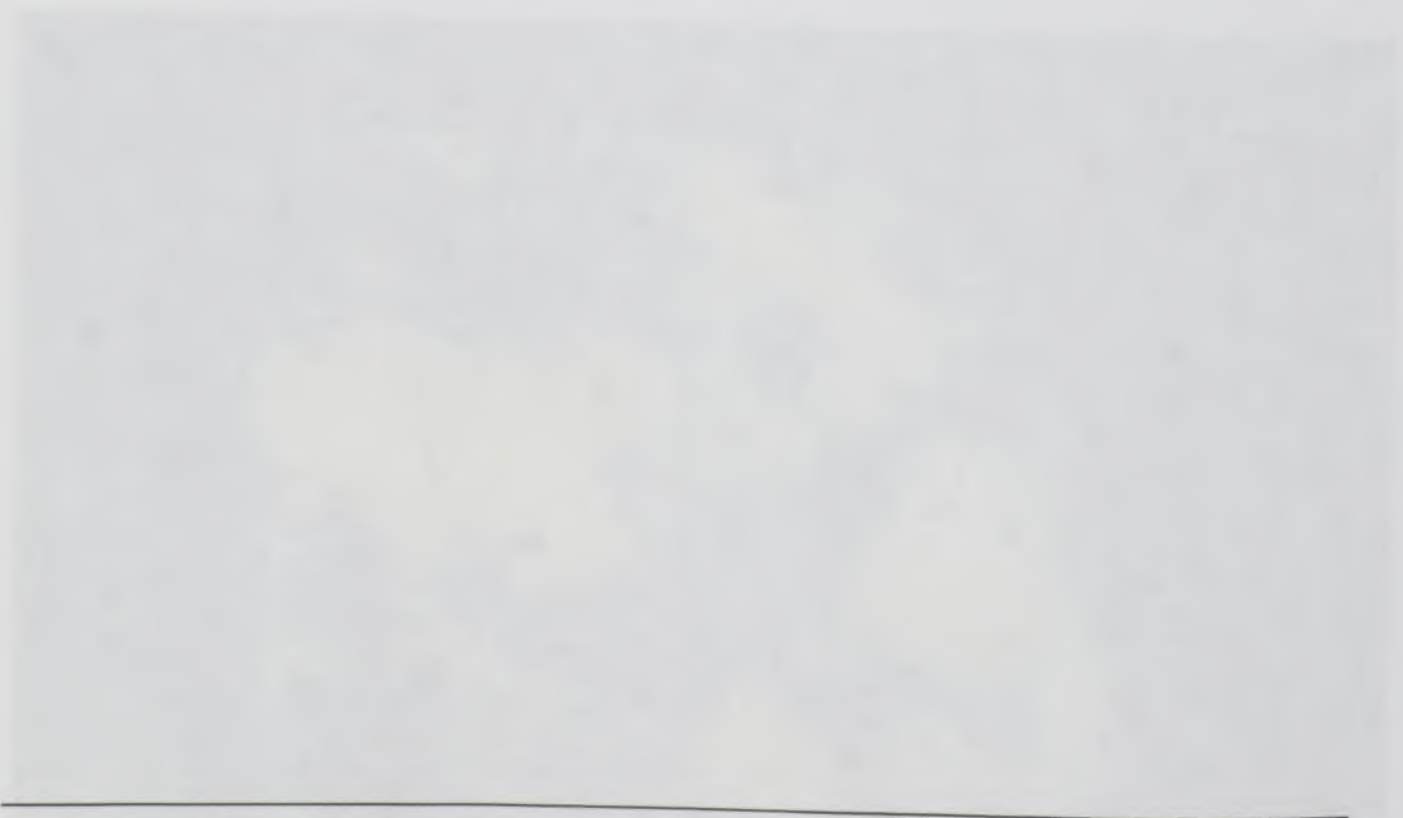
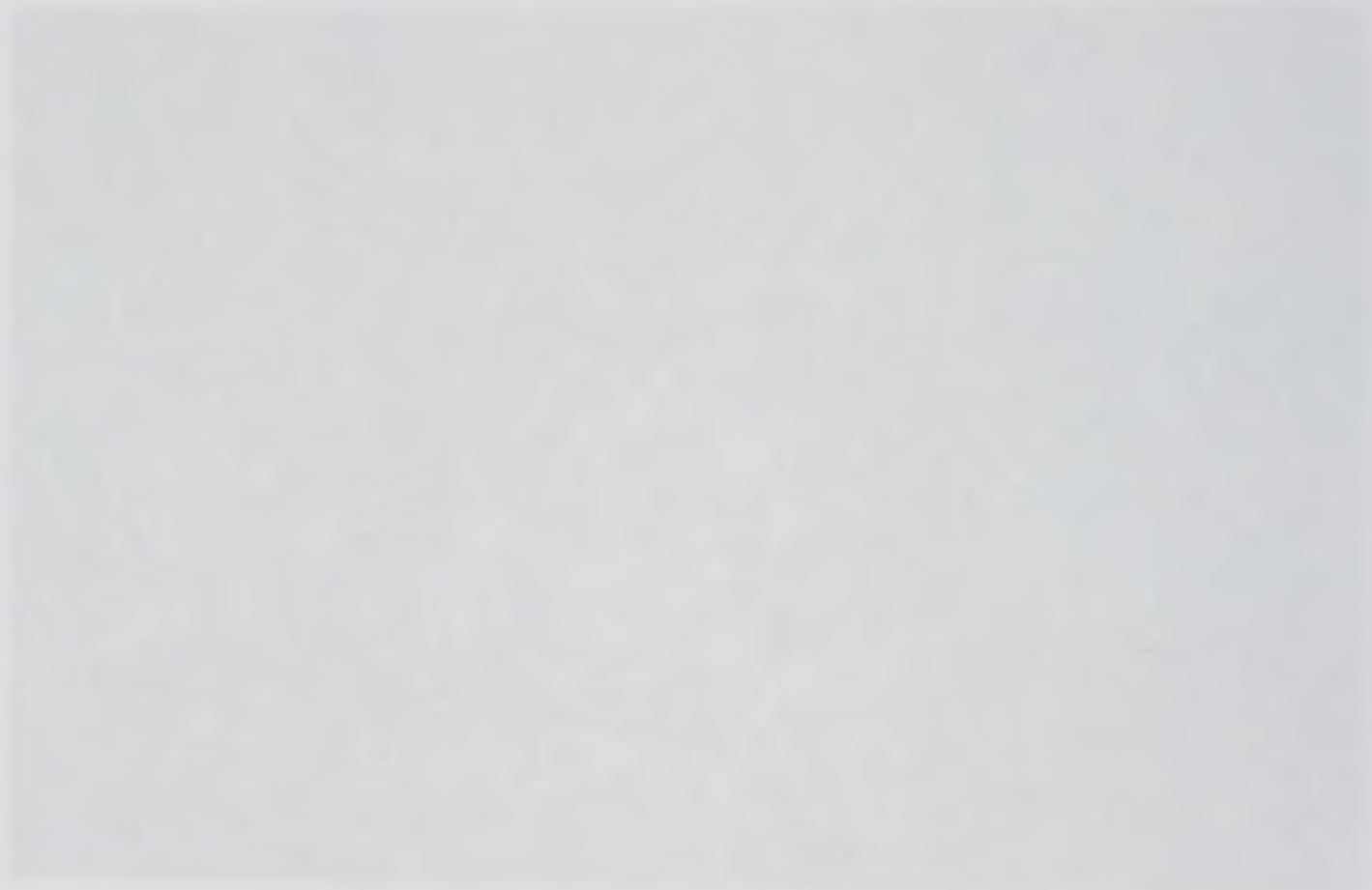


Figure 5.4 Annealed quartzite exhibiting a low energy configuration with 120° triple junctions. Sample 56151, width of view 4mm

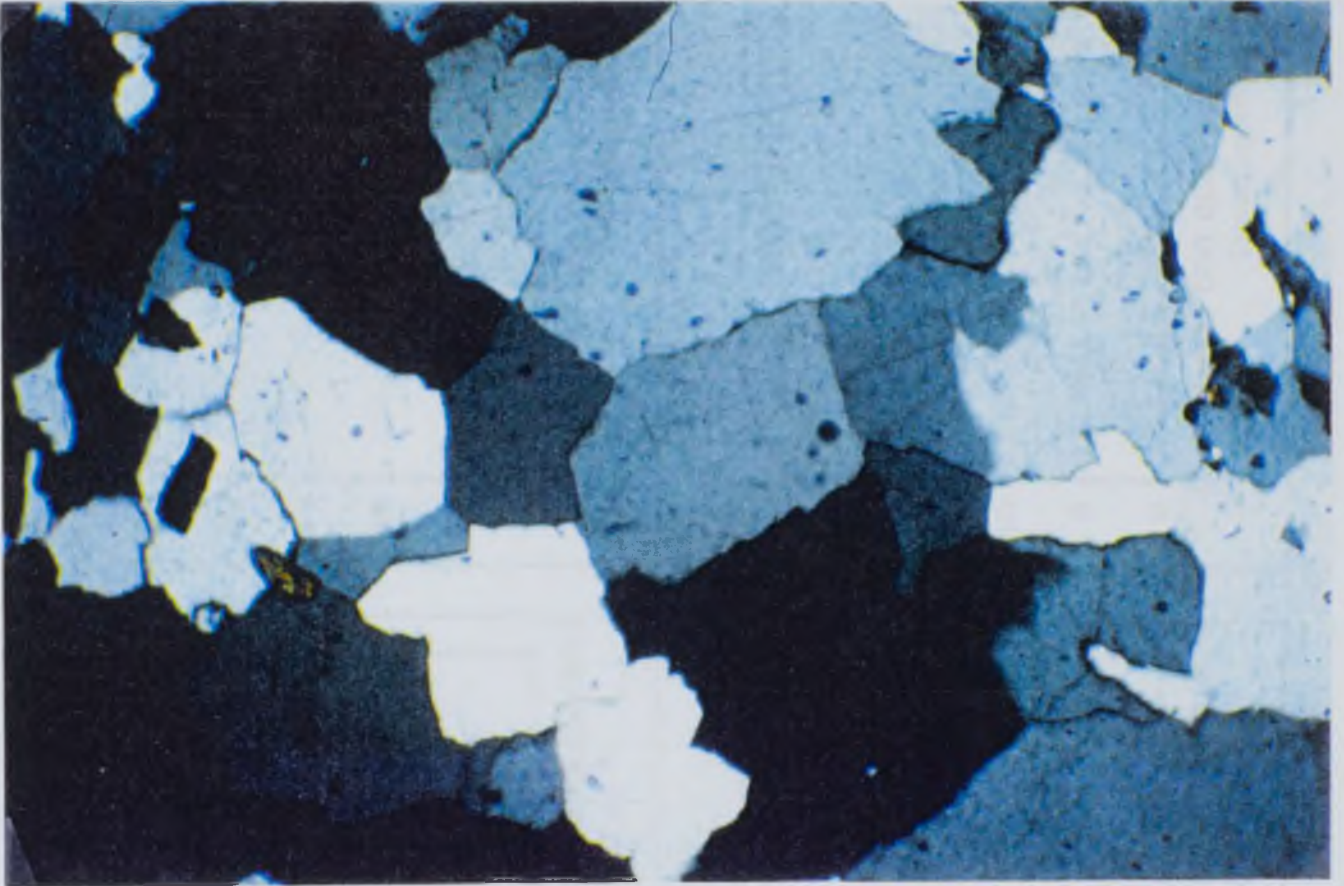


Figure 5.5 Graphs indicating the variation in the percentages with respect to distance from the Ballachulish igneous intrusion of each type of substructure (as defined by Farmer - 1992) typically developed within the Appin Quartzite.

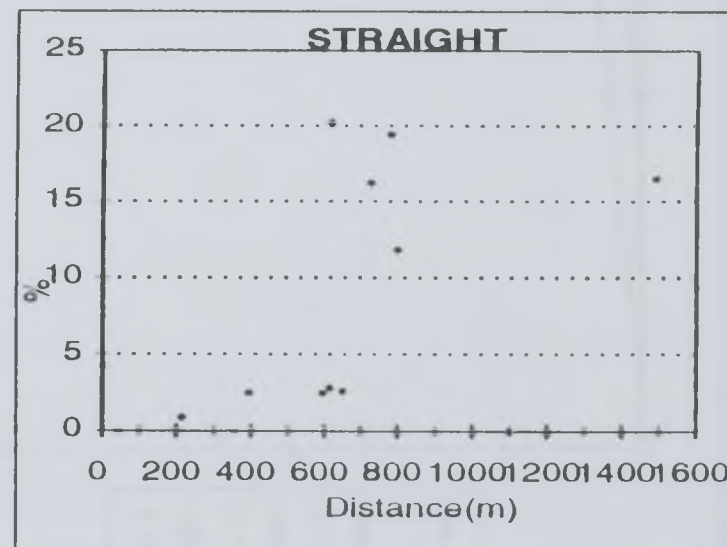
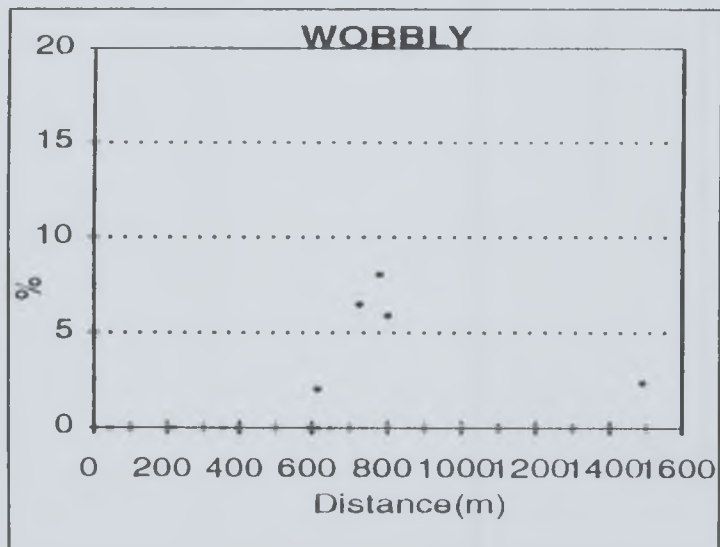
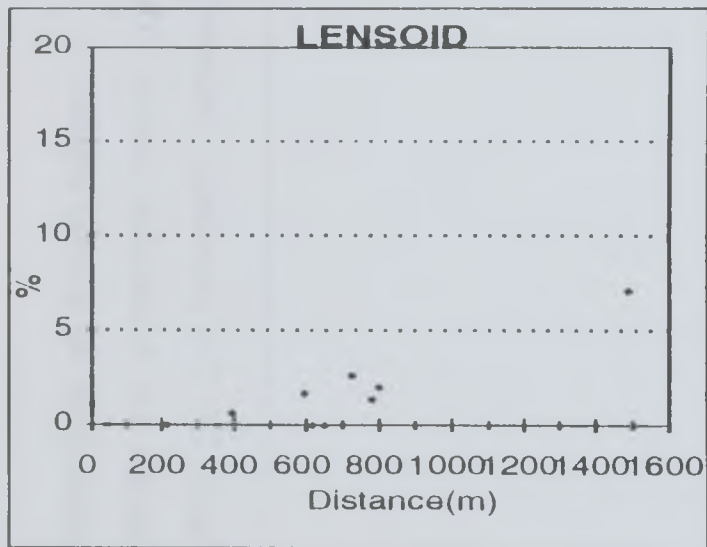
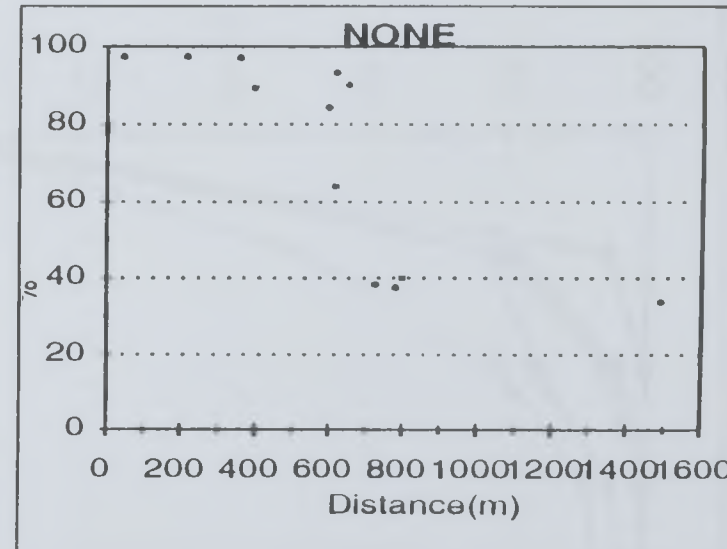
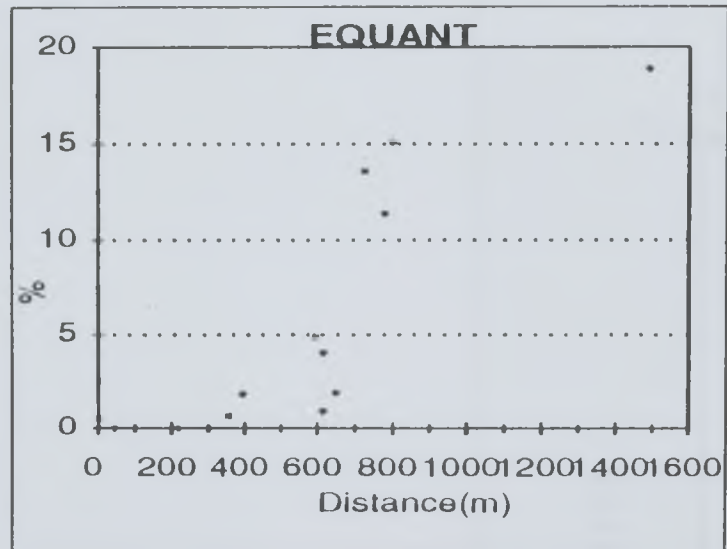
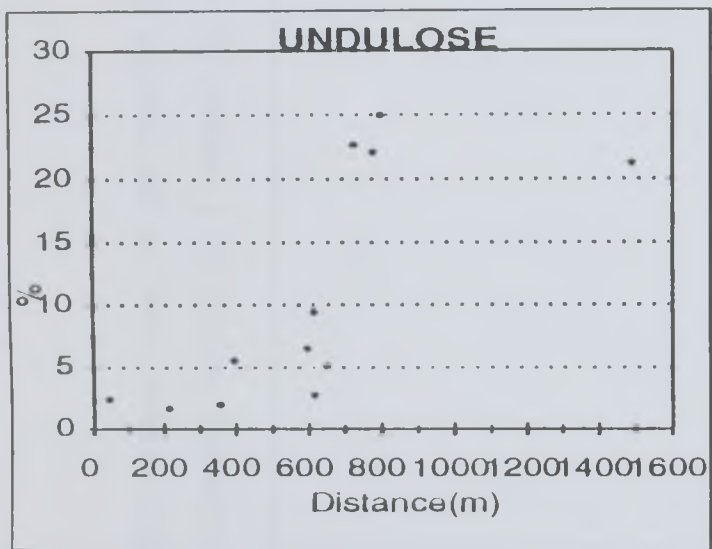




Figure 5.6 The cumulative frequency of extinction angles for a variety of samples through the Ballachulish aureole. The legend numbers refer to the distance of each sample from the igneous contact.

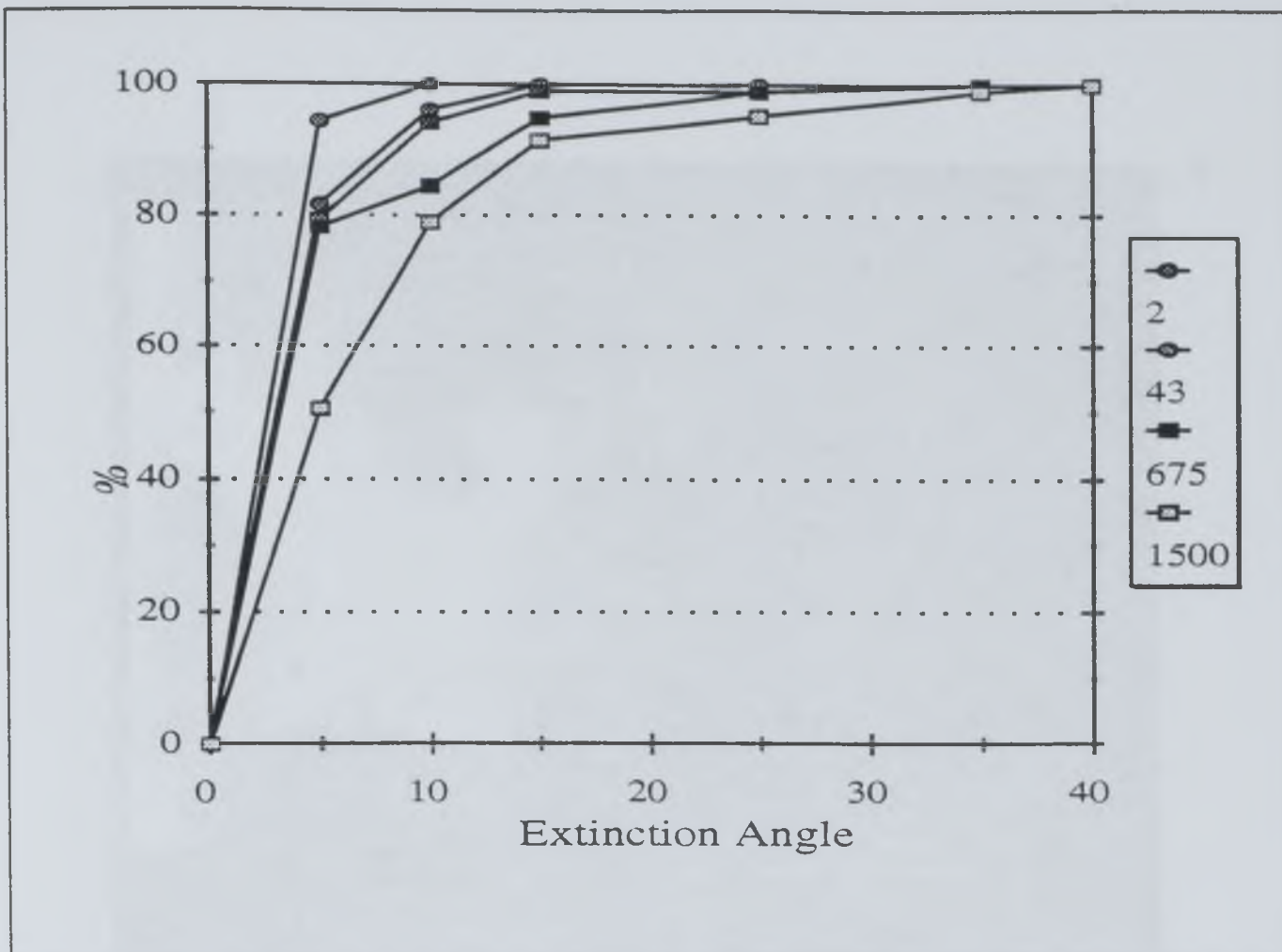
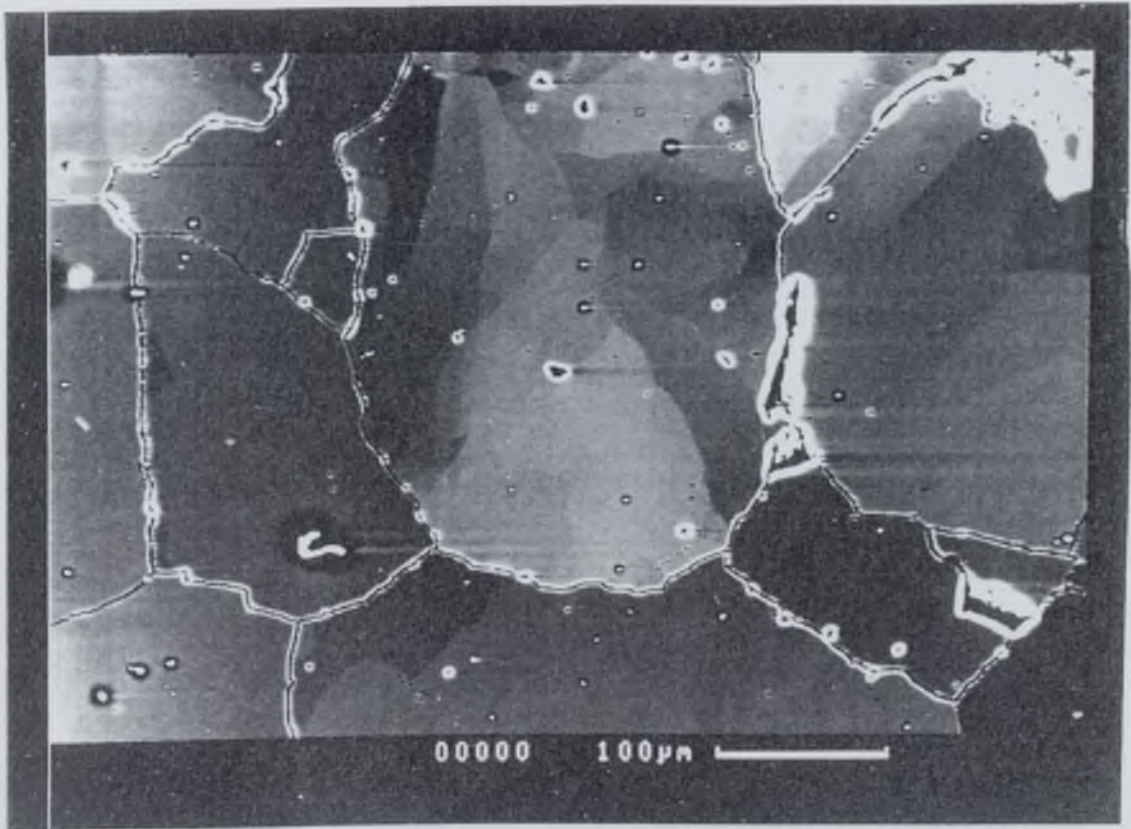
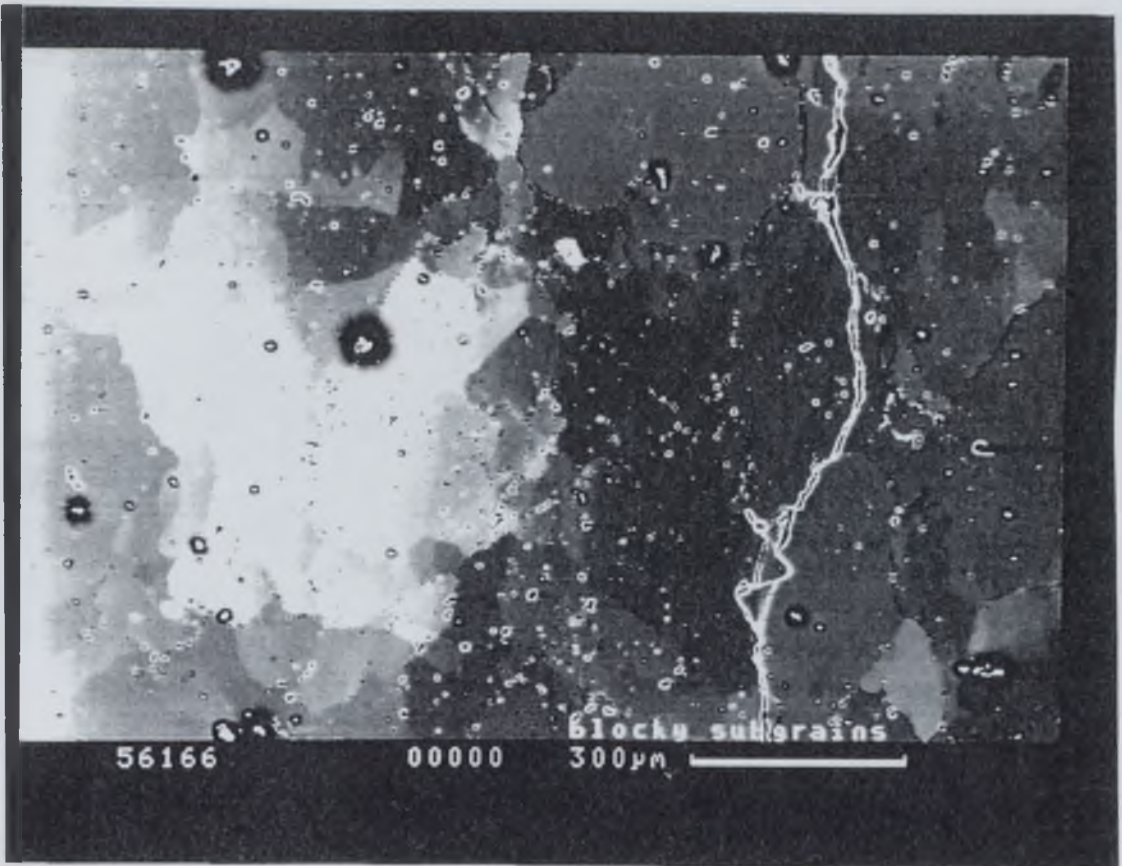
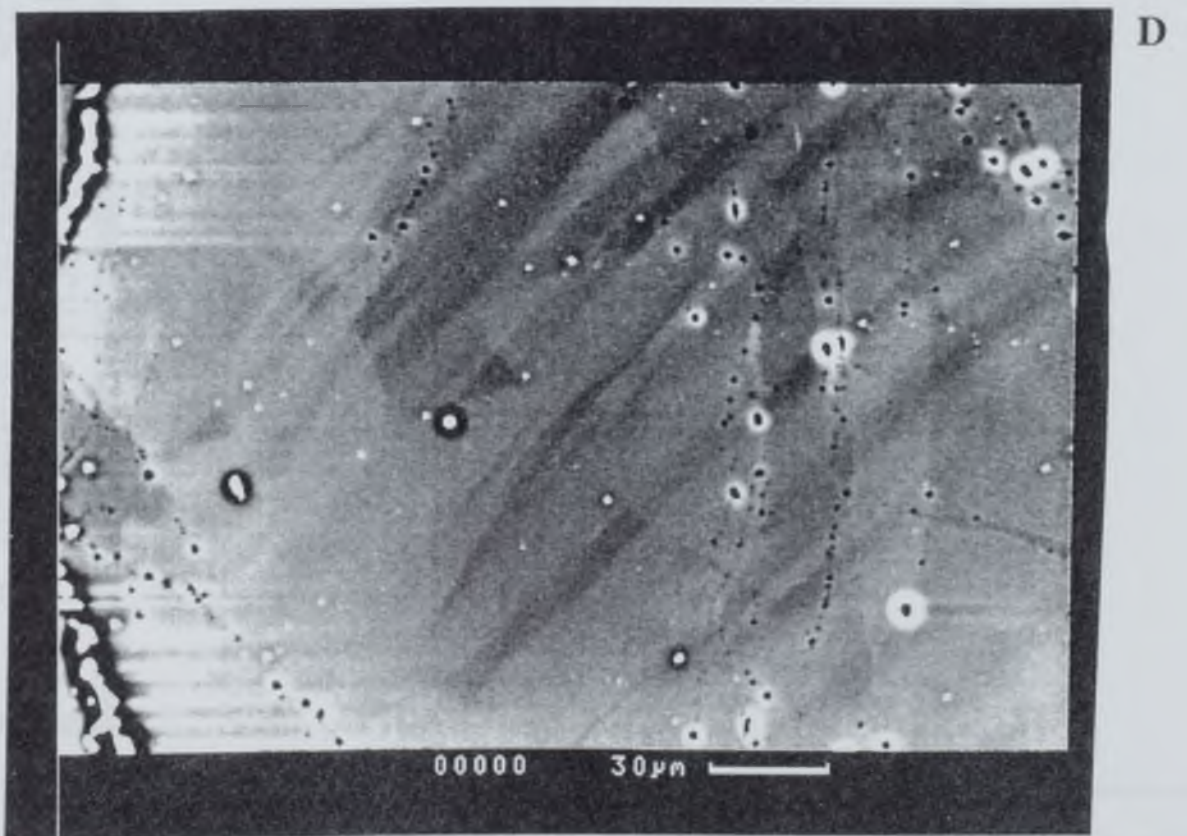
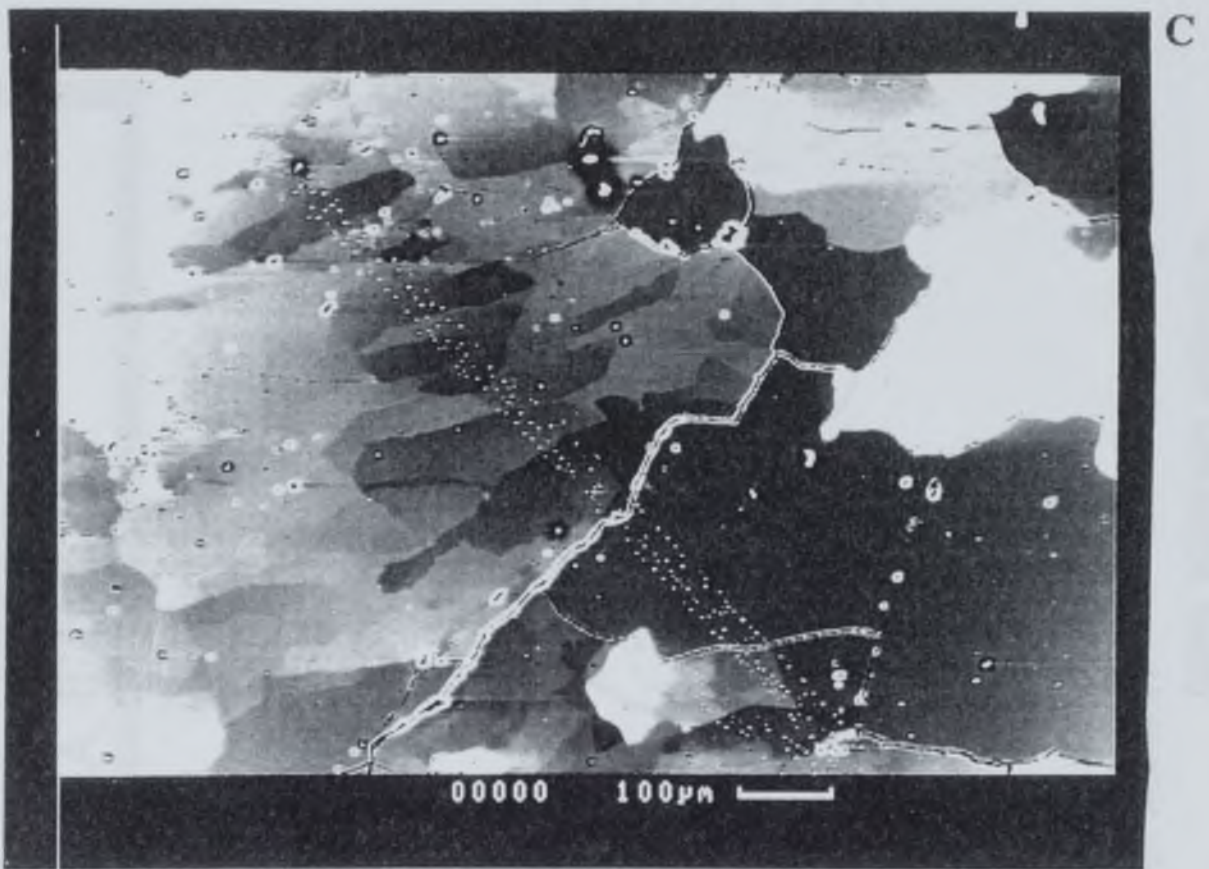




Figure 5.7 Photomicrographs of the different forms of subgrain shapes that are imaged using the SEM/OC. a-complex subgrain shapes (sample 56157), b-equant subgrains (sample 56157), c-straight subgrains and d-deformation lamellae (sample 56157).





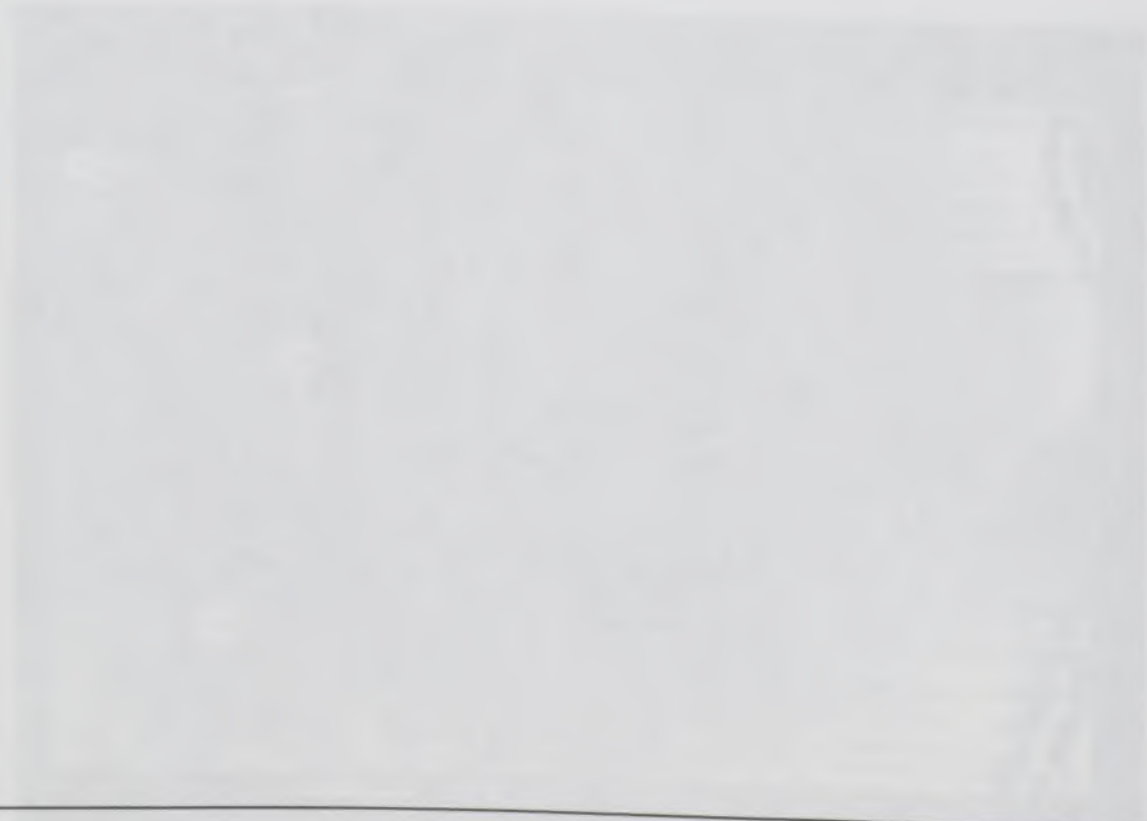
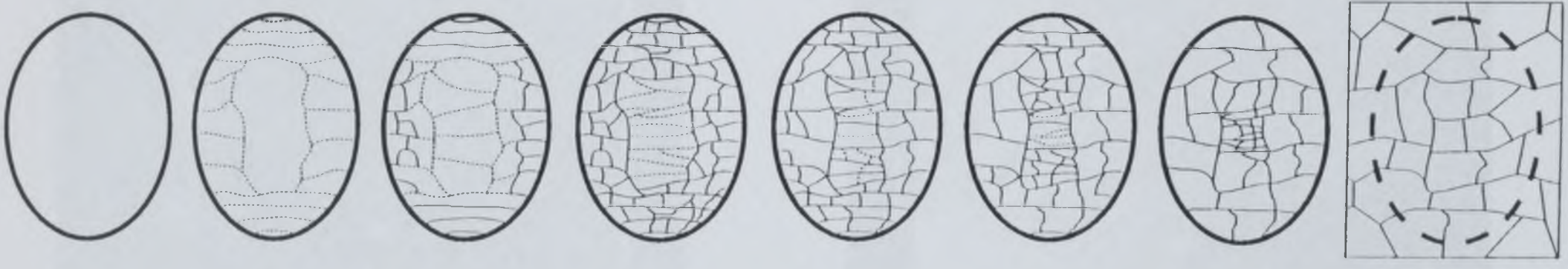


Figure 5.8 Core mantle structures which are common in deformed quartzites (from Lloyd, 1992).

SCHEMATIC DYNAMIC RECRYSTALLISATION MICROSTRUCTURAL HISTORY BASED ON GRAINS A, B AND C

Mantle
polygonal
subgrains



GRAIN A

GRAIN B

GRAIN C

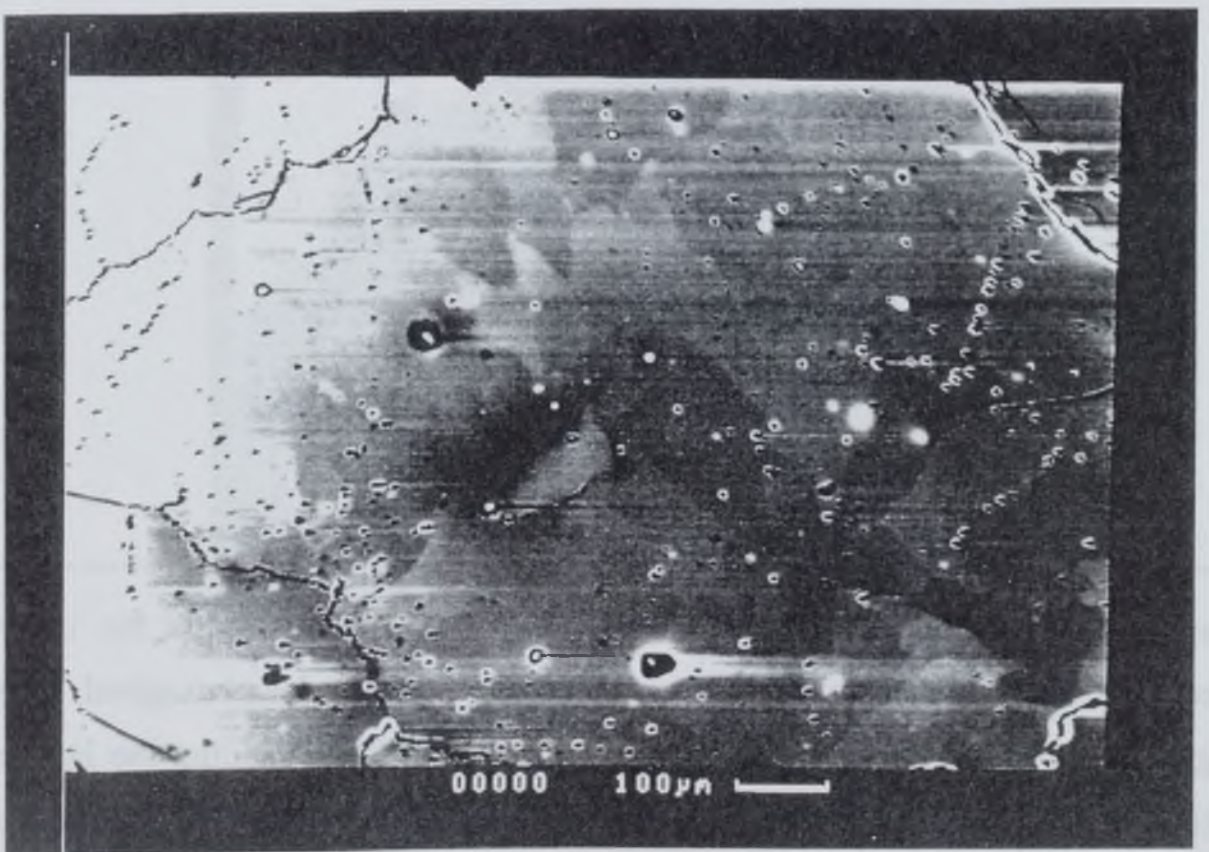
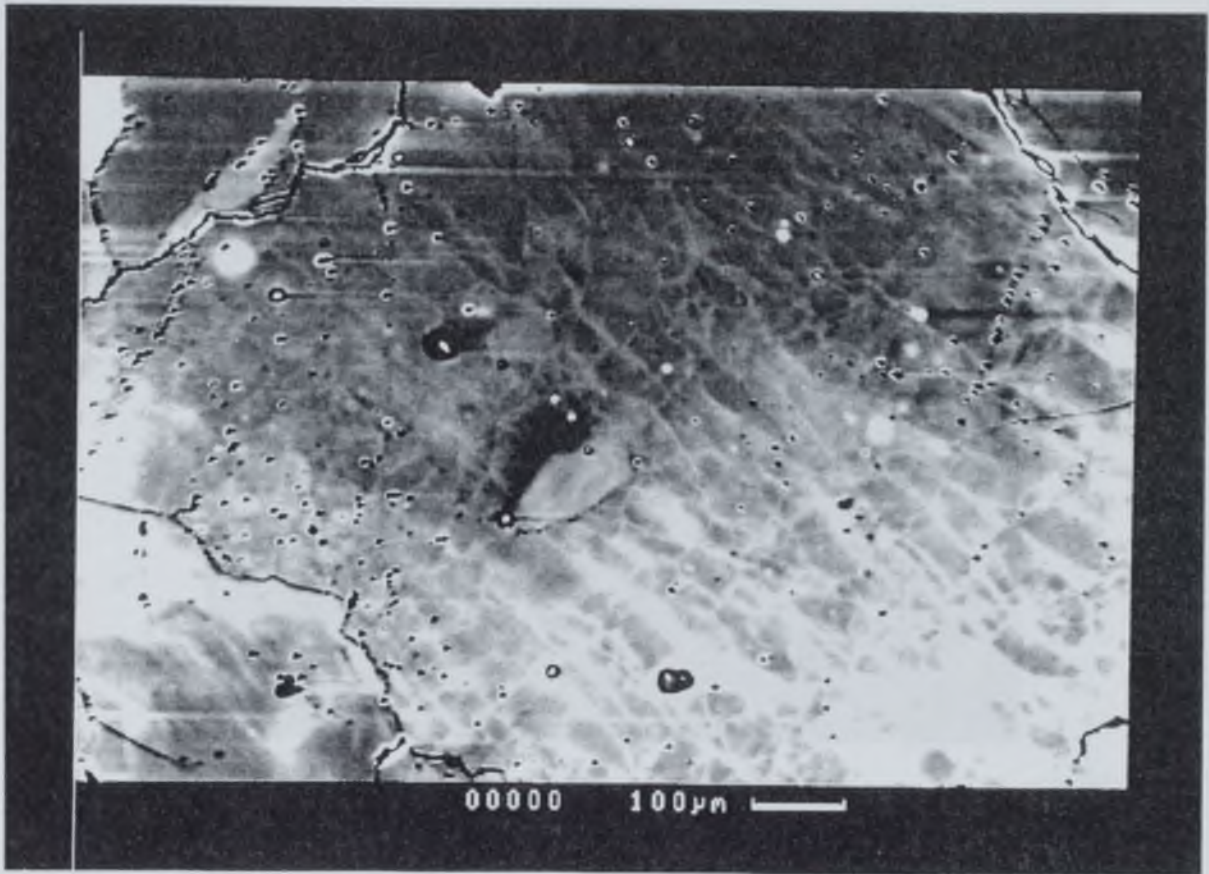
SUBGRAIN POLYGONISATION

SUBGRAIN/GRAIN ROTATION

GRAIN BOUNDARY MIGRATION

INCREASING DYNAMIC RECRYSTALLISATION

Figure 5.9 A deformed grain (from sample 56154 - 615m from the igneous contact) a- imaged using SEM cathodo-luminescence, revealing a 'mesh' structure and b-the same grain imaged using SEM/OC showing that the grain looks similar to it's neighbouring grains.



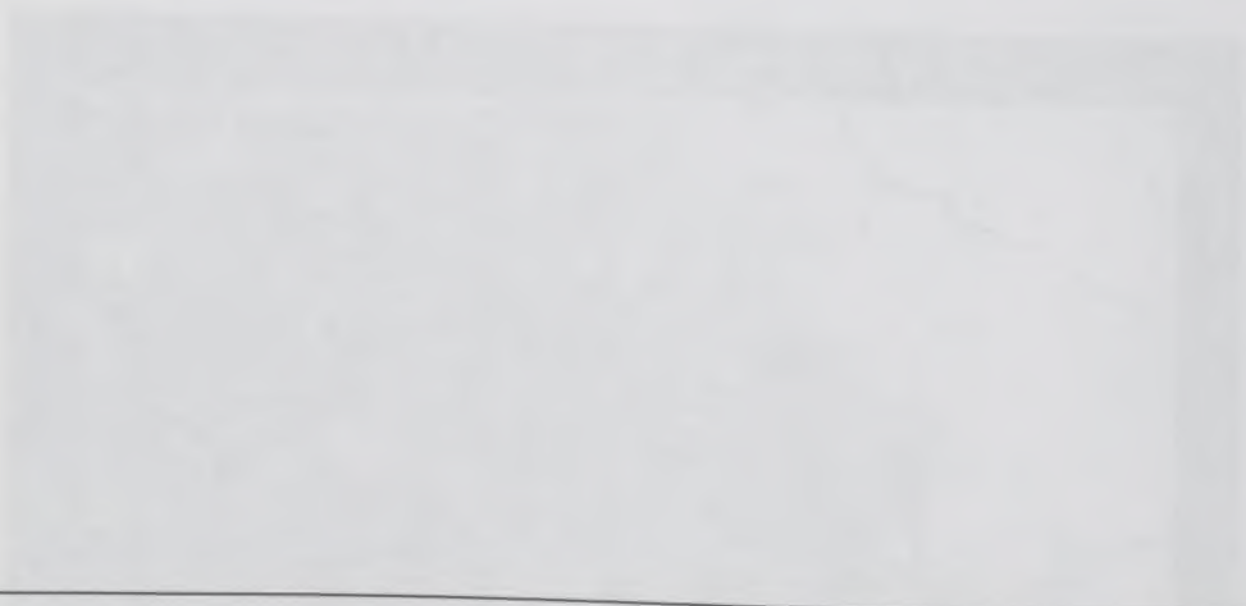
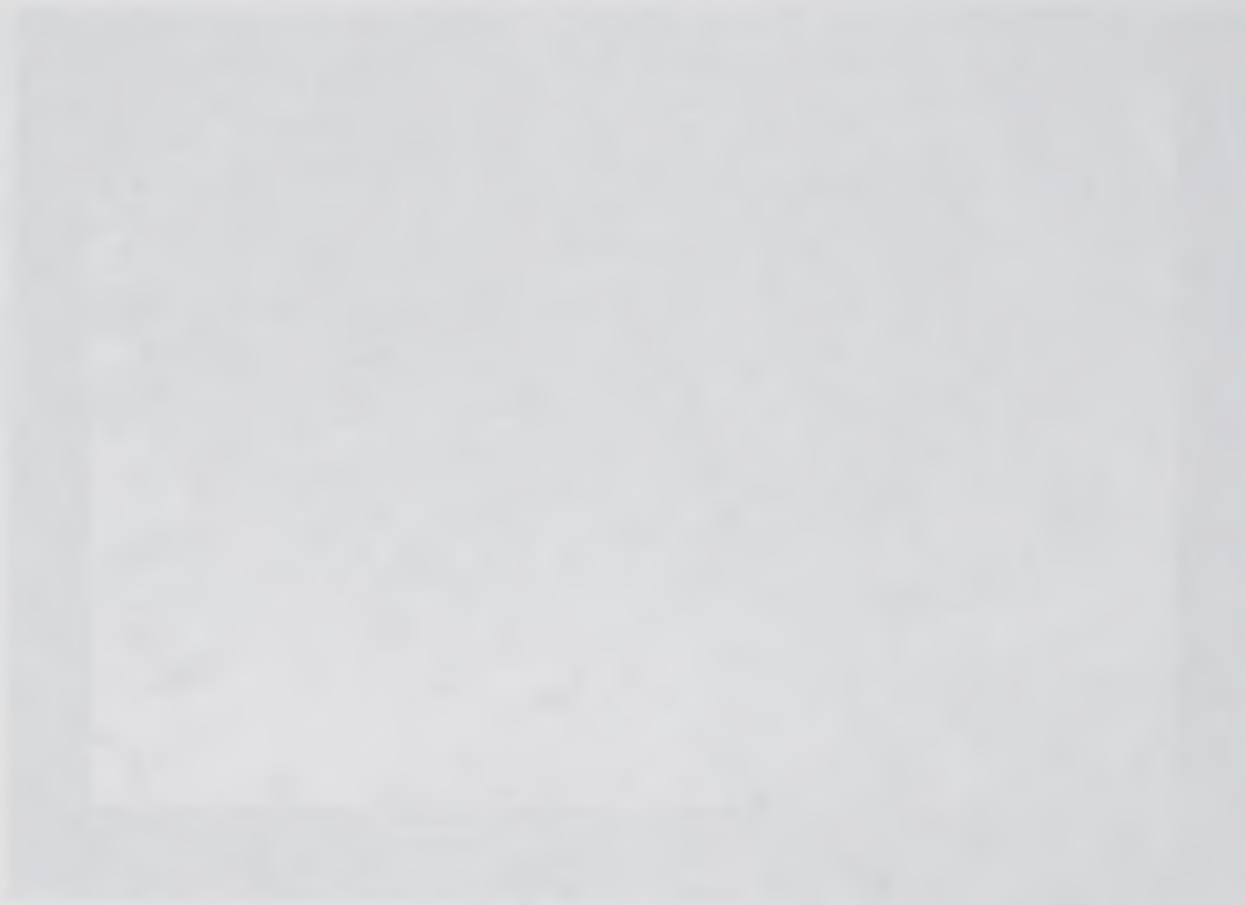
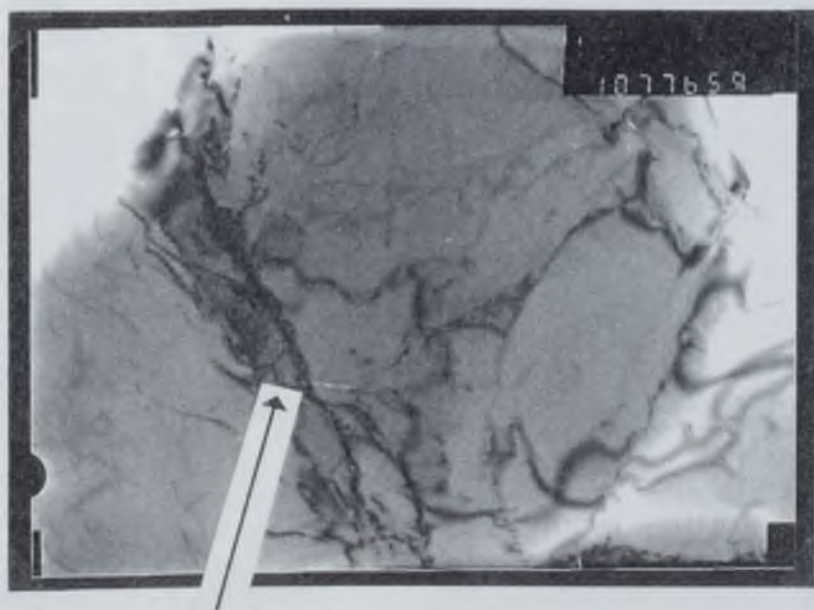
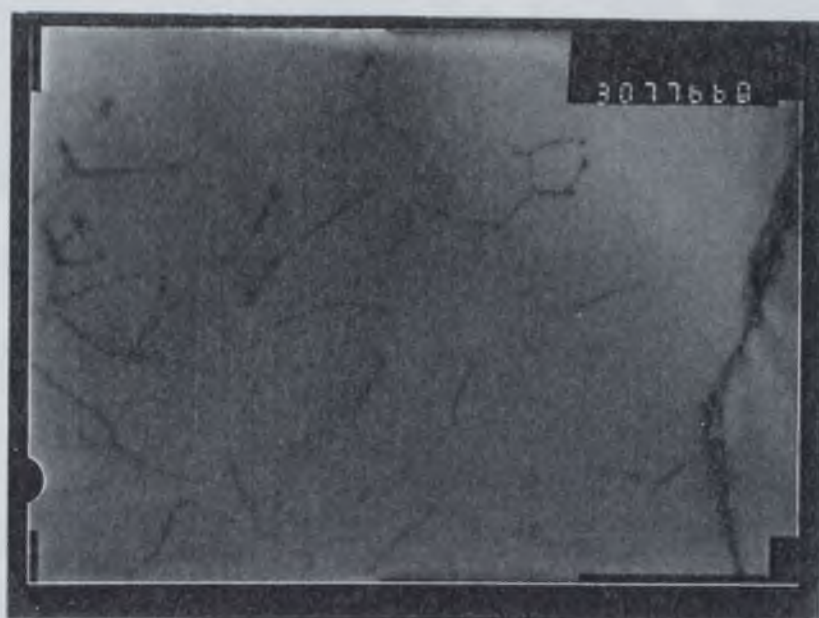


Figure 5.10 Dislocation structures in deformed samples from outside the igneous aureole. Note that the dislocations are straight and arranged into hexagonal arrays, suggesting that these rocks have recovered prior to intrusion or during the intrusion itself. The top micrograph is x30, 000 magnification, the lower micrograph is a lower magnification (x10,000) from the same area of sample. Notice the development of dislocation walls, which are separating adjacent subgrains. Sample 56150.



Subgrain Wall

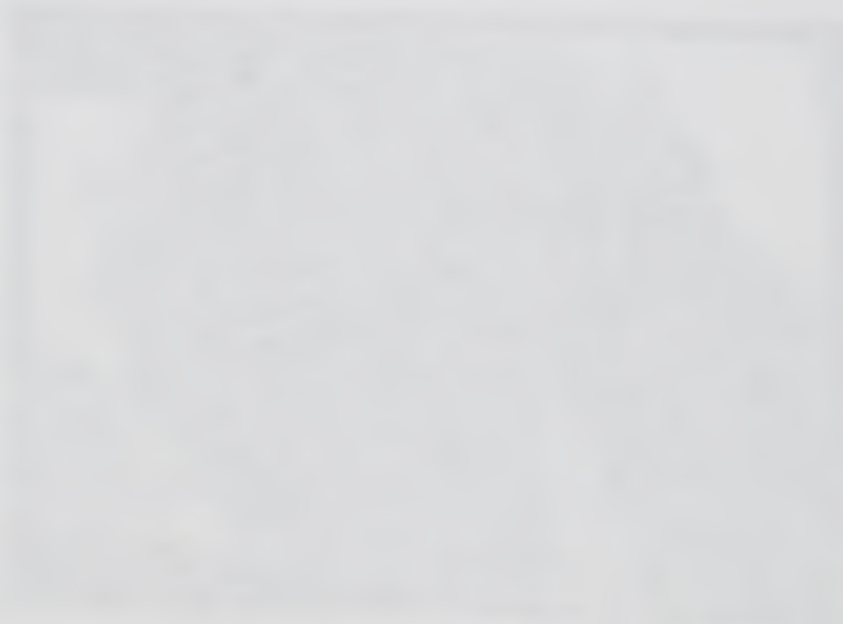
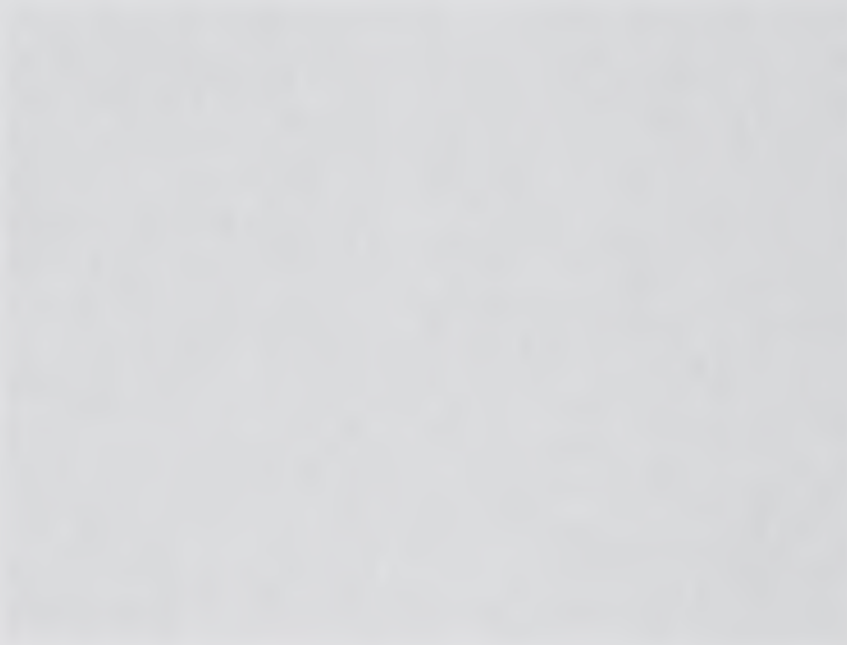


Figure 5.11 Second phase feldspars (relatively small particles) have been consumed by quartz grains which have grown during annealing.




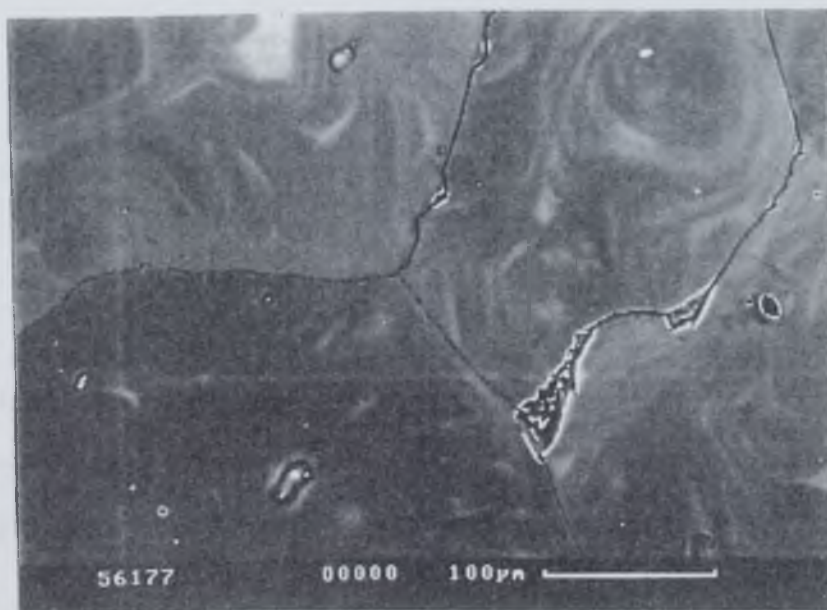
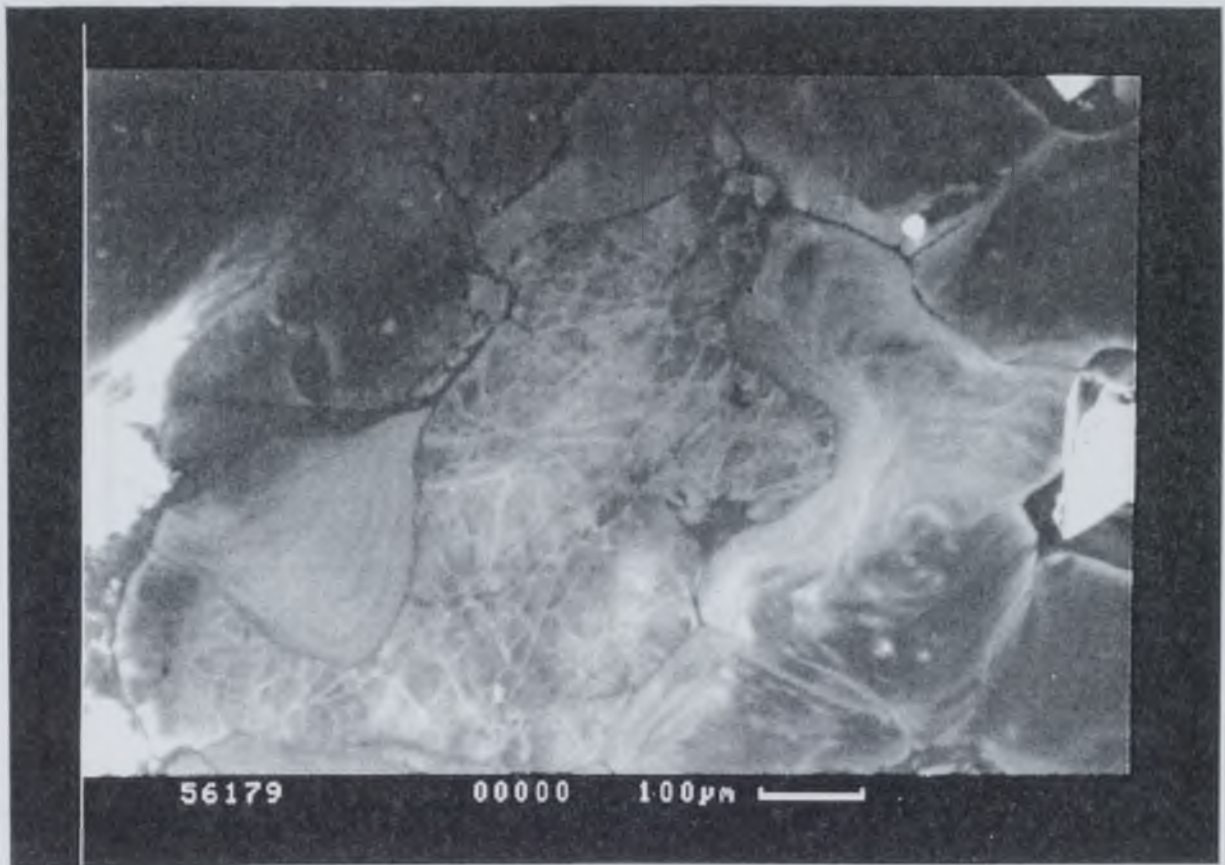


Figure 5.12 SEM Cathodo-luminescence photomicrograph. The central grain contains the mesh structures similar to those in Figure 5.9. However this sample is from within the igneous aureole, note the surrounding grains luminesce in a banded pattern that generally parallels (though not always) the grain boundaries. The banding indicates that the grain boundaries have migrated, and in doing so begun to consume the central grain. Sample 56169.

Figure 5.13 Cathodo-luminescence-banding within a grains from an annealed sample. The bands are concentric around a 'nucleation pip' within the grain in the upper right of the micrograph. This is possibly evidence that the grain nucleated during annealing and the banding is preserving the growth history of that grain. Sample 56151.



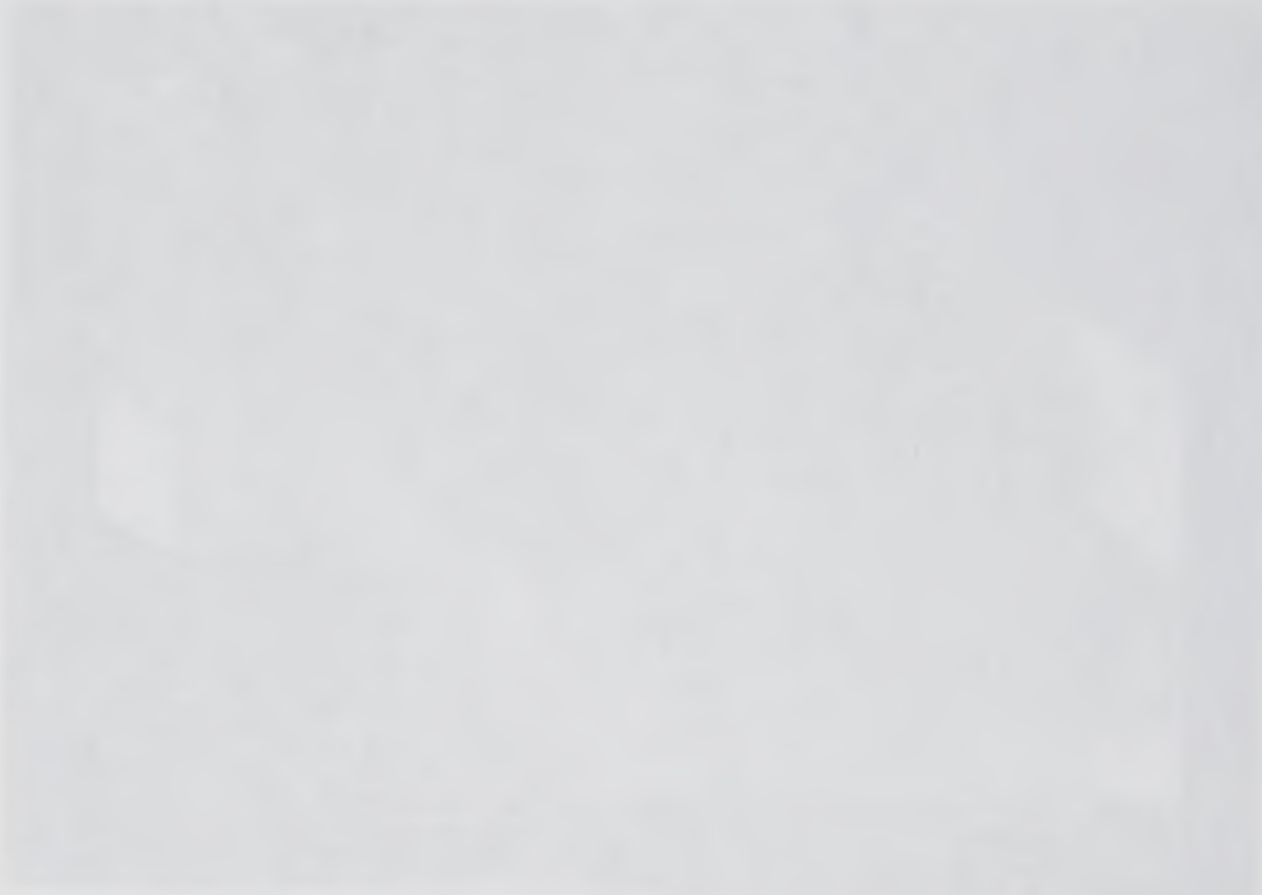


Figure 5.14 Variation in grain size with respect to distance from the igneous contact. The data is measured using linear intercept methods (see Abrams, 1971).

Figure 5.15 Variation in FCIRCLE (defined in Appendix C) with distance from the intrusion.

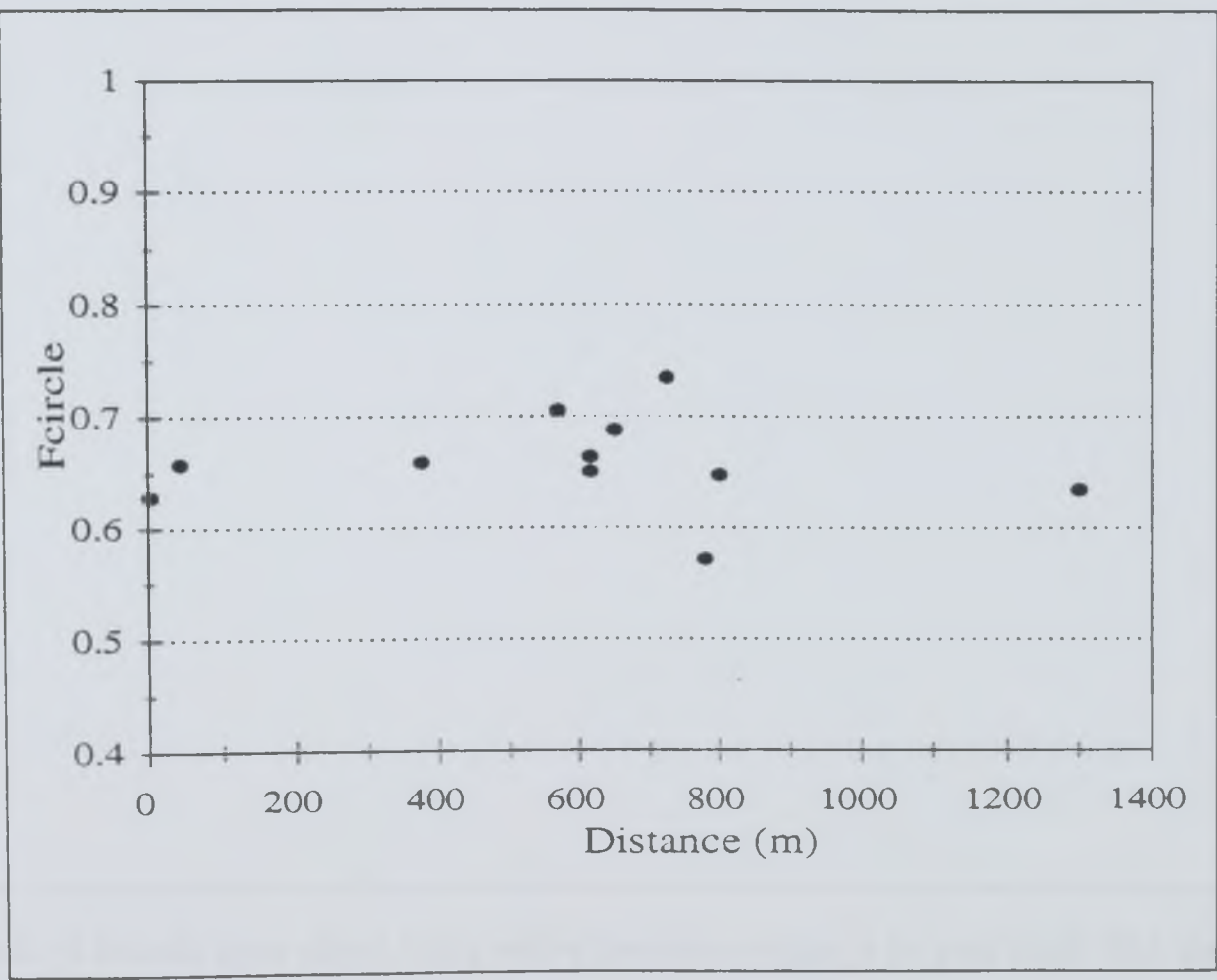
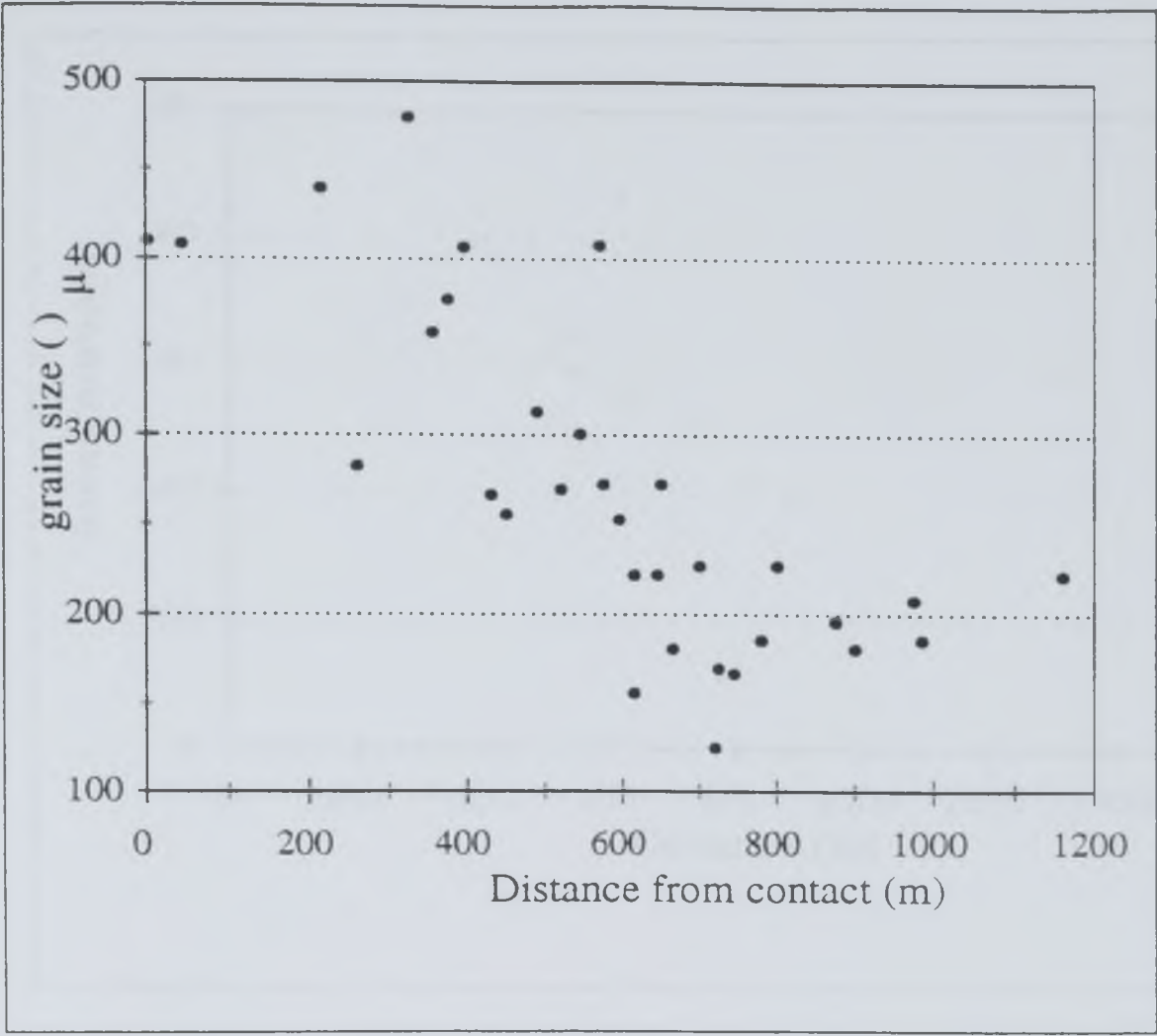




Figure 5.16 Total area of a sample contained within grains (grain area) divided by the total area of a sample contained in the grain boundaries (grain perimeter) versus distance from the intrusion, i.e. grain boundary area/unit volume.

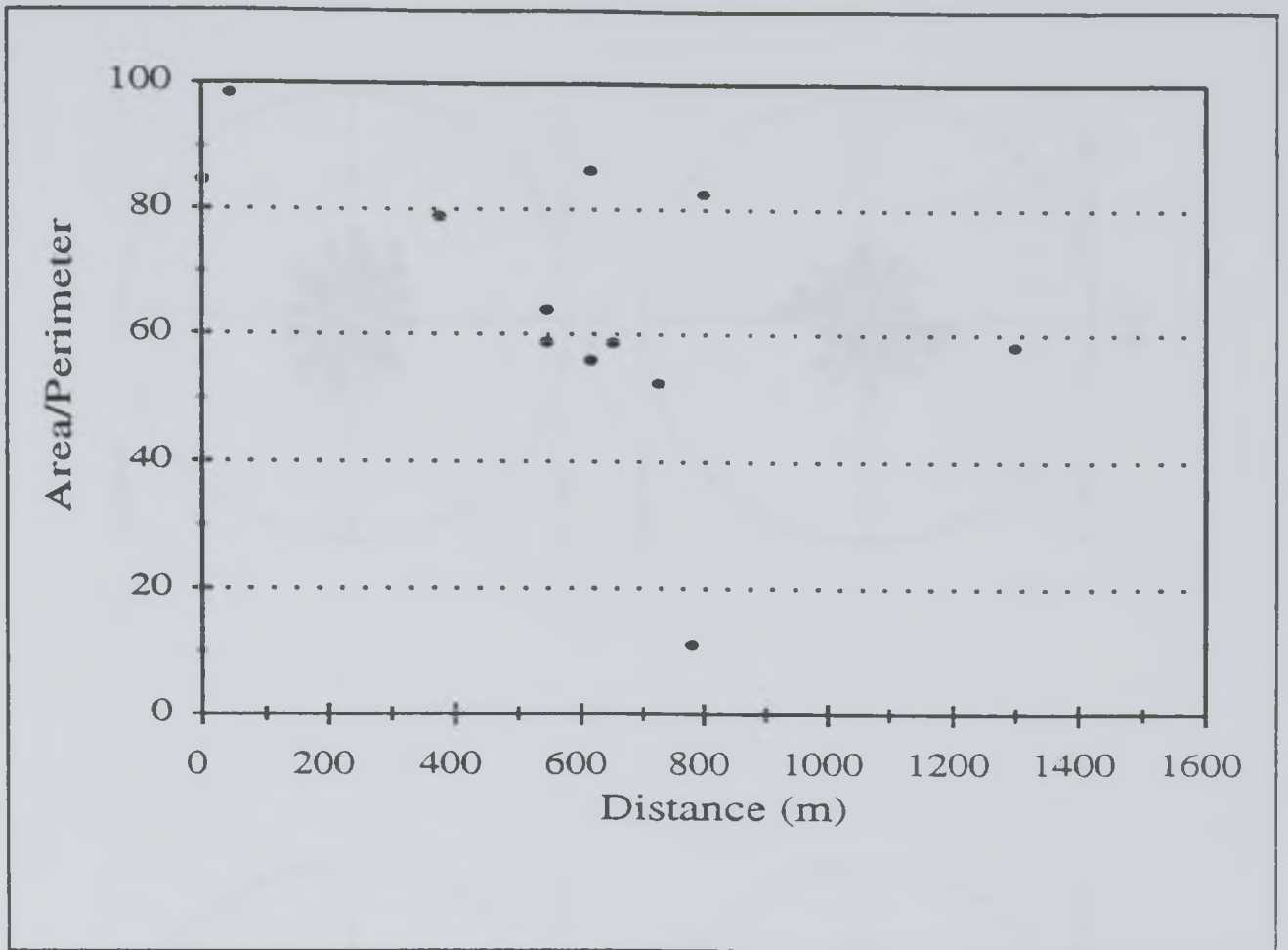
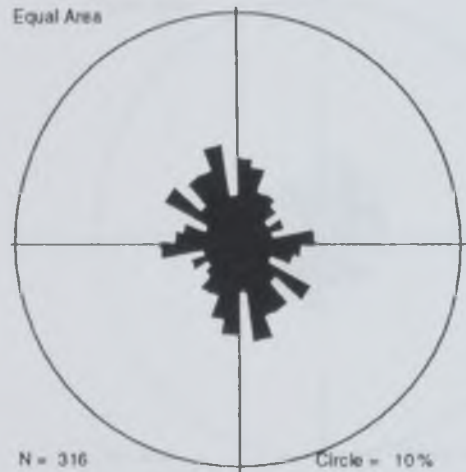
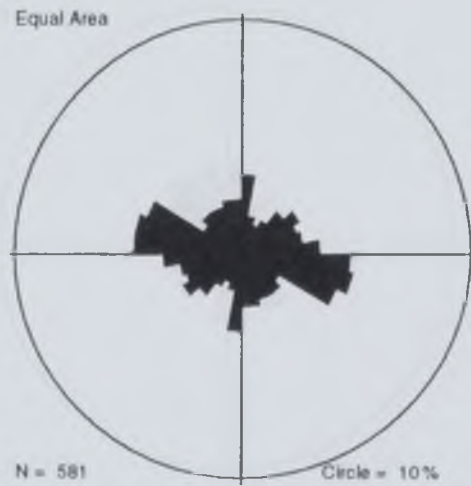




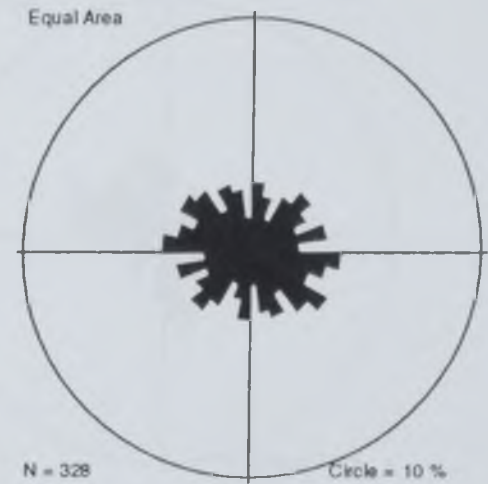
Figure 5.17 Rose diagrams showing the orientation from the image horizontal (tectonic x direction) of the maximum feret length of a grain (i.e. the long axis of a grain). If grains are elongate parallel with the x-direction they will plot as an ellipse on these rose diagrams, with the long axis in the vertical direction - i.e. the majority of grains are oriented with their long axis at a low angle to the x-direction. Samples increase in distance from the intrusion in order along page - 48-49-51-80-54-69-78-77-57-60-55.



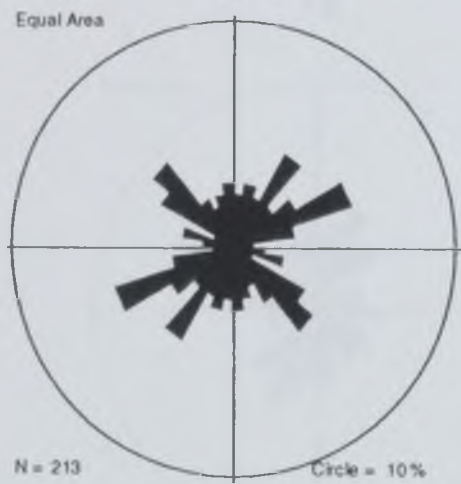
48



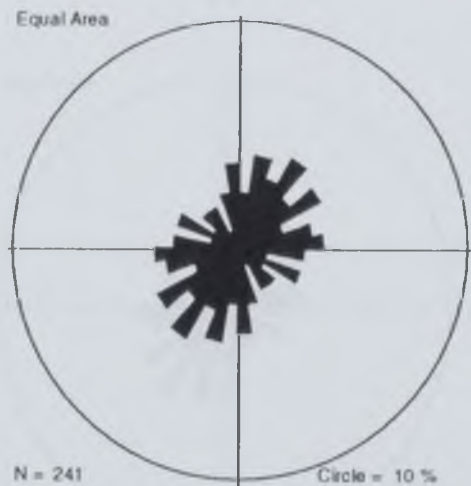
49



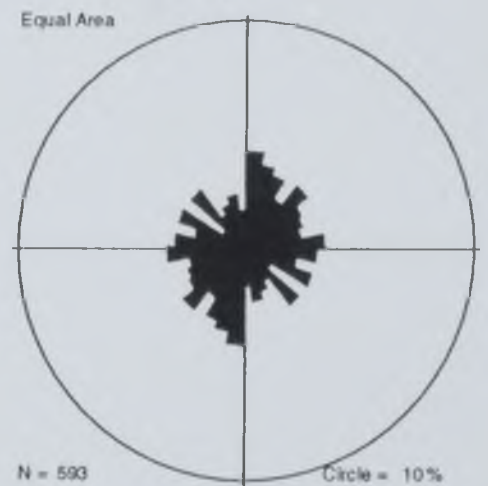
51



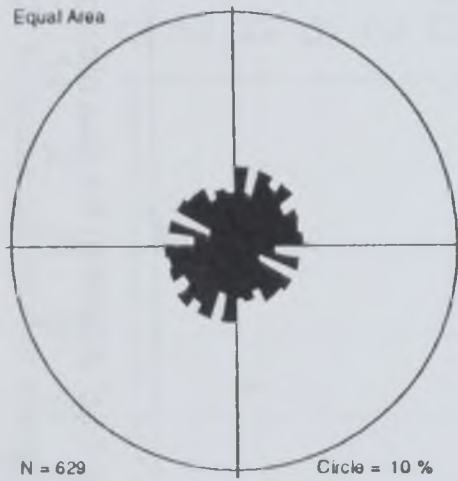
80



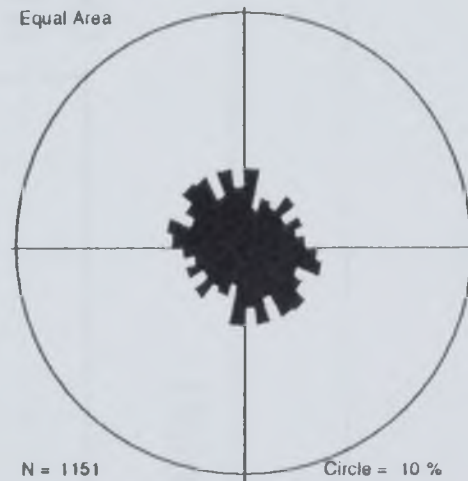
54



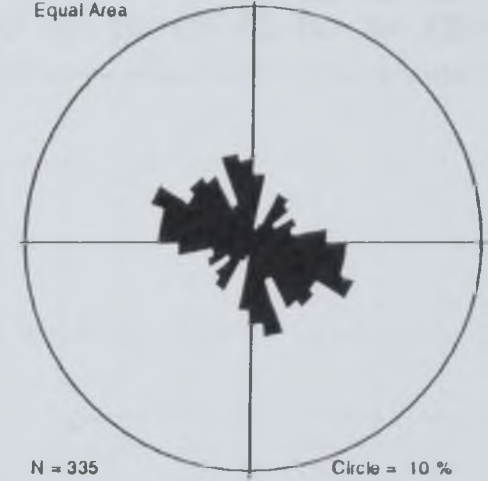
69



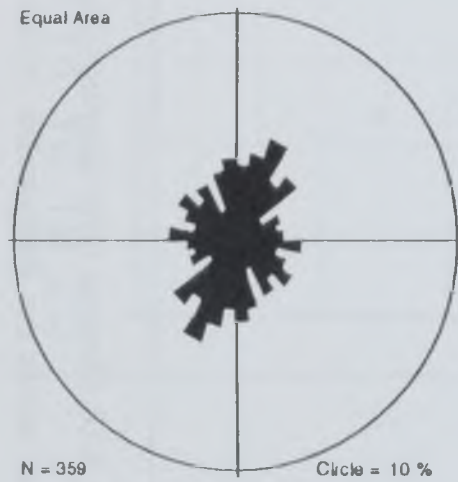
78



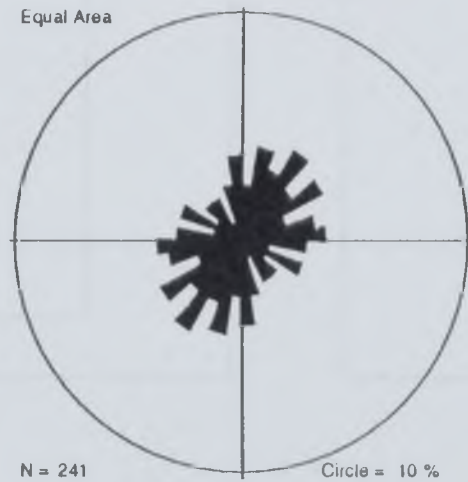
77



57

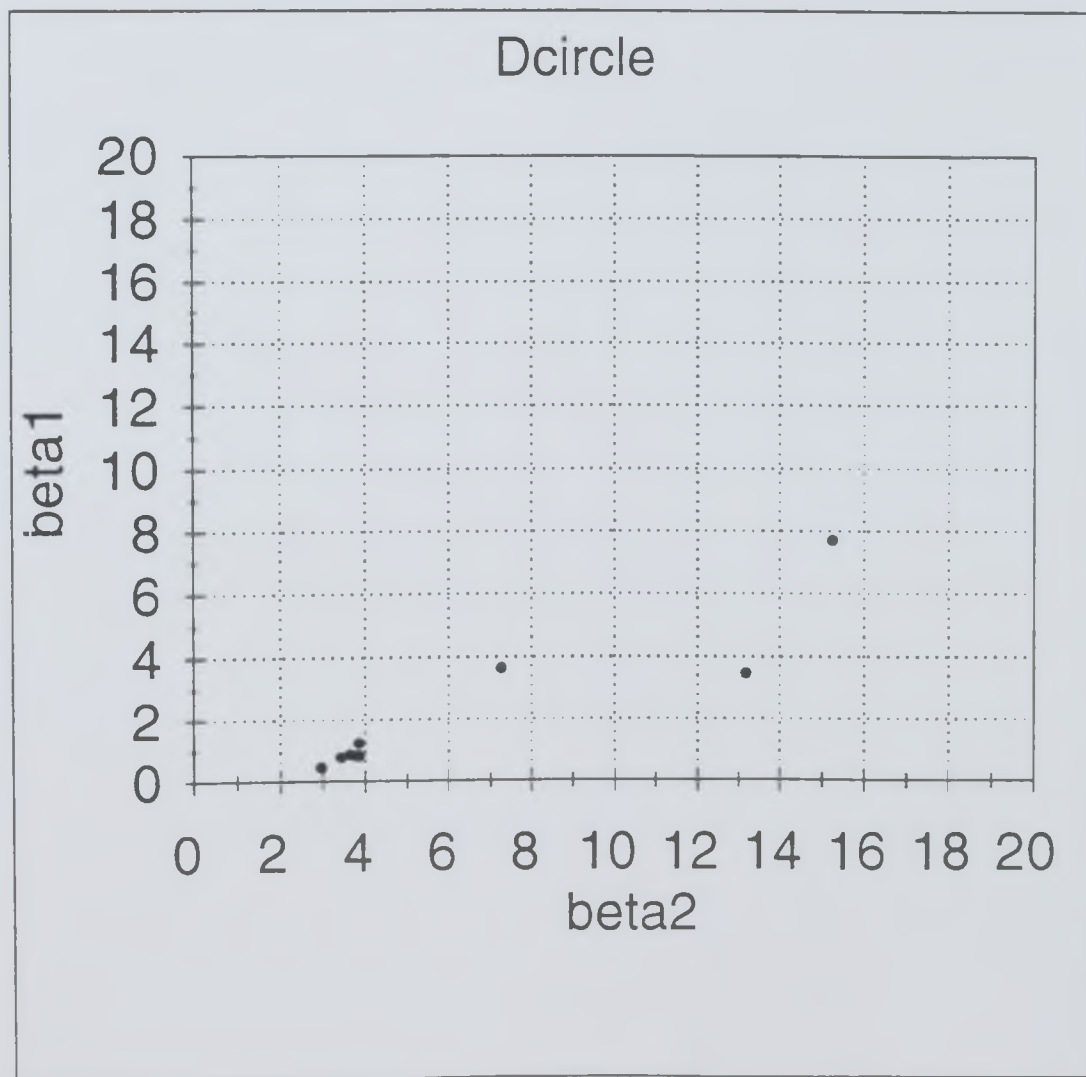
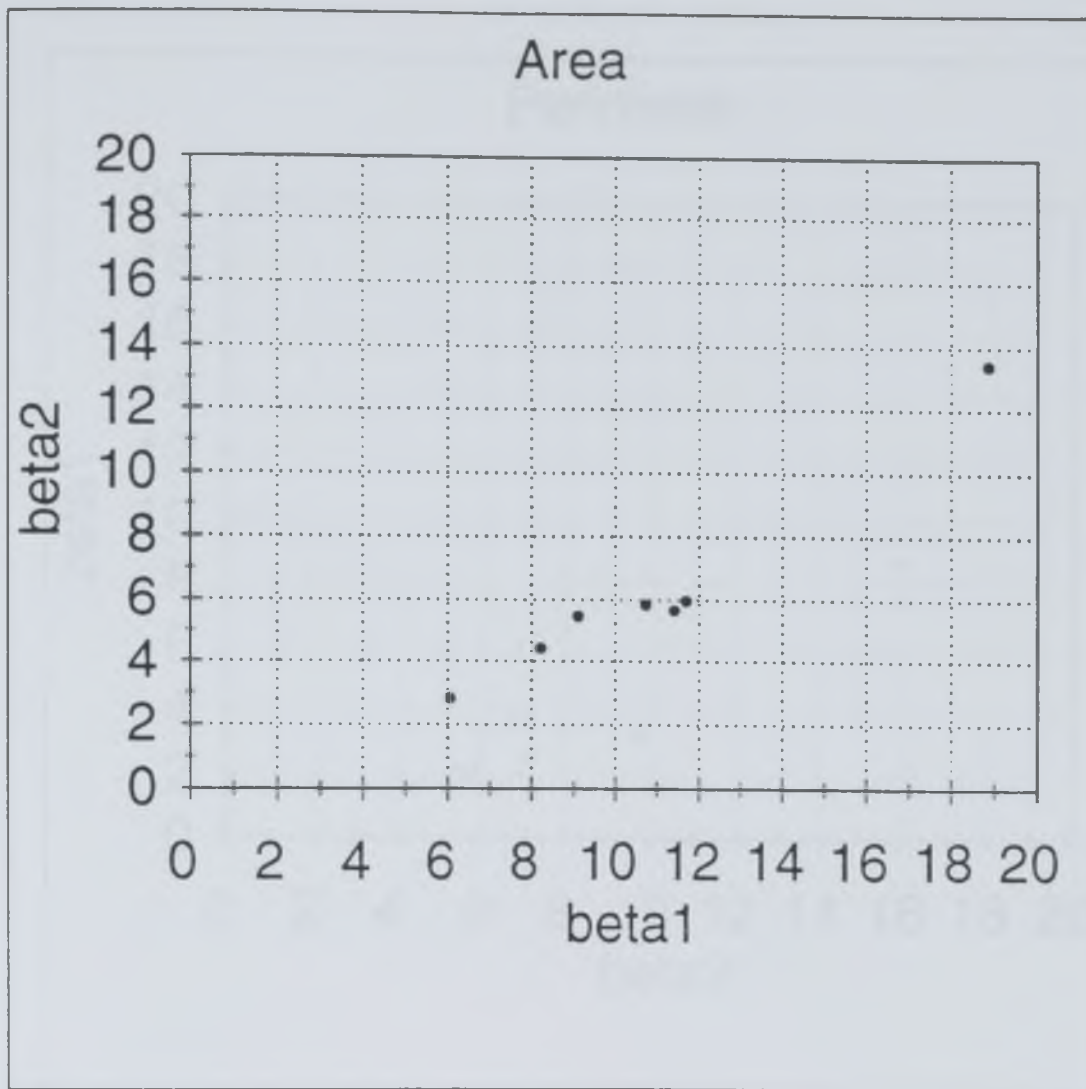


60

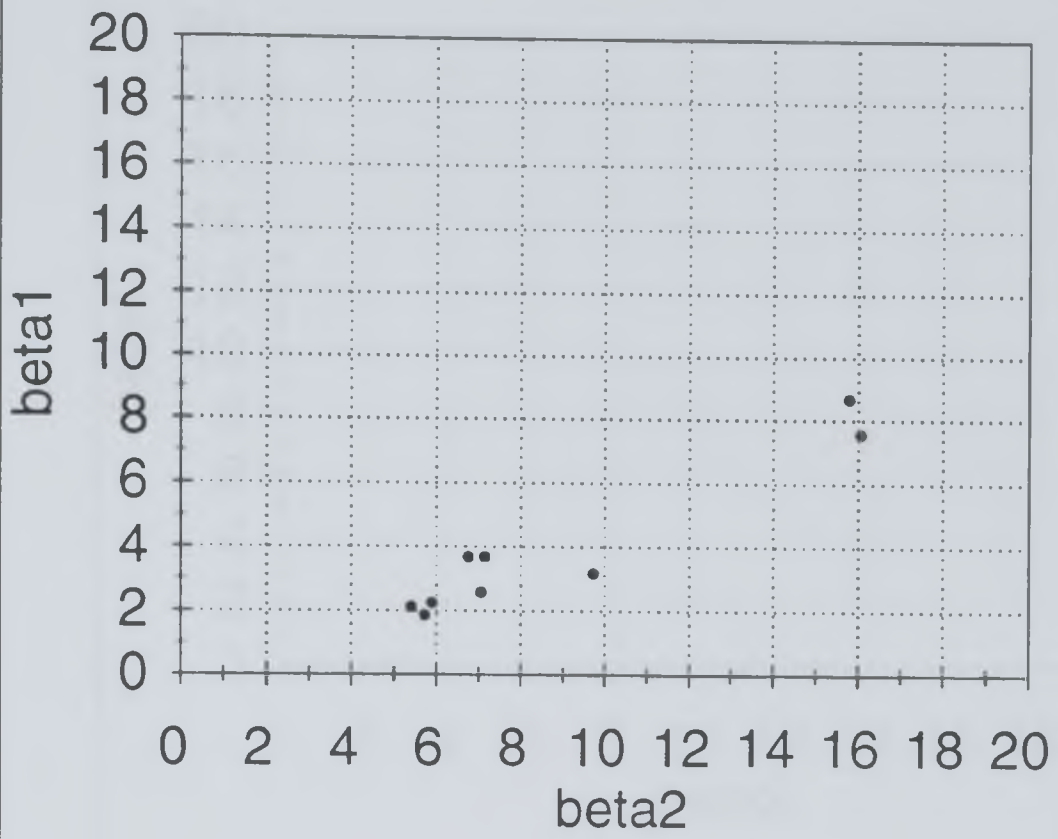


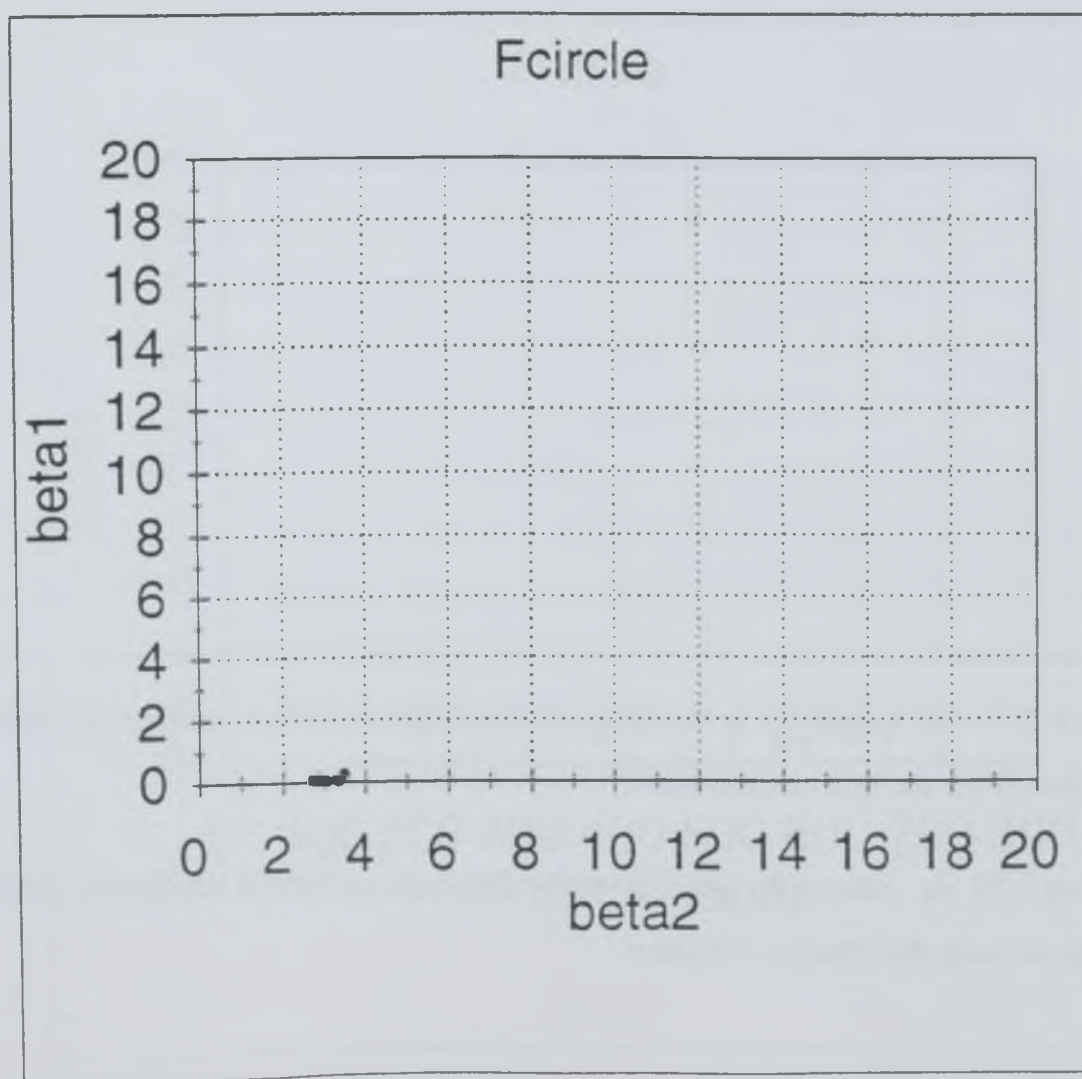
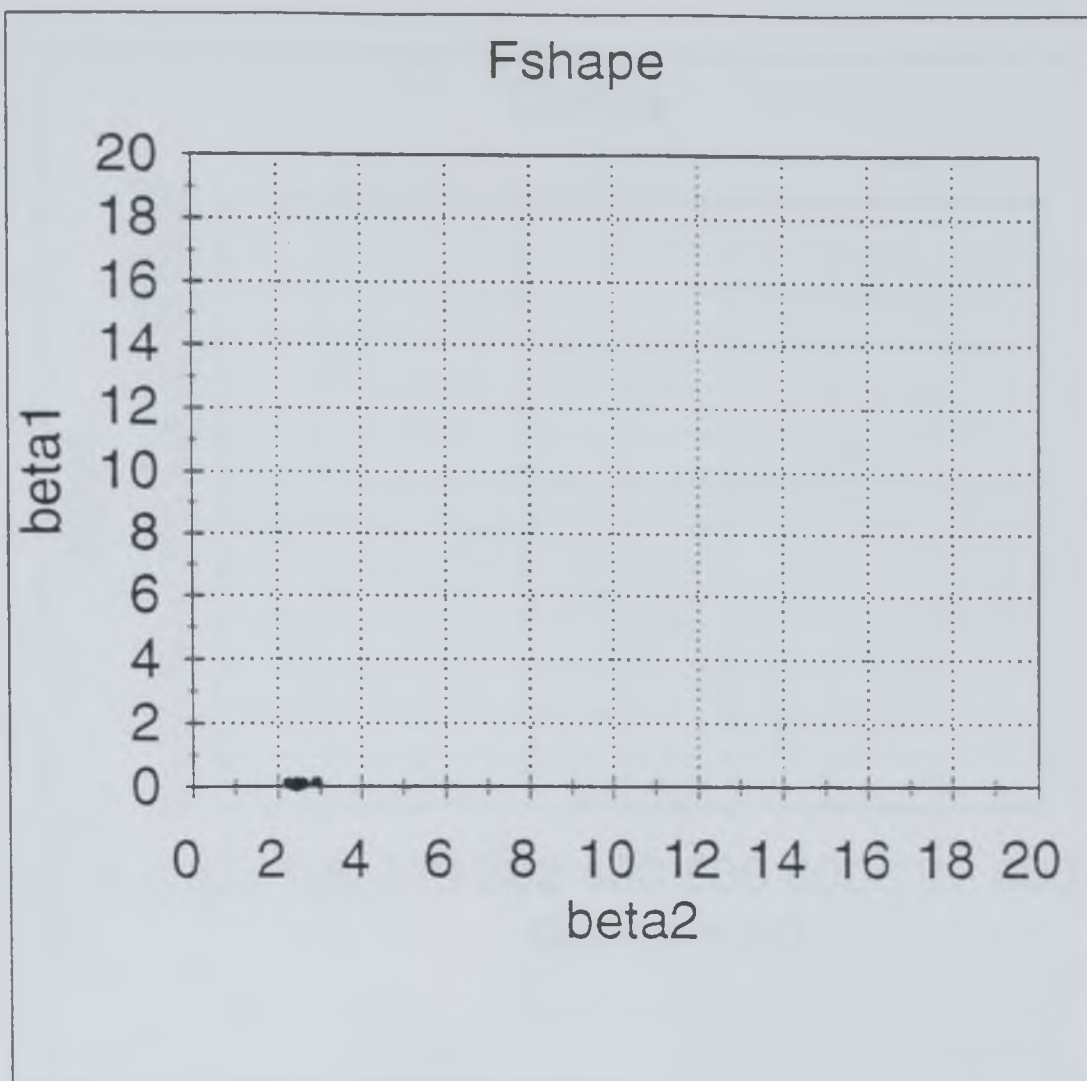
55

Figure 5.18 Moment ratio diagrams (see chapter 4 for definition) for data obtained from samples within the Ballachulish region. The diagrams indicate the nature of histogram distribution data for a variety of measurements. See Appendix C for measurement definitions.



Perimeter





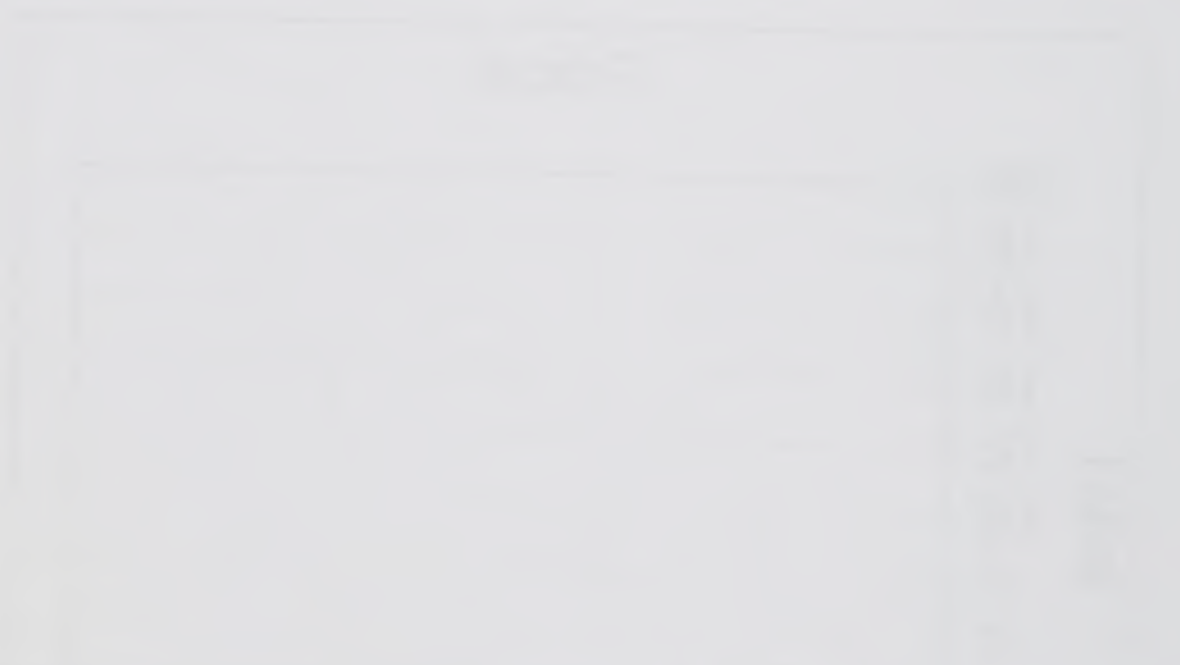
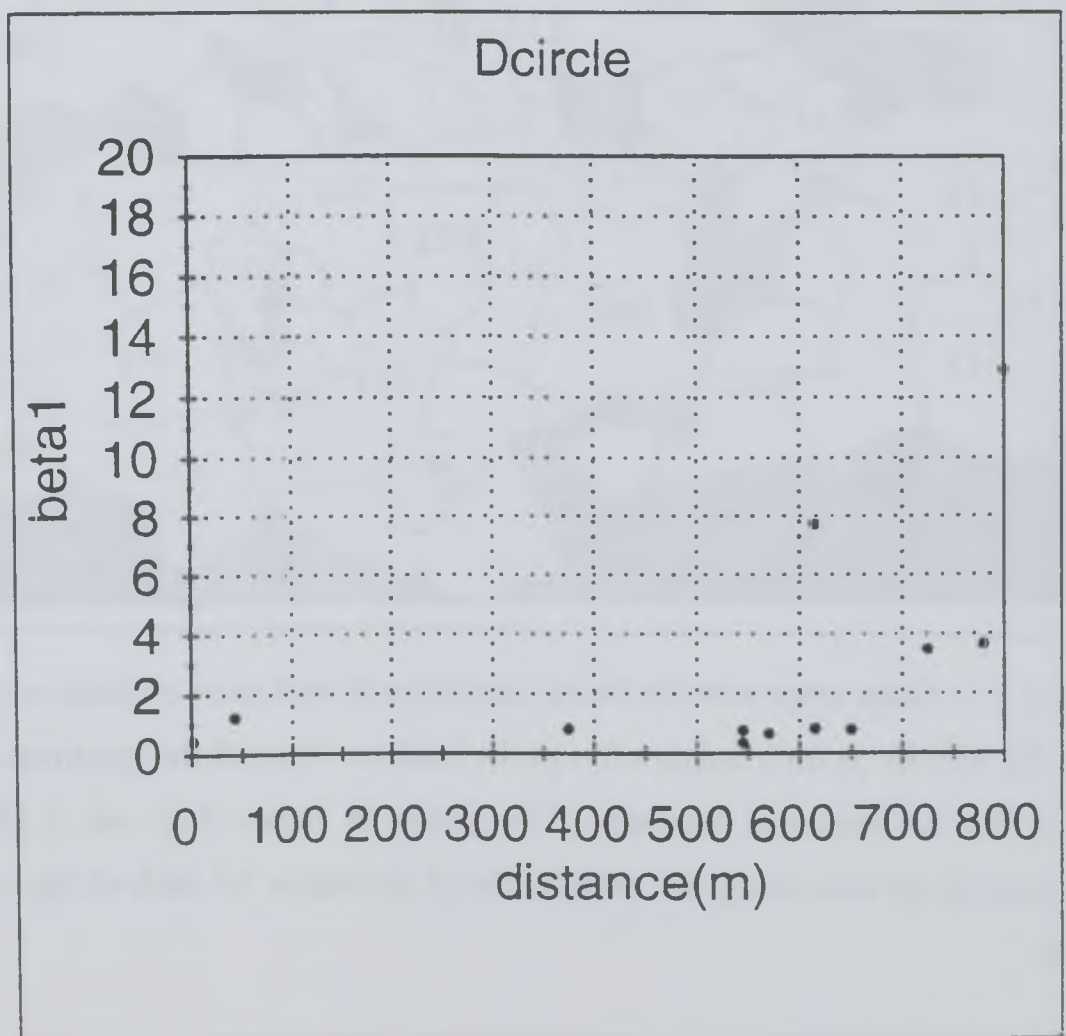
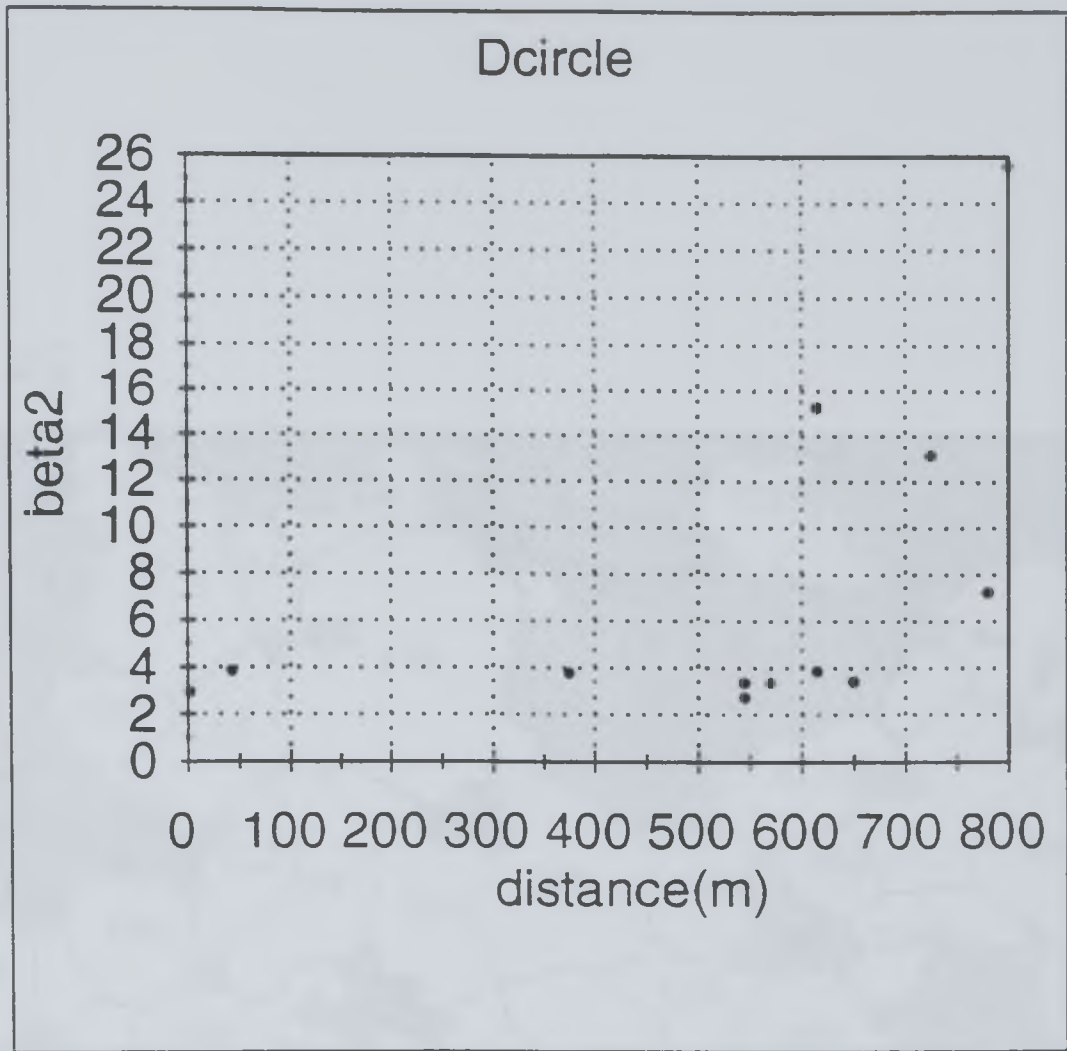


Figure 5.19 β_2 values for grain diameter distributions from a number of samples versus distance from the igneous intrusion.

Figure 5.20 β_1 values for grain diameter distributions from a number of samples versus distance from the igneous intrusion.



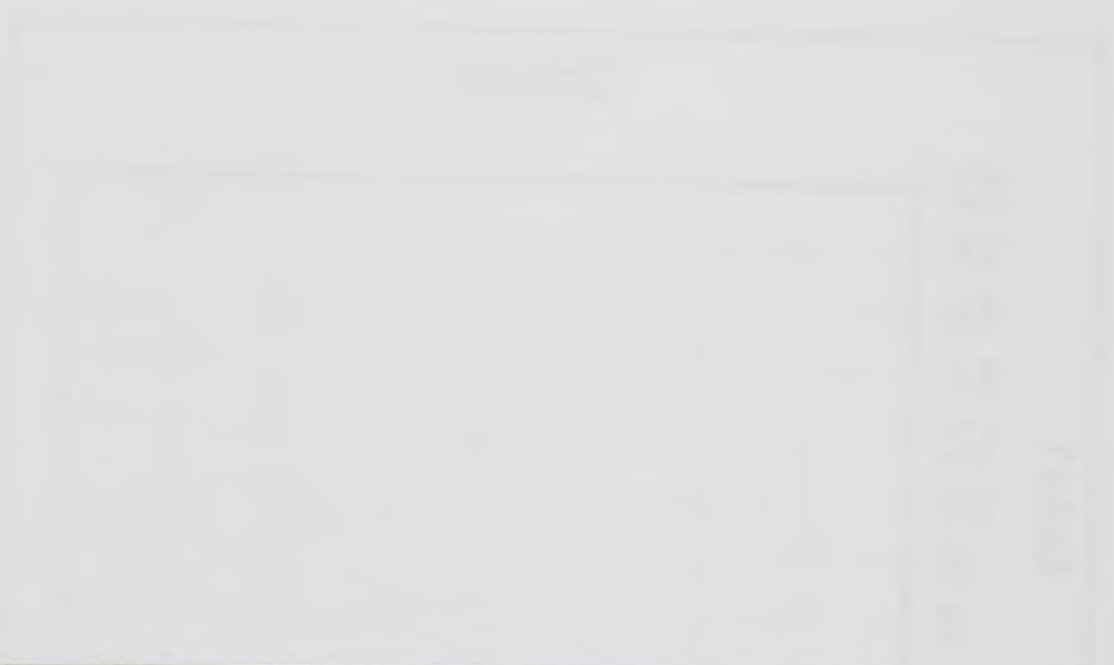
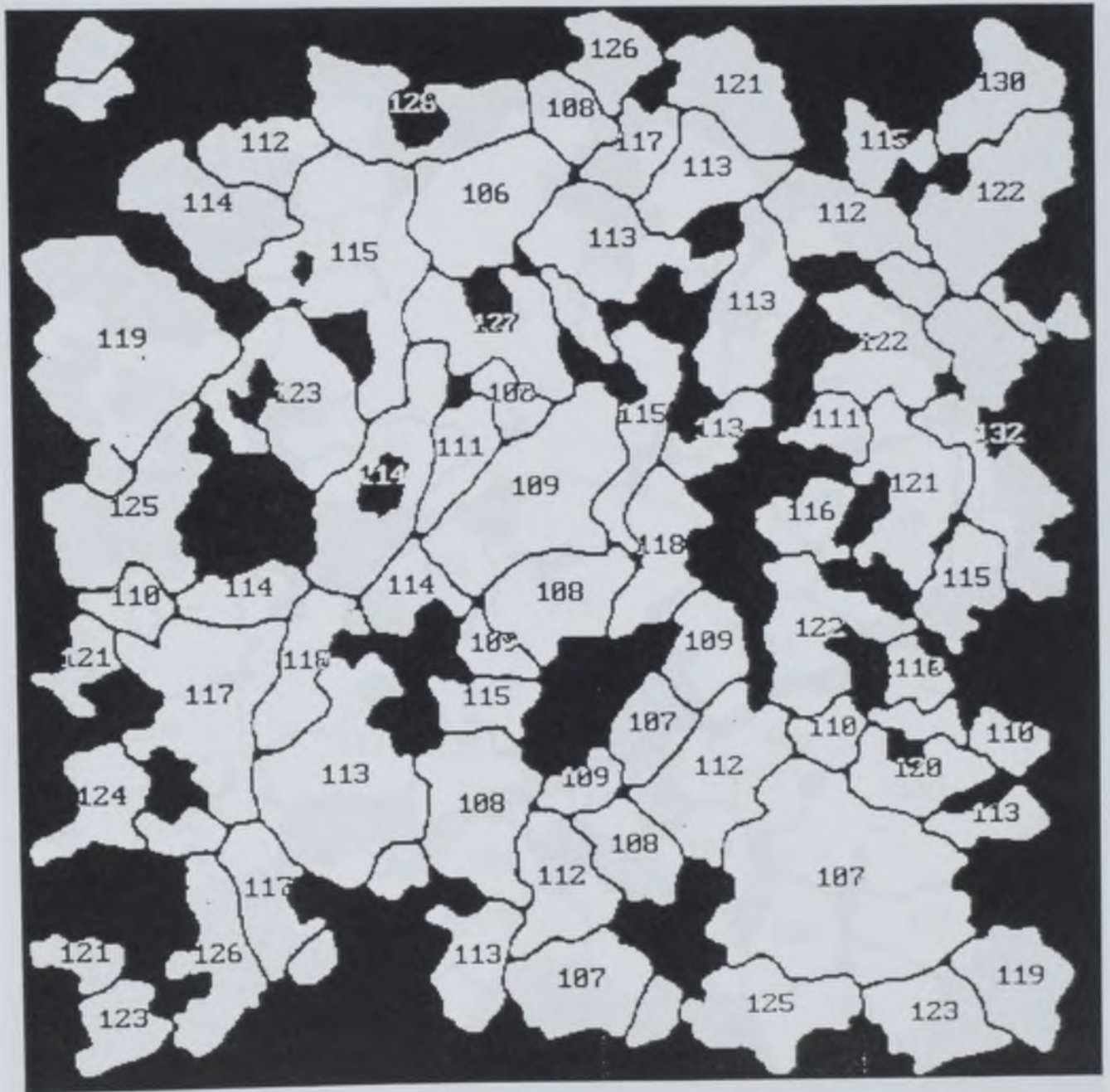


Figure 5.21 Grain maps with the fractal dimension of each grain overlain on to the image. The file number on each image refers to the final two digits of the specimen number (see Table 5.1 for specimen numbers). The graphs in Figure 5.22 and 5.23 have been constructed by calculating the average fractal dimension for each of the samples seen here.

file=49



file=78



file=60



file=55

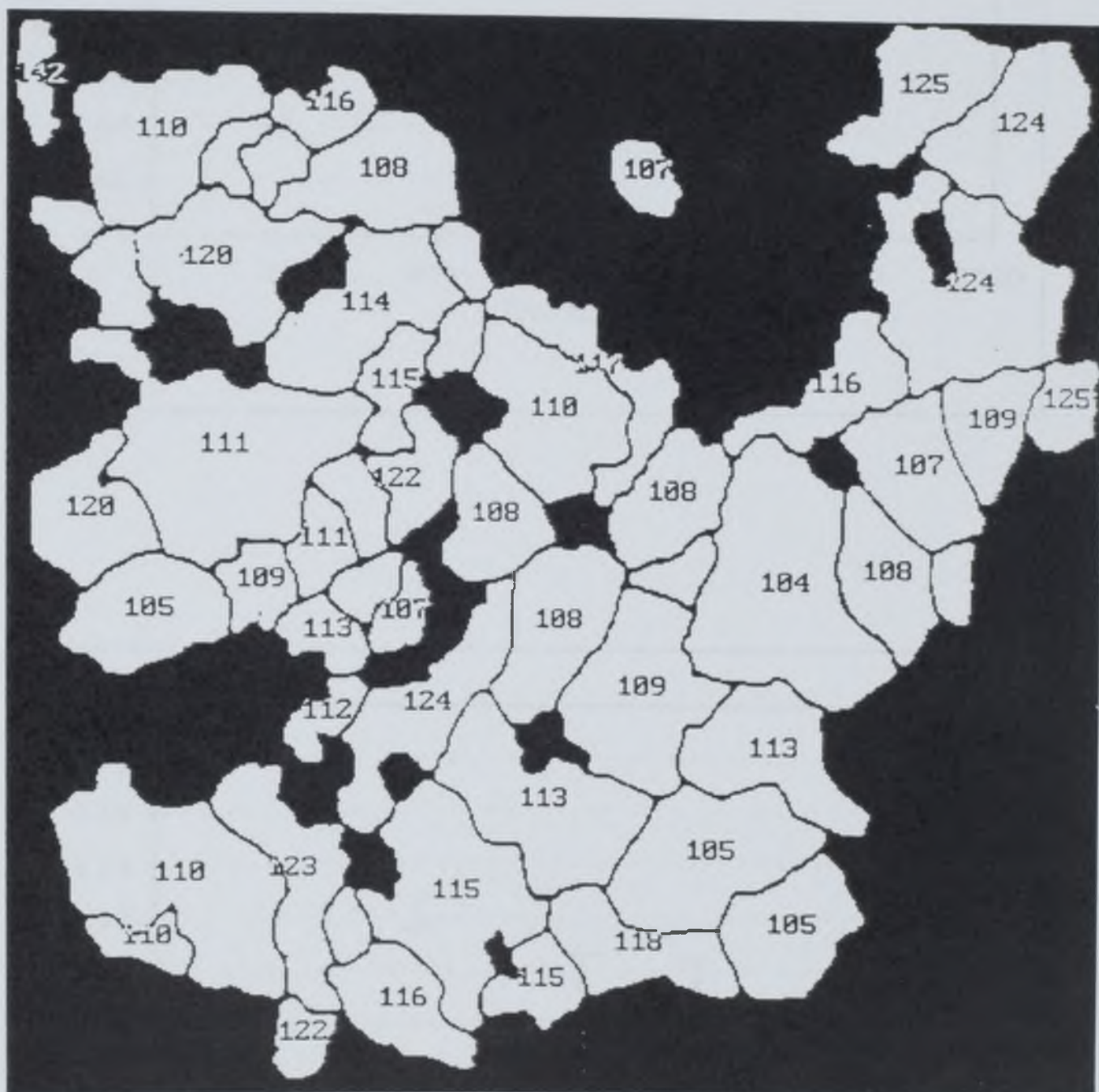
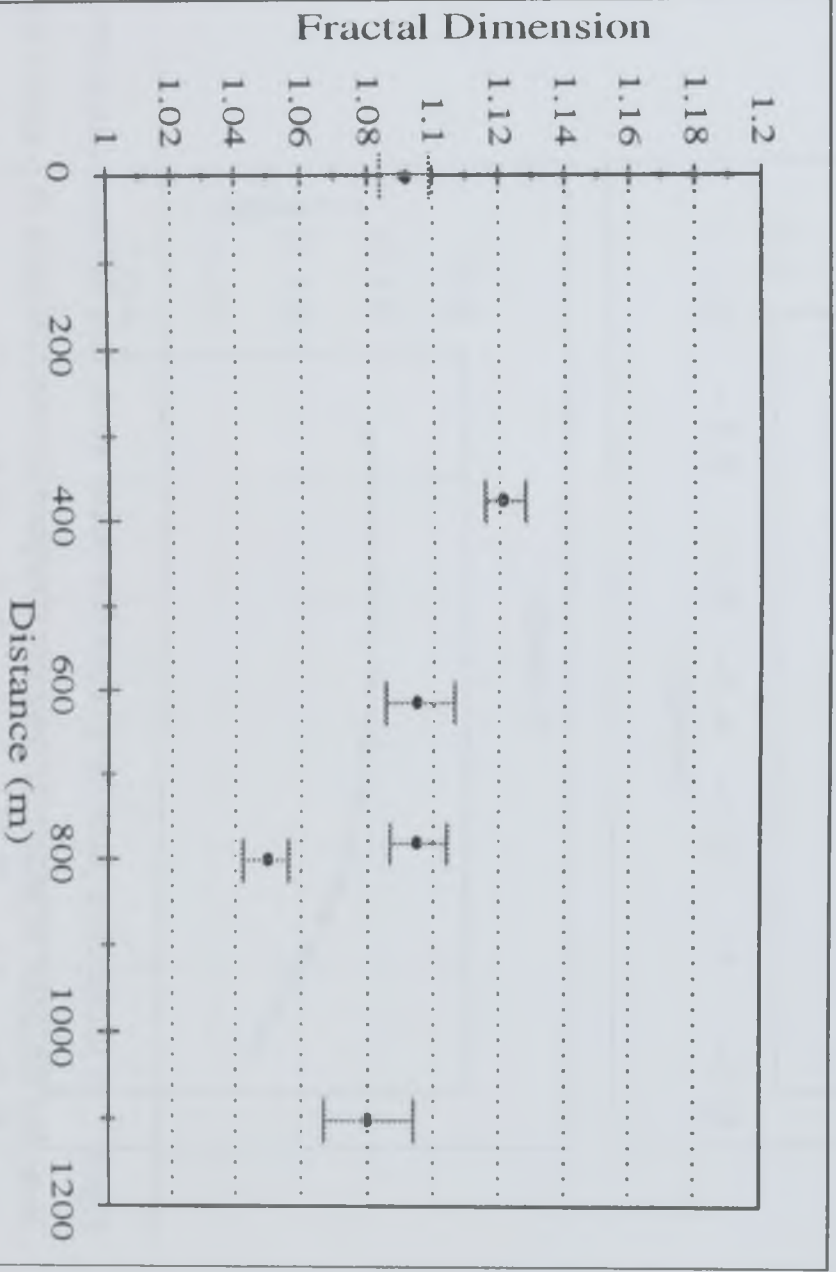
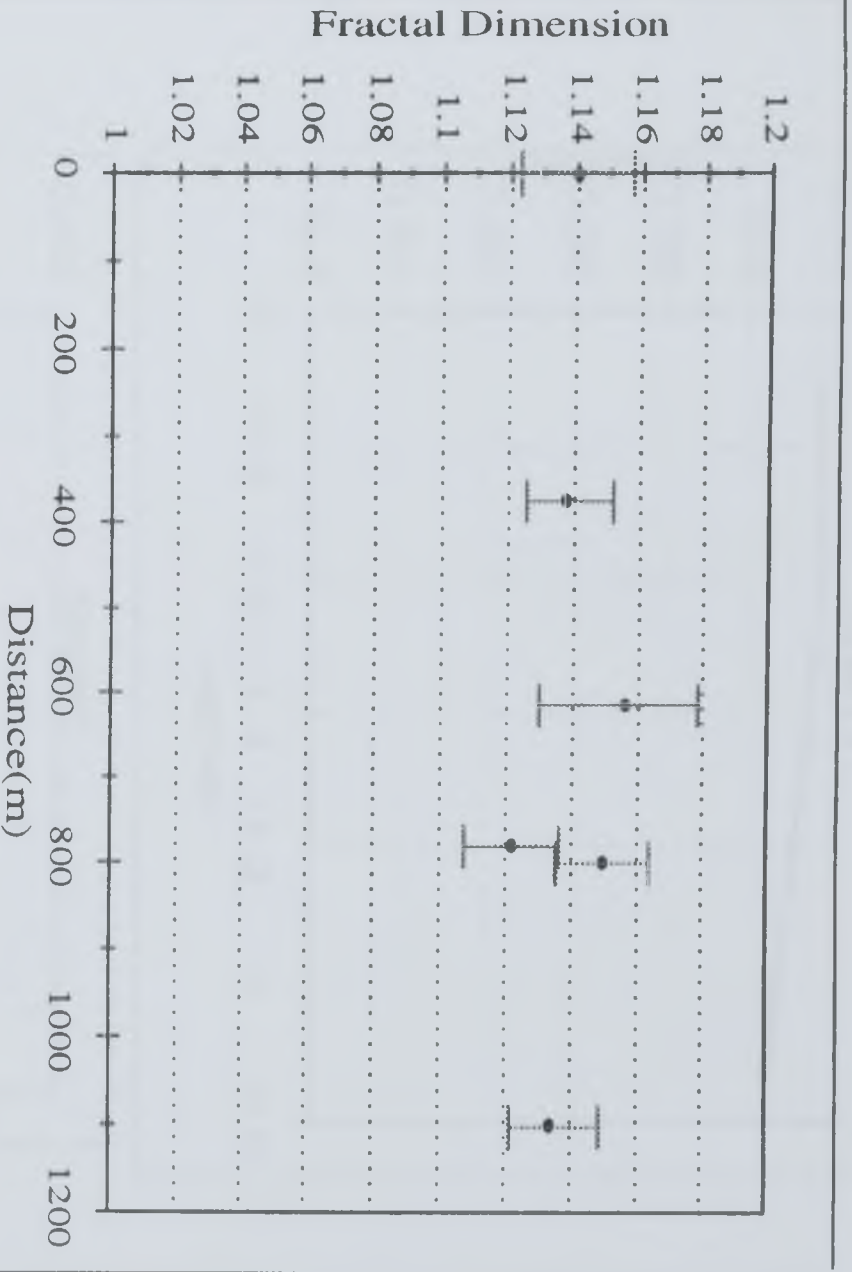




Figure 5.22 Average fractal dimension of grains within a sample versus distance from the Ballachulish intrusion.

Figure 5.23 Average fractal dimension of grains within a sample versus distance from the Ballachulish intrusion for grains which are surrounded only by quartz grains.



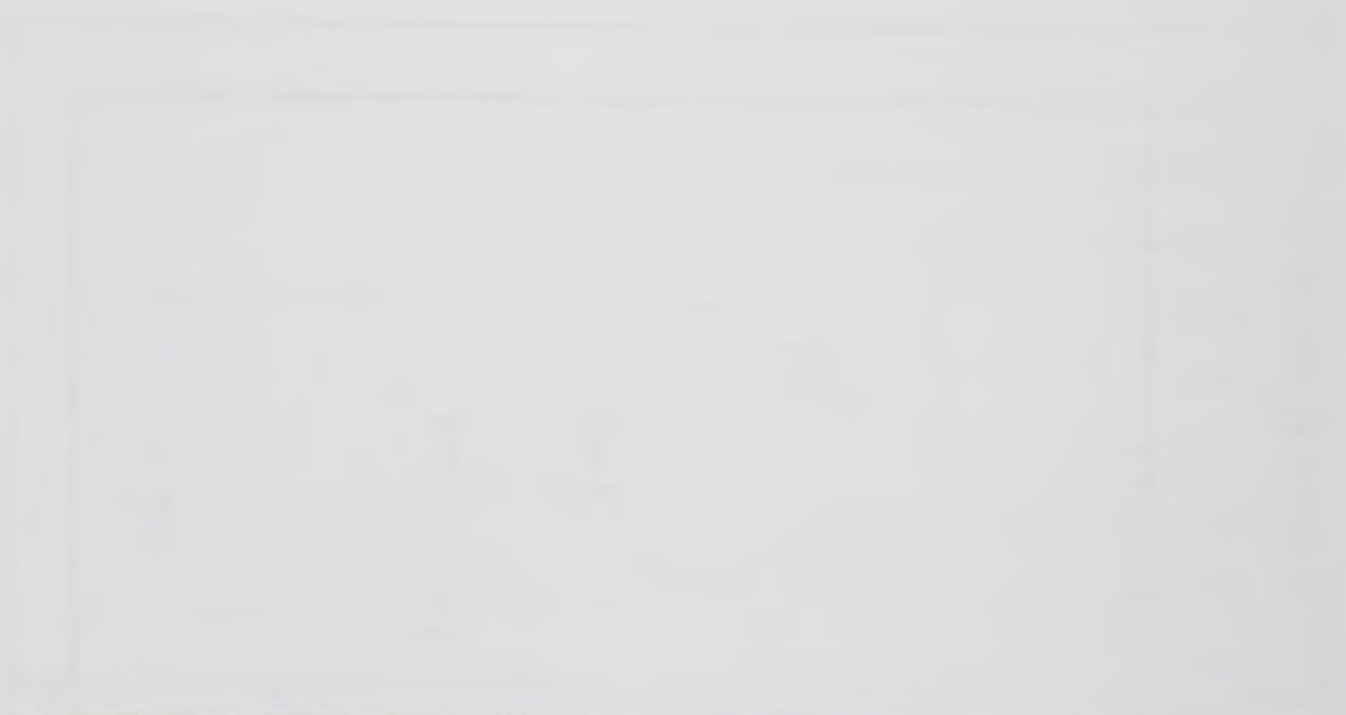
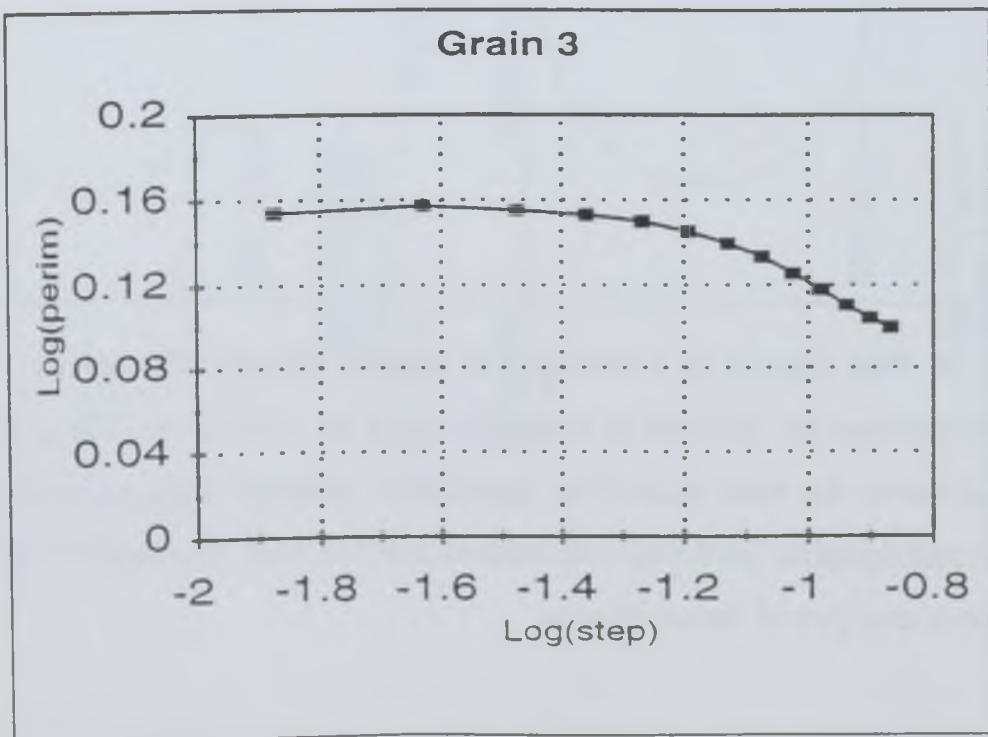
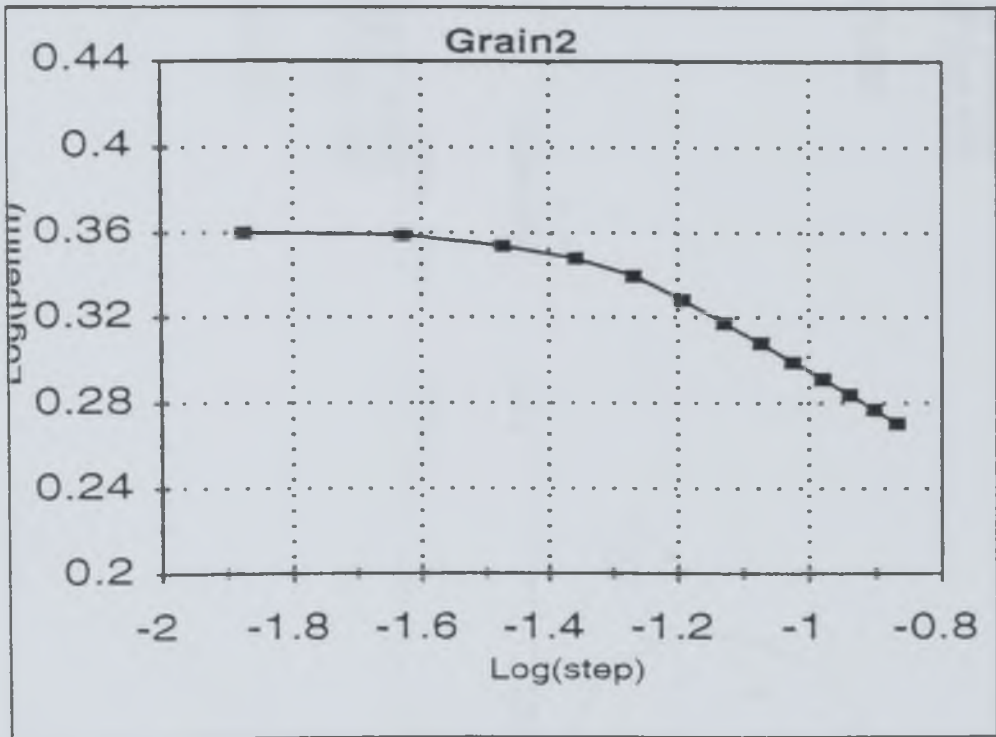
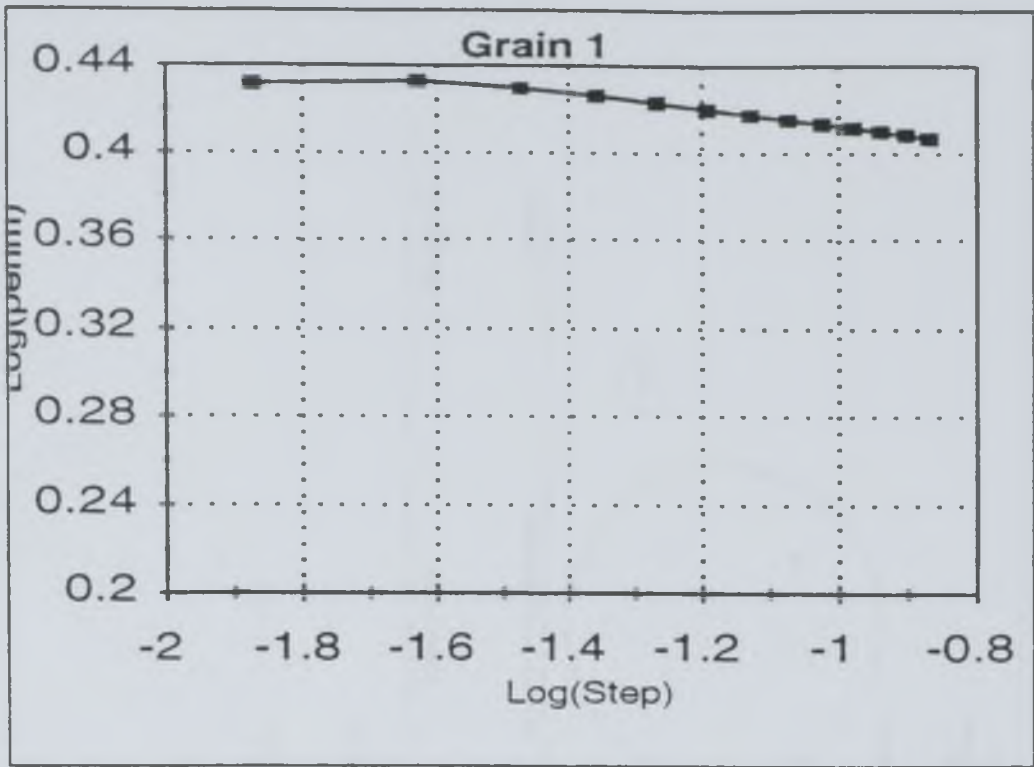
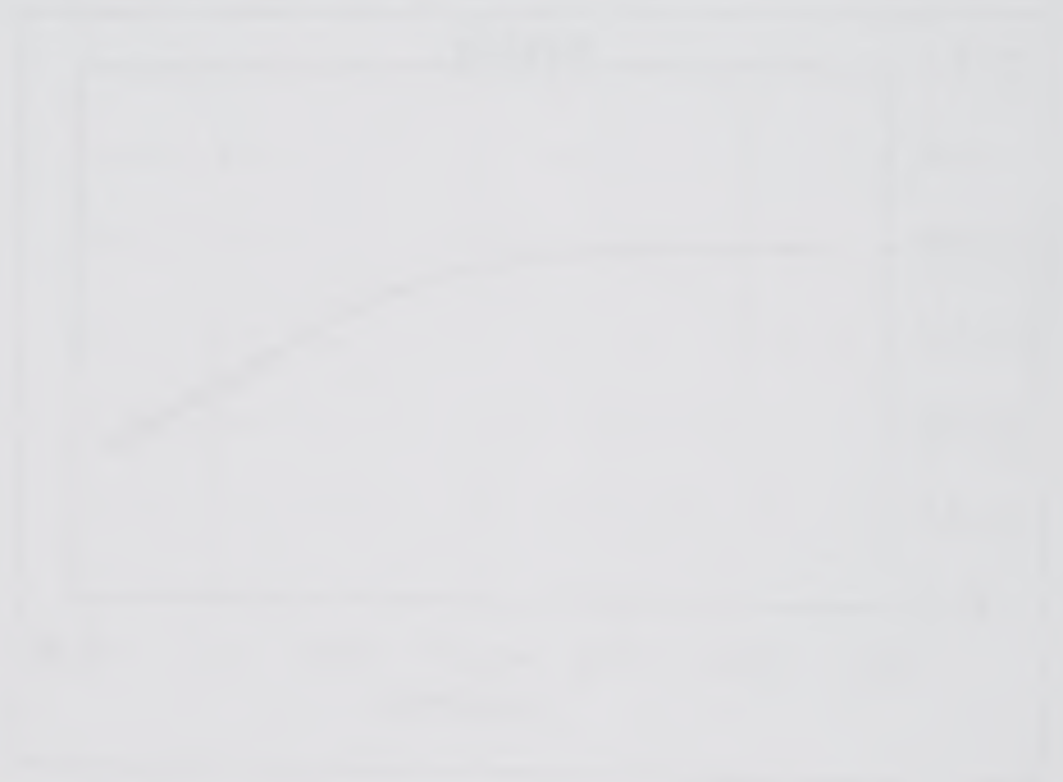


Figure 5.25 Richardson plots for a select few grains which have different characteristics. Note that the point at which the gradient changes (the inflexion point of a mixed fractal) varies from sample to sample.

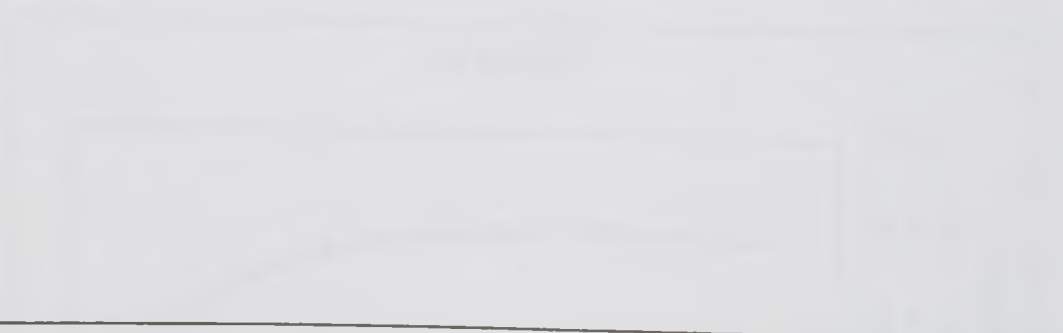




84-100



84-101



84-102

Figure 5.26 Pole figures of a selection of samples through the igneous aureole. The specimen numbers are referred to as the file name for each figure. The pole figures plot the c-axis vector for each grain in an aggregate in relation to the regional tectonic x,y,z axis. Crystallographic preferred orientations are not well developed within the Appin Quartzite in any part of the study area.

CHANNEL Texture Presentations Quartz

ID...68



Vectors = 68
Upper hemisphere

Pole Figure: (0001)
Equal Area Projection
File = N56148
Structure = Quartz
Records = 68

File= N56148 Records= 68 Groups= 1

CHANNEL Texture Presentations Quartz

ID...28



Vectors = 112
Upper hemisphere

Pole Figure: (0001)
Equal Area Projection
File = 56154
Structure = Quartz
Records = 112

File= 56154 Records= 112 Groups= 1

CHANNEL Texture Presentations Quartz

ID...51



Vectors = 86
Upper hemisphere

Pole Figure: (0001)
Equal Area Projection
File = N56149
Structure = Quartz
Records = 86

File= N56149 Records= 86 Groups= 1

CHANNEL Texture Presentations Quartz

ID...8

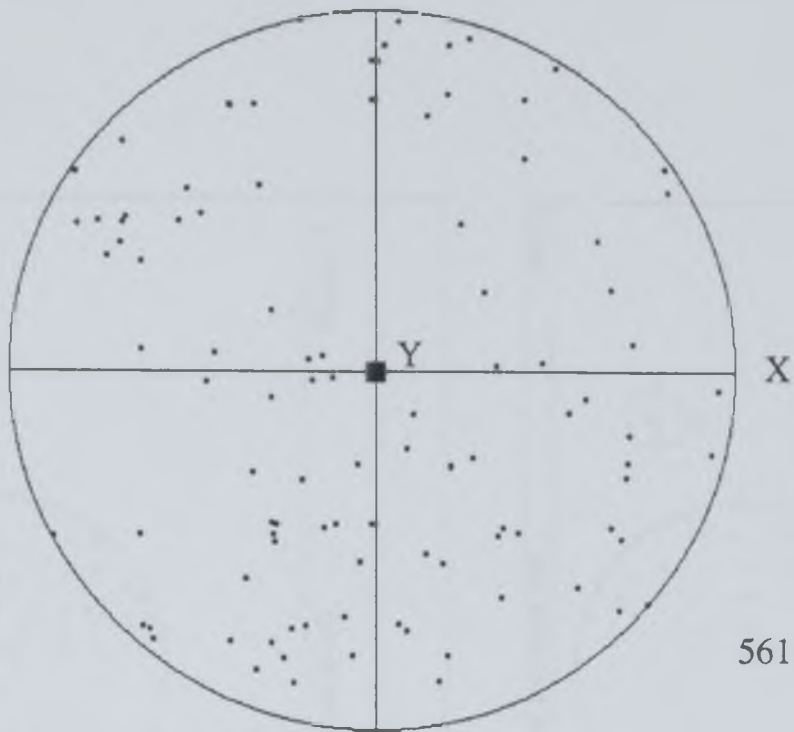


Vectors = 53
Upper hemisphere

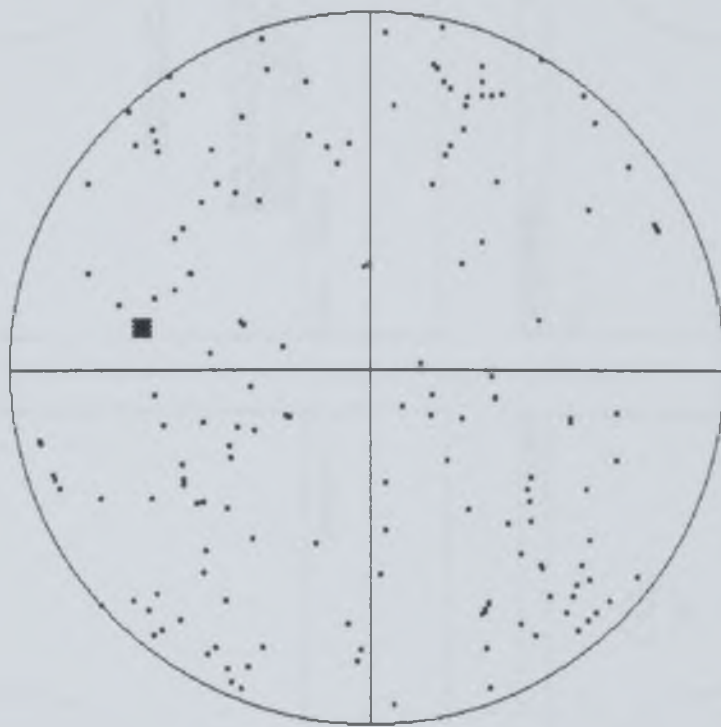
Pole Figure: (0001)
Equal Area Projection
File = 56157
Structure = Quartz
Records = 53

File= 56157 Records= 53 Groups= 1

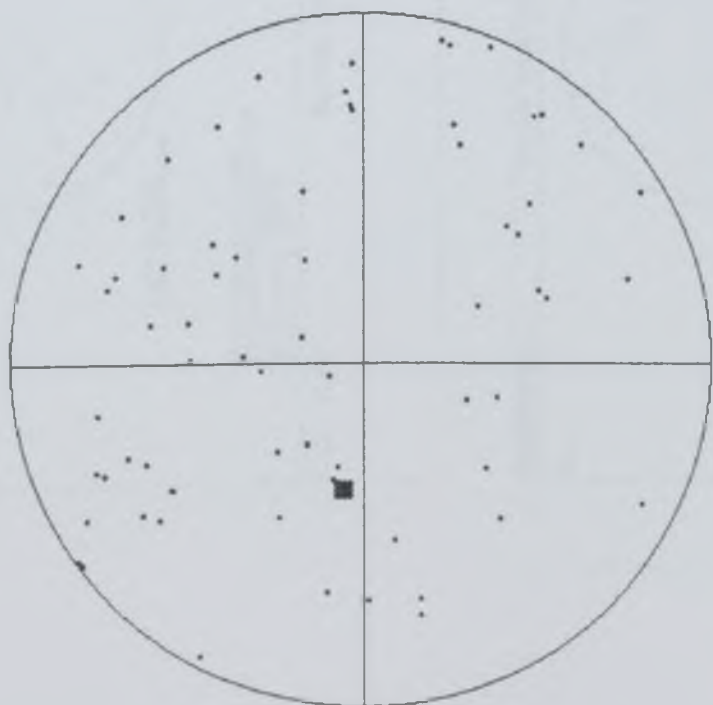
Z



56151



56169



56171

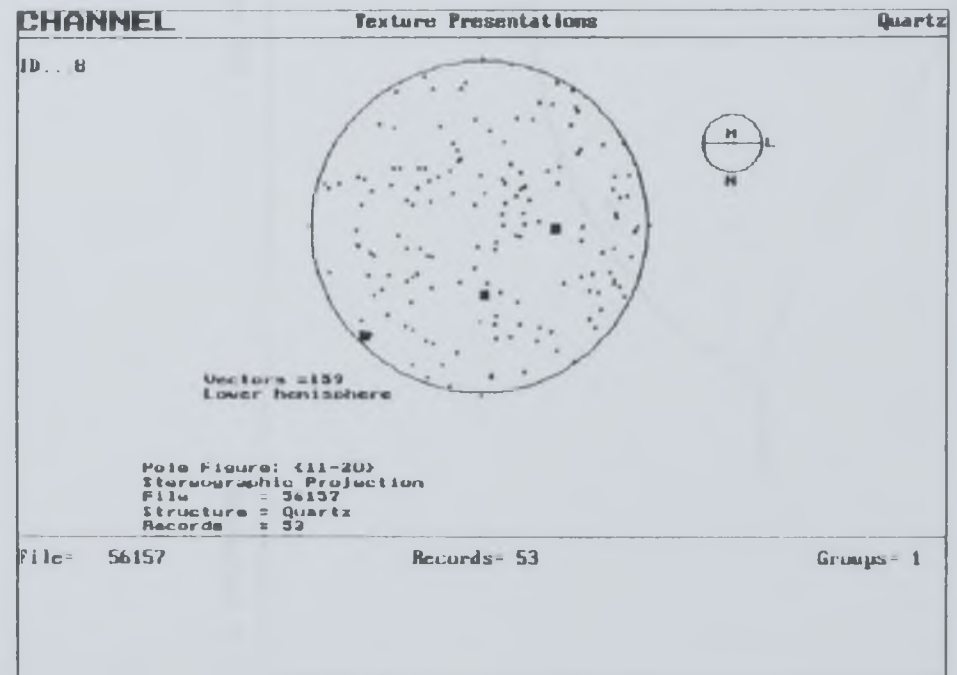
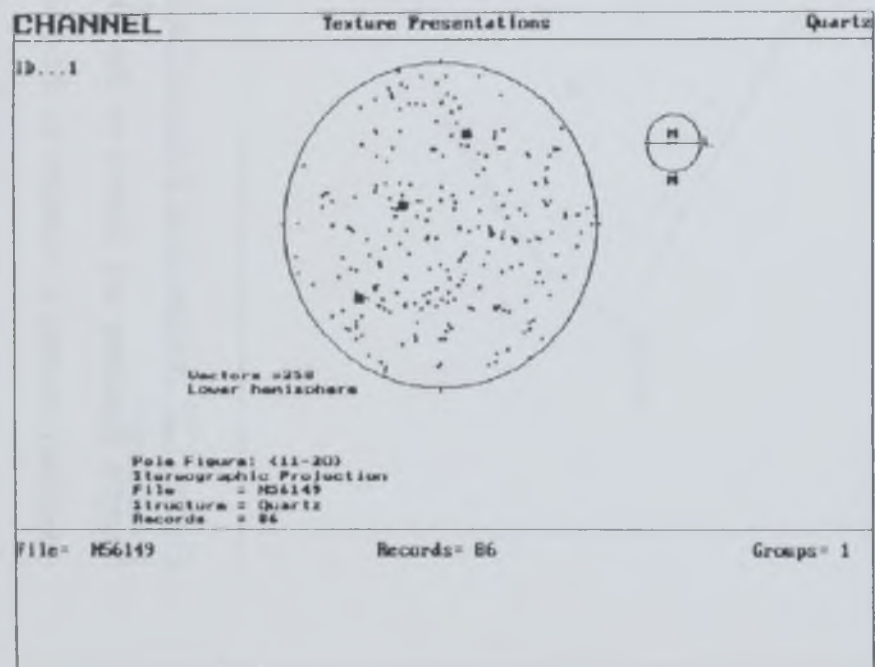
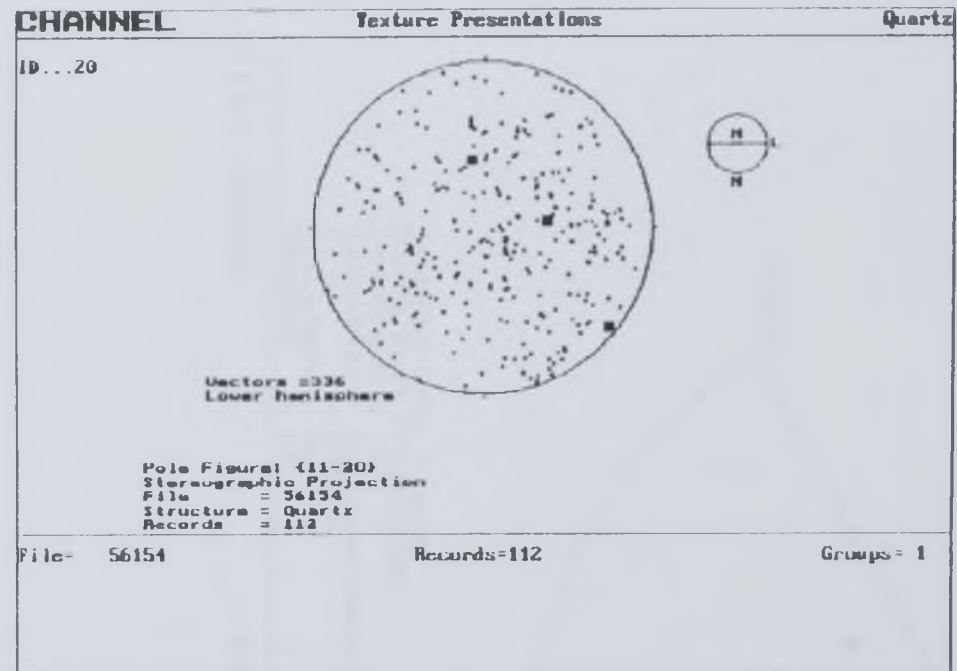
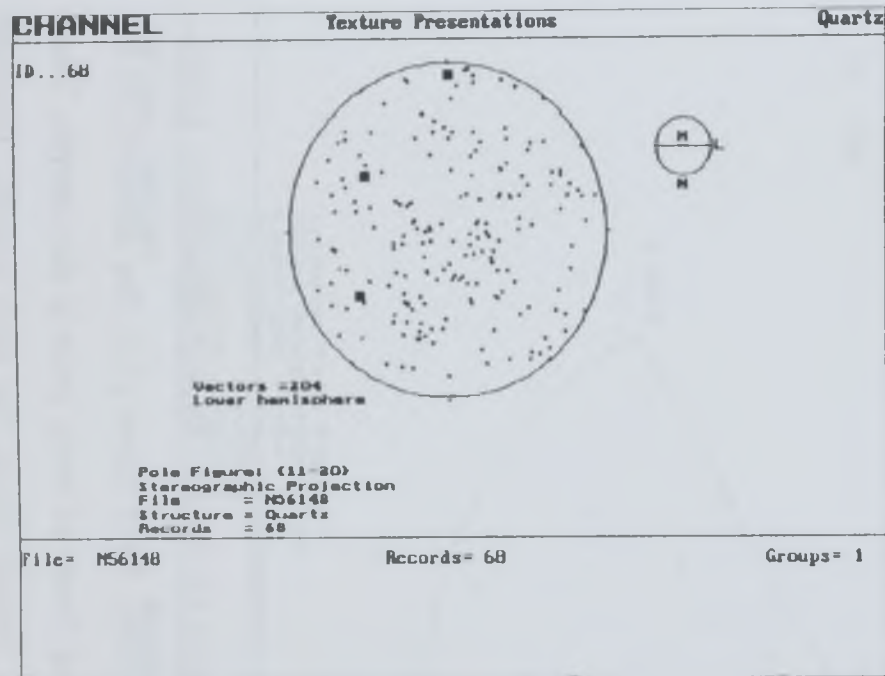


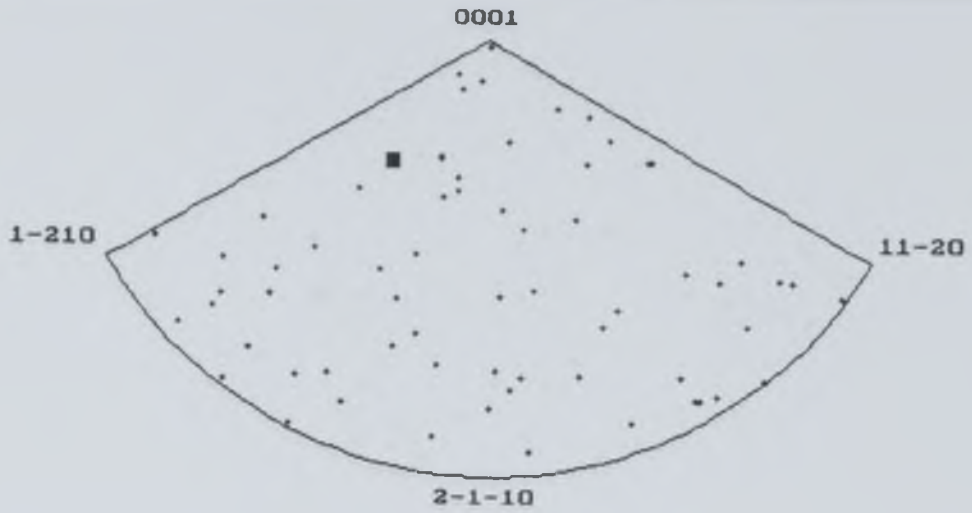
Figure 5.27 Inverse pole figures of a selection of samples through the igneous aureole. Sample numbers are shown as the file number. Each figure plots the direction of the specimen normal in relation to the reference frame of every grain in the sample. These figures depict the true three dimensional crystal texture for each sample. Preferred orientations are not well developed in this suite of rocks.

CHANNEL

Texture Presentations

Quartz

ID...68



Inverse Pole Figure
 Equal Area Projection
 LaueGroup = -3m
 Direction = Specimen normal
 File = N56148
 Structure = Quartz
 Records = 68

File= N56148

Records= 68

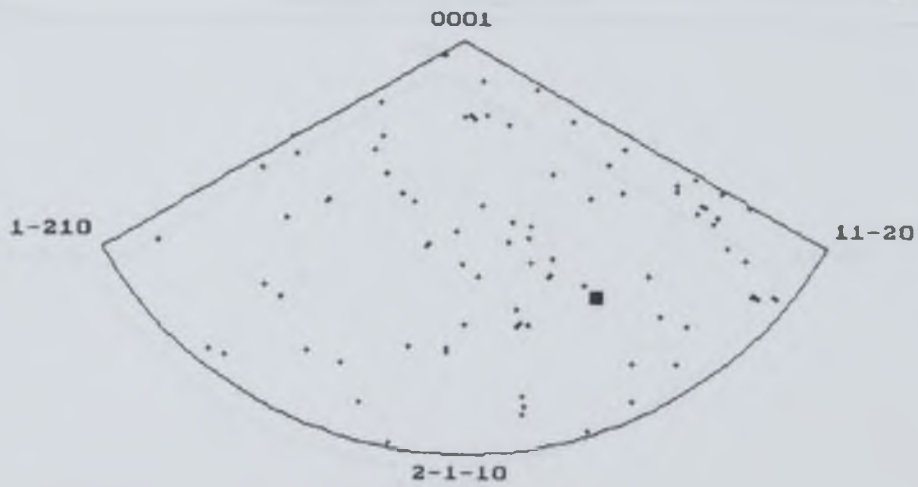
Groups= 1

CHANNEL

Texture Presentations

Quartz

ID...54



Inverse Pole Figure
 Equal Area Projection
 LaueGroup = -3m
 Direction = Specimen normal
 File = N56149
 Structure = Quartz
 Records = 86

File= N56149

Records= 86

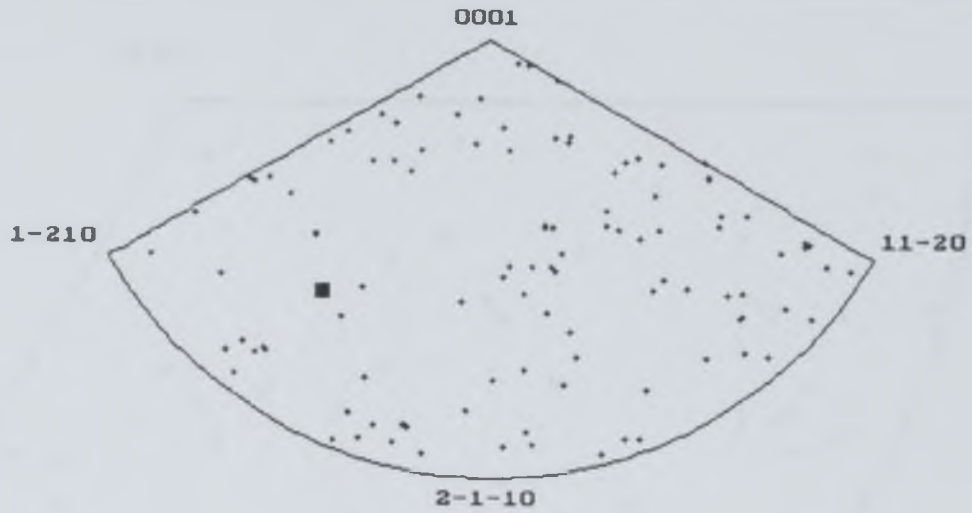
Groups= 1

CHANNEL

Texture Presentations

Quartz

ID...20



Inverse Pole Figure
Equal Area Projection
LaueGroup = -3m
Direction = Specimen normal
File = 56154
Structure = Quartz
Records = 112

File= 56154

Records=112

Groups= 1

CHANNEL

Texture Presentations

Quartz

ID...8



Inverse Pole Figure
Equal Area Projection
LaueGroup = -3m
Direction = Specimen normal
File = 56157
Structure = Quartz
Records = 53

File= 56157

Records= 53

Groups= 1

56151

0001

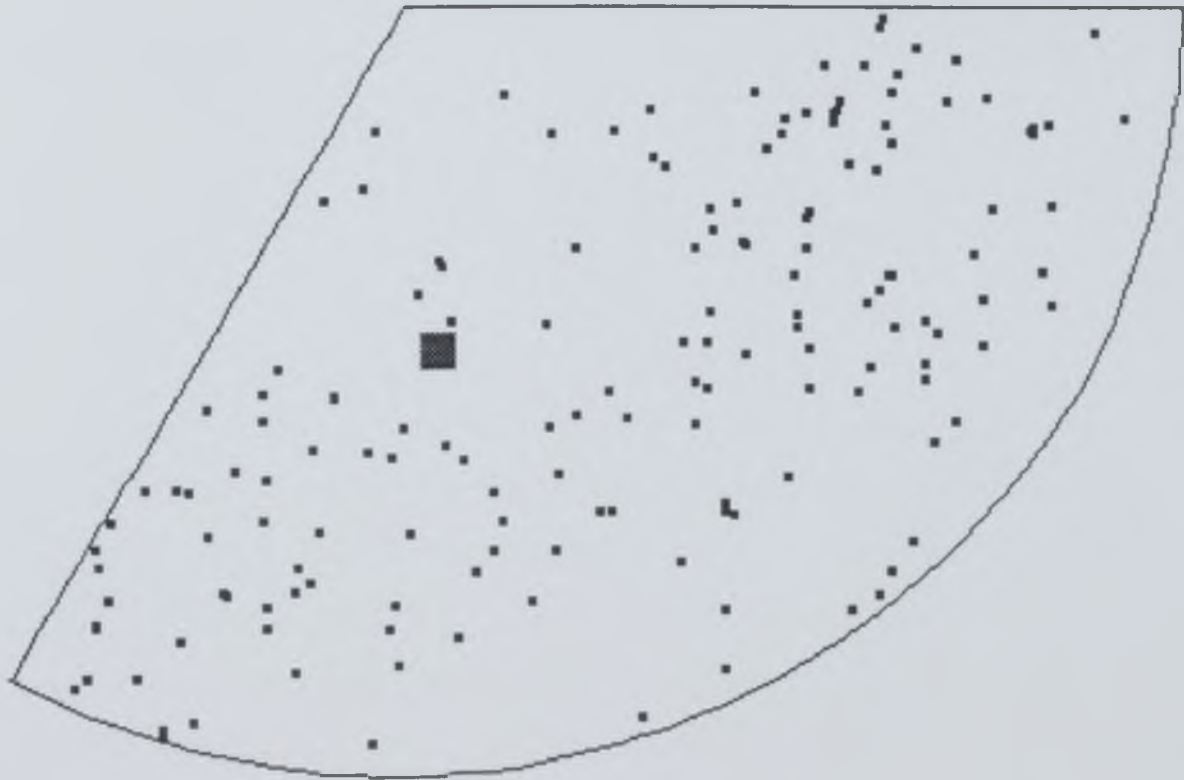
11-20

1-210

2-1-10



56169



56171

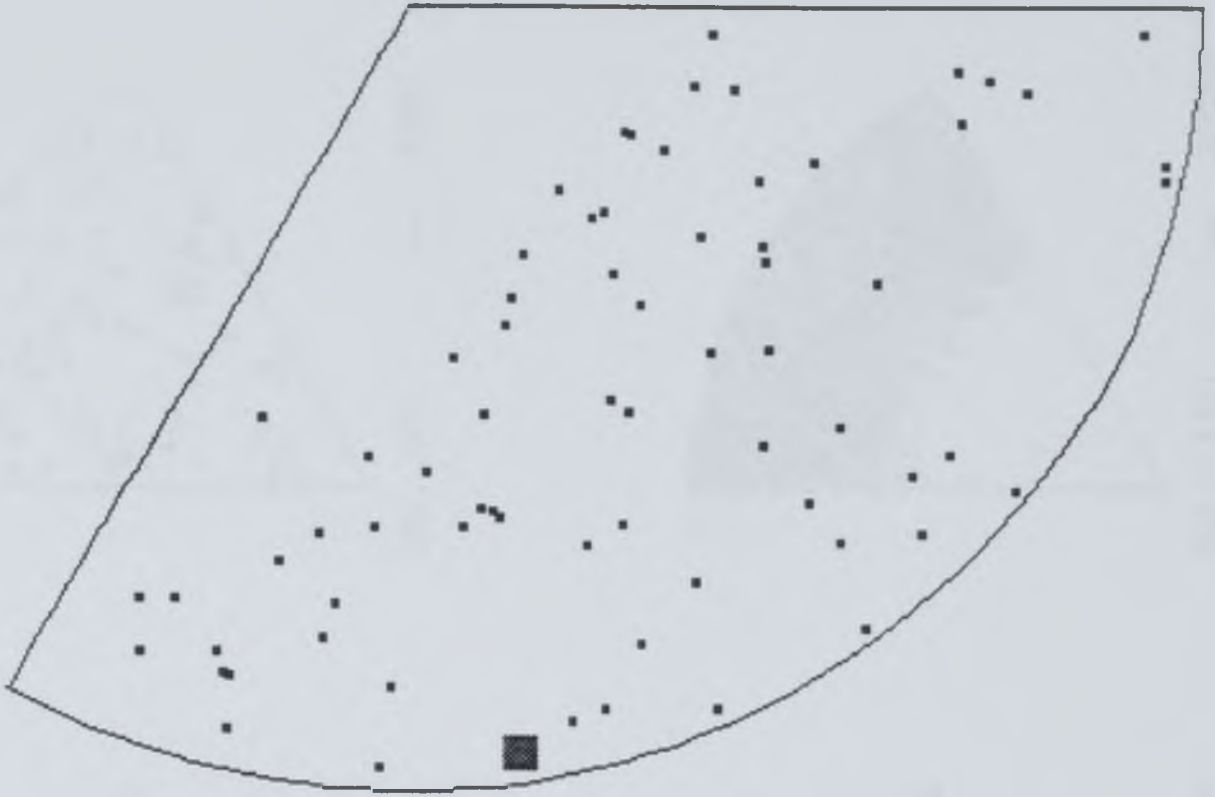
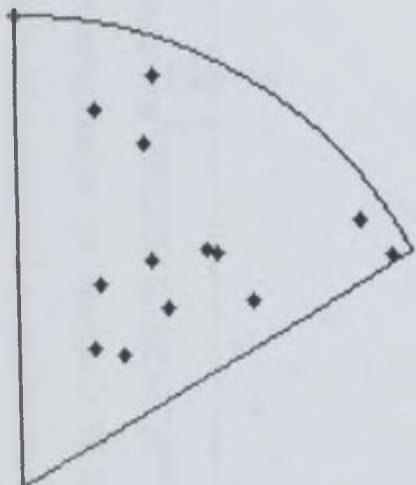




Figure 5.28 Inverse pole figure (misorientation diagrams) for sample 56154. The range of angles of misorientations plotted on each diagram is shown in the bottom left and the number of measurement in the bottom right. Note the clustering of data towards the edge of the stereonets in the diagrams representing misorientations of high magnitudes. This is a consequence of taking the lowest magnitude misorientation solutions together with quartz crystal symmetry. Crystallographic analysis of other samples reveals similar trends of the data.

File=54



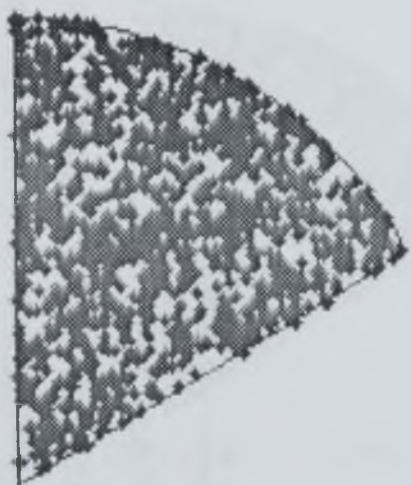
1..3 n= 14



4..10 n= 25



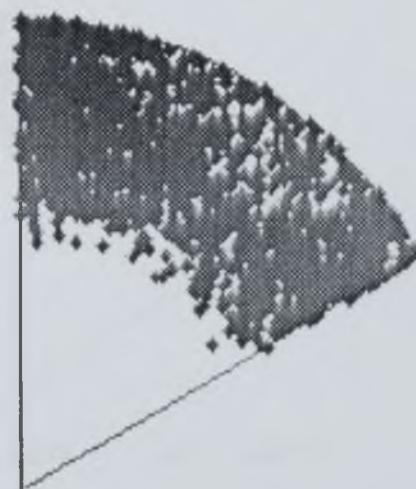
10..20 n= 135



20..56 n= 1671



57..63 n= 617

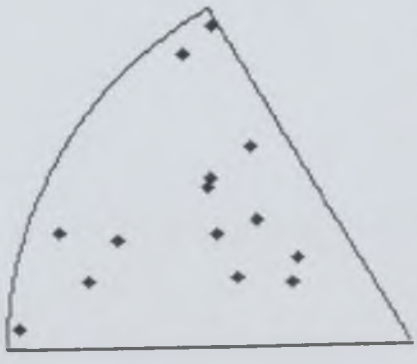


63..110 n= 3750



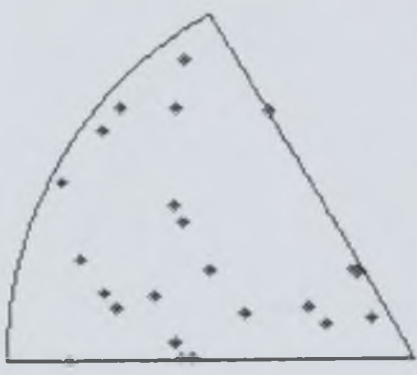
Figure 5.29 Misorientation plot from sample 56154. The angles of rotation are more clustered on this diagram in comparison with Figure 5.26. Compare the misorientation pole figure in the bottom right hand corner to the equivalent diagram in Figure 5.26. The greater degree of clustering is a consequence of quartz symmetry and has no microtextural implications.

file=54



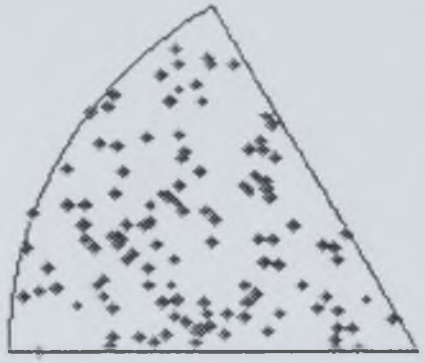
1..3

n= 14



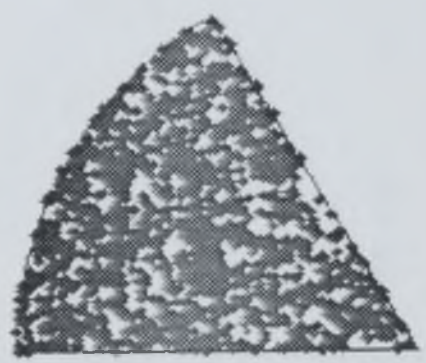
4..10

n= 25



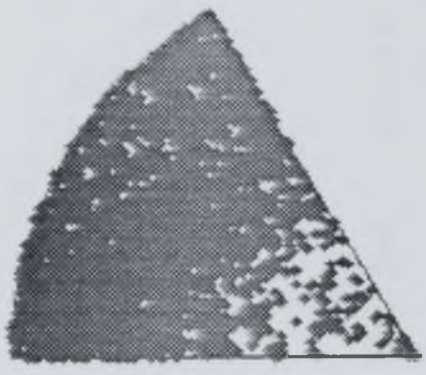
10..20

n= 135



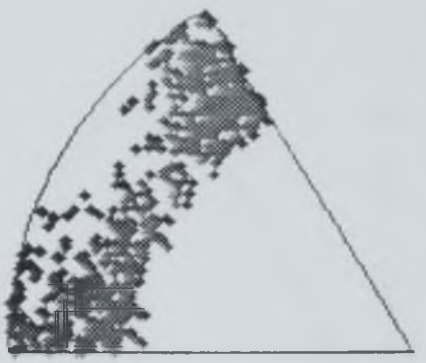
20..56

n= 1671



57..90

n= 3693

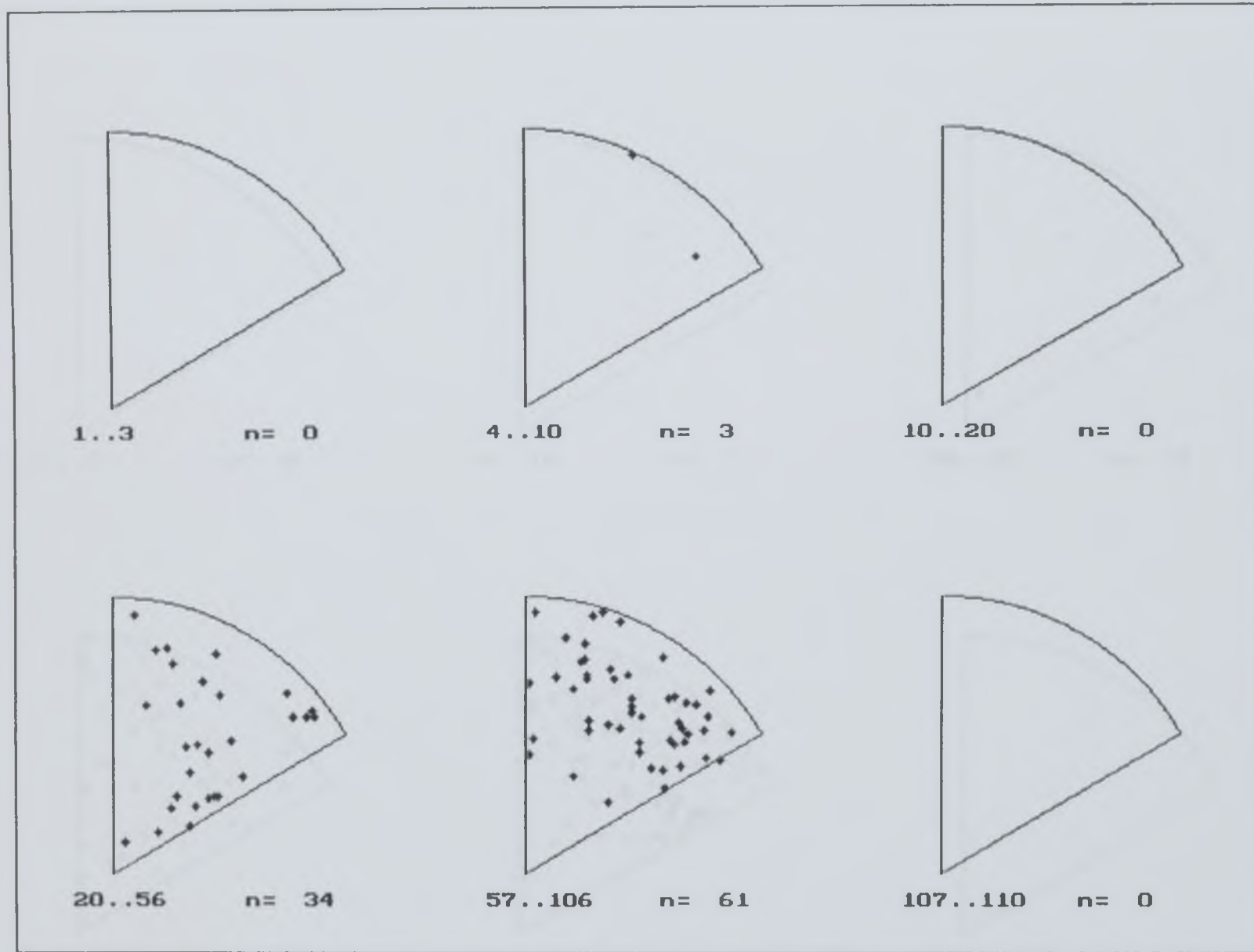


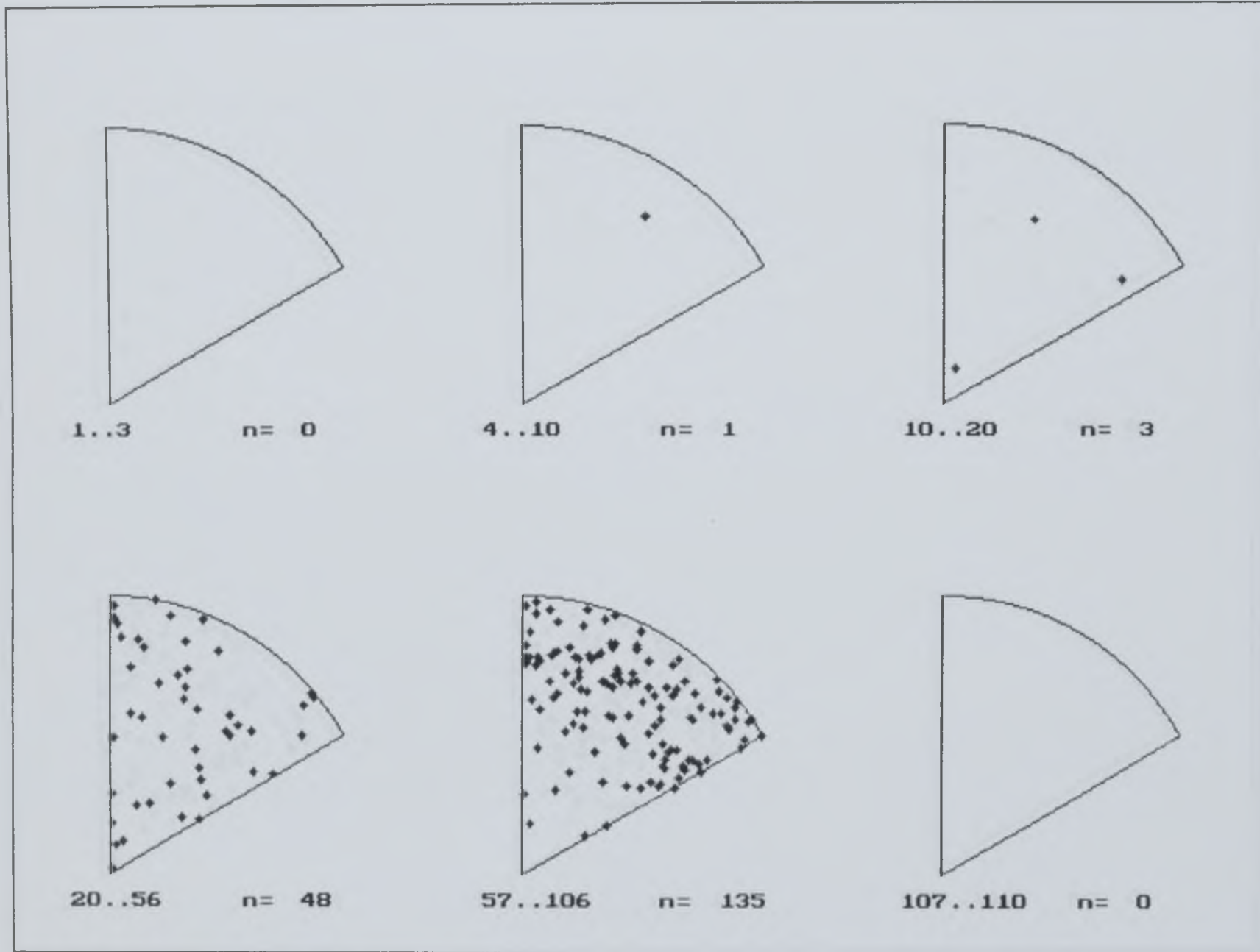
91..110

n= 674



Figure 5.30 Misorientation diagrams for a selection of samples through the Ballachulish aureole. The diagrams plot misorientations of neighbouring grains, in order to investigate only the local mesotexture.





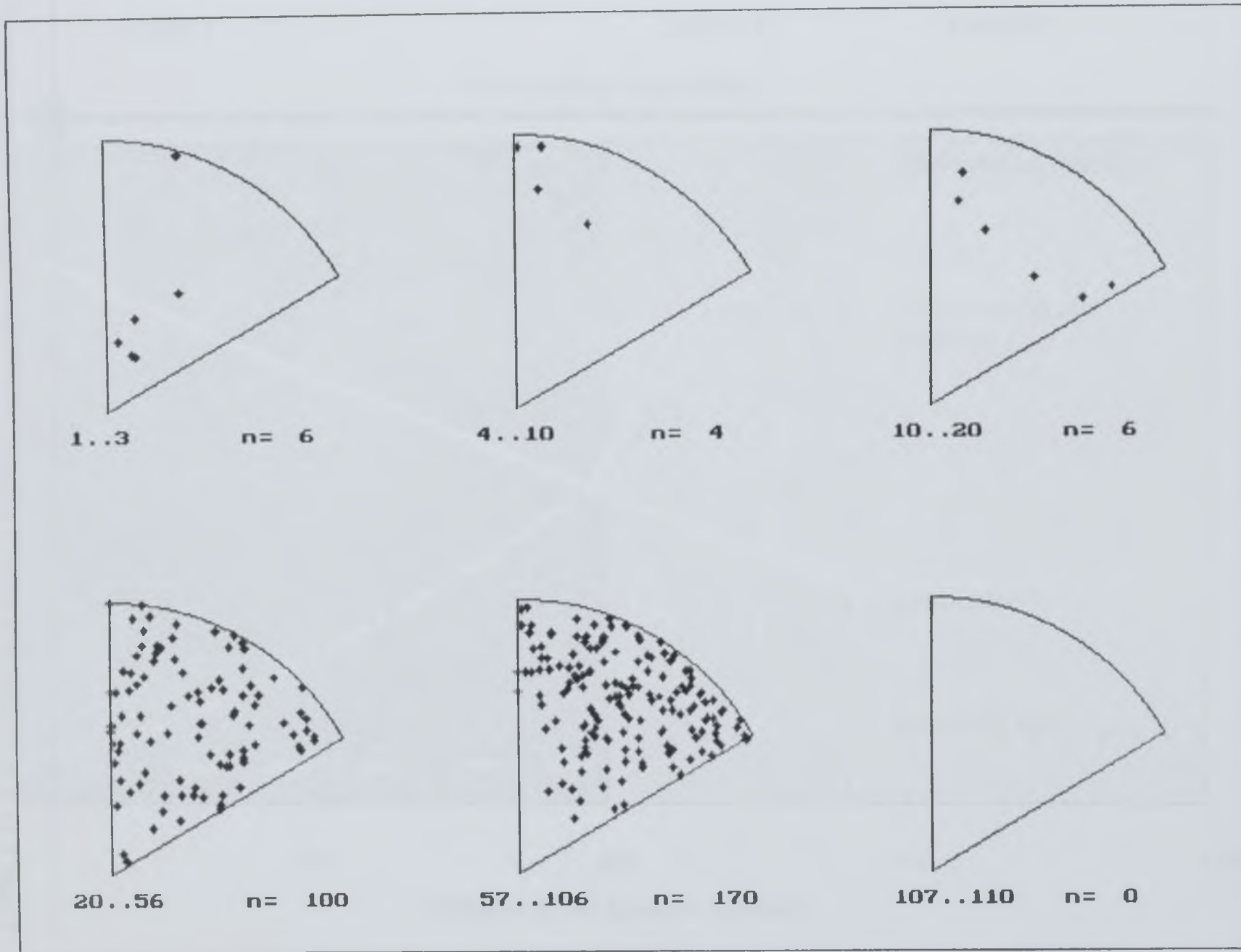
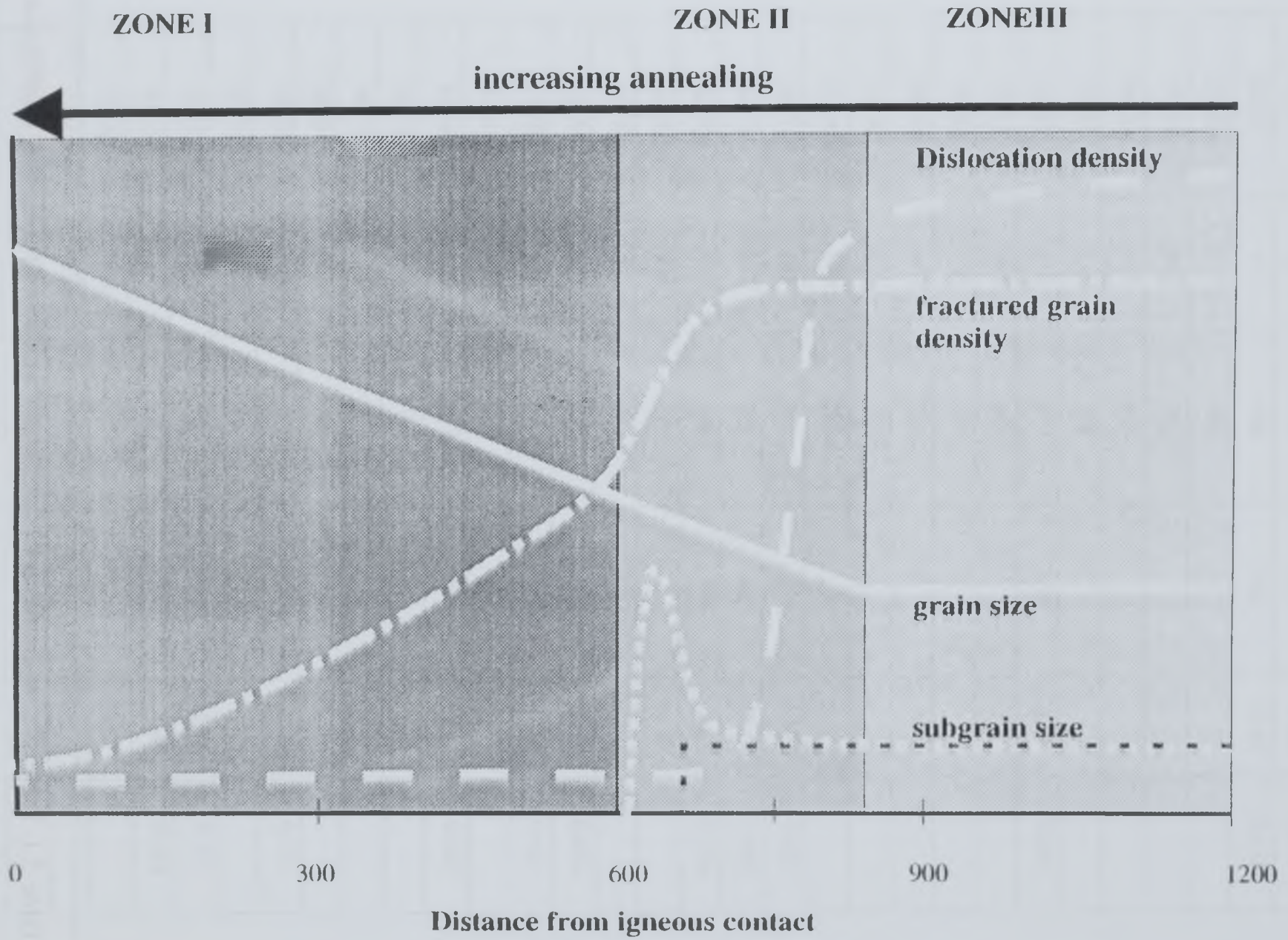




Figure 5.31 A microstructural stability diagram, schematically presents the proportions of different microstructural elements through the Ballachulish aureole. Grain size gradually increases, dislocation densities plummet at the edge of the aureole, subgrain size increases between 700m and 600m, before subgrains are annihilated.



Faint, illegible table content, likely containing specimen data, grain size, and proportions.

Table 5.1 Table of specimens used for statistical analysis during this investigation, together with grain size data, proportions of feldspar and average shape circularity factors for each sample.

Sample Number	Distance from intrusion (m)	Grain Size (linear intercept) μm	Grain Size (image analysis) μm	% Feldspar	Fcircle
56148	2	410	367	8.32	0.623
56151	43	408	362	10.67	0.658
56165	215	440			
56158	260	283			
56183	325	480			
56184	355	358			
56149	375	377	319	6.01	0.659
56185	395	407			
56186	430	267			
56187	450	256			
56170	490	313			
56369	520	270			
56171	545	301	224	10.96	0.605
56179	540	263	250	11.54	0.693
56180	570	408	385	9.87	0.706
56163	575	273			
56174	595	253			
56154	615	156	303	4.01	0.664
56178	615	222	233	13.08	0.651
56173	645	222			
56169	650	273	229	10.33	0.688
56172	665	181			
56175	700	227			
56166	720	125			
56177	725	170	193	20.76	0.731
56176	745	167			
56157	780	186	41.13	1.96	0.571
56160	800	227	282	4.46	0.484
56168	875	196			
56167	900	181			
56164	975	208			
56161	985	186			
56159	1160	222			
56155	1300	220	234	9.48	0.635

Sample No.	Grain Size (mm)	Shape Factor	Moment Ratio
1	0.075	0.5	0.1
2	0.15	0.6	0.2
3	0.3	0.7	0.3
4	0.6	0.8	0.4
5	1.2	0.9	0.5
6	2.5	1.0	0.6
7	5.0	1.1	0.7
8	10.0	1.2	0.8
9	20.0	1.3	0.9
10	40.0	1.4	1.0
11	80.0	1.5	1.1
12	150.0	1.6	1.2
13	300.0	1.7	1.3
14	600.0	1.8	1.4
15	1200.0	1.9	1.5
16	2400.0	2.0	1.6
17	4800.0	2.1	1.7
18	9600.0	2.2	1.8
19	19200.0	2.3	1.9
20	38400.0	2.4	2.0
21	76800.0	2.5	2.1
22	153600.0	2.6	2.2
23	307200.0	2.7	2.3
24	614400.0	2.8	2.4
25	1228800.0	2.9	2.5
26	2457600.0	3.0	2.6
27	4915200.0	3.1	2.7
28	9830400.0	3.2	2.8
29	19660800.0	3.3	2.9
30	39321600.0	3.4	3.0
31	78643200.0	3.5	3.1
32	157286400.0	3.6	3.2
33	314572800.0	3.7	3.3
34	629145600.0	3.8	3.4
35	1258291200.0	3.9	3.5
36	2516582400.0	4.0	3.6
37	5033164800.0	4.1	3.7
38	10066329600.0	4.2	3.8
39	20132659200.0	4.3	3.9
40	40265318400.0	4.4	4.0
41	80530636800.0	4.5	4.1
42	161061273600.0	4.6	4.2
43	322122547200.0	4.7	4.3
44	644245094400.0	4.8	4.4
45	1288490188800.0	4.9	4.5
46	2576980377600.0	5.0	4.6
47	5153960755200.0	5.1	4.7
48	10307921510400.0	5.2	4.8
49	20615843020800.0	5.3	4.9
50	41231686041600.0	5.4	5.0
51	82463372083200.0	5.5	5.1
52	164926744166400.0	5.6	5.2
53	329853488332800.0	5.7	5.3
54	659706976665600.0	5.8	5.4
55	1319413953331200.0	5.9	5.5
56	2638827906662400.0	6.0	5.6
57	5277655813324800.0	6.1	5.7
58	10555311626649600.0	6.2	5.8
59	21110623253299200.0	6.3	5.9
60	42221246506598400.0	6.4	6.0
61	84442493013196800.0	6.5	6.1
62	168884986026393600.0	6.6	6.2
63	337769972052787200.0	6.7	6.3
64	675539944105574400.0	6.8	6.4
65	1351079888211148800.0	6.9	6.5
66	2702159776422297600.0	7.0	6.6
67	5404319552844595200.0	7.1	6.7
68	10808639105689190400.0	7.2	6.8
69	21617278211378380800.0	7.3	6.9
70	43234556422756761600.0	7.4	7.0
71	86469112845513523200.0	7.5	7.1
72	172938225691027046400.0	7.6	7.2
73	345876451382054092800.0	7.7	7.3
74	691752902764108185600.0	7.8	7.4
75	1383505805528216371200.0	7.9	7.5
76	2767011611056432742400.0	8.0	7.6
77	5534023222112865484800.0	8.1	7.7
78	11068046444225730969600.0	8.2	7.8
79	22136092888451461939200.0	8.3	7.9
80	44272185776902923878400.0	8.4	8.0
81	88544371553805847756800.0	8.5	8.1
82	177088743107611695513600.0	8.6	8.2
83	354177486215223391027200.0	8.7	8.3
84	708354972430446782054400.0	8.8	8.4
85	1416709944860893564108800.0	8.9	8.5
86	2833419889721787128217600.0	9.0	8.6
87	5666839779443574256435200.0	9.1	8.7
88	11333679558887148512870400.0	9.2	8.8
89	22667359117774297025740800.0	9.3	8.9
90	45334718235548594051481600.0	9.4	9.0
91	90669436471097188102963200.0	9.5	9.1
92	181338872942194376205926400.0	9.6	9.2
93	362677745884388752411852800.0	9.7	9.3
94	725355491768777504823705600.0	9.8	9.4
95	1450710983537555009647411200.0	9.9	9.5
96	2901421967075110019294822400.0	10.0	9.6
97	5802843934150220038589644800.0	10.1	9.7
98	11605687868300440077179289600.0	10.2	9.8
99	23211375736600880154358579200.0	10.3	9.9
100	46422751473201760308717158400.0	10.4	10.0

Table 5.2 Moment ratio analysis results of grain size/shape characteristics for a variety of samples.

		β_1	β_2		β_1	β_2		β_1	β_2
Area				Fshape			Fcircle		
	48	2.84	6.05		0.07	2.51		0.04	2.8
	49	5.85	10.72		0.04	2.44		0.27	3.47
	51	5.49	9.11		0.12	2.44		0.06	3.34
	54	39.13	48.38		0.08	2.37		0.1	2.75
	55	5.68	11.41		0.14	2.91		0.09	3.3
	57	13.44	18.86		0.09	2.44		0.07	2.7
	60	103.56	121.71		0.11	2.24		0.13	2.83
	69	4.45	8.22		0	2.4		0.05	3.05
	77	101.3	165.28		0.11	2.6		0.02	2.84
	78	5.98	11.69		0.05	2.48		0.07	2.92
	71	4.48	8.24		0.06	2.29		0.01	3.12
	79	2.8	6.25		0.04	2.47		0.02	3.24
	80	0.27	2.72		0	1.72		0.48	3.17
Dcircle	48	0.45	2.96	Perim	2.25	5.89			
	49	0.82	3.79		7.57	16.06			
	51	1.24	3.85		3.69	7.15			
	54	7.72	15.26		8.67	15.79			
	55	0.87	3.65		1.86	5.73			
	57	3.65	7.26		3.69	6.75			
	60	12.89	25.63		74.96	96.59			
	69	0.78	3.43		2.12	5.41			
	77	3.48	13.18		3.18	9.73			
	78	0.82	3.86		2.58	7.05			
	48	0.45	2.96		2.25	5.89			
	71	0.76	3.38		4.44	9.68			
	79	0.35	2.75		1.62	5.4			
	80	0.66	3.38		0.29	3.27			

μ	ρ	CSL
1	1	1
1	2	2
1	3	3
1	4	4
1	5	5
1	6	6
1	7	7
1	8	8
1	9	9
1	10	10
1	11	11
1	12	12
1	13	13
1	14	14
1	15	15
1	16	16
1	17	17
1	18	18
1	19	19
1	20	20
1	21	21
1	22	22
1	23	23
1	24	24
1	25	25
1	26	26
1	27	27
1	28	28
1	29	29
1	30	30
1	31	31
1	32	32
1	33	33
1	34	34
1	35	35
1	36	36
1	37	37
1	38	38
1	39	39
1	40	40
1	41	41
1	42	42
1	43	43
1	44	44
1	45	45
1	46	46
1	47	47
1	48	48
1	49	49
1	50	50
1	51	51
1	52	52
1	53	53
1	54	54
1	55	55
1	56	56
1	57	57
1	58	58
1	59	59
1	60	60
1	61	61
1	62	62
1	63	63
1	64	64
1	65	65
1	66	66
1	67	67
1	68	68
1	69	69
1	70	70
1	71	71
1	72	72
1	73	73
1	74	74
1	75	75
1	76	76
1	77	77
1	78	78
1	79	79
1	80	80
1	81	81
1	82	82
1	83	83
1	84	84
1	85	85
1	86	86
1	87	87
1	88	88
1	89	89
1	90	90
1	91	91
1	92	92
1	93	93
1	94	94
1	95	95
1	96	96
1	97	97
1	98	98
1	99	99
1	100	100

Table 5.3 A table of possible CSL in rhombohedral crystal lattices with similar parameters to quartz. μ and ρ are account for the length ratio between the c-axis and the a-axis. For further explanation see Chapter 4 (Data calculated using program multiplicity.pas in Appenix E).

$\mu=46 \rho=25$						
	m	u	v	w	θ	Σ
	1.00	1	1	0	92.39	48.00
	1.00	1	0	1	79.66	39.00
	1.00	0	2	1	106.34	16.00
	2.00	2	0	2	79.66	39.00
	1.00	2	2	3	139.50	48.00

$\mu=33 \rho=18$						
	m	u	v	w	θ	Σ
	2.00	3	0	0	84.26	20.00
	2.00	1	1	0	55.15	42.00
	2.00	2	2	0	92.49	34.50
	2.00	0	3	0	84.26	20.00
	6.00	3	3	0	55.15	42.00
	2.00	3	3	0	114.90	38.00
	1.00	1	0	1	79.71	14.00
	1.00	2	1	1	118.97	32.00
	1.00	0	2	1	106.42	23.00
	21.00	0	0	3	9.43	37.00
	1.00	3	0	3	136.47	20.00
	1.00	1	1	3	127.38	42.00
	3.00	2	2	3	84.26	45.00
	1.00	0	3	3	136.47	20.00
	3.00	3	3	3	100.08	20.00
	1.00	3	3	3	148.79	38.00

$\mu=27 \rho=15$						
	m	u	v	w	θ	Σ
	1.00	3	0	0	122.58	39.00
	1.00	0	3	0	122.58	39.00
	1.00	1	0	1	79.98	23.00
	1.00	0	2	1	106.83	19.00
	21.00	0	0	3	9.43	37.00
	1.00	3	0	3	136.66	33.00

CHAPTER 6

MICROSTRUCTURAL PROCESSES AND STABILITY

6.1 Introduction

In this chapter, the microstructural data described in Chapter 5 are collated to develop models of the microstructural processes involved in the annealing of quartzites in a thermal aureole. The microstructural models will form a basis for developing kinetic models in Chapter 7 to describe the rates at which different microstructural elements are modified. This chapter, therefore, serves as a link between the raw input data and the quantitative models which describe the rates of microstructural changes.

Microstructural models are constructed which predict the processes by which a rock will react to its environmental conditions. Obviously this study concentrates most directly upon annealing (i.e. temperature effects), but many of the models are applicable to other dynamic regimes. Models of annealing processes are focused on the relative 'stability' of

different microstructural elements, the mechanisms by which they are modified and the driving forces behind microstructural change. The interpretations of microstructural data are discussed in relation to the three distinct aureole zones which were identified in the last chapter (Figure 6.1), as follows.

Zone I: Deformation microstructures from outside the thermal aureole.

Zone II: The zone of primary recrystallisation, where deformation microstructures are replaced by regular low energy configurations.

zone III: A zone close to the intrusion, where grain growth predominates with limited evidence of deformation preserved.

For each zone the processes involved in the evolution of grains, grain boundaries, intracrystalline substructures and dislocations are discussed. The driving forces for the modification of microstructures are discussed, with the premise that all microstructures strive to attain a thermodynamically stable or equilibrium form.

Once the main processes by which microstructures evolve have been identified for each zone, the discussion is widened to examine other microstructural processes which may strongly influence the modification of microstructures through the aureole. These include:

- Nucleation of new grains.
- Interaction of microstructures with impurities.
- The α/β quartz transition.
- Crystallographic controls upon grain growth.

Each or all of these may interact with the microstructural processes described for the various aureole zones through the aureole, thereby increasing the complexity of the particular system being investigated. Such complications need to be considered when

applying a microstructural model to theoretically describe the kinetics of microstructural evolution within this tectonic setting, or any other tectonic setting.

6.2 Zone 1 (mechanisms of deformation)

Zone 1 lies outside the thermal aureole, where thermal heating from the intrusion has had a limited effect on microstructures. The nature of the rock fabrics within Zone I reflects both the conditions and mechanisms of deformation before the intrusion. The deformation mechanisms involved are discussed on the basis of the microstructural features which each process modifies. Thus, microstructural processes operating on the grain scale are described initially, followed by those operating on the subgrain and dislocation scales.

6.2.1 Grains/Grain Boundary Processes

The average grain size from the rocks within Zone I is 180μ . This is similar in magnitude to the grain size of many sedimentary sandstones, suggesting that there has been little or no grain size reduction within the Appin quartzite during Caledonian deformation. The undulose nature of grain boundaries is indicative of grain boundary migration. Undulations form as relatively unstrained grains begin to consume more deformed grains, but the development of grain boundary migration microstructures is limited to only small scale undulations on the boundary (Figure 6.2). Amoeboidal grain shapes commonly observed in many highly deformed mylonites (White 1973 Law 1987 Law and Knipe 1989 and Urai et al. 1986) are developed within rocks from Zone I.

6.2.2 Subgrains

The presence of subgrains within a deformed rock is evidence that dislocations have recovered during deformation into low energy subgrain boundaries. These consist of arrays of dislocations which separate areas of pristine crystal forming the subgrain volume (White 1973; White 1976; Urai et al. 1986 and Knipe 1989). The mechanisms by which subgrain boundaries form is by dislocation glide and climb.

The behaviour of individual dislocations contrasts quite markedly with subgrain boundaries in Zone I. The form of subgrains within deformed samples is somewhat varied, the graphs in figure 5.5 indicate that many forms of subgrain types occur, e.g. straight, wobbly, equant and lensoid, as defined using the classification scheme described in Chapter 4. The different forms of subgrains suggests that each grain in a sample has accommodated deformation in a different manner. The proportion of the different subgrain types remains constant through Zone I, evidence that subgrains remain unaltered because temperatures were not high enough to induce subgrain annealing. Subgrains sizes (which range from 10μ - 30μ) remain constant throughout the outer zone of the aureole (although within any one sample there are a wide variety of subgrain types - see Figure 5.5), again suggesting that subgrains have not undergone any form of annealing within Zone I.

The relative stability of subgrains within Zone I will be examined in Chapter 7 using a variety of kinetic models to describe the rates at which these microstructures may alter. The sessile nature of subgrains may be related to (1) the nature of the kinetics controlling subgrain modification (see Chapter 7); or (2) forces preventing subgrains from evolving to their equilibrium state as predicted by kinetic models. Such forces are related to the configuration of microstructures and the presence of impurities and are discussed further in Section 6.5.1.

6.2.3 Mesh Substructure Visible With CL

The mesh substructures observed via CL (Figure 6.3a) are a new type of microstructure previously undocumented. This microstructure has obviously accommodated strain within rock specimens and therefore contains information about the conditions and processes involved during deformation. Two possible processes may explain the occurrence of such a microstructure: (1) CL is merely picking out a subgrain boundary network and (2) CL is imaging a fracture network.

(1) Subgrain Hypothesis

If the mesh structure is related to the subgrain structure within a grain it can therefore be attributed to dislocation recovery processes. Orientation contrast images reveal that

associated with the luminescent mesh structure are small changes in crystal orientation (Figure 6.3b). It is possible that subgrain boundaries may be the feature within these grains which luminesces, either because of the concentration of defects within the subgrain boundary or because of the concentration of chemical impurities within the subgrain walls. Luminescence has been reported within natural aggregates as a result of both defect density and chemical variation.

(2) Fracture Hypothesis

An alternative explanation for the formation of the mesh microstructure is that the grain has at some stage in its history been fractured. During fracturing fluids may invade the grain. Obviously, chemical impurities can therefore be introduced which subtly alter the chemical composition of the quartz grain along the fractures. This chemical variation is then imaged under SEM/CL conditions. Alternatively, if quartz is precipitated along the fractures at a lower temperature than the grain formed, then this may also lead to variation in the CL signature

Figure 6.4 presents of a chemical analysis performed across a mesh structure using a microprobe. The analysis shows that chemical concentrations are theoretically beneath detectable limits. However, when the results are compared to a grain which does not contain this mesh structure, the chemical concentrations of Fe^{2+} and Mn^{2+} are consistently more varied within grains with the mesh structure. Therefore, chemical variation across these grains is the most likely cause of the distinctive cathodoluminescence signature. Chemical species may become concentrated in either of the above models within dislocation walls (in a similar manner that impurities become concentrated along grain boundaries) or along fracture sets (as a consequence of introduction of impurities during the fracture process).

Unfortunately, there is insufficient evidence to distinguish between either of the explanations presented above. However, the CL networks are far more regular in appearance than a typical subgrain network within grains from these aggregates (compare Figure 6.3a to Figure 6.3b). It is, therefore, reasonable to suppose that the mesh structure is a completely different microstructure from subgrains. For this reason,

together with the evidence that the 'mesh' system is frequently associated with fluid inclusion trails (which are frequently associated with fracturing in rocks), the mesh microstructures are interpreted as healed fractures, dating from either the pre-sedimentation history or early in the deformation history of the Appin Quartzite.

6.2.4 Dislocations

Dislocations, present in all the samples throughout samples from Zone I, indicate that intracrystalline crystal plasticity has played an important role during deformation (Van der Merwe 1950, Friedel 1964, White 1973,). Dislocations are the basic microstructural element utilised to induce deformation within a grain and they also serve as a driving force for intercrystalline softening by recovery (White 1976, Urai et al. 1986).

The quantity of dislocations, in the Appin quartzites are compatible with the expected values for deformed tectonites (see White, 1973 and 1977). However, well organised straight dislocations which commonly form hexagonal arrays are not typical of those developed in deformed rocks. This contradiction suggests that whilst during deformation dislocations have been produced to accommodate strain, the shapes of these dislocations have since been altered during the subsequent geological history. The dislocation microstructures now preserved within these samples contain evidence of not only deformation, but also of the environmental conditions through which the rock has passed since that deformation. In other words, these dislocation textures reveal that temperatures have been sufficient to cause some degree of recovery.

Hexagonal arrays of dislocations are typical recovery microstructures, normally developed within rocks which have attained high temperatures. It may be therefore inferred that the shapes of dislocations have been altered after deformation by recovery processes. The degree to which the dislocations recover is dependant on the temperature history after deformation. It is possible that the recovery of dislocations occurred after deformation either during thermal relaxation of the whole region from $\sim 500^{\circ}\text{C}$ or a result of the thermal affects of the Ballachulish intrusion.

The major point to note about dislocations is that they reveal evidence of recovery even at distances in excess of 2000m from the igneous intrusion. Thus, dislocations, unlike

other microstructural elements which show no sign of recovery in this zone, are 'unstable' and their shape, form and density are easily modified. Dislocations are therefore very susceptible to alteration, either syn-tectonically or post-tectonically, via small changes in the deformation environment or, more importantly, as temperature conditions change post deformation.

6.2.5 Summary of Deformation Processes in Zone I

Deformation processes have been accommodated predominately by intracrystalline processes involving the formation, glide and recovery of dislocations into subgrain walls during subgrain rotation. Intercrystalline processes (e.g. grain boundary migration) operate to a limited extent, creating an undulose geometry to many grain boundaries. Fracturing processes have been active within a number of grains at some point during the geological history of these rocks to produce what have been termed 'mesh' microstructures. Whether the fracturing microstructures are relict structures from the protolith from which the sediments were eroded before the Appin quartzite was deposited (a pre-sedimentary model), or whether these grains have reacted in a different manner to the Caledonian deformation (a post-sedimentary model) is still open to question.

6.3 Zone 2 Primary Recrystallisation

Zone II extends from 800-600m from the igneous intrusion and contains much of the critical information used to assess microstructural stability. With proximity of the granite the microstructures are gradually annealed as normal grain growth processes interact with processes more commonly associated with recovery of microstructures in dynamic regimes (i.e. primary recrystallisation). Within Zone II microstructures evolve from their pre-intrusive deformational state (fine grain size, many intracrystalline substructures and dislocations) to an annealed, lower energy configuration in which substructures within grains have been annihilated and grains have coarsened.

Individual microstructural elements (grains, subgrains, dislocations etc.) are discussed separately below in terms of the mechanisms by which they react to the thermal effects of

the Ballachulish granite. For each microstructure, interpretations are made based on the thermodynamic/kinetic reasons for their 'stability' or 'instability'.

6.3.1 Grains/Grain Boundaries

The coarsening of grain size within the Ballachulish aureole, together with the modification of grain shape, is perhaps the most obvious textural modification during annealing. Grain coarsening can be detected within samples at 800m from the igneous contact. Beyond 800m, grain size is fairly stable at around 180 microns. Within Zone II there are a variety of driving forces for grain coarsening and correspondingly there are a number of processes by which an aggregate may coarsen. However, the growth zones imaged using SEM/CL (see Figure 6.5) are evidence that grain boundary migration is the main mechanism by which grain coarsening occurs. Triple junctions also need to migrate as grain boundaries migrate and grains coarsen in order to maintain equilibrium dihedral angles. The grain boundary migration is driven by both surface energy requirements and strain incompatibilities within the aggregate.

Grain growth driven by surface energy requirements were discussed in detail in Chapter 2. Surface energy induced grain boundary migration naturally contributes to grain coarsening within Zone II. However strain energy variation between grains (a relict of the deformation before the intrusion) also induces grain boundary migration. As deformation substructures are eradicated, and with them strain variations, surface energy induced grain boundary migration will dominate. This is apparent between 700m and 600m from the granite, where deformation microstructures have been removed.

Primary recrystallisation is a recovery process similar to dynamic recrystallisation in that it is driven by strain energy variations between grains within an aggregate. It is a most effective method by which a deformed microstructure may be replaced by a typical annealed microstructure. Grain boundaries migrate during primary recrystallisation consuming 'deformed' grains, which are high energy features due to strain energy associated with elastic strain around dislocation cores. Conclusive proof that primary recrystallisation has been active within Zone II is shown in Figure 6.5 by the growth zones within coarsening grains. In Figure 6.5, a strain free grain is migrating through a fractured grain thereby lowering the total energy of the system. Similar grain boundary

migration processes also occur between grains which are not fractured. Highly strained grains are replaced by grains which have less strain energy. Thus, a hierarchy of stability is produced within an aggregate, the most stable grains being those with the least strain energy. It is these grains which grow at the expense of the less stable grains. The graphs of substructures within grains (see Figure 5.5) show the gradual replacement of deformed grains with subgrain structures and/or undulose extinction, by grains that have no substructures (i.e. strain-free grains) between 700m and 600m.

Grain boundaries reorganise themselves into regular forms at an early stage in the annealing process. This is reflected in grain shape measurements from within Zone II which are similar in to shapes developed even in the most annealed samples near the intrusion. This suggests that grain boundaries are very susceptible to alteration at high temperatures and will rapidly straighten into regular shapes during the annealing process. The rapid equilibration of grain boundaries explains why shape parameter and fractal measurements of grain shapes are similar throughout the aureole rather than exhibiting marked trends (see Figures 5.24/5.25). However, image analysis data indicate that there are small changes in grain shapes at around 800m from the contact. Thus, grain boundaries are reconfigured during the initial stages of primary recrystallisation.

Irregular grain boundaries are able to straighten by migration of the irregularities/steps parallel to the grain boundary until the step is eradicated at a triple junction. As the step reaches a triple junction, the junction itself migrates. As the aggregate coarsens there will be considerable movement in triple junctions as grains swap their neighbours (Figure 6.6a) and as grains coarsen (Figure 6.6). Similar triple junction migration processes have been described by Jessell (1986).

6.3.2 Subgrains

Subgrains, which remain unaltered during thermal relaxation after peak regional metamorphism have been shown to reflect the deformation the rocks had suffered before the intrusion of the Ballachulish Granite. It is worthwhile reviewing the data of subgrain textures within Zone 2. At 800m, subgrains are present in 65% of grains and yet within just 200m along the transect (i.e. at 600m) subgrains have been almost completely

annealed (85% of grains have no substructures whatsoever). Three mechanisms may be responsible for the annihilation of subgrain, as follows.

(1) Subgrains are annealed passively as a grain boundary migrates through a grain and in doing so incorporates in the grain boundary any intracrystalline features.

(2) Subgrain boundaries are able to migrate such that subgrains coarsen in a similar manner to grains/grain boundaries under the influence of subgrain boundary surface energy and strain energy either side of the boundary.

(3) A combination of grain boundary migration and subgrain boundary migration such that subgrains gradually become more misoriented as dislocations climb into the boundaries and eventually become high angle boundaries, whereupon they are able to migrate and eradicate surrounding subgrains as migration proceeds.

The evolution of substructure type through Zone II indicates that there is only limited change in the relative proportions of the different types of substructures (see Chapter 5). The main change is the replacement of grains with substructures by those without.

Subgrain boundary migration has been reported by a number of authors during well controlled annealing experiments (Li, 1972; Jessell, 1986 and Means, 1989). It is probable that annealed specimens from Ballachulish have at some stage undergone subgrain boundary migration. However, the evidence for this is quickly eradicated as migrating grain boundaries (and possibly subgrain boundaries) during primary recrystallisation rapidly consume subgrains. Evidence that subgrains may migrate during the initial stages of annealing comes indirectly from the grain shape analysis presented in Chapter 5. If the microstructure of subgrains remained unaltered during primary recrystallisation, a migrating grain boundary would be expected to reflect the shape of the subgrain structure within the grain which is being consumed. This is because the grain boundary would consume each subgrain within a grain in a step by step process, one subgrain at a time, thus the shape of the migrating grain boundary will be irregular. In Zone II grain shapes are relatively euhedral. This evidence may be used to infer that

subgrain boundaries do indeed migrate, creating homogeneous grain interiors, thus enabling grain boundaries to migrate as straight, linear features.

6.3.3 'Mesh' Grains

Grains exhibiting a mesh microstructure have been interpreted as fracture microstructures resulting from deformation either pre or post sedimentation. They will therefore be referred to as 'fractured grains'. Fractured grains (e.g. Figure 6.5) are the most stable of all the microstructures observed in this study. They remain unchanged at 600m from the igneous contact, and examples have even been found at the igneous contact itself. The behaviour of these grains gives a unique insight into the competition in rocks between thermodynamic driving forces and rate controlling kinetics.

The fractured grains are deformed microstructures associated with high internal strain energy. It would therefore be expected that such microstructures would be eradicated during the incipient stages of the annealing process (i.e. there is a thermodynamic driving force to destroy the fractured grains). However, in this example, the kinetics of microstructural evolution overcome the thermodynamics to prevent the fractured grains from annealing. The kinetic effect responsible for the stability of the fractured grains is an extreme form of pinning. This is demonstrated in Figure 6.5, a cathodo-luminescence image of a fractured grain surrounded by grains with no deformation microstructures. The non-deformed grains are seen to have growth bands parallel to their grain boundaries, which suggest that these grains are gradually consuming the fractured grains. However, the consumption process has not reached completion because the fracture network within the grains are barriers to grain boundary migration. As the grain boundary migrates, fluid inclusions and impurities, which are present in the fractured grains, reduce the mobility of the grain boundaries. Thus, the drag forces on the migrating boundary are increased, inhibiting further movement of the boundary and the boundary becomes pinned. Eventually, the grain boundary is able to overcome the drag forces either as impurities diffuse from the boundary or the driving force for migration increases e.g. by the input of more thermal energy. Migration then resumes until impurities build up again and drag forces once more pin the boundary. Thus, a stop start grain boundary migration process is envisaged, whereby a boundary migrates, becomes pinned and then migrates again as pinning forces are overcome.

Further evidence for the irregular motion of a migrating grain boundary is seen in Figure 6.5. The growth bands in a neighbouring grain preserve the progression of the grain boundary through the fractured grain. The growth zones probably result from chemical variations at the migrating grain boundary front, caused by the slight variation in the chemistry of impurities being incorporated on to the grain boundary. Thus, each growth zone reflects a change in the chemical composition at the migrating grain boundary front (cf. Knipe and McCaig, 1994).

Impurities may react in a number of ways during grain boundary migration. The growth zone pattern therefore will be a reflection of the interaction of impurities with the migrating front. If a grain boundary removes all chemical impurities away as it sweeps through a grain, the resultant CL signature would be homogeneous in the growing grain. On the other hand if migration was rapid and a grain boundary was unable to clear the impurities away, the grain behind the migrating boundary would have a spatial distribution of impurities much the same as the original grain that had been consumed. The fact that the CL banding is a homogeneous linear feature and not chaotic along the boundary suggests that chemical impurities were swept along with the grain boundaries until the boundaries became pinned, at which stage the chemical species could equilibrate within the grain boundary before further migration of the boundary and incorporation of more impurities of slightly different composition. Equilibration of the impurities along the grain boundary would thus produce a homogeneous chemical composition within the boundary, giving rise to a homogeneous CL banding pattern in the wake of the migrating boundary.

Where drag forces dominate because of impurity content, either on a grain boundary or within a grain (i.e. fractured grains), a grain boundary may never be able to migrate. This explains the presence of a limited number of such grains throughout the aureole even at the igneous contact. This is an example of thermodynamics providing a driving force for microstructural change. However, the kinetics are so sluggish that the energetically favoured form is never achieved. The behaviour of these fractured grains contrasts markedly with other grains within the rock because their impurity content prevents them from being consumed by grain boundary migration. This is an example of a quartzite microstructure which prevents the aggregate as a whole reaching equilibrium, even

though it is composed of the same material (i.e. quartz). Impurities and second phases within rocks have frequently been shown to exert drag forces which slow down the rates at which microstructures may alter. However, this is clearly different, here is a rare example where one type of microstructure is preventing other microstructures (composed of the same material within the same aggregate) from evolving as expected.

The stability of these fluid inclusion rich fractured grains emphasises a detail about the effects of the bulk fluid content of a rock on deformation. In rocks with a high fluid content, hydrolytic weakening of dislocations lowers the stress at which a dislocation will glide (Blacic and Cristie, 1984). Thus, the material is softer, making it more susceptible to deformation. However, if all the fluid within a rock is contained along healed fractures similar to those in the Appin quartzite, the OH molecules are not located at the cores of dislocations, where they are able to promote weakening, but are sealed in fluid inclusions. Thus, the fluid-rich rock is 'harder' and less susceptible to deformation because these types of microstructures are less susceptible to grain boundary migration processes. When assessing the influence of fluids on the kinetics of deformation and metamorphic processes it is not enough to measure the bulk fluid content it is a necessity to analyse the rock fabrics and assess the distribution of the fluids within the microtexture.

It has been shown that to hydrolytically soften a material, the OH bonds need to react with dislocation tips (Blacic and Cristie, 1984). However, in microstructures such as the fractured grains described above, the fluid is contained along fractures and in fluid inclusions. It is therefore important to predict whether it is thermodynamically possible and kinetically viable to diffuse fluids from inclusions to dislocation cores. In order to diffuse an atom of fluid away from a fluid inclusion, the surface energy per unit volume will increase (see Equations 6.1) because the surface energy (related to surface area) is proportional to the radius of the inclusion squared, whilst the volume is proportional to the radius cubed. In other words:

$$G \propto 4\pi r^2$$

$$\Delta G \propto 4\pi (r - \delta r)^2$$

$$V = \left(\frac{4}{3}\right)\pi r^3$$

$$\Delta V = \left(\frac{4}{3}\right)\pi (r - \delta r)^3$$

Equation 6.1a-d

where G is Gibbs free energy, r is the radius and V is the volume of a fluid inclusion. Thus it is energetically unfavourable to diffuse material away from a fluid inclusion to a dislocation core.

6.3.4 Dislocations

Within Zone II dislocation microstructures related to deformation are annihilated. The dislocations which remain tend to be straight, linear features, substantially altered from the hexagonal dislocation arrays observed in Zone I. The original dislocation structures typical of Zone I have been modified during annealing by climb, cross slip and mutual annihilation of dislocations. It is also possible that most of the original dislocations have been destroyed by other microstructural processes (e.g. grain boundary migration, subgrain boundary migration). Thus, the only remaining dislocations are those which formed during the grain boundary migration process. Klapper (1980) has shown that linear screw dislocations are common as a result of grain growth processes at a surface where a step originates. Preferential attachment of growth units along the step causes the step to spiral around a dislocation, allowing the dislocation and the surface to advance (Figure 6.7). Although this model has been proposed for growth of a mineral from a fluid phase, it is possible that a similar mechanism could occur at a step on a grain boundary. Considering that linear defects are common within Zone II 'spiral' growth (Figure 6.7) is a plausible mechanism for grain boundary migration within these rocks.

6.4 Zone III (Normal Grain Growth)

Apart from a limited number of fractured grains, deformation related microstructures are not found in samples 600m or less from the igneous intrusion. In these aggregates it is reasonable to suppose that primary recrystallisation has eradicated the deformed

microstructures and that the textures had become uniform. There is therefore no longer a driving force for strain induced grain boundary migration. However, throughout Zone III the grain size continues to coarsen. The mechanism responsible for coarsening has changed from strain induced grain boundary migration in Zone II to surface energy induced grain boundary migration in Zone III.

Normal grain growth has been shown to produce a distinctive lognormal grain size distribution (Atkinson 1988, Louat 1974). However, such a grain size distribution has been shown not to have been attained in any of the samples from the Ballachulish aureole because of the influence of second phase feldspar impurities. Nevertheless, the process of grain growth within quartz domains is the same, irrespective of the presence or absence of feldspar impurities. Surface energy induced grain boundary migration is therefore responsible for growth of grains within Zone III, in a similar manner to normal grain growth observed in experimental annealing of monomineralic materials (Atkinson 1988). The mechanisms of normal grain growth were reviewed in Chapter 2. Evidence of grain boundary migration is again revealed by growth bands on SEM CL-images of the rocks.

The main mechanisms of microstructural modification in each of the zones within the Ballachulish aureole have been distinguished. The following sections highlight various processes which may exert an influence on annealing throughout all the zones.

6.5 Controls on Microstructural Development

One of the most fundamental aspects of the microstructural development within the Ballachulish aureole is that microstructures (at all scales) do not evolve in a gradual manner. Rather, there are sudden changes in the characteristics of microstructures at specific distances from the intrusion. These changes indicate that in natural rocks the processes of annealing cannot be described by relatively simplistic microstructural models such as strain induced grain boundary migration and surface energy induced grain boundary migration. Microstructural evolution is complicated by:

- (1) Interaction of different microstructural processes.

(3) Other impurities are more difficult to detect, particularly using SEM techniques. However, it is probable that impurities exist on grain and subgrain boundaries. Solute atoms of impurities may also exist on grain boundaries, subgrain boundaries, within grains and at dislocation cores.

The possible effects of each type of impurity will now be examined, predicting which microstructures may be affected and where in the aureole their influence may be greatest. Note that much of this section is hypothetical because time has not permitted a detailed analysis.

6.5.1.a Feldspar Impurities/Fluid inclusions

When a migrating quartz:quartz grain boundary encounters a feldspar impurity, the migration process becomes inhibited because there cannot be a simple transfer of atoms across the interface (due to the chemical compositions involved). Grain boundaries therefore become 'pinned' in the presence of second phase materials (see Figure 6.8). If grain boundaries are prevented from migrating in the presence of the second phases, the basic mechanism by which grains coarsen will also cease. Thus, the size and distribution of feldspar impurities controls the degree to which a migrating grain boundary is pinned.

Away from the igneous intrusion the grain size of quartz crystals is relatively low, but close to the contact the grain size is large. Thus, the nearer the contact, the more likely it is that any one grain will come into contact with a feldspar impurity and potentially become pinned. This model of pinning would suggest that pinning may affect grain size change to a greater extent the greater the grain size of the quartz (i.e. close to the intrusion). However, this simplistic model fails to account for changes in the size and characteristics of feldspar impurities as a result of Ostwald ripening towards the intrusion (Ostwald ripening is a diffusion process causing second phase particles to coarsen during annealing).

Poirier (1985) shows that the degree to which a grain boundary is pinned is dependent on the driving force for grain boundary migration as well as the characteristics of the second phase impurities. If the driving force for migration is high such that a grain boundary is

mobile, it may actually by-pass an impurity. The impurity therefore becomes included within a grain. Figure 5.12 is an example from Ballachulish where most of the feldspar is contained within quartz grains, suggesting that grain boundaries were mobile enough to by-pass impurities. As grain coarsening proceeds, the surface energy of grains per unit volume decreases. Associated with this must be a decrease in the driving force for grain boundary migration. Thus, it is feasible that as coarsening proceeds within an aggregate grain boundary mobility gradually decreases and grain boundaries become more susceptible to drag forces, such as pinning (Covey-Crump and Rutter 1989).

The main conclusion of the above discussion is that feldspar impurities exert a greater influence on grain growth as the aggregate coarsens. The grain size data from Buntebarth and Voll (1991) indicate that grain growth is rapid between 800m and 300m from the intrusion and then slows down (see figure 5.15). This may be a direct result of drag forces beginning to dominate as grain size increases. The grain size data presented in this investigation, from impure quartzites, reveals that grain sizes are less than those reported for pure samples by Buntebarth and Voll (1991). Thus, it may be inferred that in these samples pinning by feldspars is affecting the behaviour of microstructural modification.

6.5.1.b Solute Impurities

This section is hypothetical because no data have been collected on the solute content within rocks through the Ballachulish aureole. Notwithstanding this, it is still important to attempt to predict where, and how in the aureole solute atoms may control the processes and rates of microstructural change. Unlike feldspar impurities, solute impurities may occur on an atomic scale. They may therefore alter the behaviour of every type of microstructure present in an aggregate. They may pin grain boundaries, subgrain boundaries, prevent movement of twin boundaries, cause dislocations to become sessile, or even enhance the mobility of dislocations via hydrolytic weakening.

Because solute clusters are relatively small, if a grain or subgrain boundary is mobile it is likely that the solutes may be pushed along on the grain boundary as it is migrating. Conversely, if a microstructure has a low mobility, the solutes may prevent that microstructure from moving. Another consideration is the density of solute clusters on a

microstructure. This may be clarified by considering a grain boundary, migrating and gradually picking up more and more solute atoms as it sweeps through a rock. Eventually the density of solute atoms may become so great that the grain boundary becomes pinned.

In the Ballachulish setting there is a limited amount of microstructural evidence for the interaction between solutes and annealing processes (mainly because of the scale at which the samples have been observed). However, grain growth within Ballachulish initiates suddenly at 800m from the intrusion. This is not a feature that would be expected from simple microstructural models, which would predict a more gradual evolution of microstructures. The Ballachulish aureole provides evidence that grain growth is hindered at distances >800m from the intrusion where grain boundaries are immobile. Eventually at 800m, grain boundaries receive enough thermal energy from the intrusion to overcome drag forces and coarsening proceeds at rates predicted by grain growth models. Similar drag forces may also explain the sessile nature of subgrains until 700m, at which stage the subgrains rapidly alter their configuration and disappear.

6.5.1.c Summary

The above discussion identifies impurity content within a rock as a fundamental consideration when interpreting annealed microstructures. Impurities affect both the processes and kinetics of microstructural evolution at all scales of observation. The kinetic aspects of impurities are investigated in detail in chapter seven by comparing the Ballachulish data set with models of microstructural modification within pure quartzites.

6.5.2 Nucleation

For a new grain to develop during recrystallisation, it must start as a very small region and then grow. The new grain embryo may be an area with a different crystal orientation from the surrounding material (i.e. a new grain) or an area of different composition (i.e. a new phase). Initially, the surface to volume ratio is high, making the nucleated area unstable. However, if the nucleated region is large enough, the driving force to grow becomes greater than the driving force for the nucleated pip to disappear (Kingery et al. 1976). Two types of nucleation have been described (Kingery et al 1976): (1)

homogeneous nucleation, where a new species is nucleated in a perfect lattice (or from a liquid) and (2) heterogeneous nucleation, where a new species nucleates at an interface, structural imperfection or at the site of impurities. Heterogeneous nucleation is energetically more favourable than homogeneous nucleation. It is therefore more common for new grains to nucleate at grain boundaries, subgrain boundaries and impurities. Preferential nucleation at structural imperfections was observed during an experiment to deform dichlorobenzene (R.J.Knipe, pers. comm.) and is shown in Figure 6.9 where a small pink crystal nucleates at the site of a kink. The newly nucleated grain has an exceptionally low strain energy. It therefore quickly consumes the surrounding grains, all of which have a higher strain energy (strain is revealed in the images as undulose extinction and kink bands within individual grains). This is an example of dynamic recovery by nucleation and grain boundary migration. During primary recrystallisation and normal grain growth in the Ballachulish, new strain free grains may nucleate at any time, driven by the thermal energy from the intrusion. Nucleation has major implications for both the kinetics of grain growth and the processes by which rocks anneal in the Ballachulish aureole.

Once normal grain growth dominates within the aureole, the potential for nucleation of new grains will decrease because there are fewer sites for heterogeneous nucleation. Because homogenous nucleation is more difficult, there will be fewer nucleation events. In Zone II there is a large benefit to be gained by nucleating a strain free grain and allowing it to grow at the expense of highly strained grains because there will be a large reduction in the total free energy of the system associated with new strain free grains. Covey-Crump (pers. comm. 1995) has shown examples of primary recrystallisation in calcite where grain growth occurs only in those grains which have nucleated during the early stages of recrystallisation. The sites at which new grains nucleate are located on twin boundaries, subgrain boundaries and grain boundaries (i.e. heterogeneous nucleation occurs). All other 'old' grains are eradicated by 'new' nucleated grains. Once the initial fabric is totally replaced by nucleated grains, normal grain growth ensues. Importantly, the aggregate of growing grains has evolved into an aggregate of nucleated grains, potentially unrelated to the original fabric.

Evidence of nucleation during primary recrystallisation within Zone II is shown in Figure 5.13. Growth zones within one grain are clearly concentric about a central point. It has been shown that the growth zones track the history of a migrating grain boundary. However, in this example the fact that all the grain boundaries may be traced back to one point within a grain indicates that the grain nucleated during annealing.

There is a decrease in the grain size of samples between 1000m and 700m from the contact (see figure 5.15). This may be related to nucleation events which produce smaller grains. The mean grain size of the aggregate is therefore reduced. Voll and Bunterbarth (1991) interpreted the decrease in grain size as a consequence of subgrain coalescence, whereby subgrains combine to form new grains. This interpretation is plausible, but unfortunately there is no evidence within these rocks for subgrain coalescence. On the other hand evidence is presented here to indicate that nucleation may be a common process.

6.6 Crystallographic Control on Growth

6.6.1 Introduction

Crystal preferred orientation (CPO) potentially controls grain growth processes and kinetics by:

- Preferential growth of grains with a particular orientation (which in turn may relate to the internal microstructures).
- Development of Crystallographic preferred orientation (CPO) in the bulk aggregate.
- Preferential growth/stability of grains which have low energy grain boundaries.

It is critical to assess the extent to which crystallographic orientations may influence the process of grain growth. Crystallographic controls on grain growth may have profound effects on the kinetics of grain growth, thus it is necessary to explore all possible interactions between grain growth and crystal orientations.

6.6.2 Crystallographic Preferred Orientation

6.6.2.a CPOs in Zone I

Crystallographic preferred orientations (CPO) have not developed within Zone I. These rocks preserve evidence of deformation before the intrusion of the granite. The lack of CPOs therefore indicates that crystal plastic deformation has been relatively minor in the area sampled. For example, there are no shear zones along the transect through the aureole. The presence of dislocations and subgrains demonstrate that deformation processes have been active, but have not been strong enough to produce crystal fabrics.

6.6.2.b CPO Development in Zones I&II

In both Zones II and III CPOs are again not developed. Although certain grain orientations may grow preferentially to other orientations locally within the aggregate, the process does not produce a CPO in the bulk aggregate. Preferential growth of grains with specific orientations during annealing has been documented by some authors (e.g. Gleason and Tullis 1990- Figure 6.10, Neuman 1995). Figure 6.10 are examples where the protolith prior to annealing has had a strong preferred crystallographic fabric. The process of preferential growth is inferred to be associated with preferential grain boundary migration obliterating grains with a high strain energy. The association of strain energy with crystal orientation (Lister 1977 and Knipe and Law 1987) therefore causes grains in orientations which have a high internal strain energy to be consumed by grains in orientations which have a low strain energy.

At Ballachulish, CPOs have not developed during annealing, probably because the original deformation was not intense enough to produce definite relationships between the internal strain energy of individual grains and their crystallographic orientation. These samples therefore are ideal to investigate the kinetics of grain growth because the controlling forces for grains growth, surface and internal strain energy, are effectively unrelated to crystal orientations.

6.6.3 Misorientation Analysis

Even though no overall bulk fabric CPOs exists within the Ballachulish suite of rocks, it is possible that on a local scale grain boundaries may develop very specific low energy orientations with respect to the grains on either side. Again, it is important to investigate such a phenomena because local controls on grain boundary processes could have serious consequences for the kinetics of microstructural evolution during annealing.

The misorientation analysis (Chapter 5) reveals that no preferred misorientations occur in any of the zones along the transect. Furthermore, within all the samples along the transect (both with deformed and annealed microstructures), coincident site lattice misorientations (CSLs) occur only as frequently as would be expected in a random aggregate of grains. This indicates that low energy grain boundaries are no more stable than high energy non-CSL boundaries. In this example of annealing low energy grain boundaries have little or no influence on the evolution of the rock. This conclusion is contrary to many investigations into annealing in metals/ceramics in which CSL misorientations tend to be more common than expected (e.g. Randle 1991 and Grimmer 1989 and Lartigue 1988). The lack of CSL grain boundary misorientations may stem from the fact that there are so few CSL relationships in quartz (see Chapter 4 - Table 1 and McLaren 1986).

The lack of CSL misorientations may be explained by neighbour swapping. This is depicted in Figure 6.6, where a CSL low energy grain boundary has formed. The grain boundary has then migrated under the influence of surface energy. Notice that as soon as the CSL grain boundary meets another grain boundary one grain is lost and the two grains either side become neighbours and in doing so the CSL relationship is destroyed. Alternatively, a non-CSL grain boundary may migrate through a CSL boundary, consuming it in the process and again producing a non-CSL boundary with the next grain. The presence of impurities at grain boundaries may affect the formation of CSL relationships, but as yet no work has been undertaken to investigate such controls.

6.7 Initiation of Grain Growth

Coarsening of grains in the Ballachulish aureole is detected at about 800m from the igneous contact, a distance where the maximum temperature attained was 625°C. This temperature coincides with the temperature of the α/β phase transition in quartz, from trigonal structure (α quartz) to hexagonal structure (β quartz). Voll (1969) suggested that the α/β inversion may be responsible for triggering grain coarsening within the Ballachulish aureole. However, Bunterbarth and Voll (1991) retracted this conclusion, on the basis that the α/β quartz transition would be at 650°C in impure quartzites (the data is taken from measurements of the α/β quartz transition Granite - Molen 1981), and thus coarsening initiates at a lower temperature than the transition. Figure 6.11 indicates that the quartz inversion at 0.28GPa would be 640°C. Because the Appin quartzites have just 10-15% feldspar, it is estimated that this will have limited effect on the inversion temperature. Thus, it is felt that coarsening does occur near the transition. It may be impossible to assess definitely whether the α/β inversion does trigger coarsening in the Ballachulish aureole. However, the α/β inversion may have a considerable influence on the microstructural evolution. Intimately associated with the transition from α to β quartz is the generation of Dauphiné twins (a 60° rotation around the c-axis (Nord 1993) and a small volume change.

Knipe, 1981 estimated that the α/β quartz transition may increase the stress acting upon an aggregate by one order of magnitude. This could potentially enhance grain boundary migration by introducing more strain variations into the aggregate. Gault (1949), Thomas (1945) and Heaney and Veblen (1991) have shown that the α/β transition will induce Daupiné twins in the majority of grains in an aggregate. Twin boundaries potentially increase the number of potential sites for a heterogeneous nucleation event to occur. The production of numerous low energy newly nucleated pips promote primary recrystallisation, causing the abrupt initiation of grain growth at the 625°C isograd.

6.8 Summary

The mechanisms involved in microstructural evolution have been analysed for the three zones which have been identified within the Ballachulish thermal aureole. It is to be

noted that any one mechanism by which rocks are annealed is not always mutually exclusive to any one zone, there is frequent overlap. However, the most simplistic way to discuss these processes is to link each process to the zone within which it is most dominant.

6.8.1 Zone I - Processes of deformation

Three main processes have operated in order to produce the deformed microstructures observed outside the aureole, as follows.

- Intracrystalline slip, evidenced by a high density of dislocations.
- Intracrystalline recovery - hexagonal dislocation arrays and subgrains are present.
- Dynamic recrystallisation, as shown by irregular grain boundaries, due to grain boundary migration and subgrain rotation via dislocation climb and glide into subgrain walls.

In addition, a hitherto unrecognised microstructure, an intracrystalline mesh network, has been observed and attributed to healed fractures which developed either via brittle deformation in the pre-sedimentary protolith, or during the early stages of deformation of the Appin Quartzite.

6.8.2 Zone II - Primary Recrystallisation

The eradication of deformational microstructures during primary recrystallisation occurs during the early stages of annealing. The mechanisms for primary recrystallisation are strain induced grain boundary migration together with surface energy induced grain boundary migration. Evidence for these is as follows:

- Dislocation microstructures indicate that recovery processes have been dominant in these aggregates. Elongate linear defects do exist, which may relate to spiral grain growth during grain boundary migration.

- Subgrains remain unaltered even after grain growth has initiated. The subgrain structures rapidly disappear between 700m and 600m from the contact. Two processes may be responsible for the alteration of subgrains: (1) subgrain boundary migration (i.e. subgrains migrate into grain boundaries). (2) annihilation as grain boundaries migrate (i.e. they are consumed passively on to grain boundaries).
- Fractured 'mesh' grains are the most stable microstructure, examples are found throughout Zone II and even into Zone III where all other deformation related microstructures have long since disappeared.

6.8.3 Zone III

Normal grain growth occurs in this region. The driving force for grain growth is surface energy associated with grain boundaries. Thus, the Gibbs free energy of the aggregate is decreased as the total grain boundary area decreases during coarsening.

6.8.4 Other Controls on Evolution of Microstructures at Ballachulish

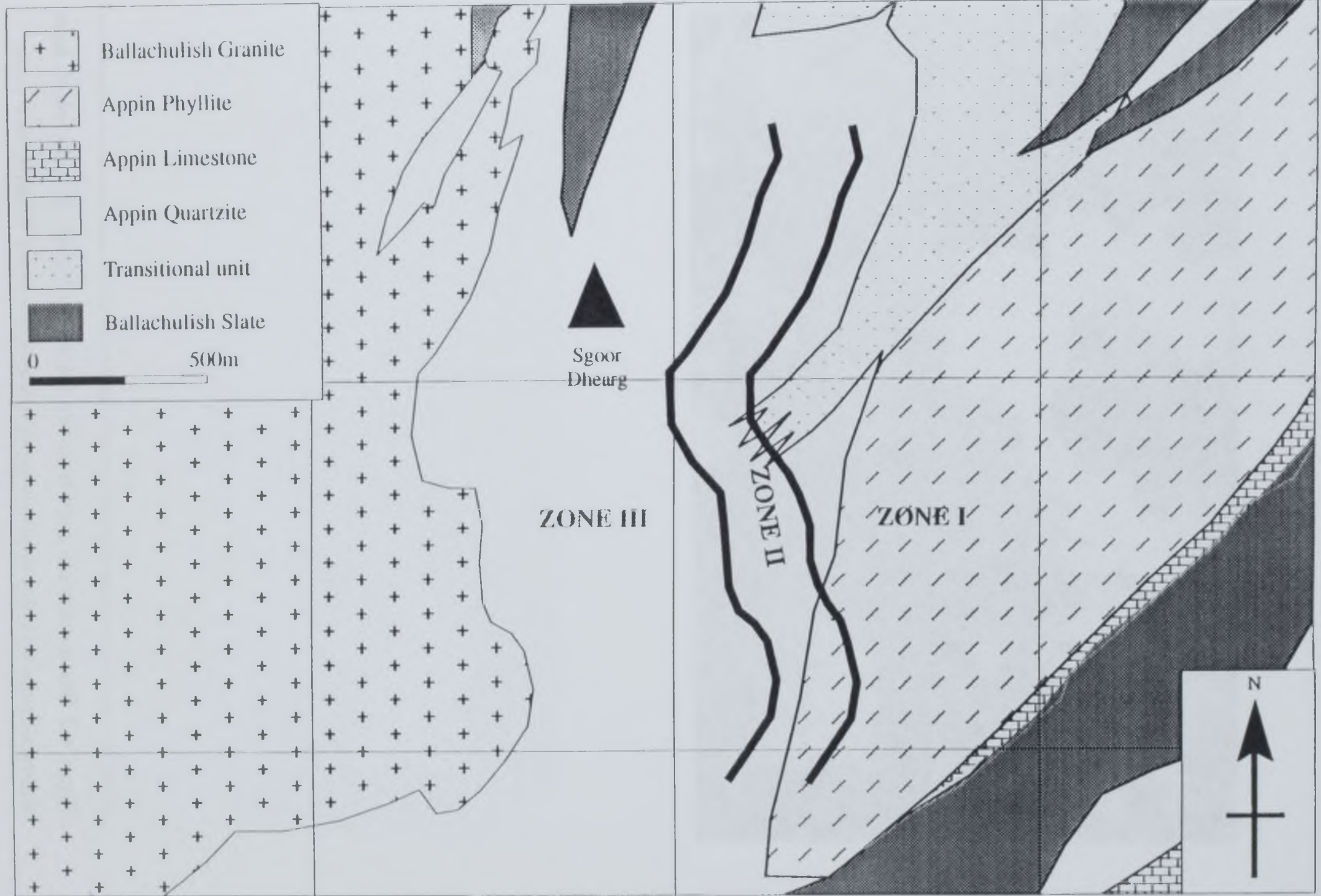
In the Ballachulish aureole it is shown that the simplistic models of grain growth described above via grain boundary, subgrain and dislocation processes do not adequately describe the mechanisms by which the microstructures are annealed along the traverse at Ballachulish. The following processes have been identified as significantly altering the behaviour of microstructural modification from that expected in the microstructural models presented above.

- Impurities affect the growth rate of grains, subgrains and dislocation arrays. Different types of impurities (i.e. feldspar, solute atoms or fluid inclusions) are predicted to influence different microstructures at different stages during the annealing process. The interaction of impurities with any one type microstructural element (e.g. grain, subgrain or dislocation) is dependent upon the driving force for modification together with the density of impurities in contact with that microstructure.

- Nucleation is identified as a process which is common during primary recrystallisation. This may lower the average grain size in samples and may also disassociate the developing texture with that of the pre-annealing texture.
- Rocks at Ballachulish have neither crystallographic preferred orientations nor misorientations, and CSL boundaries are not produced, making these rocks ideal for studying the kinetics of grain growth, without added crystallographic complications.
- The α/β quartz transition may potentially help the initiation of grain growth by straining the rocks, thereby increasing the likelihood of nucleation events and increasing the stored strain energy in the rock. A high strain energy may supply the grain boundaries with extra driving force giving them the mobility to overcome solute drag.
- The fractured 'mesh' microstructures are stable features, even though they have a high fluid content (in the form of fluid inclusions). Fluid content has been shown by many authors to make microstructures less stable. This example indicates that it is not just the amount of fluid present in a microstructure which determines its stability, but the location and/or distribution of the fluid within the microstructure.

These complications to the simple annealing system cited above are investigated further in Chapter 7 by considering how microstructures should react to the igneous intrusion using simple monomineralic kinetic models. Departure of the observed microstructures at Ballachulish from the results of the kinetic models may then be interpreted using evidence from the microstructural models which have been outlined, together with the potential for these models to be complicated by other microstructural processes.

Figure 6.1 Geological map of area of study, the aureole has been divided into three zones, each zone is typified by a collection of microstructures which reflect the processes which occur in that zone. **Zone I** - unannealed rocks at distances greater than 800m from the intrusion; **Zone II** - zone of primary recrystallisation (between 800 and 600m) and **Zone III** - a zone of normal grain growth (at distances less than 600m from the intrusion).



55

54



Figure 6.2 The amoeboidal grain boundary shapes are typical of rocks which have undergone grain boundary migration during a deformation event. Width of view 1mm.

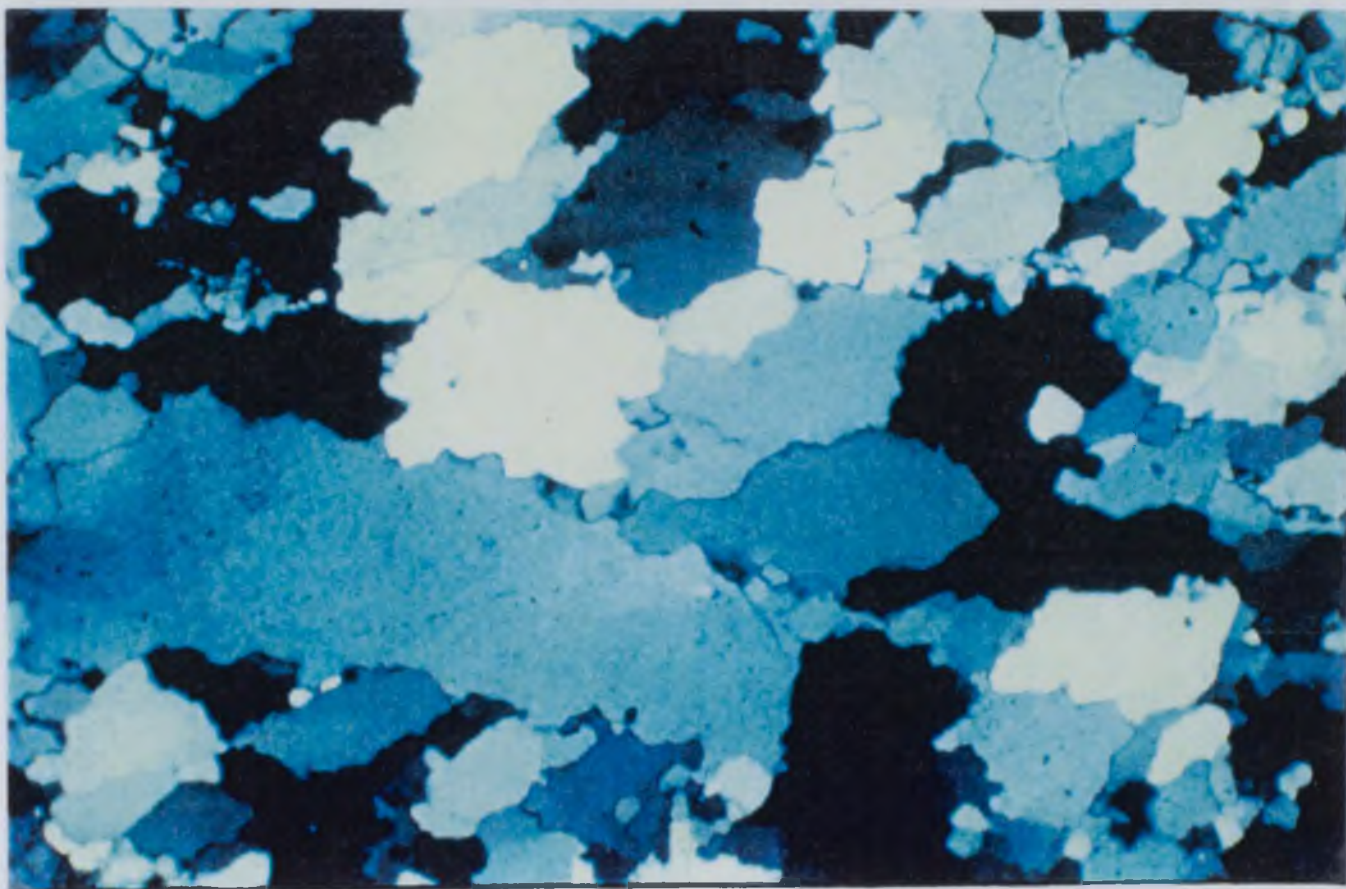




Figure 6.3 a: Cathodo-luminescence image of a deformed rock exhibiting a 'mesh' microstructure (the central grain in the image). b, The same grain as in a, imaged using SEM/OC, the mesh structure cannot be distinguished from a typical subgrain microstructure which occurs in all the surrounding grains.

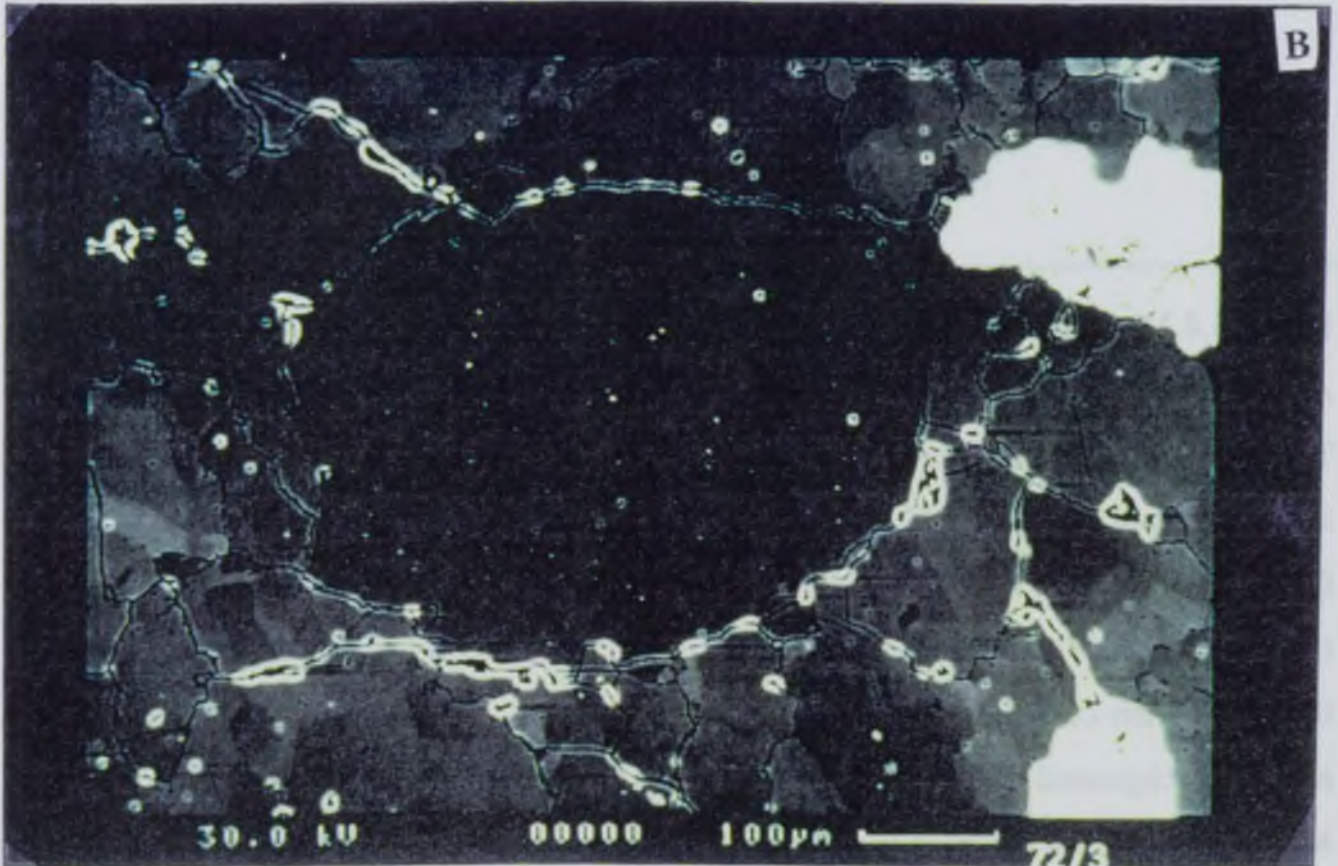
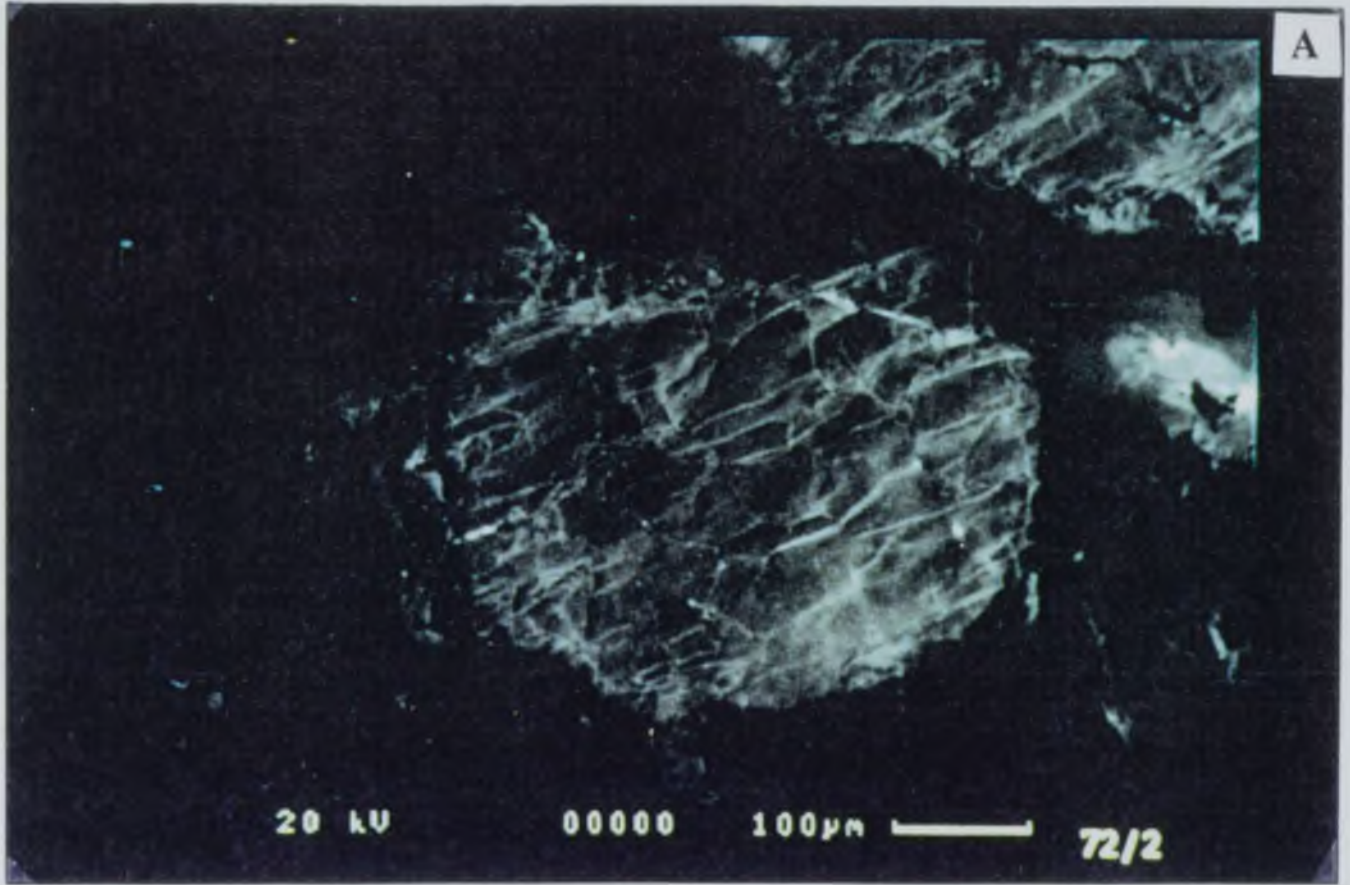
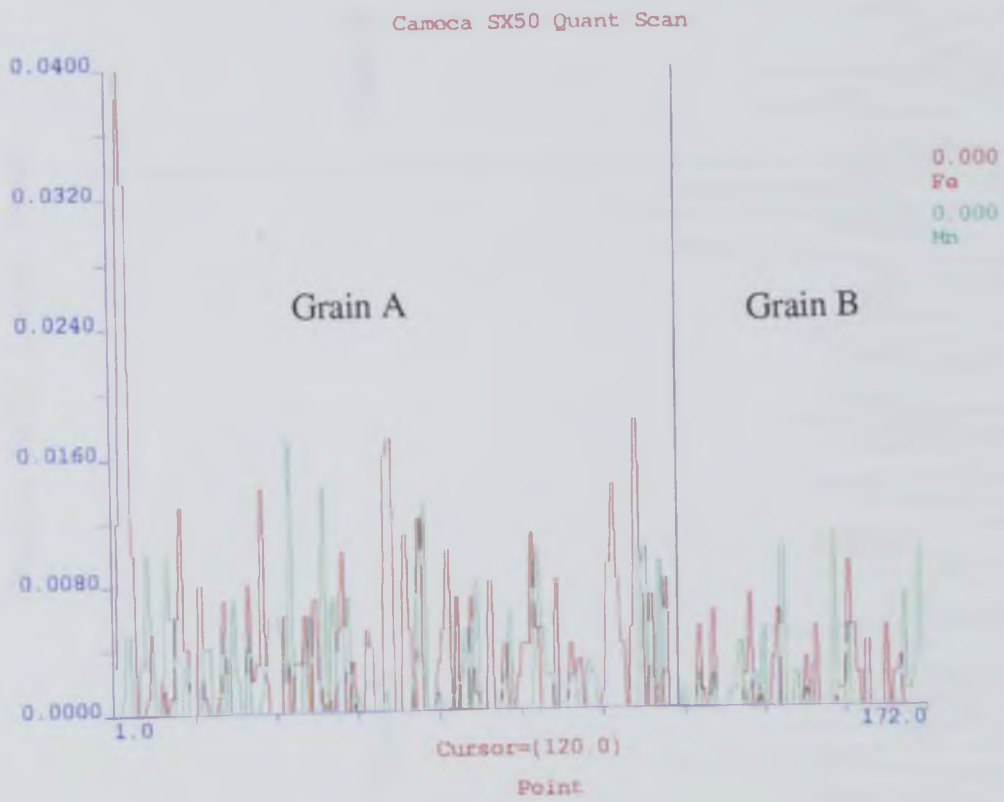
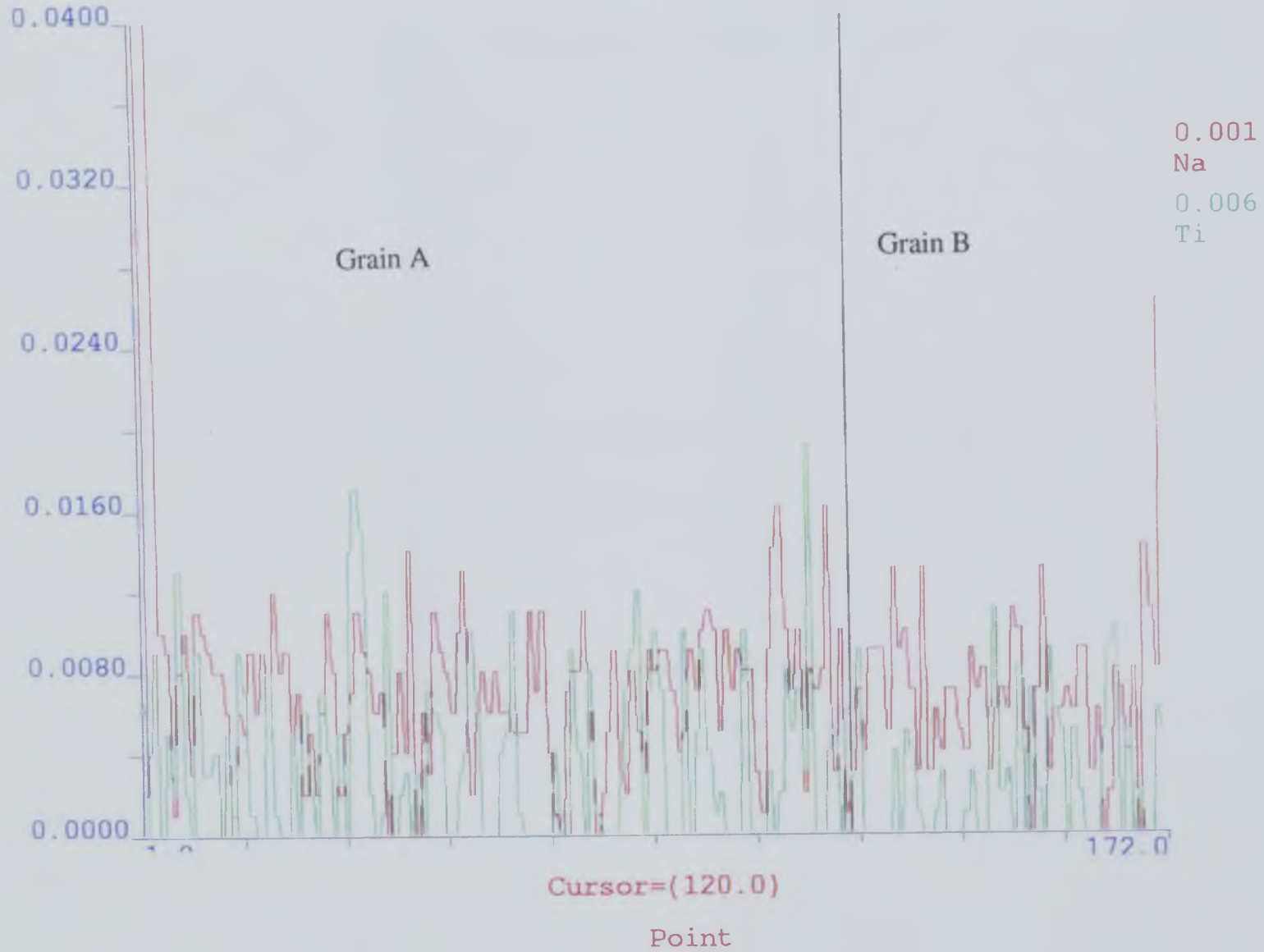
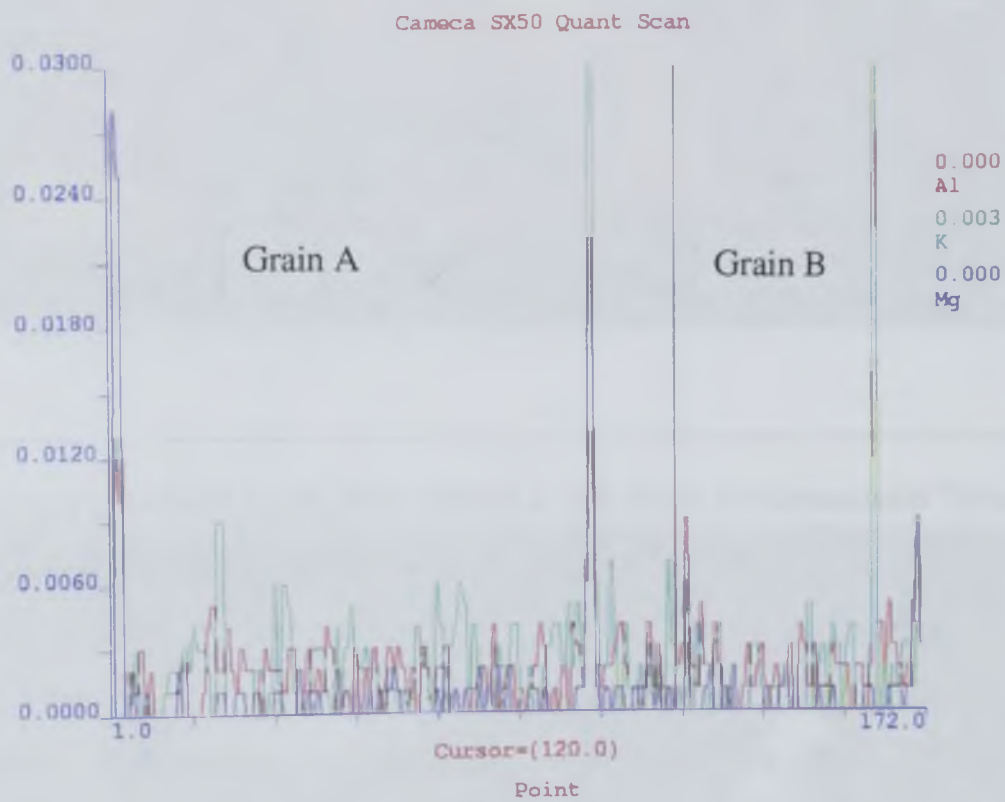


Figure 6.4 Microprobe analysis along a traverse through two neighbouring grains, grain A exhibits a mesh microstructure, whilst grain B has no intracrystalline microstructures. The diagram opposite and on the following two pages are analyses of different elements along the same traverse. The black line is the grain boundary separating the mesh grain (<120 on the x-axis) from the grain which doesn't exhibit a mesh microstructure (values on the x-axis >120). The analysis is theoretical below detection levels, yet the data from the Mesh grain contains distinctive peaks. These peaks are interpreted as real data and not just background data, the reasoning behind this is the fact that the peaks of Fe and Mn are consistently higher in the mesh grain than for the other grain in the traverse. The analyses for Na, Ti, Al, K and Mg show no specific trends other than background noise.



Cameca SX50 Quant Scan





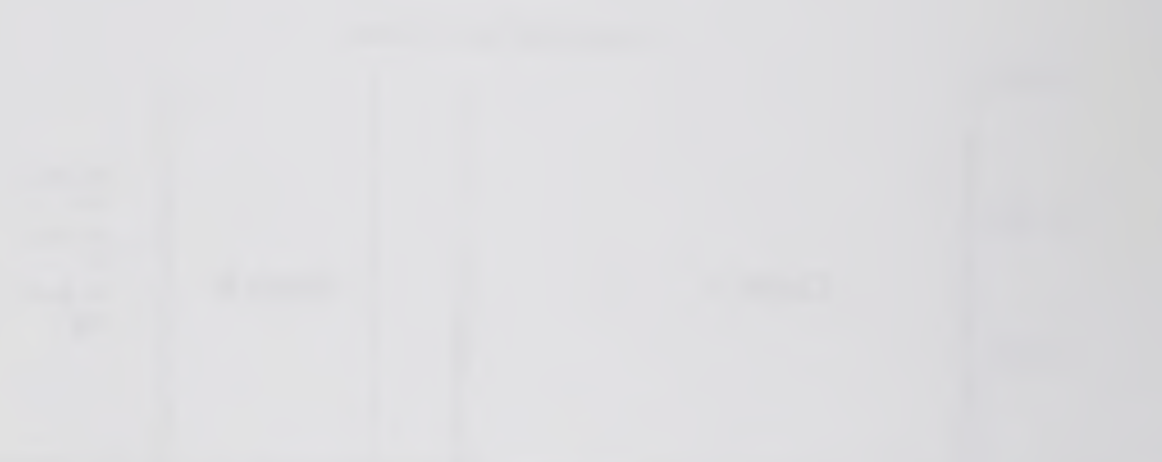
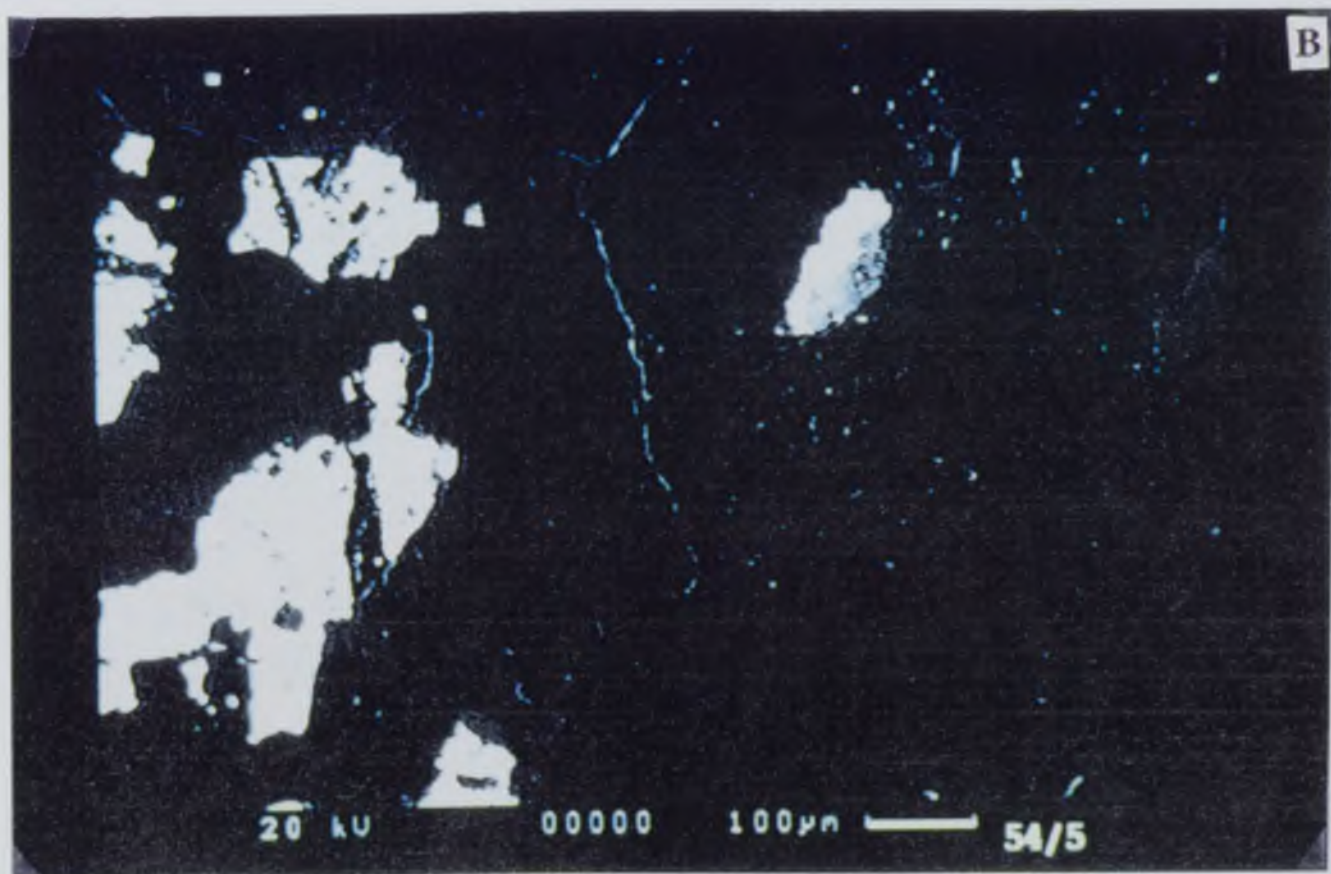
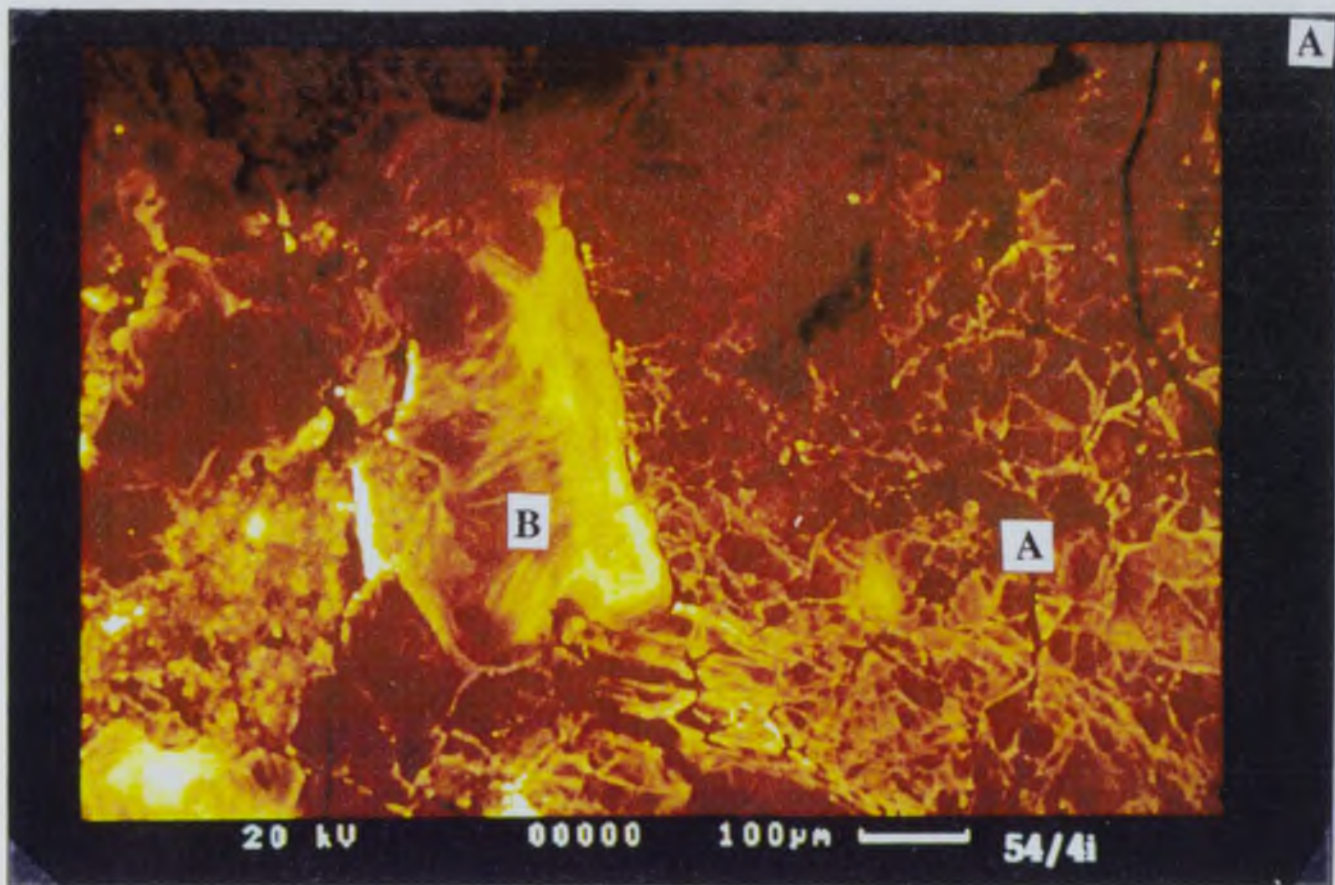


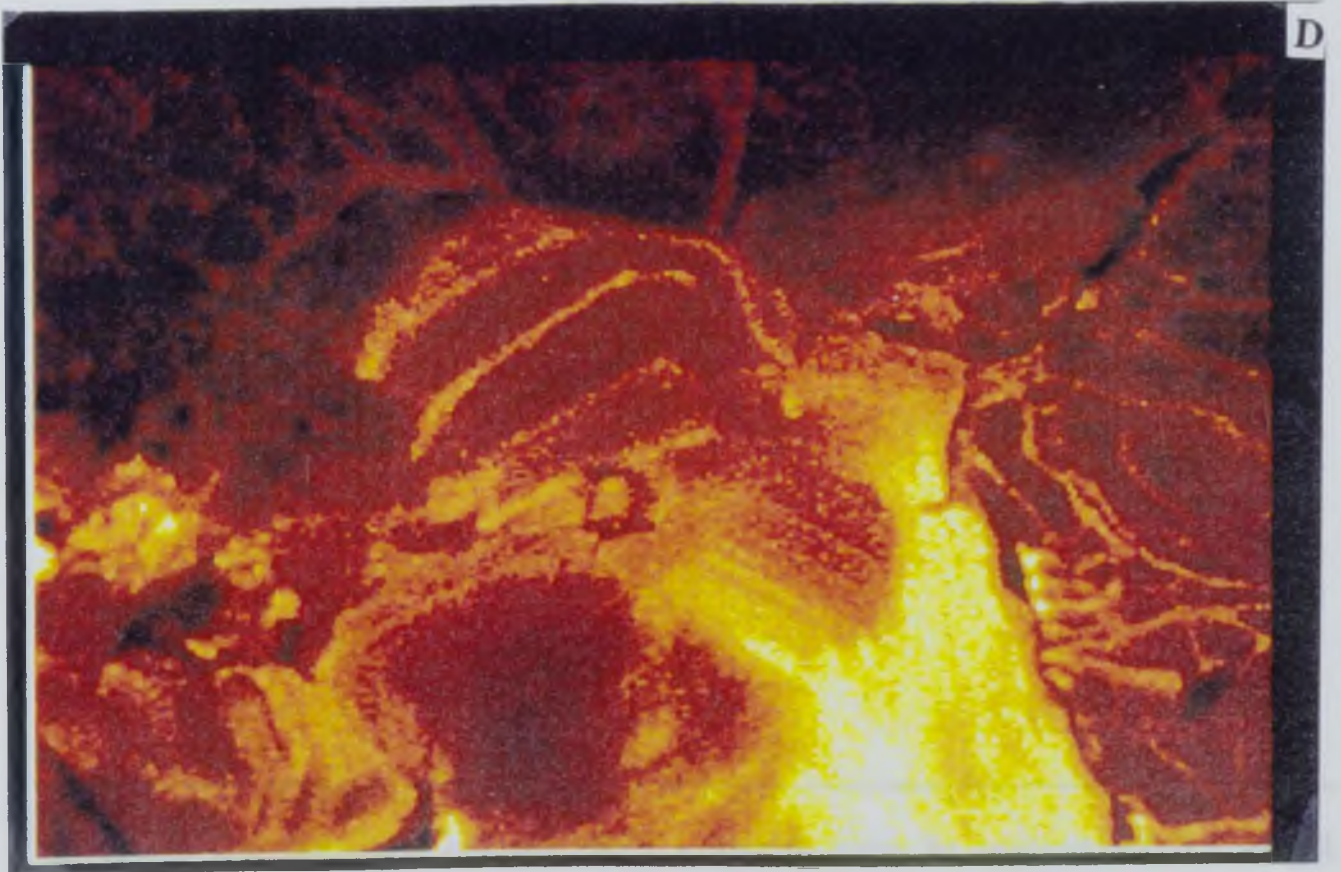
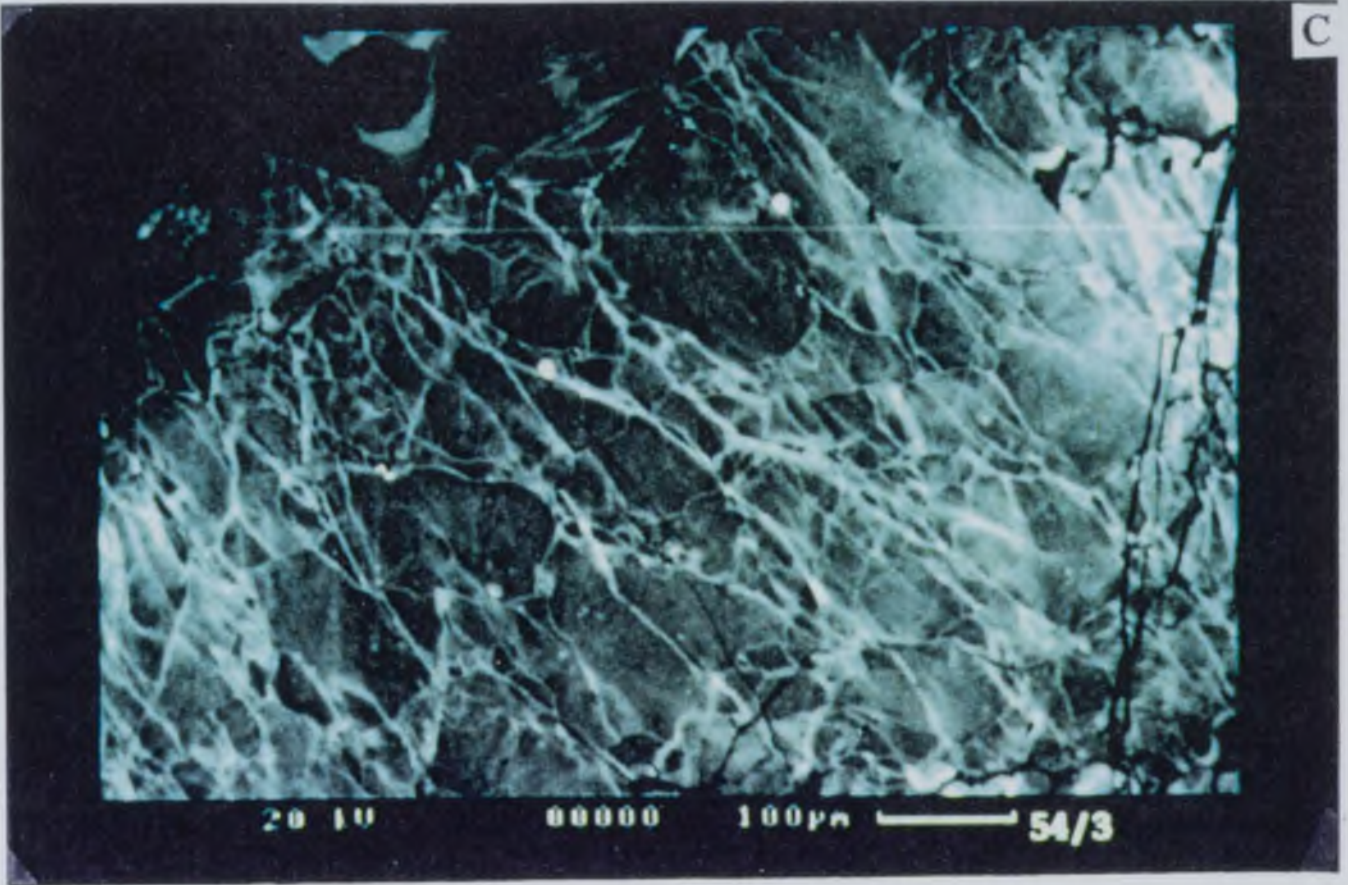
Figure 6.5 a) A 'mesh' microstructure (grain A) - a feature reflecting a fracturing process is developed adjacent to a grain with no deformational substructures (grain B). Note the growth zones in the surrounding grains. The separation of these growth zones enables the rates of grain boundary migration to be assessed, the wider the spacing the more rapid the migration. The growth zones are not well developed adjacent to the fractured grain suggesting that this grain is preventing grain boundary migration by the mesh microstructure, i.e. the mesh microstructure pins the movement of the grain boundary. On the other hand the growth zones at the ends of grain B are widely spaced, suggesting relatively rapid migration. Image is a false coloured SEM/CL image.

b) SEM/OC image of the same area of the sample.

c) The mesh microstructure at a higher magnification.

d) Growth zones within grain B have been enlarged to reveal the variation in spacing between the top of grain B and the right hand side of the grain which abuts against the mesh microstructure.





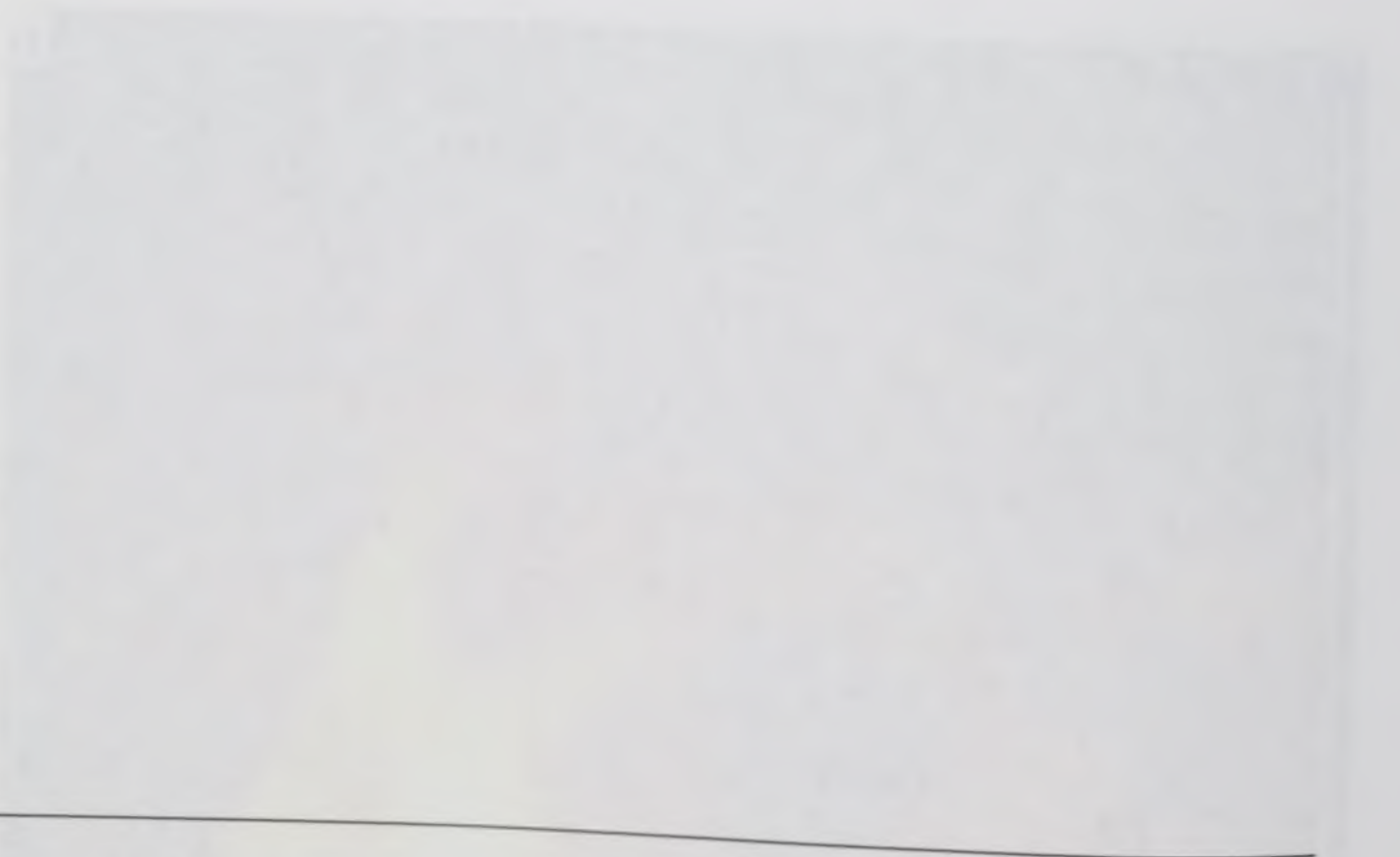
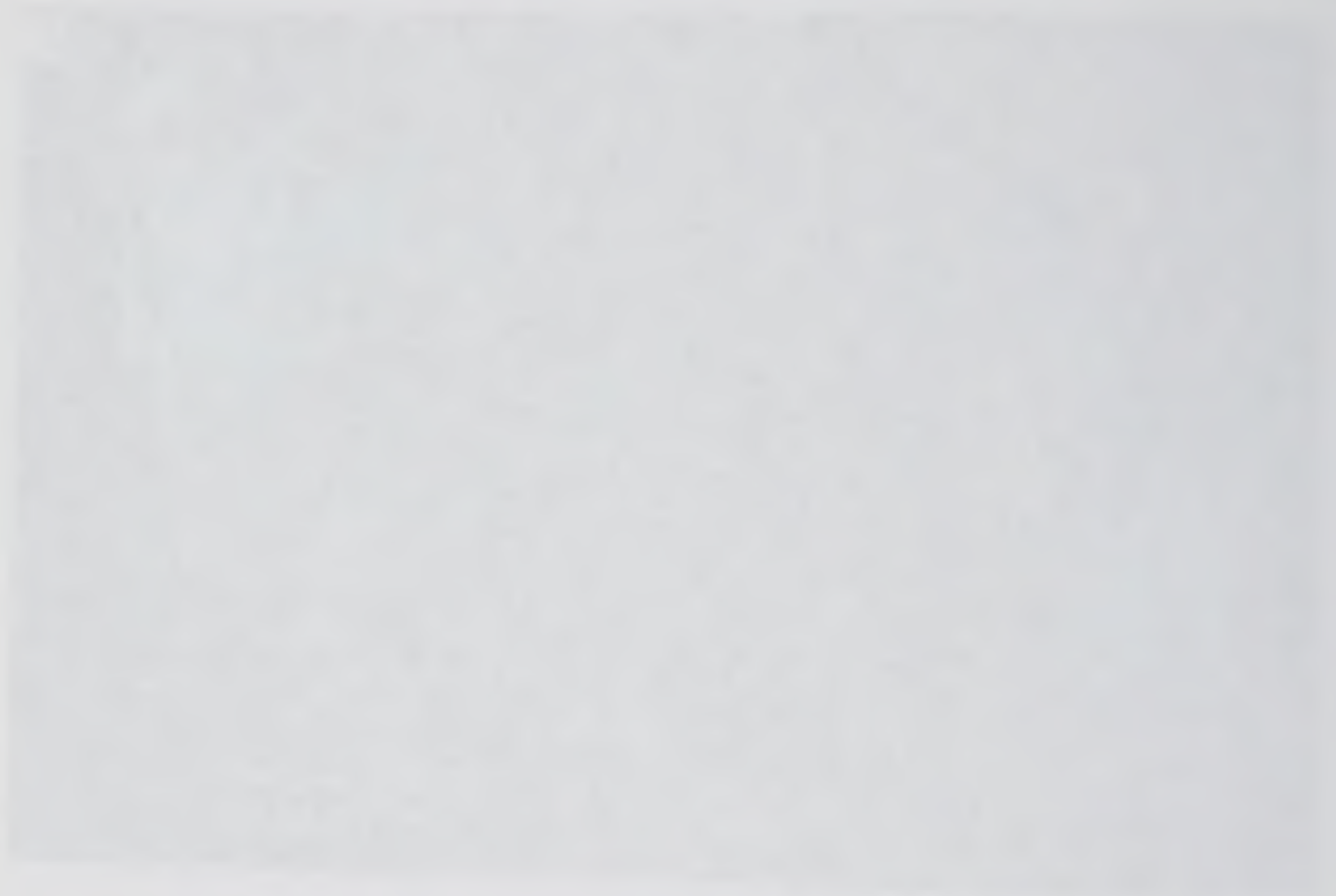


Figure 6.6 Mechanisms of grain growth - triple junction migration and neighbour swapping (modified from Jessel 1986).

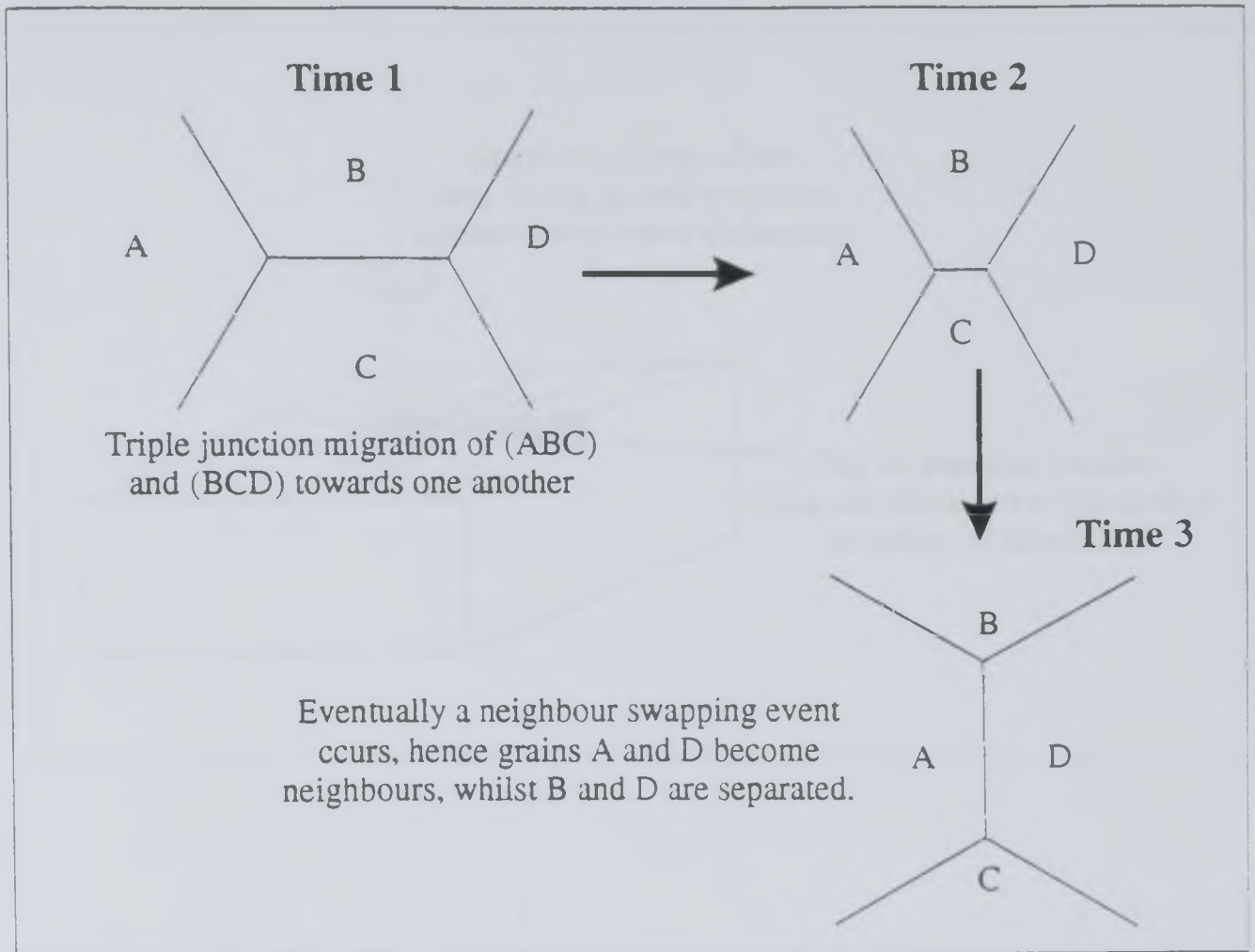


Figure 6.7 Growth of an interface in a spiral fashion, as atoms preferentially attach to the step on the interface. This process has been shown to produce linear screw dislocations. Although, this type of process was envisaged during growth of a mineral phase from a liquid Klapper 1980, similar kinks and steps on a grain boundary may result in similar mechanisms occurring during grain boundary migration.

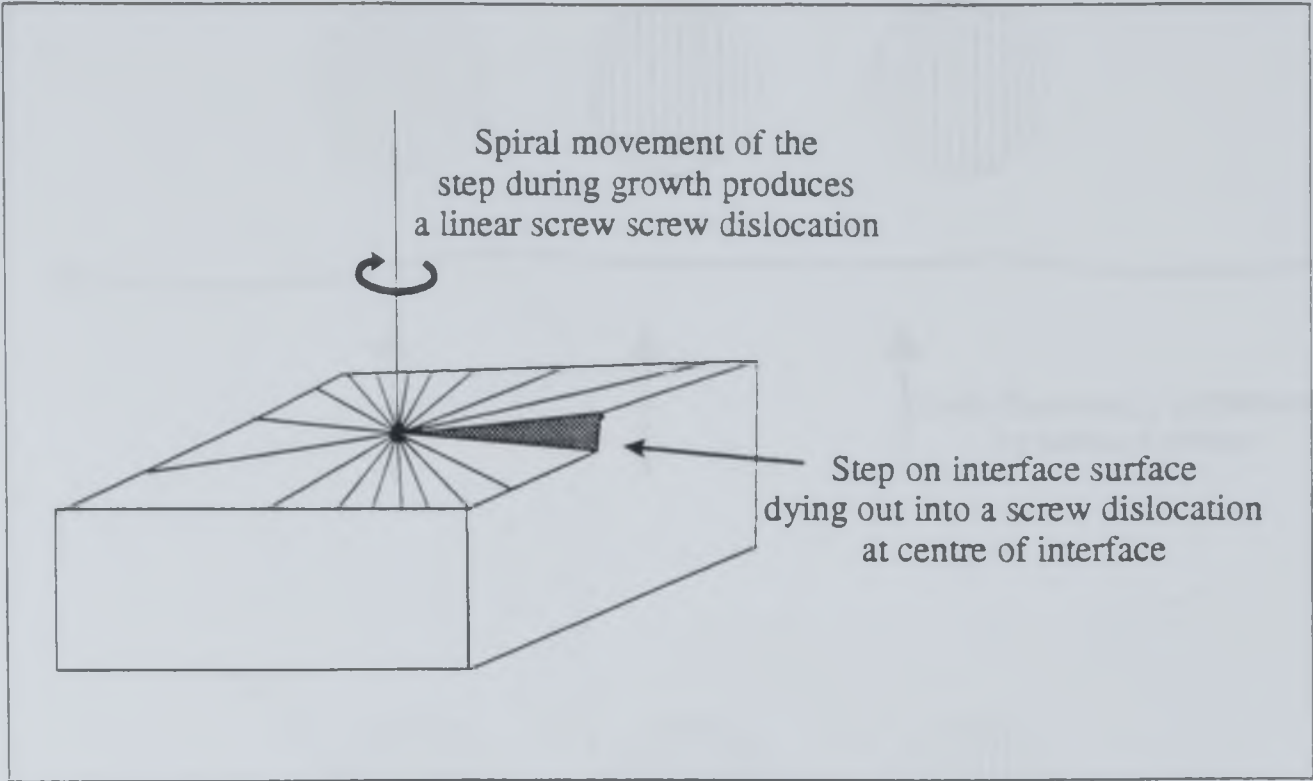




Figure 6.8 Second phase particles may hinder the migration of a grain boundary by 'pinning'. The degree to which a boundary is pinned is dependant upon both the size/distribution of the second phases and the mobility of the migrating boundary.

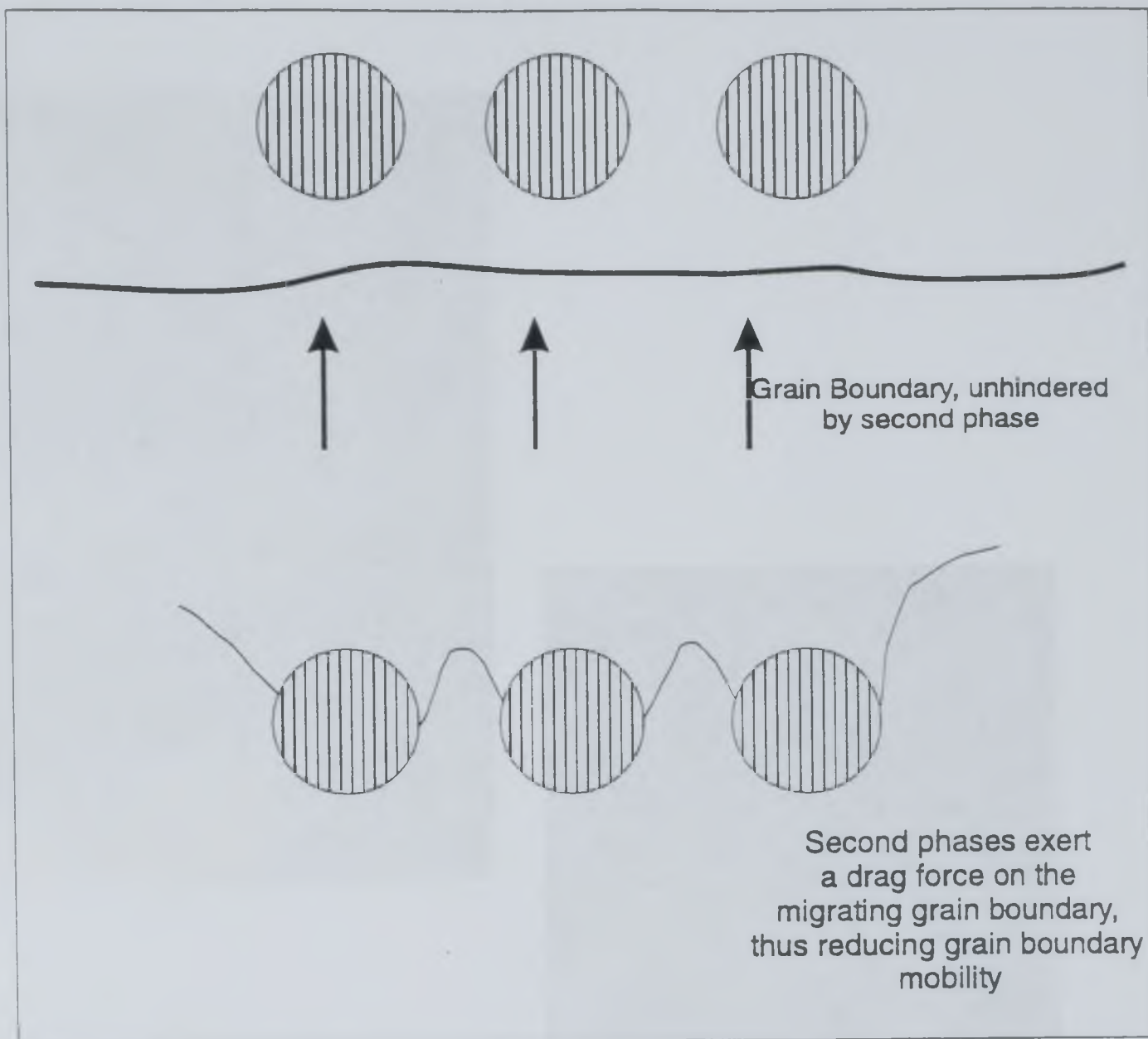




Figure 6.9 Nucleation event (crystal a) in a dichlorobenzene deformation experiment. Figures a, b and c are photographs taken at progressive stages of deformation. Note that once grain a has nucleated it gradually consumes neighbouring grains which have a high strain energy (reflected by undulose extinction and kink bands).



B



A



C




Figure 6.10 The effect annealing may have on crystallographic preferred orientations. The diagrams are schematic pole Figures describing both the type of CPO prior to annealing and the CPO after annealing. The experiments (a,b,c) were performed at increasing temperatures - a was deformed in the dislocation creep field, b in the dislocation climb and c dislocation creep together with grain boundary migration). Diagrams are compiled from the results described by Gleason and Tullis, 1990.

Deformed Fabrics

Annealed Fabrics

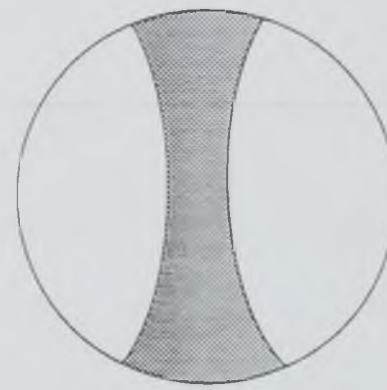
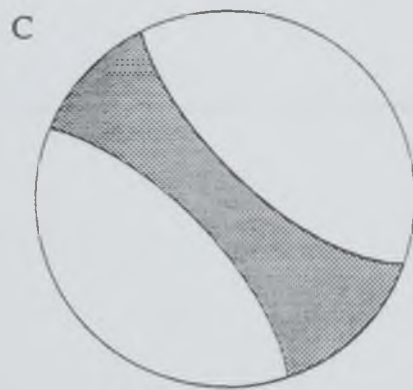
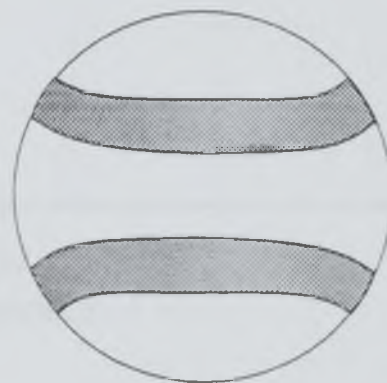
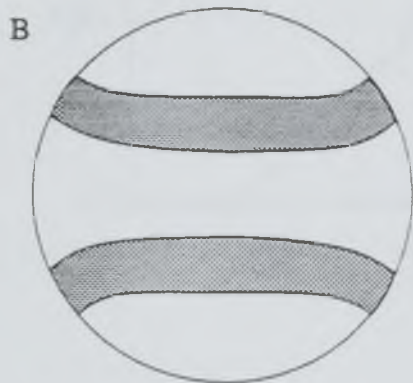
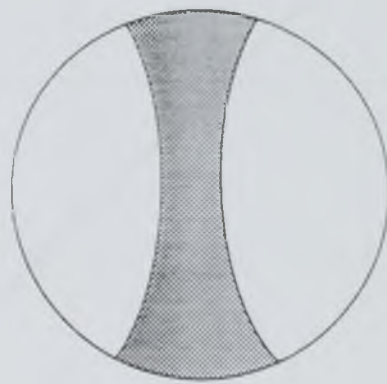
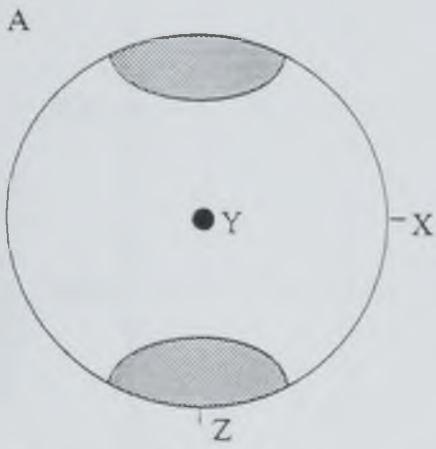
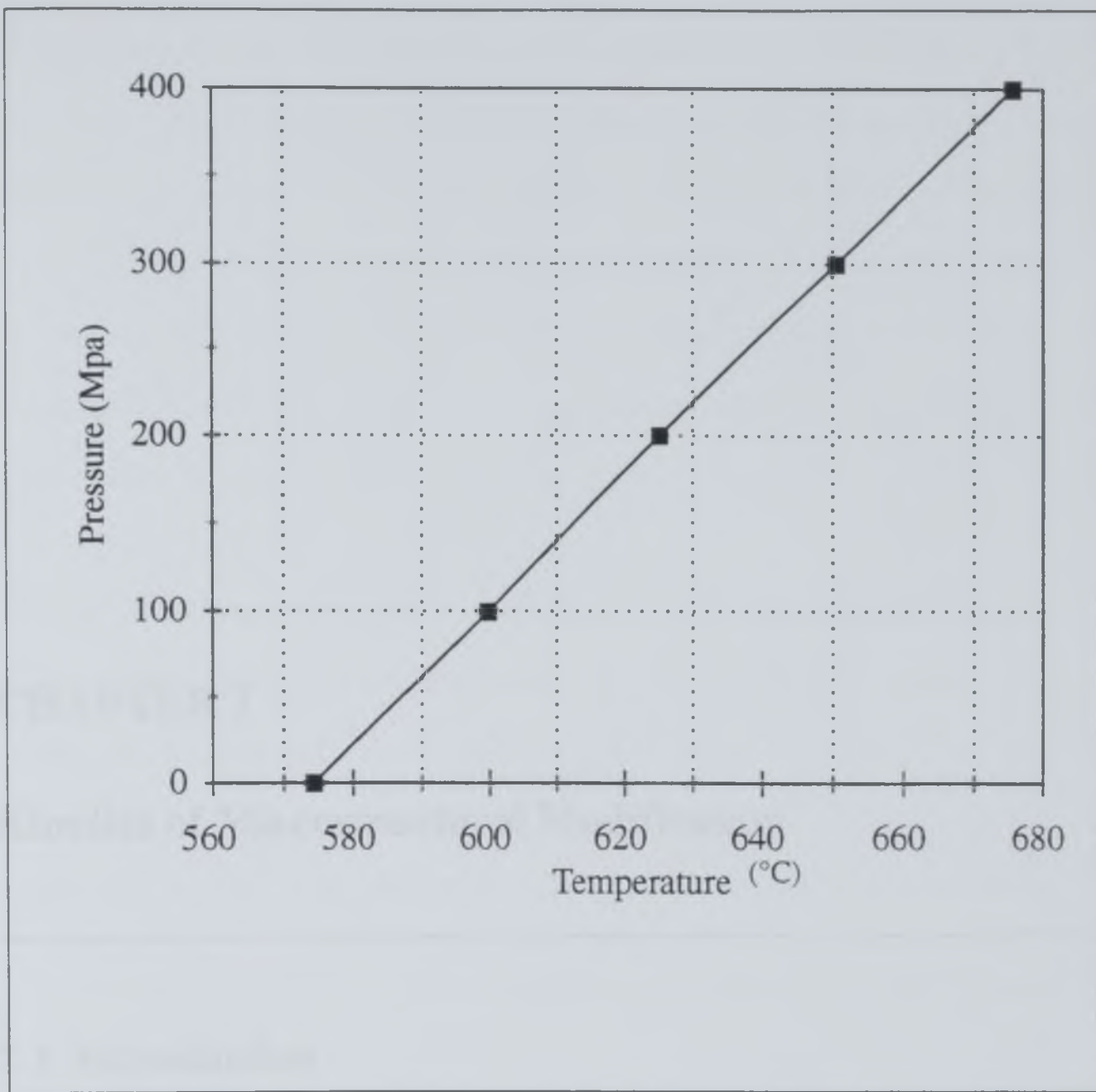


Figure 6.11 The variation of the temperature of the α/β quartz transition with increasing pressure (calculated from Shen et al. 1993). The pressures at Ballachulish are estimated at 0.28-0.3 Gpa by various authors (see Voll et al. 1991).



CHAPTER 7

Kinetics of Microstructural Modification

7.1 Introduction

For many years metamorphic and structural geologists have been striving to accurately predict the rates of geological processes (Rutter 1976; Twiss, Fisher 1978 Knipe 1989 and Lasaga 1986). The metamorphic geologist is only able to assess the pressure/temperature paths of rocks when the rates of the reactions used to predict tectonic conditions are thoroughly understood. The structural geologist interested in the rates of deformation in major fault zones needs to understand the kinetics of the various mechanisms by which rocks deform (Groshong 1972; Jamison and Spang 1976; Twiss 1977,1986; Mercier et al. 1977; White 1979; Christie et al. 1980; Ord and Hobbs 1989). Furthermore, any geologist using rock mineralogy or textures must calculate the degree

to which these features truly reflect the conditions within the Earth's crust (Hobbs et al 1986 and Sibson 1986). It is therefore crucial that we examine how rock mineralogy/textures may be altered during the rock evolution in order that we may answer the question: 'Do these rocks preserve information about the crustal conditions of pressures/temperatures, or have the rocks undergone subtle changes during their progression to the Earth's surface?' (Olgaard and Evans 1983; Kasen, 1983; Grant et al. 1984; Knipe 1989, Handy 1990).

This chapter investigates the kinetics of annealing within the relatively simple regime of the Ballachulish aureole, and applies the results of both theoretical and empirical models to other tectonic regimes. The chapter includes:

- Theoretical models of annealing (based on the processes identified in Chapter 6).
- A comparison of the kinetic models to the microstructural data set from Ballachulish (cf. Chapter 5).
- An analysis of the kinetic models to understand why there are discrepancies between these and the actual data from Ballachulish.
- An examination of how the models may be altered to predict more precisely the microstructural evolution at Ballachulish.
- Discussion of the implications of the Ballachulish data set for the kinetic models (i.e. are the models applicable to real geological situations?).
- Application of information gathered from Ballachulish to other tectonic regimes.

The kinetic analysis undertaken is described on a microstructural basis. Initially, the modification of grain microstructures are discussed, followed by kinetic models describing the evolution of subgrains through the Ballachulish aureole. Finally, a model is presented to show the alteration of microstructures that would be expected in a shear zone/fault zone after deformation, when the rocks are undergoing pressure and temperature changes.

Throughout this chapter, the fundamental aim is to present theoretical models which describe the rates of microstructural change and then to compare these models with the microstructural data/ interpretations which have been presented in previous chapters. A recurring theme therefore is the variation of the theoretical predictions of microstructural change from the real observations. This is because the natural system at Ballachulish is more complex than the kinetic models can describe. In nature drag forces together with the interaction of a number of microstructural processes may alter the kinetics of microstructural change. Thus, it is important to emphasise and understand just how these processes alter the kinetics of microstructural change in the geological setting at Ballachulish or any other geological regime.

Similar studies into the kinetics of grain growth at Ballachulish have been undertaken (Bunterbarth and Voll 1991 and Joesten 1992). This investigation is more detailed than either of the above because it investigates both a variety of microstructures and also the implications of impurities on kinetic models. All the calculations presented in this chapter are derived using the thermal models of the Ballachulish aureole as computed using the program Contact8.pas (Appendix A).

7.2 Grain Scale Kinetic Models of Annealing in the Ballachulish Aureole

7.2.1 Introduction

The kinetic analysis of grain size changes through the Ballachulish aureole is presented in two sections.

(1) Grain size changes in monomineralic quartzites. The data comes from Buntebarth and Voll (1991). Using data from petrographically monomineralic phases enables an assessment to be made of the affects solute clusters and/or precipitates may have on coarsening.

(2) Grain size changes in polymineralic quartzites using the data presented in Chapter 5. These samples enable a comparison to be made with monomineralic grain coarsening, in order to assess to extent to which relatively large second phase minerals (observed using optical microscopy) may influence coarsening and which region of the aureole these influences are most predominant.

7.2.2 Grain Coarsening Kinetic Model

Chapter 2 presented the theoretical derivation of kinetic equations used to describe grain coarsening within aggregates. The basic form of the equations are (Feltham 1957; Kingery 1976; Joesten 1983; Atkinson 1988 and Joesten 1992):

$$d \propto kt \qquad \text{Equation 7.1}$$

where k is a temperature dependent diffusion coefficient and t is time. In this geological setting the temperature is not constant. Thus, non-isothermal grain coarsening models are required to describe the microstructural evolution. It is necessary to calculate changes in a microstructural element by integrating the above equation through a temperature time history for each point within the aureole (using Contact8 -Appendix

A). Figure 7.1 shows the evolution of temperature in the Ballachulish aureole as a function of time (the data is calculated using contact8.pas - Appendix A).

The theory of the kinetics of grain coarsening by normal grain growth has been described in Chapter 2. Joesten (1983) developed an integrated form of Equation 7.1 to describe normal grain growth within a non-isothermal regime:

$$\frac{l_i^2 - l_0^2}{2} = k \int_{t_0}^t \frac{1}{T(t)} e^{-\frac{Q}{RT}} dt \quad \text{Equation 7.2}$$

where l_i and l_0 are the grain size and initial grain size respectively, R the gas constant, T temperature and t time. This formula has a theoretical basis described by Atkinson (1986). The pre-exponential factor (k) is a material parameter which describes the surface energy of grains, together with the mobility of atoms within the grain boundary. Q is the activation energy needed to diffuse the atomic species responsible for grain boundary migration within a material.

In the setting of Ballachulish we know the original grain size, the grain size at various distances from the igneous intrusion and the thermal history of the aureole. We may therefore calculate possible values for the pre exponential factor (k) and the activation energy of diffusion in quartz from the relationships in equation 7.1. The methods employed to recover values of k and Q are described by Joesten (1991). A graph of variation of $\log(l_i^2 - l_0^2)$ versus distance from the igneous contact is essentially a graphical solution of equation 7.1, the intercept value of $l_i^2 - l_0^2$ on the y-axis being proportional to k and the slope of the line proportional to Q . The equation may be solved at 0m from the contact using the a value of $k = l_i^2 - l_0^2 / 2$ and an arbitrary value of Q . Using these values of Q and K the time integral is solved for each point in the aureole. The process is then repeated adjusting the value of Q until the calculated grain size for each point in the aureole most closely matches the actual grain size. Figure 7.2 shows one such example using values of $k = 5.329 \times 10^{-6} \text{ } ^\circ\text{K/s}$ and $Q = 210000 \text{ J/mol}$. These figures are recovered using grain size data from Buntebarth and Voll (1991) which are taken from pure quartz samples within the Ballachulish aureole, the thermal model used is calculated from the program contact8.pas.

Buntebarth and Voll (1991) presented a slightly different model for grain coarsening, whereby the grain size is related to the time integral by an exponential of 3:

$$\left(\frac{L}{L_0}\right)^3 - 1 = kt \quad \text{Equation 7.3}$$

They inserted a threshold temperature into the Arrhenius constant because there seems to be a limit of 625°C below which coarsening does not occur (i.e. rocks at distances greater than 750m from the contact have not coarsened as they have not attained the threshold temperature). The Arrhenius coefficient then becomes:

$$k = k_0 \left(e^{-\frac{Q}{RT}} - e^{-\frac{Q}{RT_0}} \right) \quad \text{Equation 7.4}$$

Joesten (1991) has suggested this kinetic model is not applicable to Ballachulish as it has no experimental or theoretical basis and it overestimates grain size throughout the aureole. Thus, for this investigation only the equations as defined by Joesten (1983) have been used (Equation 7.2).

7.2.3 Monomineralic grain coarsening

7.2.3.a Comparison of theoretical model to Ballachulish Data

The non-isothermal coarsening model presented in Figure 7.2 has been produced using a temperature history for the aureole calculated by contact8.pas (see appendix A and Figure 7.1). The model indicates that there are major differences between what we actually see at Ballachulish in terms of grain coarsening and the model's predictions. Three regions may be defined where the relationship between the theoretical kinetic model and the observed grain size values change.

- (1) The actual grain sizes measured and the grain size calculated from the model are in close agreement between 0-600m from the igneous intrusion.

(2) At distances greater than 600m the observed grain diameters diverge from the model predictions, plummeting to values which are far lower than expected.

(3) At distances greater than 750m grain size measured from samples are stable. Such stabilisation is not predicted from the kinetic model until 2000m from the igneous intrusion.

The parameters which have been input into the kinetic model cannot be changed to fit the Ballachulish data. For example, if the activation energy (Q) was increased, coarsening would indeed become inhibited in the outer parts of the igneous aureole and it would be possible to predict a grain size of 0.143mm at 750m from the contact. However, an increase in the activation energy would result in a gross underestimation of the grain size at the igneous contact. It can therefore be seen that no individual kinetic model can adequately describe the microstructural trends within the Ballachulish aureole. Thus, microstructural modification in the Ballachulish aureole is more complicated than the kinetic models can describe.

The microstructural evolution within the Ballachulish aureole is dominated by three zones, each with distinctive microstructures. Within each zone, the rates of microstructural change are also different. It is therefore useful to describe the kinetics of each zone as a separate entity. Thus, the activation energy in equation 7.2 may be altered to fit the observed grain size data at Ballachulish with a separate kinetic model for each of the zones. The activation energies which most adequately describe the microstructural evolution of the individual zones are (the calculations have been performed using a Mixedac.Pas - see enclosed diskette):

	Activation Energy (J/mol)
Zone I	240,000
Zone II	155,000
Zone III	212,000

The activation energies quoted in the table above reveal how different microstructural processes may radically affect the rates at which a textures evolve. The relationship between the effective activation energy for each of the zones and diffusion processes are unclear. For example, do chemical impurities interact with diffusing species to decrease the rates of diffusion in Zone I, or in Zone II is rapid diffusion occurring along microstructural features (i.e. subgrain walls and dislocations)?

7.2.3.b Microstructural Controls on Grain Sizes at Ballachulish

Each zone within the aureole has been examined to determine those microstructural controls on the evolution of microstructures which may result in the observed microstructures departing from the predictions of the kinetic models. The kinetic analysis has indicated that the behaviour of rocks is more complex in nature than laboratory experiments or theoretical models predict. The following discussions use the microstructural observations (cf. Chapter 5) to interpret which microstructures/processes cause these rocks to behave differently than expected, thereby characterising the important controls on microstructural modification within the aureole.

Zone I (deformational microstructures)

Evidence has been presented in Chapter 6 to show that nucleation of new grains during the first stages of annealing is common. This would reduce the mean grain size that is measured from a sample because newly nucleated grains are small. It is therefore plausible that nucleation is responsible for the variation in observations from the theoretical models. However, wholesale nucleation of grains at distances between 750m and 2000m would produce a microstructure with few deformation-related substructures, and yet deformation microstructures are preserved throughout this region, even at 700m from the intrusion. Thus, a nucleation model to explain inhibited grain growth may be discounted on the grounds of microstructural evidence.

Alternatively, the presence of small concentrations of impurities/solute atoms attracted to the core of grain boundaries (Lucke and Stuwe 1971; Poirier 1985) may reduce the capability of a grain boundary to migrate by impurity/solute drag (essentially a small scale pinning of grain boundaries - see Figure 7.3). Thus, although our monomineralic

coarsening model (which takes no account of drag forces) predicts grain growth, it is in fact inhibited because impurities prevent grain boundaries from migrating. Figure 7.4 (from Poirier 1985) indicates that as the driving force for grain boundary migration becomes greater, grain boundaries are able to break free from the impurities and migrate as predicted in the monomineralic models. Within the Ballachulish setting it can be seen that it is at 750m that grain coarsening ensues. If impurity drag is responsible for inhibition of grain growth at distances >750m, it is at 750m when the driving forces for grain growth become large enough to overcome impurity drag.

Zone II - Rapid grain growth (Primary Recrystallisation)

At the outer boundary of Zone II the grains are c. 150 μ smaller than the normal grain growth model predicts. If normal grain growth occurred in the rocks once impurity drag had been overcome, the grain size at the igneous contact would be expected also to be 150 μ below the estimated value. However, at the contact the values of the model and the observed value are similar. Between 750m and 600m from the igneous contact the observed grain size increases more rapidly than the theoretical grain size during grain growth and hence the discrepancy is reduced. Thus, in this region (Zone II) grain growth is far more rapid than anticipated. Again, the microstructures developed within Zone II hold evidence for the mechanisms of enhanced grain growth. It is within Zone II that deformation related microstructural features such as deformation lamellae, subgrains and grain boundary shapes, are eradicated and replaced by an annealed microstructure. The process by which this occurs, outlined in Chapter 6 is dynamic recovery (otherwise known in a static regime as primary recrystallisation). During primary recrystallisation, the driving force for grain growth isn't just a reduction in surface energy of grain boundaries (although this may still play a part), but predominantly a reduction in strain energy causing strain induced grain boundary migration within the aggregate. The rate at which grains within an aggregate grow depends on the variation in strain between grains and the types of microstructures developed within the aggregate (e.g. dislocation density, subgrain size/misorientation, twins, deformation bands, etc.).

Ardrade and Abaov (1966) and Covey-Crump and Rutter (1989) have suggested that the rate of grain growth during primary recrystallisation obeys the empirical relationship,

$$N_D = N_0(1 + p \exp(-Qt))$$

Equation 7.5

in which $N_D = 1/D$ ($D =$ grain diameter), N_0 and p are constants dependent on temperature and initial grain size respectively. Kinetics of coarsening, as described by equation 7.5 enhance the growth rate relative to that expected from normal grain growth models described earlier by Equation 7.2. Grain growth is not modelled using this formula because Covey-Crump and Rutter (1989) do not define the dependence of the constants with temperature. Without this information it is not possible to integrate the equation through the non-isothermal temperature history at Ballachulish.

7.2.3.c Zone III - Normal Grain Growth

A normal grain growth model is presented in Figure 7.6, predicting the evolution of grain size in Zone III from an initial grain size of 425μ , which is the grain size produced after primary recrystallisation has reached completion. This shows that the theoretical normal grain growth model closely matches the observed values of grain size in monomineralic samples (measurements from Buntebarth and Voll 1991).

The observed grain diameters are slightly smaller than the theoretical grain diameters at distances of less than 150m from the intrusion, an observation also made by Joesten (1991). Joesten (1991) indicated that it was possible that grain size diameter stabilised at distances less than 150m from the intrusion. Such a phenomena, whereby grain size stabilises during grain growth, has been described by Covey-Crump and Rutter (1989) (see Equation 7.5). Abaov (1971) views decreasing growth rates as a result of solute atoms accumulating on the grain boundaries during migration until the boundaries become pinned by solute/impurity drag (for further reviews see Grant et al. 1984 and Kasen 1983). Solute drag may be more pronounced in aggregates with a large grain size because the driving force for growth reduces as a function of grain size (Atkinson 1989). Second phase impurities therefore may add to the effect and further inhibit grain boundary migration.

Impurity Controls on Grain Growth

It has been shown that impurity content along grain boundaries, or within grains (as they are consumed) may greatly influence the rates of grain growth by exerting drag forces upon migrating boundaries. Drag forces have been shown to possibly be of greatest importance in the outer aureole (Zone I) and the inner aureole (Zone III). It is these zones where the driving force for grain boundary migration is low, either as a consequence of low temperatures (in the case of Zone I) or low energy grain boundaries because of the large grain size in the case of Zone III - cf. Chapter 5).

It is possibly the most important conclusion to make from this investigation that impurities, at all scales, may alter the rates and processes of microstructural evolution. The role of impurities on microstructural evolution both in the Ballachulish aureole and in other geological settings is crucial for future investigations. We need to characterise the following:

- (1) The scale (i.e. solute atoms, grain boundary precipitates or second phase particles), and type of impurities which affect the microstructural evolution of quartzites in specific parts of the aureole.
- (2) The mechanisms of interaction between the different types of impurities and individual microstructures. For example, are impurities consumed by a migrating grain boundary; are they swept along in front of a grain boundary; or do they pin the grain boundary?
- (3) Impurity processes as a result of their interaction with microstructures. This may be illustrated by considering solute/precipitate clusters which have been inferred to prevent grain coarsening in the outer aureole. When eventually grain boundaries become sufficiently mobile to overcome the pinning forces, what is the effect on the impurity configuration/content within the rock.

The next section deals with the potential effects of second phase impurities (i.e. feldspar) on grain coarsening at Ballachulish. It would be interesting to also investigate the chemical variation of a variety of chemical species throughout the aureole in order to

determine if there is any dynamic variation in chemistry as a result of microstructural processes.

7.2.3.d Summary

The kinetic model for normal grain growth in the Ballachulish aureole reveals that the actual observed grain sizes are somewhat more complex than the model predicts. Briefly: grain growth is inhibited in the outer aureole (Zone I) by impurity/solute drag; it initiates at 750m from the contact (Zone II) by dynamic recovery processes, probably dominated by strain induced grain boundary migration; whilst normal grain growth occurs in Zone III, with the observed and theoretical grain sizes being in close agreement, although it is possible that the growth rate begins to slow down in the inner aureole (<150m from the contact).

7.2.4 Grain coarsening in Polymineralic Samples

7.2.4.a Introduction

The discussion of grain growth thus far has concentrated on monomineralic samples using grain size data from Buntebarth and Voll (1991). In this section, grain size data collected during this investigation from samples which have between 10 and 20% feldspar impurities are inspected. Quartzo-feldspathic rocks such as these are far more common in geological settings than pure quartzites. Producing kinetic models of quartz coarsening in impure quartzites in the Ballachulish setting, will aid prediction of how polyphase rocks may react to temperature histories in other tectonic settings.

7.2.4.b The Kinetic Model

In the quartzo-feldspathic samples examined within this study, observed grain sizes are considerably lower than the observed grain sizes reported by Voll from pure quartzites (compare Figure 7.3a with Figure 7.3b). Feldspar impurities obviously hinder grain growth, thereby the kinetics depart from normal grain growth kinetics.

Two approaches may be taken to model the effect of impurities on grain growth. The first method accounts for the effects of second phases on the mobility of grain boundary migration (Hillert 1965). The second method is an empirical approach which describes the grain growth using 'effective activation energy'. Hillert's method accounts for the pinning effects of second phases based on the size and distribution of these phases and thus calculate the extent to which grain growth is inhibited. Such an approach is complex in both defining the energetics of pinning and the distribution of the second phases. This will not be dealt with any further.

The grain coarsening of impure quartzites is calculated in exactly the same way as for monomineralic coarsening, by solving Equation 7.2. It will be shown that the reduced grain sizes result in the calculated activation energies being higher for polymineralic rocks than when the coarsening equation is solved for monomineralic samples.

The material constant Q (unlike monomineralic samples), is an 'effective activation energy which describes grain growth in polymineralic rocks. This is a useful concept because an effective activation energy may be used by other workers interested in grain growth in polymineralic rocks, where there is a less well constrained thermal framework, as in the Ballachulish aureole.

Figure 7.7 is a polymineralic kinetic model to describe grain growth within the Ballachulish aureole. The model keeps the pre-exponential factor (K) the same as for the monomineralic model and then alters the activation energy in order for the model to predict the observed grain size changes in polymineralic rocks through the aureole. The effective activation energy for diffusion which fits the polymineralic data set (Figure 7.3b) is 223000 J/mol at a K value of $5.329 \times 10^{-6} \text{ m}^2\text{K/s}$. Note that the values of grain size near the contact are considerably smaller than the kinetic model predicts. It is plausible that this is not only related to solute drag (as discussed with respect to the monomineralic kinetic model) but to a greater degree by impurity drag by the second phases. Although impurity drag affects all the samples through the aureole (impeding the rates of grain growth), the affects of impurities may become increasingly important at greater grain sizes. Atkinson (1988) has shown that the driving force for grain growth gradually diminishes as grains reach greater and greater diameters. As the driving force for growth diminishes, the ability for grain boundaries to overcome drag forces also

diminishes (see Figure 7.4). Thus the competition between driving forces and drag forces may explain the departure of the observed grain sizes from the calculated grain size in the kinetic model.

The effect of grain size on growth rates may be investigated using normal grain growth models at constant temperatures. These effects have been modelled using a constant temperature coarsening model for initial grain sizes of 0.1mm and 0.01mm at temperatures of 600°C, 800°C and 1000°C (this is a repeat of the models presented in Joesten 1991). It is seen that there is a lag time before grains begin to grow. The length of the lag time is proportional to the initial grain size. Thus, small grains grow relatively rapidly (after just 1 year at an initial grain size of 0.01mm), yet larger initial grain sizes have a longer time period before the onset of growth (c. 100 years for an initial grain size of 0.1mm). Eventually logarithmic growth is attained, shown by the straight line on the graphs in Figure 7.8. The significance of this is that at the stage logarithmic growth occurs for a particular initial grain size, anything which originally had a smaller grain size has caught up and thus both samples would have the same grain size. Figure 7.8 shows that a quartz aggregate coarsening for 8000 years at a temperature of 800°C will reach a grain size of 200 μ for any samples which had an initial grain size of less than 0.1mm. In other words grain sizes will have equilibrated irrespective of the variation of the initial grain size.

The equilibration of grain sizes during annealing has profound implications for structural geologists/geophysicists studying deformation features within shear zones or in folded regimes. Grain size reduction within tectonites is often the main evidence used to indicate that a rock has been deformed (Twiss, 1977; White 1975). Furthermore, it is frequently used to infer the stress magnitude which the rock experienced during deformation. In an area of shear zones it is often seen that grain sizes within the shear zones (where deformation is localised) are far smaller than the surrounding undeformed rocks. Typically within a shear zone grain sizes may reach as little as 30 μ . Figure 7.8 reveals that if this deformed shear zone was kept at 600°C for just 1 million years then the grains within the shear zone would equilibrate with surrounding non-deformed rocks with an initial grain size of 100 μ . If this situation did arise it would be very difficult, perhaps impossible (in the absence of strain markers), to recognise that a shear zone had ever been situated in that area.

7.3 Kinetics of Subgrain Coarsening

Subgrains are potentially the most accurate means with which to investigate the kinetics within the Ballachulish annealing framework. Impurities and solute atoms on grain boundaries can have considerable influences on the kinetics of grain growth and deformation substructures may cause grain kinetics to depart from the expected simple normal grain growth in impurity free aggregates. Subgrains, potentially, interact in a different manner with second phase particles, precipitates and solute atoms. Thus, it is necessary to undertake a kinetic analysis of subgrain evolution and compare the results to the Ballachulish aureole (the microstructural analysis of subgrains was presented in Chapter 5/6).

It is well established that dislocation cores (especially when located within a subgrain boundary) have attraction forces capable of trapping diffusing solute atoms (Blacic and Christies, 1983). Three types of calculations are used to model the evolution of subgrains in the Ballachulish aureole, as follows

(1) A normal grain growth model, which is identical to that of the monomineralic model grain growth model (section 7.2.3) except that the initial grain size is 20μ (i.e. the subgrain size of rocks which are unaffected by the igneous intrusion) instead of 143μ which was used in the grain coarsening model. This model treats subgrain boundaries in the same manner as grain boundaries in that they have a surface energy driving subgrain boundary migration. Thus, subgrains may react in a similar manner to grains when temperatures increase sufficiently to permit coarsening on a geological timescale. The diffusion coefficients and activation energies used to predict the evolution of subgrain size through the Ballachulish aureole are the same as those used in the monomineralic grain coarsening models (section 7.2.3).

(2) A model which recalculates the pre-exponential factor in the normal grain growth equations to account for the lower surface energies associated with subgrain boundaries.

(3) A subgrain growth model, in which coarsening is controlled by the rates at which the dislocations forming the subgrain boundary are able to climb.

7.3.1 Results

Simple Subgrain Growth Model

The predicted coarsening of subgrains within the Ballachulish aureole is calculated using the monomineralic growth model presented in section 7.2.3 and the temperature history in Figure 7.1. Values of Q (activation energy) and k (pre-exponential factor) are 210000 J/mol and $5.329 \times 10^{-6} \text{ m}^2\text{K/s}$ respectively.

The theoretical model indicates that subgrains would be expected to start coarsening at distances of 2700m from the igneous contact (see Figure 7.10). Their size should become a logarithmic function of distance from the intrusion from 1500m to the igneous contact, plotting as a straight line on Figure 7.10. The initial growth rate of subgrains is far greater than the growth rate of grains predicted from the monomineralic grain coarsening models (Figure 7.2) up until 600m from the igneous contact at which point growth rates of both grains and subgrains become equal. This variation in growth rate between models with different initial grain size is expected, and reflects the lag time in grain growth associated with a larger initial grain size in comparison to 20 μm subgrains (described above). Importantly, this model predicts that at 600m from the igneous contact subgrains would be indistinguishable from grains because their sizes have homogenised.

In this model, subgrains are predicted to disappear throughout the outer aureole (i.e. at distances >2700m), which is clearly this is not the case. Again actual observations at Ballachulish indicate that the natural processes are more complex than kinetic models predict. The gradual coarsening of subgrains from a distance of 2500m is not observed in the Ballachulish aureole. Subgrains, occurring in rocks at 700m, have subgrain sizes of a similar size to samples from 3000m (c. 30 μ), whilst the model predicts the subgrains to be 180 μ at 700m. Evidence from the aureole shows that subgrain coarsening possibly only occurs between 600m and 700m (cf. Chapter 6), indicating that subgrains are a highly stable microstructure.

A number of possibilities exist to explain why subgrains are not seen to coarsen at distances greater than 700m. Firstly, the kinetic model chosen to describe subgrain coarsening is not appropriate (one of the two models presented below may be more applicable). This means that forces other than those involved in reducing subgrain boundary surface area control the reaction of subgrains to temperature. For example, it is possible that dislocation climb controls the evolution of subgrains, or subgrain evolution is controlled by internal strain differences across subgrain boundaries. Secondly, subgrains accommodate strain within grains in the lowest energetic form possible. Any alteration of their configuration driven by surface energy requirements may reduce the total energy of the subgrain system rather than increase it. Thus, subgrains, once formed, are stable and their configuration remains difficult to alter.

Low Energy Subgrain Boundary Model

Joesten (1983) calculated a pre-exponential factor for grain growth in quartz using the Christmas Mountains aureole of $k = 5.32 \times 10^{-7} \text{ }^\circ\text{K/s}$ and an activation energy of $Q=210000 \text{ J/mol}$. The pre-exponential factor has been theoretically shown by Hillert (1965) and Joesten (1983) to equal:

$$k = \frac{4\gamma_i V_i D_{0(gd)}}{R \delta} \tag{Equation 7.6}$$

where γ_i is the surface energy of quartz, R is the gas constant, and $\frac{D_{0(gd)}}{\delta}$ is the coefficient for diffusion of i in its grain boundary of width δ (after Turnbull 1951 and Kingery et al. 1976). Joesten used a value of 0.605 J/m^2 for the surface energy of quartz (Brace and Walsh 1962) in order to calculate the other values in Equation 7.6. In this subgrain model, the process is reversed. The values of the diffusion coefficient and atomic volume calculated by Joesten (1983), together with a reduced surface energy term (see below), are used to recover a value of k appropriate for a subgrain boundary. The value of the surface energy of a subgrain is calculated using an equation derived by Kingery et al. (1976) whereby the surface energy of a subgrain boundary is:

$$\gamma = \frac{G b^2}{D 4\pi(1-\nu)} \ln \frac{D}{b}$$

Equation 7.7

in which G is the shear modulus, ν is the atomic volume, D the spacing of dislocations in a subgrain wall and b the Burgers vectors of the dislocations. Using a Burgers vector value of 5 angstroms, and a misorientation between two subgrains of 5° , the surface energy of a subgrain may be calculated at 0.0414 J/m^2 . This in turn generates a value of $k = 3.634 \times 10^{-7} \text{ }^\circ\text{K/s}$. Using this value of K , together with an activation energy of 210000 J/mol the amount by which subgrains coarsen from an initial subgrain size of 20 microns may be calculated (Figure 7.11). The results indicate that subgrain boundaries should be more stable than grain boundaries, shown by the fact that this model consistently predicts lower subgrain sizes than the model using variables calculated from the subgrain growth model presented above.

The predictions from this model closely match the actual evolution of subgrain sizes through the Ballachulish aureole. Subgrains remain relatively unchanged up to 700m , at which point they are consumed on to migrating grain boundaries. This is an important conclusion because the model provides a link between direct observations and the potential physical process which may control this behaviour. However, the fact that the model fits the observed data at Ballachulish does not necessarily prove that it is the actual mechanism by which subgrains react to temperature.

Dislocation Climb Model

The third model explores the possibility that subgrains may migrate under the direct control of the dislocations which form the subgrain boundaries. The lattice around a dislocation by definition becomes warped and consequently associated with every dislocation is a fixed amount of elastic energy (dependant upon the Burgers vector of the dislocation). The elastic energy surrounding a dislocation is enough to cause dislocations to climb, and in doing so reduce the energy of the system. If a subgrain boundary is formed by a number of dislocations, it follows that by collective climb of these dislocations, the subgrain energy may be reduced. Collective dislocation climb is

equivalent to subgrain boundary migration. Thus, it is possible to assess the rates at which subgrains can grow by studying the velocities at which dislocations climb.

Poirier (1985) derived a relationship to describe the velocity of dislocation climb at a fixed temperature:

$$V_c = \frac{2\pi}{\lambda} D_{sd} \frac{\sigma\Omega}{KT} \quad \text{Equation 7.8}$$

where λ is the distance from a dislocation where there is no strain associated with the dislocation, D is a self diffusion coefficient (here the diffusion of oxygen in quartz), σ the applied stress acting on a rock, Ω is the atomic volume and K is Boltzman's constant.

Equation 7.8 is solved numerically through a temperature time history for each point in the Ballachulish aureole. It is possible to assess the distance a dislocation is capable of climbing anywhere along the transect. Figure 7.11 depicts the relationship between the distance a dislocation may climb during the thermal evolution of the Ballachulish aureole and the distance by which a subgrain boundary can migrate.

The equations have been solved for values of $\Omega^3 = (2 \text{ burgers vector})^3$ and $(5 \text{ Burgers vectors})^3$. In the model using 2 Burgers vectors, a subgrain boundary is able to migrate by 10 microns by 700m from the intrusion. This potentially could result in a subgrains doubling their diameter, a result which is plausible from the examination of subgrain structures (more detailed image analysis is required on the subgrain size through the outer parts of the aureole). The model using $\Omega^3 = (5 \text{ burgers vectors})^3$ overestimates the subgrain size dramatically. However, it is important not to discount this as a possible kinetic model for subgrain evolution, because subgrains may be affected by solute drag in a similar manner to grain boundary migration. Thus, it is wrong to assert that a model using a burgers vector of 2 is valid merely because it correlates well with the observed data. It is equally possible that the Ballachulish data set is adversely affected by processes which are not accounted for in any of the above models (i.e. solute drag).

Summary

- Three models have been presented to describe subgrain evolution within the Ballachulish aureole. Two of the models (normal grain growth and the dislocation climb) predict that subgrains are unstable microstructures and should be annealed long before there is any evidence of grain growth. The third model (using a reduced pre-exponential factor) accurately predicts the evolution of subgrains which is observed in the Ballachulish aureole. However, it is possible that any of the above models is appropriate. The models which indicate subgrains are unstable may be correct because in the Ballachulish aureole they are stabilised by other influences (e.g. impurities). A detailed microstructural and microgeochemical analysis of subgrains at the TEM scale of observation is needed to prove or disprove any of the subgrain modification models. Any investigation of this kind should involve detailed laboratory work on pure and impure samples.
- The main conclusion to draw from the analysis of subgrain stability is that more detailed work is required to develop a model which unequivocally describes the rates of subgrain changes in tectonites. Such work must involve laboratory investigations, theoretical modelling and testing upon real geological samples.

7.4 Grain Coarsening during Regional Metamorphism/Deformation

7.4.1 Introduction

Thus far kinetic models of microstructural evolution have been confined to the Ballachulish aureole. This section discusses the applicability of the information, which has been gathered from Ballachulish, to other tectonic regimes. A number of models are presented which speculate about the rates at which microstructures evolve during two common tectonic phenomena, burial and exhumation. The discussions are separated into models describing the following:

- (1) A mylonite undergoing exhumation.
- (2) A fault rock which is buried.

The kinetic models which are presented are simple, non-isothermal grain growth models for monomineralic quartzites. The temperature histories through which the rocks evolve are hypothetical and yet typical for rocks undergoing burial or exhumation within mountain belts. Temperature is altered linearly with respect to time; in the case of the exhumation model it gradually decreases, whilst for the burial model it gradually increases.

7.4.2 Exhumation of a Deformed Tectonite

Typically, rocks having undergone deformation attain grain sizes of $100\mu\text{m}$ or less. The object of this exercise is to predict the evolution of grain sizes of a deformed quartz tectonite with an initial grain size of $100\mu\text{m}$ as the tectonite is exhumed to the earth's surface. The rate of exhumation is varied to account for exhumation in different tectonic settings. Two exhumation rates are modelled, $0.35^\circ\text{C}/\text{Ka}$ and $0.035^\circ\text{C}/\text{Ka}$ respectively. The former exhumation rate is rapid, at similar rates to that inferred from work in the Nanga Parbat region of the Himalayas (Magennis 1993), the latter is a fairly slow exhumation rate typical of many orogenic belts that have undergone Barrovian metamorphism (Dempster 1985).

Essentially, these models assume a rock to have deformed at peak metamorphic temperature, creating a grain size of $100\mu\text{m}$. Immediately following deformation the rocks are exhumed at a constant rate, thereby temperatures gradually decrease. Thus, grain growth will occur in a retrograde temperature path. For each of the two exhumation models, grain size is calculated for peak metamorphic temperatures of 1000, 800, 600, 400 and 200°C .

Results

Figure 7.12 presents the results of coarsening models using cooling rates of 0.35 and $0.035^\circ\text{C}/\text{Ka}$. The salient features of the models are as follows,

- At peak temperature of 400°C and less no coarsening occurs in either of the models (0.35 or $0.035^\circ\text{C}/\text{Ka}$).

- In the model for peak temperatures of 600°C coarsening does occur, albeit slowly. With exhumation rates of 0.35°C/Ka grain size almost doubles, whilst the 0.035°C/Ka exhumation model predicts the initial grain size to increase to 150µm.
- A comparison between the models for peak temperatures of 1000 and 800°C at exhumation rates of 0.35°C/Ka reveals that between 200,000 and 300,000 coarsening ceases. This is an actual cessation in coarsening and not just a decrease to imperceptible levels.
- The cessation of coarsening in the 1000°C model is at 930°C, whilst in the 800°C peak temperature model coarsening ceases at 730°C.

Interpretation

The fundamental control upon coarsening is the temperatures which have been attained during the rock's history. At 400°C there is little chance of grain microstructures annealing, even over a geological timescale. However, rocks which reach 600°C, even for limited time periods may be susceptible to annealing.

In the model exhuming at 0.035°C/Ka, with peak temperatures of 600°C, the grain size almost doubles. The microstructural analysis at Ballachulish indicated that once the grain size had doubled deformation features had been removed by primary recrystallisation. Therefore, it is possible to speculate that any rocks undergoing the exhumation history modelled here with peak temperatures of 600°C would not reveal any deformation features. On the other hand, the model exhuming at 0.35°C/Ka the grain sizes are predicted to be smaller after exhumation. These rocks would probably still preserve evidence of their original deformation at 600°C. It can be seen that these models provide a basis by which we can predict the rates of uplift necessary to preserve deformation features within rocks that deformed in the mid/lower crust.

The results of the exhumation models indicate that grain coarsening, in this retrograde temperature history, ceases completely. A cessation of coarsening in retrograde temperature paths in the Christmas Mountain aureole has also been observed by Joesten

(1983). This surprising result is a consequence of the fact that both exhumation rates and the peak temperatures directly effect the amount of annealing.

The models show that peak temperatures together with exhumation both contribute to the degree of annealing of tectonites. This is illustrated by examining the cessation of grain coarsening during the reterograde temperature time paths. Why does coarsening continue down to temperatures of 750°C for rocks which were deformed at peak temperatures of 800°C, yet in the rocks with peak temperatures of 1000°C coarsening stops at higher temperatures of 930°C (exhumation rate is 0.35°C/Ka - see Figure 7.13)? The answer to this question lies in the rate of change in temperature through time, i.e. the exhumation rate. Initially, because of the high temperature, grain size increases rapidly (nearly an order of magnitude in 1000 years for peak temperatures of 1000°C). The critical point is that as grain sizes increase the driving force for annealing decreases; it is more and more difficult to grains to grow. This phenomena has already been discussed in relation to theoretical models at constant temperatures, with the main result that smaller grain sizes coarsen more rapidly than larger grain sizes. The cessation in coarsening results from the combination of this 'grain size factor' together with the ever decreasing temperatures as the rocks are exhumed. Thus, three variables control the stage at which grain coarsening stops: (1) peak temperature, (2) exhumation rate and (3) grain size.

7.4.2.a Summary Of Exhumation Models

These models indicate that in a retrograde temperature time path, grain coarsening will become inhibited. The control on the temperature at which coarsening ceases is dependant on the initial temperature, the initial grain size and the cooling rates (i.e. exhumation rates).

The models presented above envisage grain coarsening using the most simple kinetic model (i.e. normal grain growth in monomineralic quartzites). The data from Ballachulish indicates that this is a good first approximation to describe coarsening of aggregates. However, more work would be useful to examine coarsening during exhumation using effective activation energies for the various stages of coarsening (i.e. primary

recrystallisation and solute drag), and effective activation energies for two phase materials.

During any investigation into microstructural evolution in regional geological settings, it is worthwhile calculating the temperature history after the deformation (even if it can only be calculated roughly), and to assess whether the rocks should have undergone grain growth, using the models presented above. Data from the Ballachulish aureole indicates that certainly during the initial stage of annealing, grain growth may be inhibited by solute/impurity drag. Thus, although the models for pure materials may predict annealed microstructures to occur in a rock, deformation microstructures indicate that annealing has not actually taken place. In such circumstances, it is reasonable to suppose that solute drag/impurity drag is an important constraint on the microstructural evolution preventing the production an equilibrium annealed microstructure.

7.4.3 Burial of A Fault Rock

As a rock is buried, it may suffer a number of deformation events each with different characteristics. For example, a rock may fault at shallow depths and then as burial continues deform in a crystal plastic fashion. Thus a rock will undergo various deformation mechanisms in a variety of environments.

An early deformation event may effect the style of a later deformation event. For example faulting and fracturing may be the dominant process by which deformation is accommodated at shallow depths. Commonly associated with brittle deformation is grain size reduction. The finer grain sizes within fault zones have frequently been inferred as a cause of reactivation of faults during later deformation events (both in brittle and crystal plastic deformation regimes). The burial models presented in this section examine whether it is a realistic assumption to make that grain sizes within what was previously a fault maintain their reduced grain size during burial. It is possible that a fault may anneal completely and therefore not provide a region of weakness within a rock in which strain may localise in a crystal plastic deformation event. Thus, it is important to assess the stability of fault rocks as they undergo a prograde metamorphic temperature path.

The grain growth models at constant temperatures (Figure 7.8) indicate that as time proceeds grain size differences between rocks of different initial grain size are eradicated. It is possible to predict from kinetic models how long it would take a cataclastic fault rock (with a reduced grain size) to equilibrate with the wall-rock (undeformed rock). Frequently geologists presume that once a rock has undergone deformation and grain size reduction it will be an area where subsequent deformation will preferentially localise. The homogenisation of grain sizes between aggregates which initially had different grain sizes during grain growth indicates that this is an unrealistic presumption. If a rock has undergone substantial grain growth, the grain size throughout the rock volume will homogenise, eradicating regions of microstructural weakness which may later act as instabilities.

In the Ballachulish aureole data is presented (cf. Chapters 5/6) to show that the presence of second phases or solute atoms may hinder grain growth (i.e. impurities stabilise microstructures). Thus, the grains within a rock which has no impurities coarsen more than those in an impure rock. If during faulting, fluid influxes along a fault zone, impurities may be introduced along the fault. During burial of the fault, the impurities may stabilise microstructures within the fault zone in relation to the rocks outside the fault, which have had no fluid influx. Variations in grain size will thus be maintained during burial and the fault zone may remain as a weaker zone of rock prone to becoming a microstructural instability during plastic deformation.

Figure 7.13 is a comparison of two coarsening models, one a pure quartzite and the other an impure quartzite, which are annealed by grain growth during prograde metamorphism. The coarsening of the pure rock is modelled using the diffusion variables from Joesten (1983), whilst impure samples are modelled using an effective activation energy derived from the quartzo-feldspathic Ballachulish samples (see section 7.2.4). It is seen that after the prograde metamorphism the grain size of the impure samples is far less than that of the pure samples. Obviously during a deformation event these two rock types with differing grain sizes would react differently, potentially controlling the localisation of deformation and the mechanisms of deformation.

Olgaard and Evans (1986) performed a similar calculation, but varied the exponent (n) relating grain size to diffusion related variables (i.e. k , Q and the time integral in equation

7.2). They also concluded that grain growth is inhibited in zones with a high impurity content and that these zones could be regions where microstructural instabilities could initiate.

7.5 Conclusions

Kinetic models have been developed based on the processes which have been proposed in Chapter 6. The divergence of the theoretical microstructural data (e.g. grain size) from the observed microstructures at Ballachulish may be used to assess the applicability of the microstructural models presented.

Normal Grain Growth Model

There is significant departure between the theoretical grain size values calculated from the kinetic model and the actual grain sizes throughout the aureole, as follows.

- Outside the aureole, solute drag and impurity drag may reduce the mobility of grain boundaries, inhibiting growth. The normal grain growth model does not take this into account.
- During primary recrystallisation, grain growth is enhanced by strain induced grain boundary recrystallisation. Thus, the grains in Zone II of the aureole rapidly grow to catch up with the grain sizes predicted from kinetic models.
- The grain sizes in the inner aureole (Zone III) are similar to the theoretical expectations. Thus normal grain growth is an appropriate model for grain coarsening within this zone.
- Impurities on all scales are potentially the main cause of the discrepancies between the kinetic models and the actual data collected from Ballachulish. It is critical for future workers to analyse the types of impurities and how they interact with microstructures and at what stages in the annealing process each type of impurity is

influential. This investigation does consider the effects of second phase feldspar impurities. Detailed TEM work is necessary to characterise other types of impurities.

Growth in Impure Samples

The grain growth model using an effective activation energy for polymineralic samples can be used to predict grain coarsening which is inhibited by pinning. The model used to quantify grain sizes may change as a function of temperature in quartzo-felspathic rocks which are relatively common in geological terranes.

Subgrain Stability

Subgrain coarsening is modelled based on normal grain growth equations using activation energies and diffusion coefficients from Joesten (1983), and a lower diffusion coefficient calculated using a dislocation model of a subgrain (i.e. with a lower surface energy term). The modified surface energy term adequately models the stability of subgrains within the Ballachulish aureole, whilst the Joesten parameters overestimate subgrain coarsening.

A model of subgrain coarsening based on the rate at which dislocations can climb is inconclusive in defining subgrain coarsening because a small change in the parameters propagates into huge variations in the coarsening rates of subgrains through the aureole. It is possible that dislocation climb may control subgrain coarsening if dislocation Burgers vectors are small and the elastic strain associated with a dislocation is also small.

Grain Growth during Burial and Exhumation of Tectonites

A number of kinetic models have been calculated to indicate the change in microstructures undergoing a variety of temperature/time paths. The models indicate that it is not only temperature which controls coarsening rates, but also the initial grain size.

Constant temperature kinetic models reveal that in time an aggregate with a variation in grain size due to localisation of strain will become homogenised during annealing, either

on a prograde or retrograde metamorphic path. This has major implications for the localisation of strain during deformation of annealed rocks and on the preservation of deformed microstructures post-deformation.



Figure 7.1 Thermal evolution of the Ballachulish aureole. Temperature histories are plotted with respect to time at various distance from the intrusion. The model is produced from Contact8.pas, the input parameters are described in detail in Appendix A.

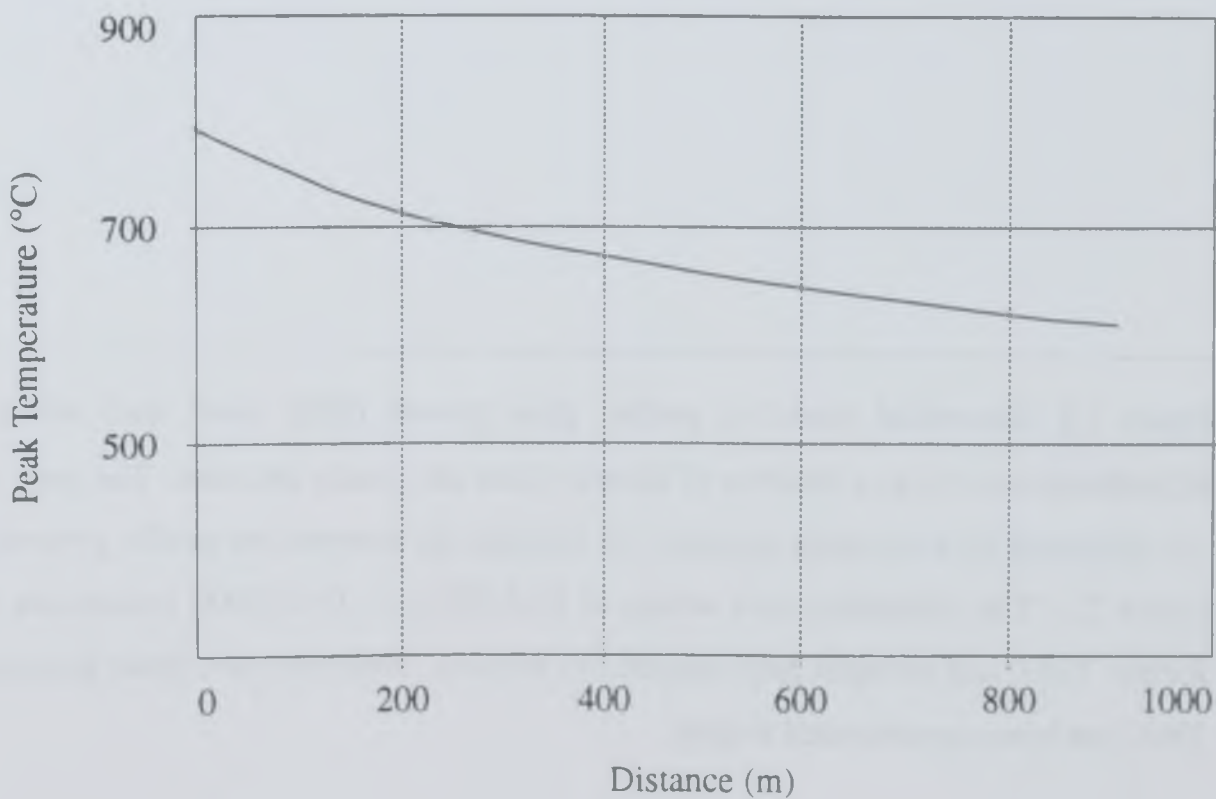
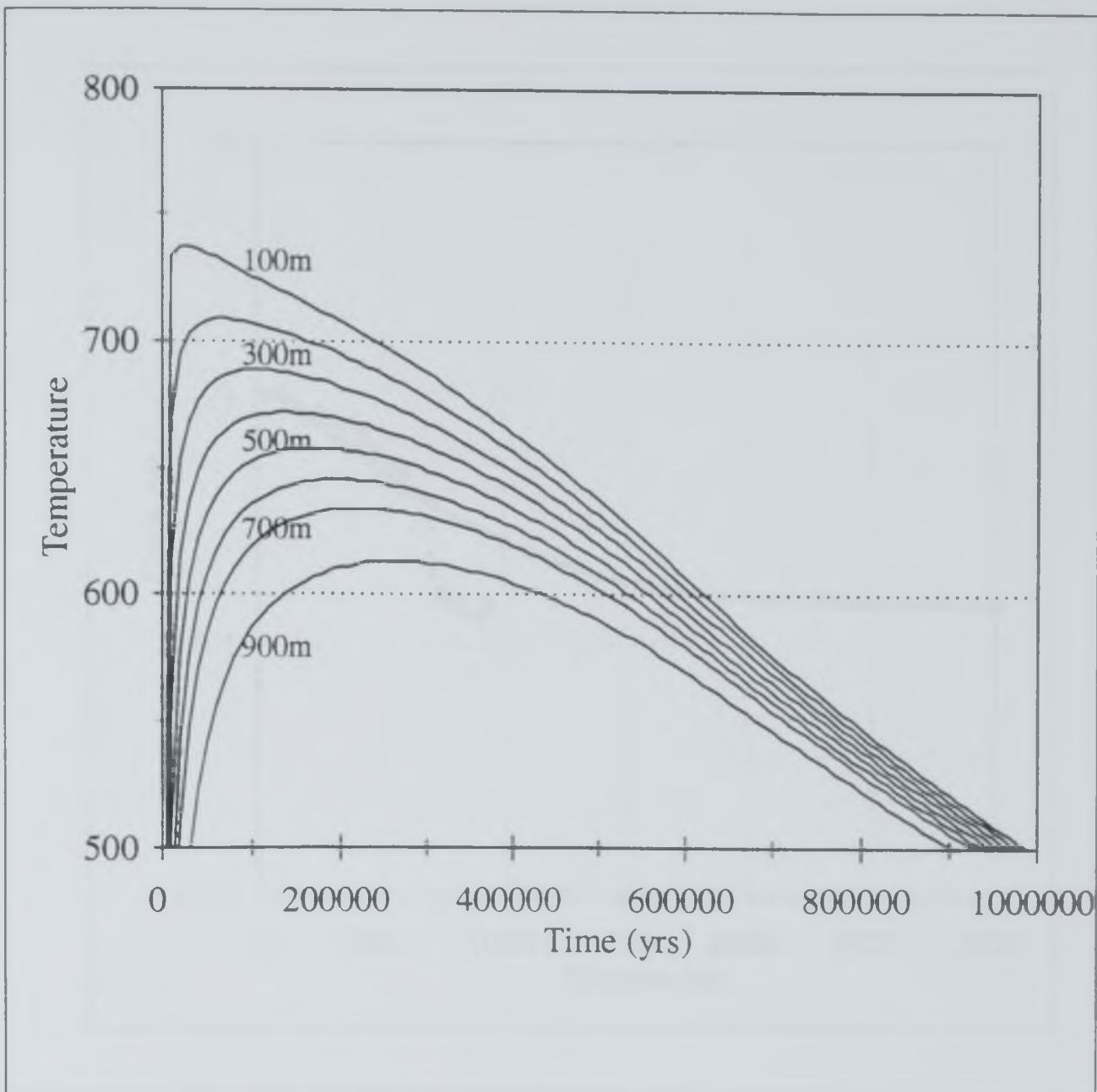




Figure 7.2 Theoretical model to predict grain growth (thick black line) within the Ballachulish aureole as a function of distance from the granite intrusion. The grain sizes are calculated by integrating equation 7.2 through the temperature profile presented in Figure 7.1. The calculation uses values of $K=5.329 \times 10^{-6}$, $Q=210000$ (values are from Joesten 1983) and an initial grain size of 143 microns. Grain size data (from Buntebarth, 1991) has been superimposed in grey.

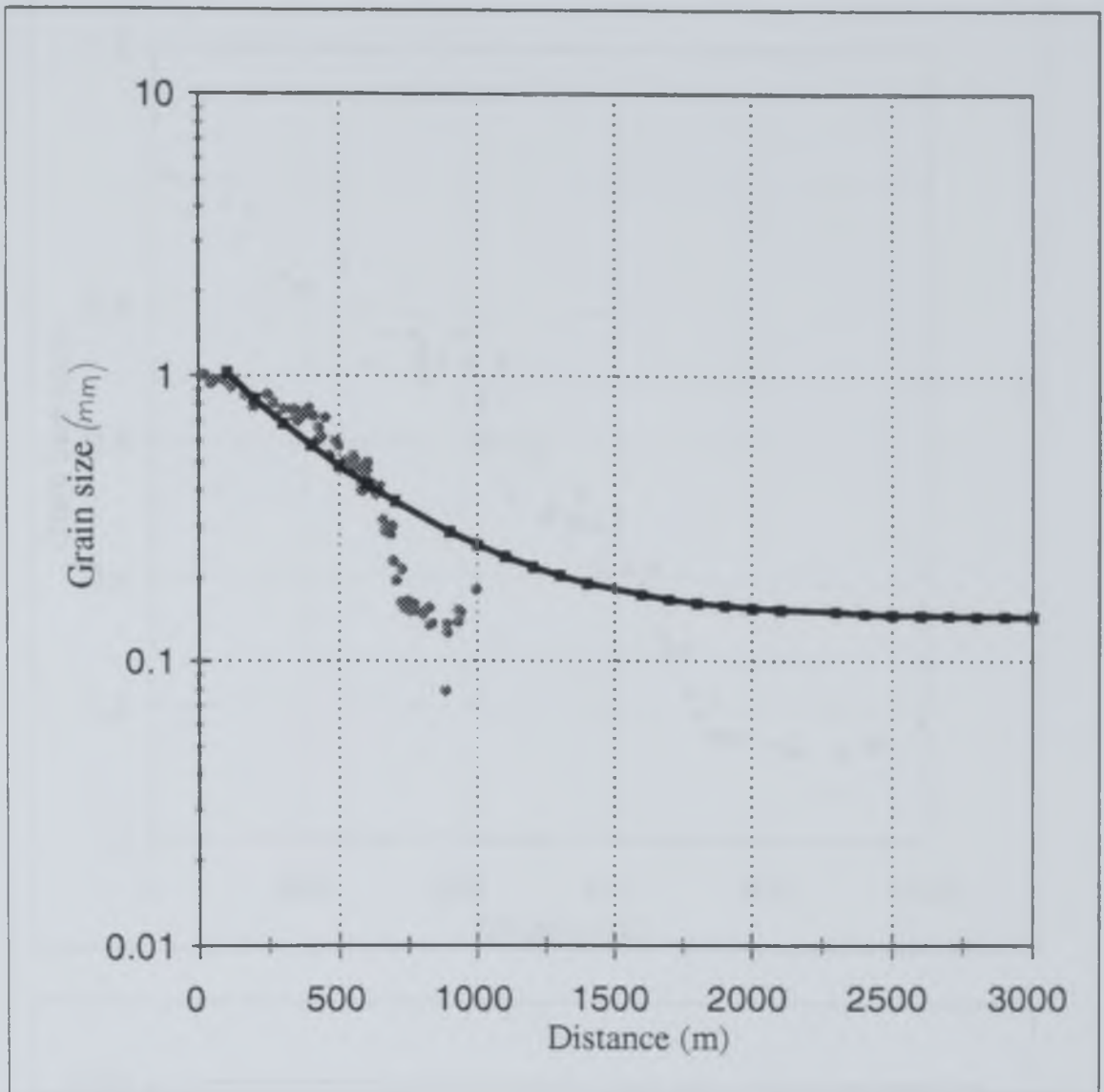




Figure 7.3 Observed grain sizes through the aureole a) pure samples (data from Bunterbarth and Voll 1991) and b) grain sizes from impure samples measured during this investigation.

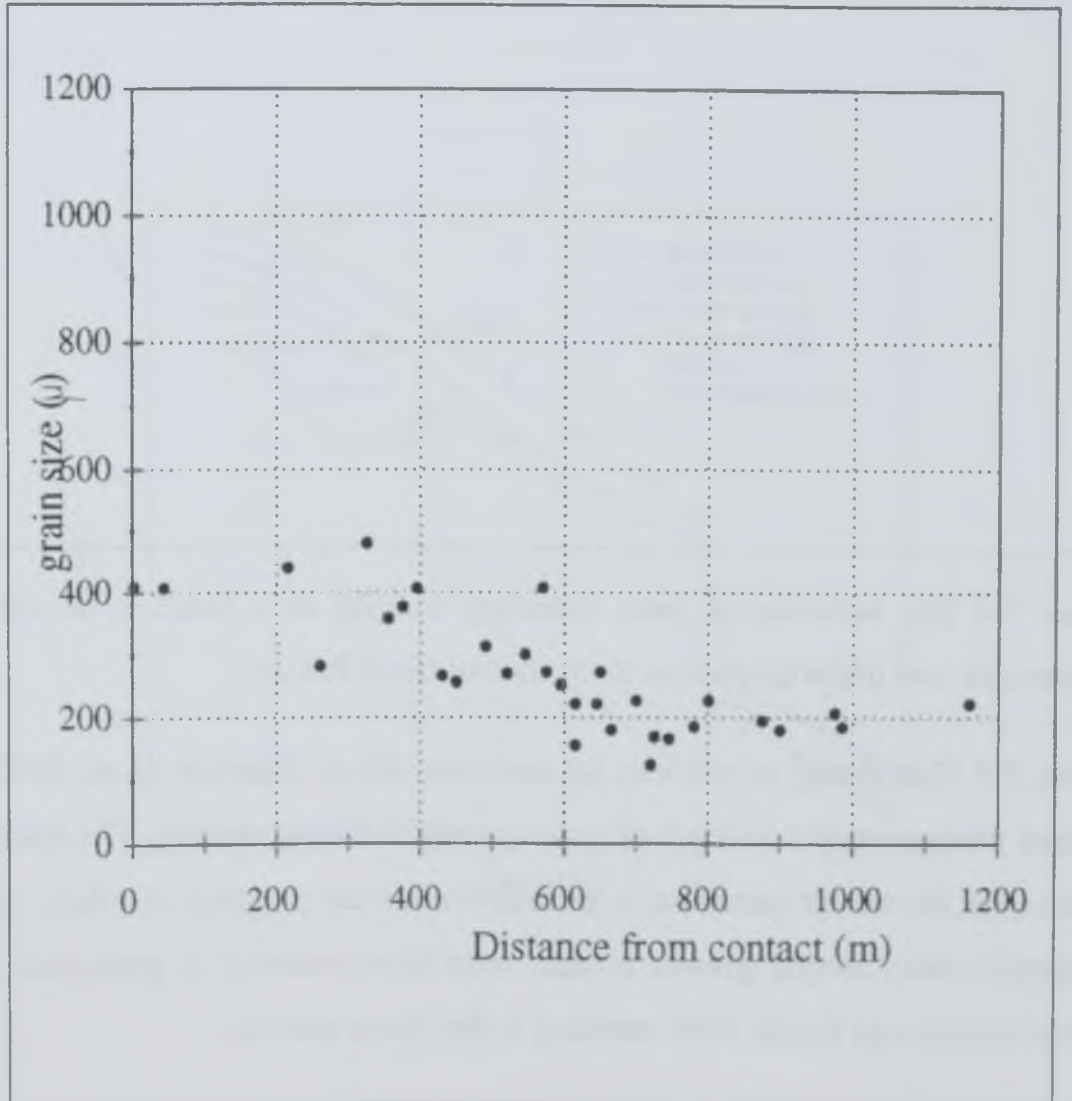
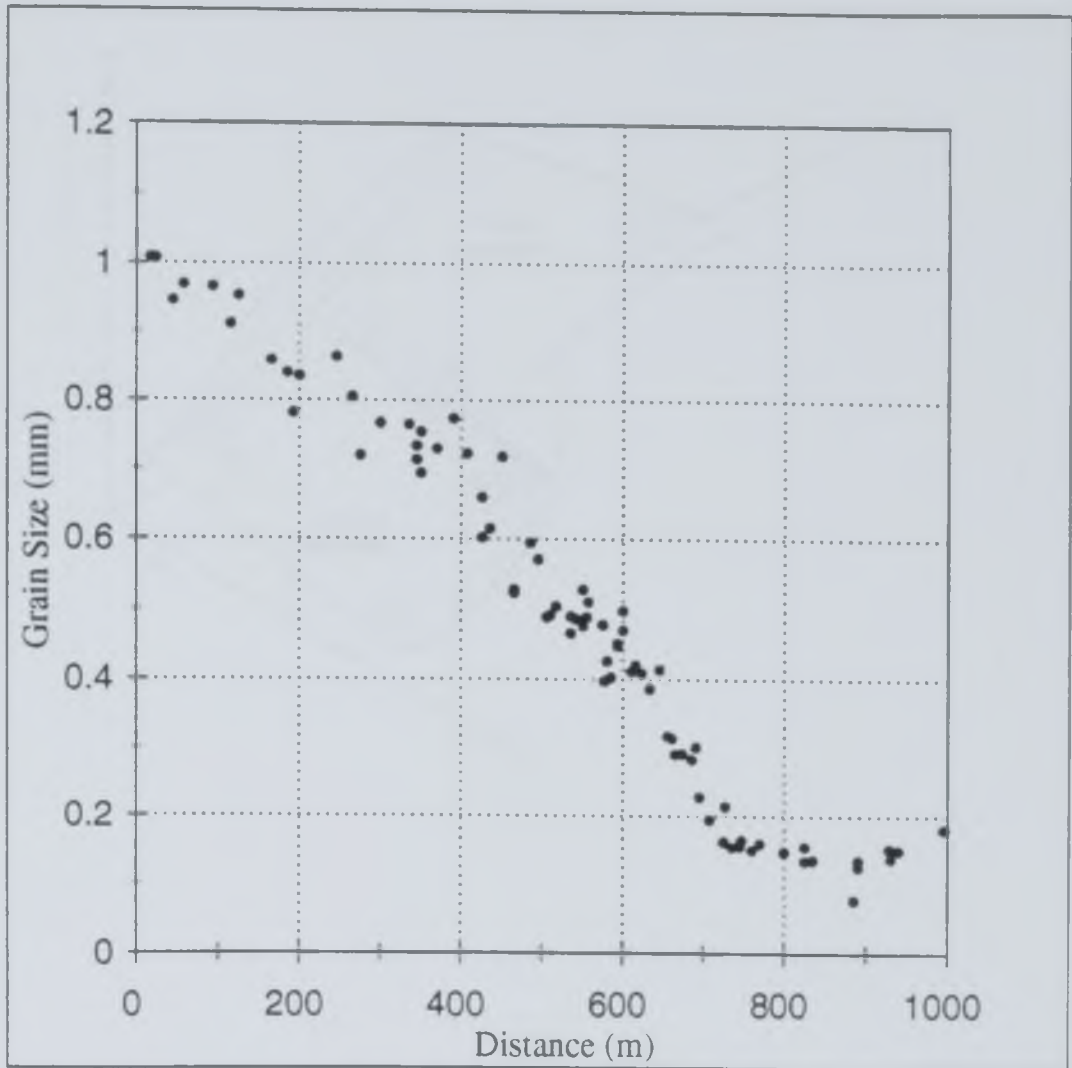




Figure 7.4 The variation of grain boundary mobility as a function of driving force, temperature and impurities/solute atom content (from Poirier).

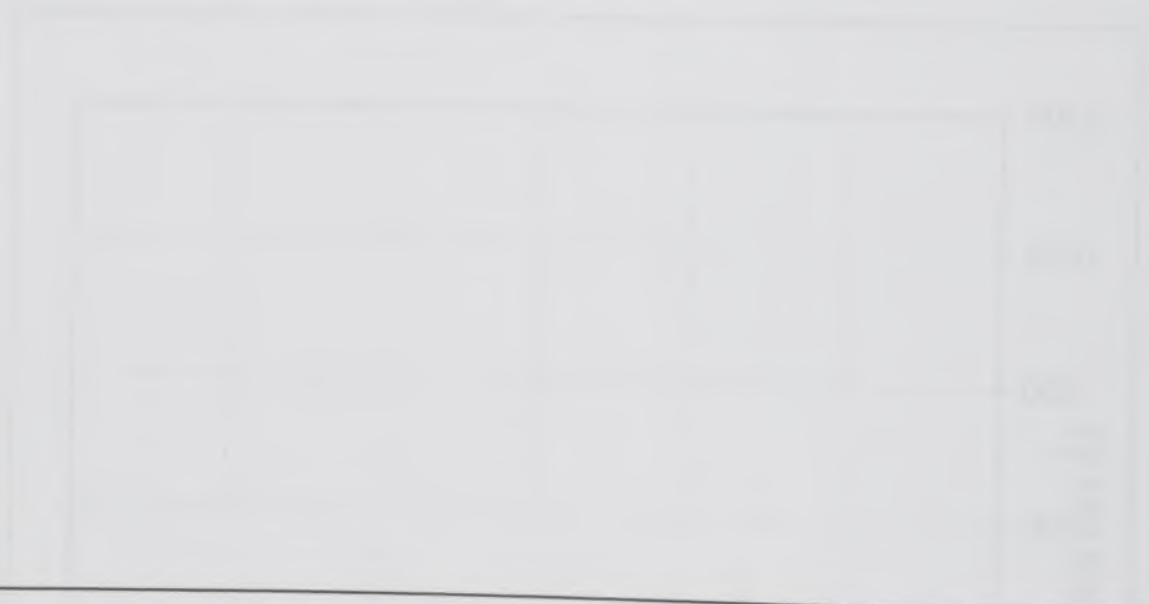


Figure 7.5 Coarsening experiment on cadmium alloys (Simpson et al. 1971) showing marked changes in the kinetics of grain growth during annealing. The microstructural reasons for the abrupt variations in growth rate are the presence of solutes and primary recrystallisation. Similar growth kinetics have been observed in geological settings by Covey-Crump and Rutter 1989, working in the Naxos aureole.

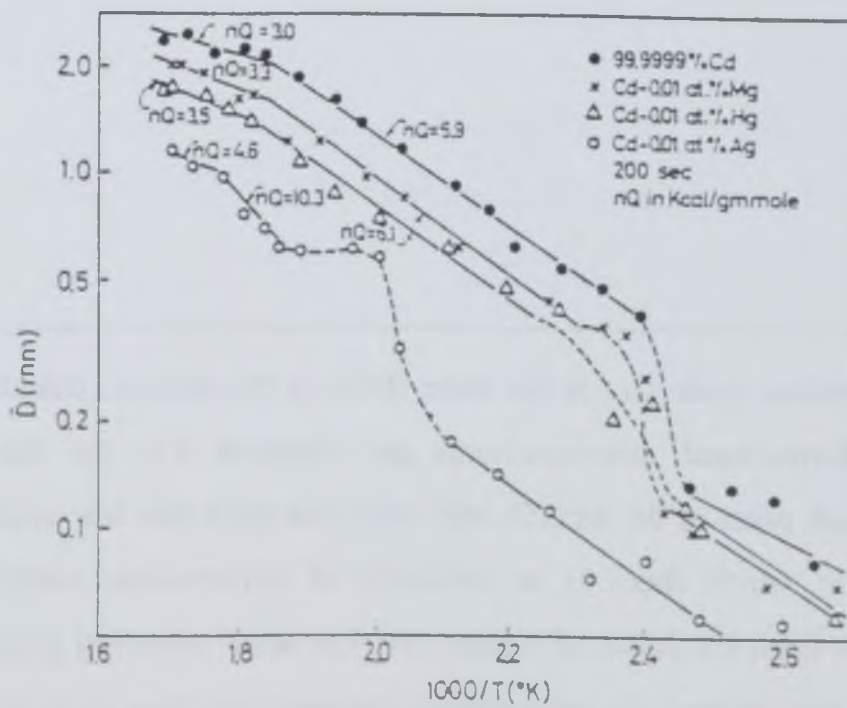
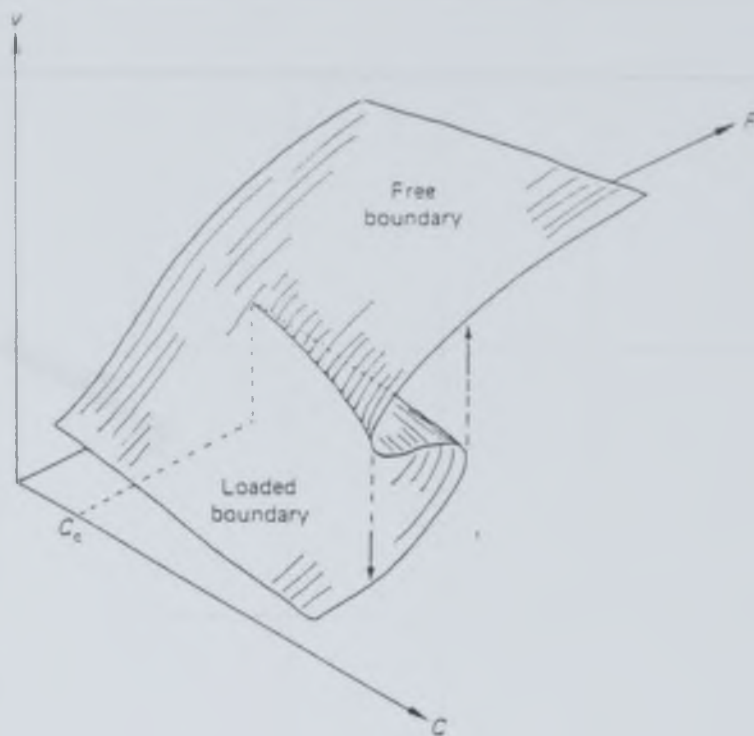




Figure 7.6 Theoretical grain size in the inner 600m of the aureole, calculated from the stage when deformational microstructures are annealed (i.e. the time integral is calculated for each point in the aureole only when the grain size has reached 0.47mm - the grain size at which there is no evidence of deformation within aggregates). Theoretical grain sizes are drawn as a black line. The actual observed grain size through the aureole are also plotted for comparison, showing that there is a close agreement between theoretical grain size and the actual observed grain size in zone III of the aureole. Grain size data (from Buntebarth, 1991) has been superimposed in grey.

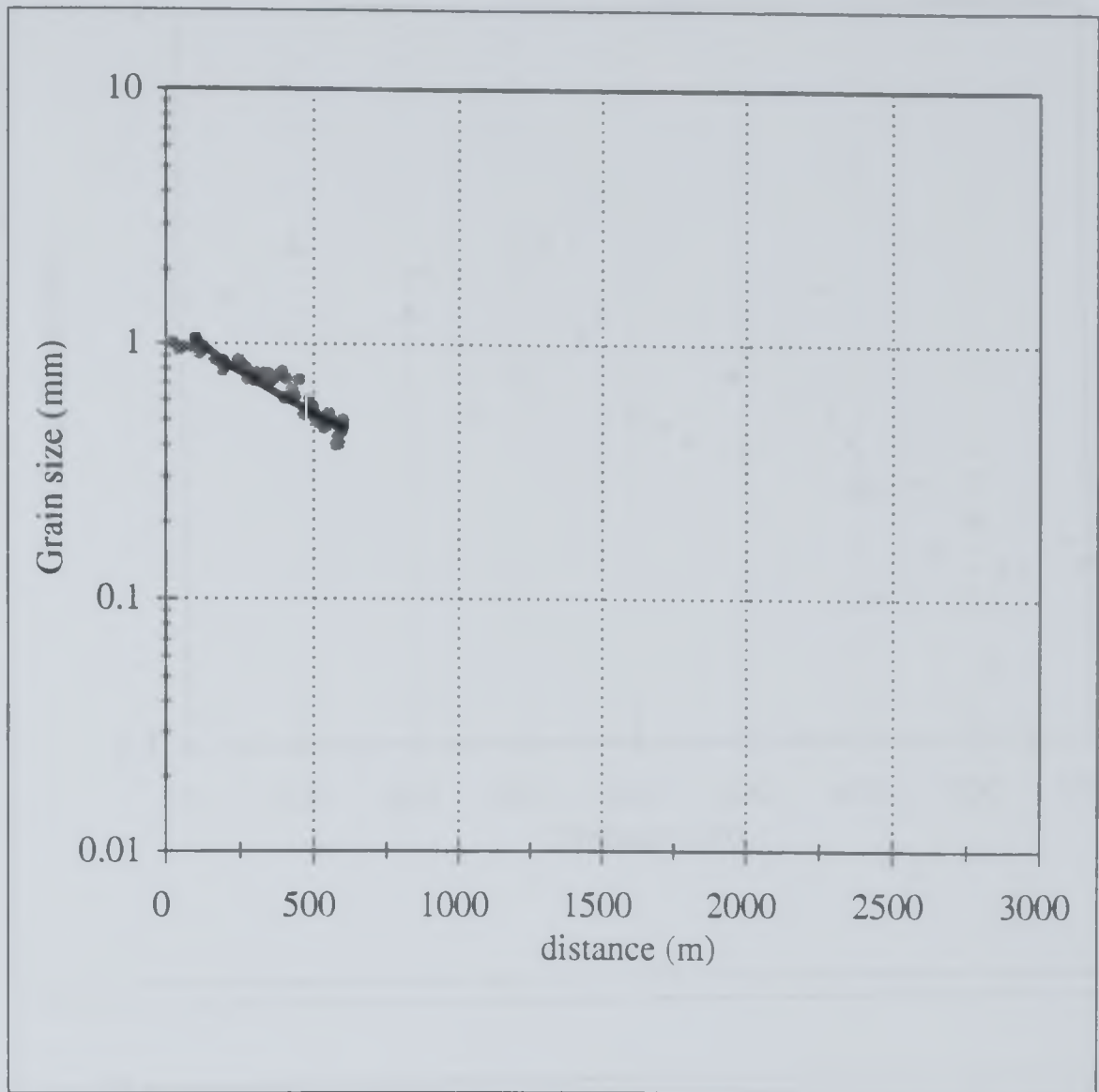




Figure 7.7 An empirical grain coarsening model for impure quartzites (black triangles), in which the activation energy term (Q) has been modified in the coarsening equations until the theoretical grain size data fits the grain size data from Quartzo-feldspathic samples measured during this study. Activation energy = 223000 J/mol and the pre-exponential factor $K = 5.329 \times 10^{-6} \text{ m}^2\text{°K/sec}$. The grain size data measured for this investigation are superimposed in grey.

Figure 7.8 Grain growth in quartzites at constant temperatures of 600, 800 and 1000°C. The models have been produced with initial grain sizes of 0.01mm and 0.1mm. It can be seen that fine aggregates coarsen more rapidly than coarse aggregates, and eventually their grain size 'catches-up' with the aggregates with a coarser initial grain size. Such grain size dependant coarsening may result in a homogenisation of rocks which initially had a heterogeneous grain sizes.

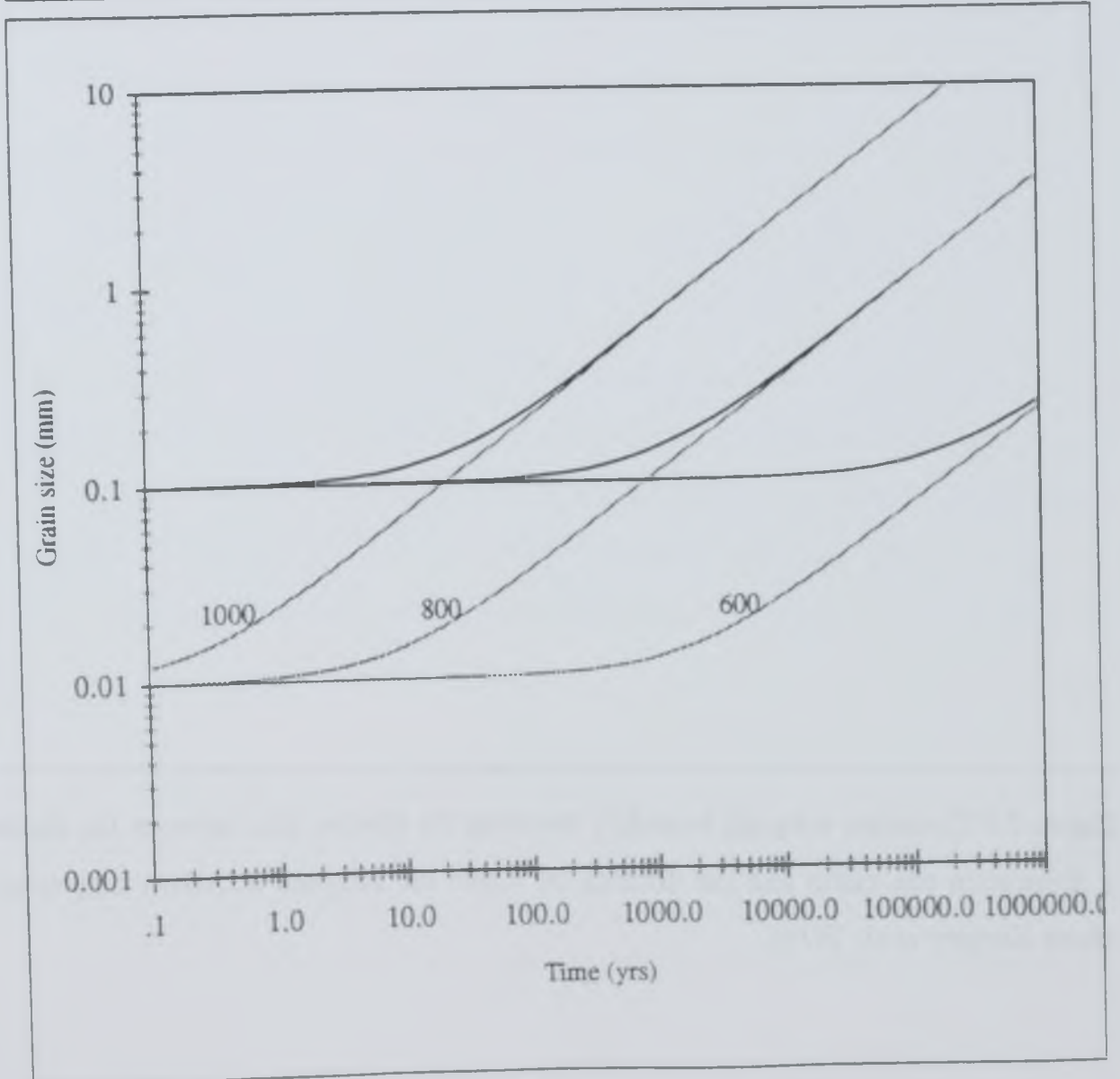
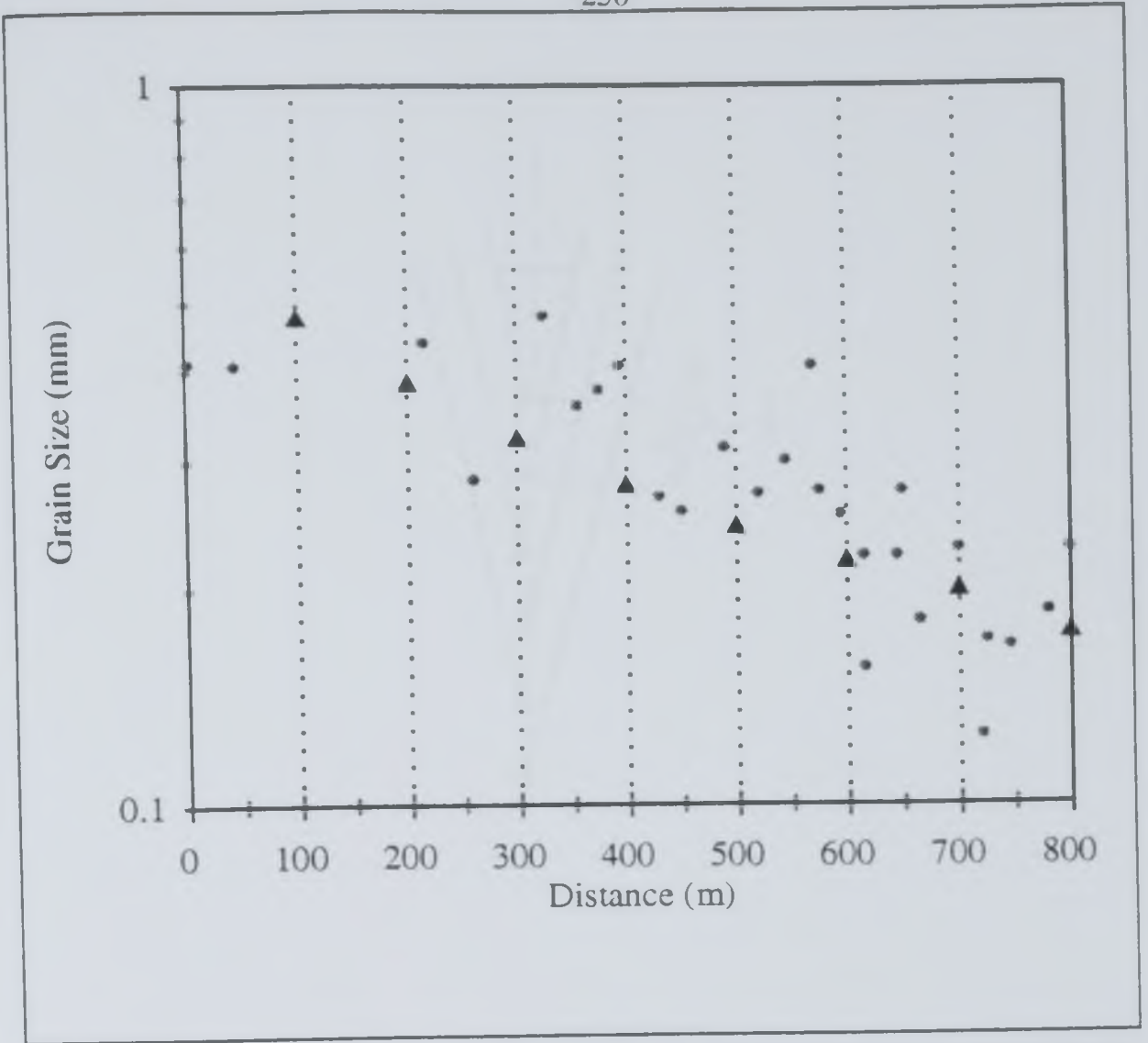


Figure 7.9 Geometry subgrain boundary revealing the relationship between the distance a dislocation can climb and the distance by which the subgrain boundary may migrate (from Kingery et al. 1976).

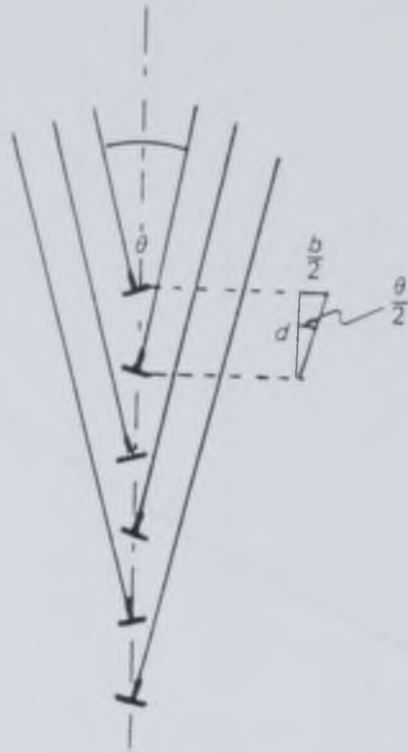


Figure 7.10 Model to show coarsening of subgrains within the Ballachulish aureole. The model treats subgrain growth identically to normal grain growth, and therefore growth may be calculated using the equations of Joesten (1983, Equation 7.2), however the initial grain size is the average subgrain size of aggregates from outside the igneous aureole ($20\mu\text{m}$).

Figure 7.11 Subgrain coarsening within the Ballachulish aureole is possibly controlled by the rates at which the dislocations (the main constituent of a subgrain boundary) can climb. The graph indicates the distance a subgrain boundary can migrate during contact metamorphism at Ballachulish. The input parameters are discussed in the text.

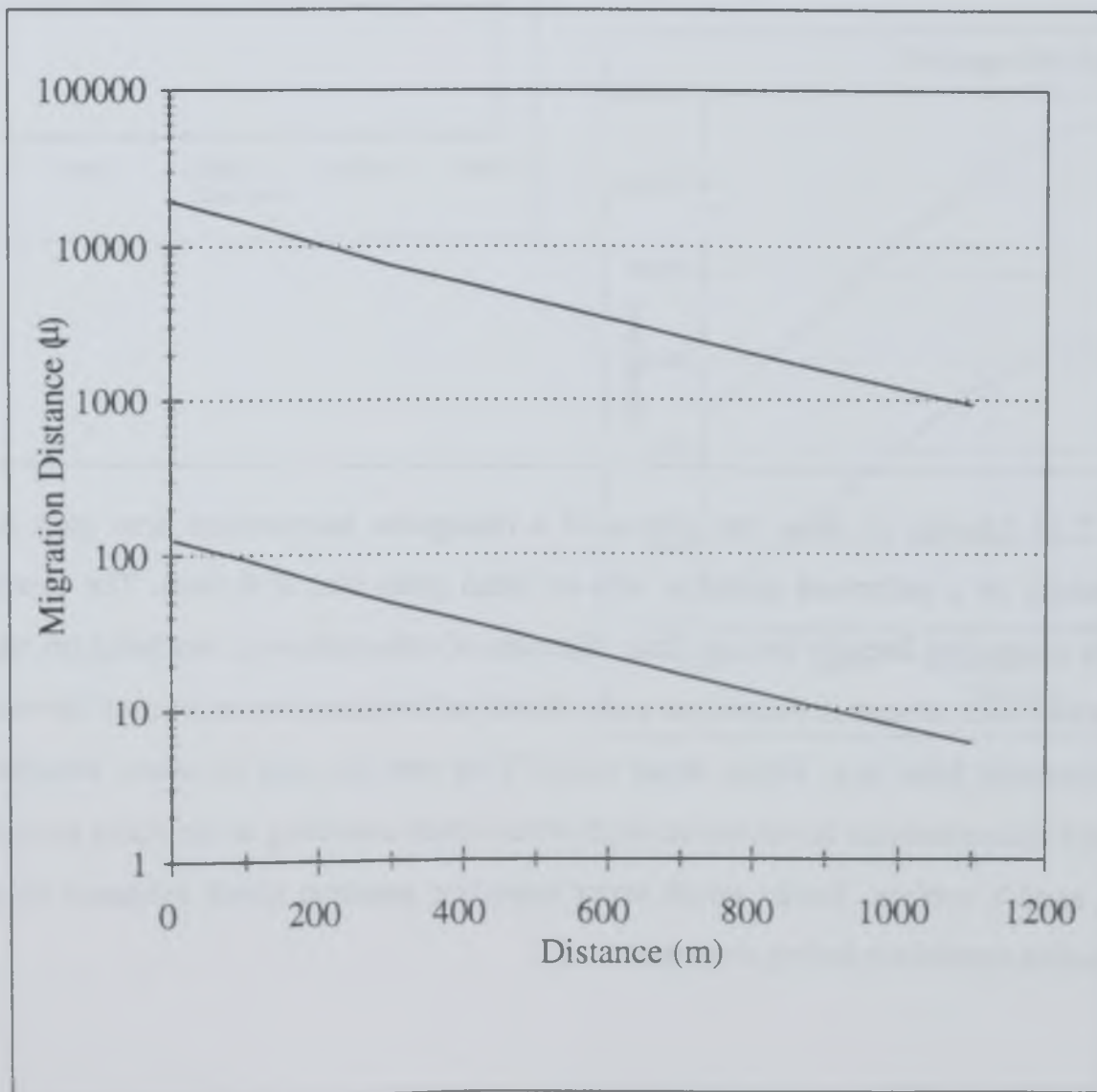
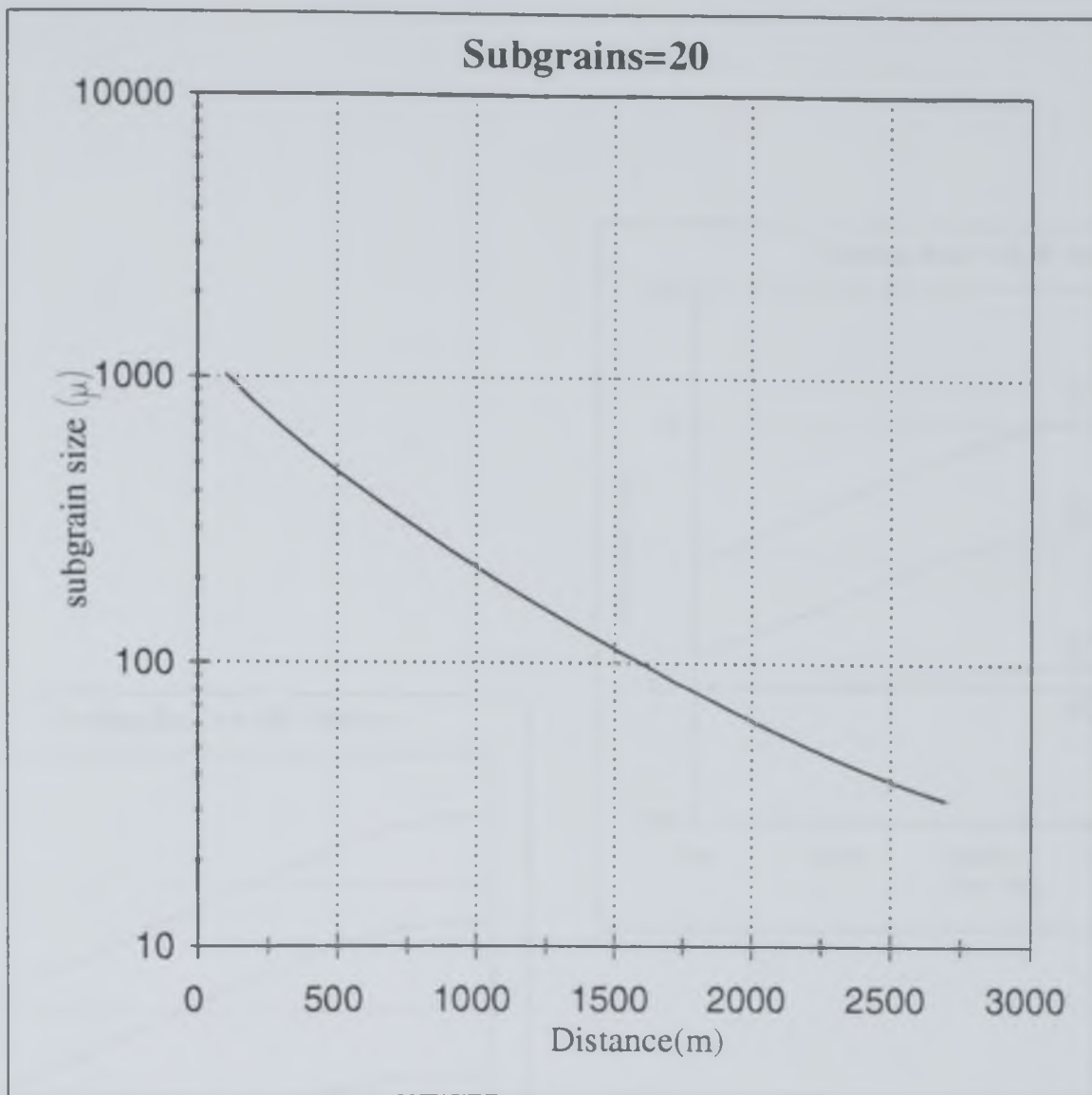




Figure 7.12 Models to show the effects of a retrograde temperature time path (i.e. exhumation) on a deformed quartzite with an initial grain size of 0.1mm. The thermal histories decreasing linearly through time. The rates of exhumation are modelled on rapid exhumation rates as seen in Himalayas and a slower exhumation rate as inferred for many other mountain belts (e.g. Moine thrust zone). They may be used to assess whether a deformed microstructure developed at depth would resist annealing as the rocks progress to the earth's surface. Rocks which resist annealing preserve direct evidence of the deformation conditions during orogenesis

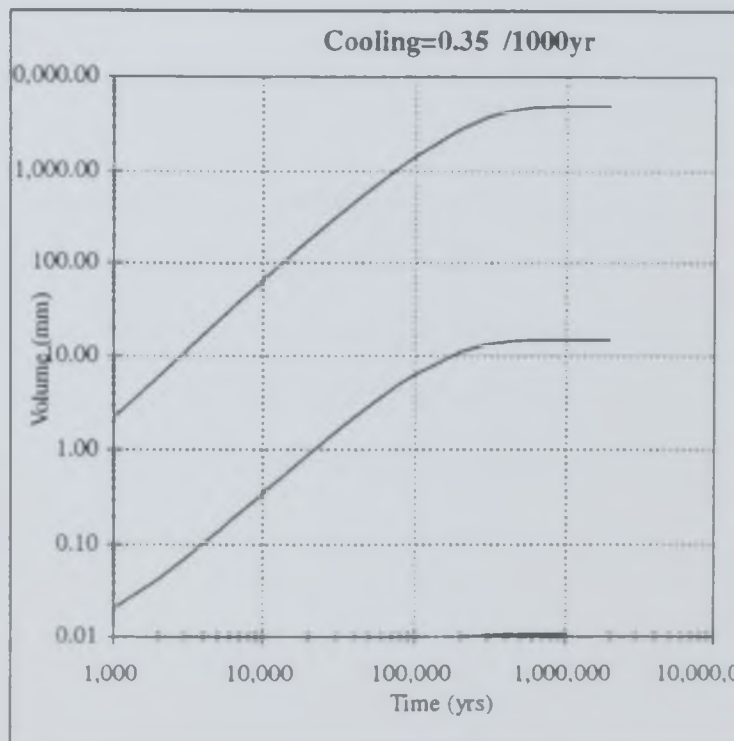
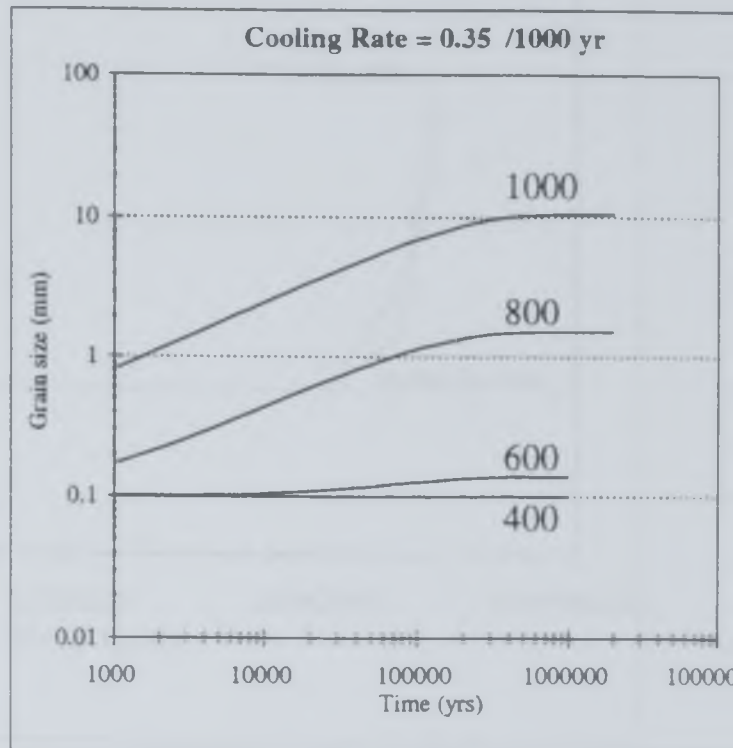
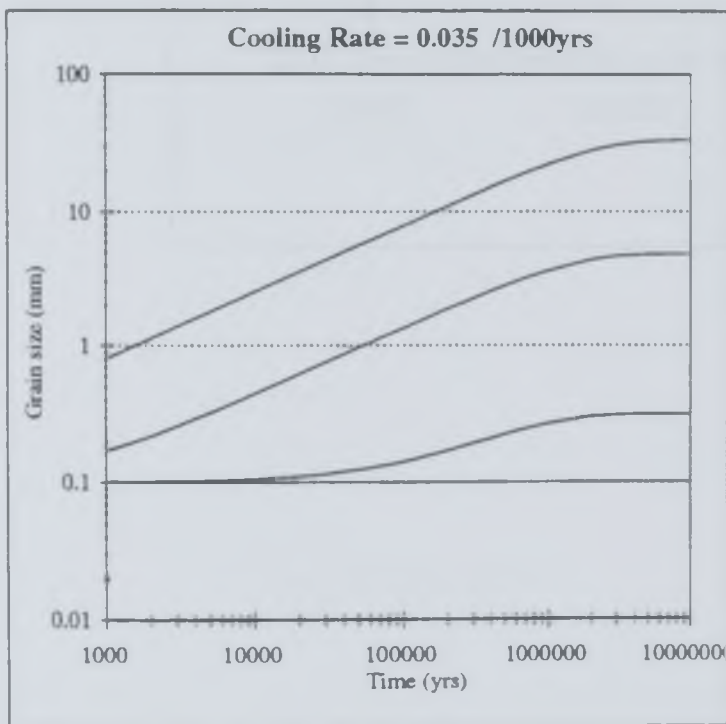
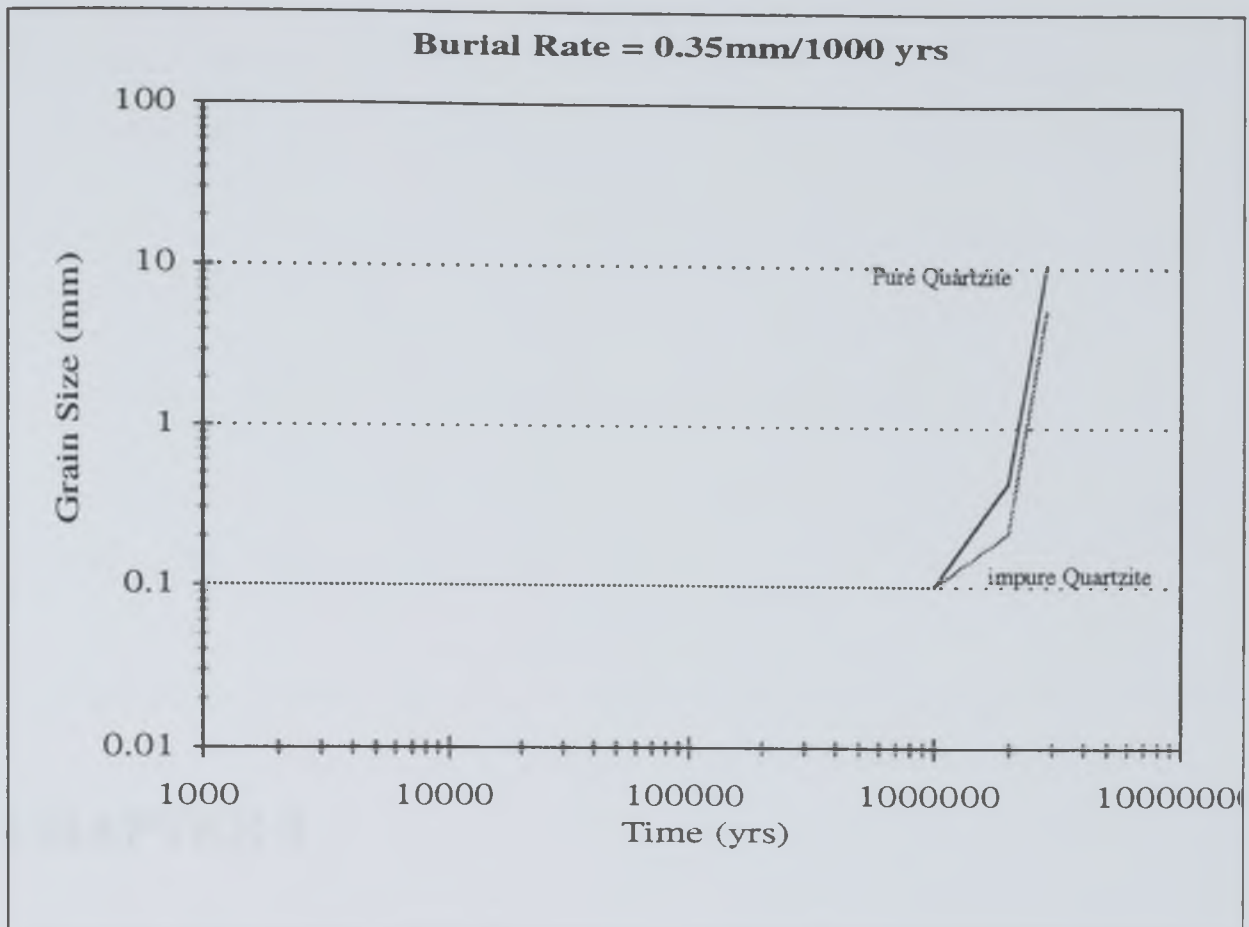


Figure 7.13 Coarsening models for prograde temperature time paths for quartzite (i.e. burial of a fault rock) with similar feldspar contents to that of the Appin quartzite. These models have been calculated using 'effective activation' energies calculated in Figure 7.7.



CHAPTER 8

CONCLUSIONS

8.1 Introduction

The Ballachulish aureole provides a unique opportunity to investigate the mechanisms and rates of geological processes over geological timescales. Many aspects of the geological history have been well constrained by numerous authors (see bibliography in Voll et al. 1991). These detailed petrological, geophysical and theoretical analyses of the Ballachulish aureole were used as a the basis for the investigation presented in this thesis. In particular, this thesis has integrated these data to:

- quantify rock textures.
- constrain the rates of textural change.

Using the data acquired during this research, it has been possible to:

- construct models of textural evolution (microstructures, microtextures and mesotextures);
- predict the rates at which different microstructures develop (i.e. predict microstructural stability);
- constrain the effects of temperature on microstructural modification.
- Predict how microstructures may alter to maintain equilibrium with their geological environment in any tectonic regime;

Investigations by metamorphic geologists in thermal aureoles are common because of the well constrained thermal regime. However, microstructural geologists have been slow to realise the potential of such environments for studying rates and mechanisms of microstructural evolution. This is possibly because a static regime of an aureole seems somewhat removed from dynamic regimes of faults and shear zones where many microstructural geologists are interested in kinetics and kinematics. But, an aureole is a simple system without added complexities of dynamic instabilities and unknown stress configurations. This renders aureoles ideal locations for studying microstructural change.

8.2 Concerning Quantification of Microstructure

A number of techniques have been developed which enable individual microstructural elements to be quantified, as follows.

(1) A detailed examination of the rocks was made to assess qualitatively the general microstructural evolution through the aureole and to decide which microstructural features should be analysed in more detail.

(2) A statistical analysis of microstructures was performed via image analysis techniques to quantify different microstructural elements at all scales. This analysis is the basic requirement for the investigation into the rates and processes of microstructural change in the Ballachulish aureole.

(3) A crystallographic description of the rocks was performed using a variety of methods to describe the relationship between regional strain and Crystallographic Preferred Orientation, misorientation relationships between neighbouring grains and the grain boundary orientations.

8.3 Concerning Data from Ballachulish

Microstructural observations and image analysis have been used to identify three zones within the Ballachulish aureole. Rocks within each zone exhibit different microstructures, representing the different mechanisms by which rock microstructures have been altered. The zones are:

Zone I: non-annealed microstructures prevail (> 800m from the aureole);

Zone II: between 800-600m deformation microstructures (i.e. subgrains and dislocations) are progressively eradicated . Grain shapes become more regular;

Zone III: a region of grain growth, grains grow from 180 μ to 500 μ in impure samples, and from 180 μ to 1000 μ in pure samples.

A detailed analysis of grain shape through the aureole reveals that irregularities on grain boundaries are removed even at 800m from the igneous intrusion. A stable grain shape is attained within samples in both zones II and III, even though the average grain size increases. The grain size distribution becomes stable at distances of <800m.

No crystallographic preferred orientations or crystallographic misorientations are developed within this sample set. Theoretical coincident site lattices have been calculated for quartz, but are not preferentially developed within the aureole. Thus, low energy grain boundaries are not produced by annealing within this regime.

8.4 Concerning Microstructural Stability

Different microstructures react to the changing temperature conditions at different rates. In particular, each type of microstructure stabilises to a differing extent. Dislocations, dislocation arrays, subgrains and grain geometries and sizes critically affect the microstructural evolution throughout the Ballachulish aureole. Each is discussed below.

(1) Dislocations are the least stable, reacting early during annealing, if not before annealing during post-tectonic thermal relaxation.

(2) Grain shapes are the next microstructure to be modified. They become regular as grain size increases at 800m from the intrusion, before any alteration in subgrain size/configuration.

(3) Subgrains are relatively stable features, preserving evidence of their geological history for a longer time period than grains.

(4) Fractured ('mesh') microstructures are the most stable microstructure observed in the Ballachulish aureole. The mesh features remain unaltered and furthermore prevent grain boundary migration. Their stability is a consequence of their fluid inclusion and impurity content, essentially causing mesh grains to pin migrating grain boundaries. Grain boundaries are therefore prevented from consuming mesh grains, resulting in them being a very stable microstructure.

(5) Impurities (second phases, precipitates or solute atoms) severely affect the rates of microstructural modification in the Ballachulish aureole. Different microstructural elements are affected by different impurity types at different stages during microstructural development. The extent to which each microstructural element is affected in all tectonic regimes is a critical requirement for all future microstructural analysis.

(6) Evidence of the nucleation of strain free grains during the early stages of primary recrystallisation has also been presented. Nucleation may have subtle effects on

crystallographic orientations during the annealing of highly deformed rocks. However, the microtextures in the Ballachulish aureole do not permit such an analysis.

(7) The fractured (mesh) grains seen in Ballachulish have not been documented elsewhere. These types of microstructures, which are related to fluid inclusions (i.e. healed fractures) and which make the rock less susceptible to recovery, have important implications for the role of fluids during deformation. It has been shown experimentally that fluids weaken rocks by hydrolytic weakening. However, fractured (mesh) grains are an example where fluids have the opposite effect on rock strength, because they make the rock more stable by preventing grain boundary migration.

8.5 Concerning the Kinetics

The rate of microstructural changes within the Ballachulish aureole have been modelled using assumptions of normal grain growth. The diffusion and activation energy constants were taken from Joesten (1983).

The theoretical expectations of grain growth within the Ballachulish depart from the actual values for grain growth measured in this study from quartzo-feldspathic samples and also data from on pure quartzite samples (Buntebarth and Voll 1991).

For pure samples, it is shown that grain growth is inhibited between 1500m and 800m. Impurity and solute drag are thought to be responsible. Between 800m and 600m where primary recrystallisation occurs, growth rates are greater than expected, because strain induced grain boundary migration contributes to grain growth. Between 600m and the igneous contact normal grain growth kinetics do operate, with the predicted and actual grain sizes being in close agreement.

For impure samples, grain growth is inhibited throughout the aureole. An 'effective activation energy' for grain growth in impure samples has been calculated. This figure may be used as a working estimate to predict whether grain growth has occurred in quartzo-feldspathic rocks.

Two models have been described to show how subgrains should react to temperature. Firstly a normal grain growth model is described in which the pre-exponential term in the grain growth equation is reduced to account for the lower surface energies associated with subgrain boundaries. This model predicts that subgrains should be more stable than grain boundaries, which explains why they survive in Ballachulish even after grain growth has begun.

The second model that predicts subgrain growth is controlled by dislocation climb. This model is sensitive to small variations in the parameters which are input into the equations. Thus, it cannot be shown whether subgrain growth is controlled by dislocation climb, or by a more general surface energy equation.

The results of grain growth simulations using simple temperature paths and a variety of initial grain sizes indicate that as grain growth continues any original variations in grain size become ironed out. This is because initially small grains grow more rapidly than larger grains.

The temperature that a rock attains is obviously an important factor controlling grain growth because it is a diffusion related process. However, the temperature gradient (change in temperature through time) is also critical. Grain growth will not occur during a period of rapid cooling.

8.6 Future Work

(1) *Techniques*:- This investigation has quantified the characteristics of microstructures in two-dimensions (i.e. from a thin section). Techniques to quantify microstructures in three dimension by serial sectioning or by examining perpendicular sections may enable us to develop a more detailed knowledge of microstructural evolution in a variety of metamorphic, igneous and sedimentary environments. The fractal analysis of grain shapes has been an integral in characterising grain shapes over a variety of scales. It would be useful to further develop dilation techniques to in order to process the fractal data and hence classify distinctive shapes. Such a classification would enable geologists to

compare grain shapes directly within one sample, from sample to sample and even between rocks from different tectonic environments.

(2) *Ballachulish*:- It has been shown that chemical impurities, on all scales, influence the processes and rates of microstructural change in the Ballachulish aureole. However, equally as important is to investigate how microstructural processes may modify the rock chemistry and the distribution of impurities. Within this project, microstructures are characterised; further work is necessary to identify changes in the chemical attribute of minor trace elements, precipitates, fluid inclusions and second phase feldspar particles.

A late NE-SW fault (The Ballachulish Fault) cuts across the Ballachulish aureole. This fault has moved both during and after the intrusion. This is an ideal situation to research the effects the initial grain size of a rock on faulting mechanisms, because the quartzites near the intrusion had been coarsened during contact metamorphism prior to faulting.

(3) *Kinetics*:- A number of kinetic models describing the microstructural changes of grains in a regional tectonic framework have been presented. Further work is required to calculate how other types of microstructural elements (i.e. subgrains and dislocations) would change when exposed to these geological conditions.

The kinetic models from Ballachulish allow a more detailed examination of annealing and microstructural modification in other tectonic settings. An ideal location for such a study would be where there is a well constrained Pressure / temperature / strain / strain rate history. Many microstructural studies have been undertaken in The Basin and Range region of Eastern America. Deformed tectonites have been exhumed during extension. The data set, collected by numerous geologists present an ideal opportunity to test the microstructural models developed for Ballachulish in a dynamic tectonic setting.

(4) *Crystallographic Preferred Orientations*

Rocks which originally had a strong CPO prior to being annealed potentially could behave in a different manner to the Appin Quartzite at Ballachulish. Experimentally

annealing highly deformed quartzites, or doing a similar study to this in a region which had better developed crystal fabrics prior to an intrusion are necessary.

(5) *Experiments*:- This project has posed numerous questions about the mechanisms of microstructural modification over geological time. It is important to try and repeat these results in a laboratory. In doing so, the effects of kinetics on microstructural evolution are being examined, which is critical for geologists wishing to apply laboratory derived data to complex geological issues.

References

- Abaov, D.A.** 1971. The stability of grains in a polycrystal. *Metallog.*, **4**, 425-441.
- Abbruzzese, G., & Lucke, K.** 1986. A theory of texture controlled grain growth -I. Derivation and general discussion of the model. *Acta Metall.*, **34**, No. 5, 905-914.
- Abrams, H.** 1971. Grain size measurement by the intercept method. *Metallog.*, **4**, 59-78.
- Anderton, R., Bridges, P.H., Leeder, M.R., & Sellwood, B.W.** 1979. *A dynamic stratigraphy of the British Isles, A study in crustal evolution*. George Allen & Unwin, London,
- Anderton, R.** 1985. Sedimentation and tectonics in the Scottish Dalradian. *Scott. J. Geol.*, **21**, 407-436.
- Anderton, R.** 1988. Dalradian slides and basin development: a radical interpretation of stratigraphy and structure in the S.W. and Central Highlands of Scotland. *J. Geol. Soc. Lond.*, **145**, 669-678.
- Andrade En Da, C., & Aboav, D.A.** 1966. Grain growth in metals of close packed hexagonal structure. *Proc. R. Soc. Lond.*, **A291**, 18-40.
- Atherton, M.P.** 1968. The variation in garnet, biotite and chlorite composition in medium grade pelitic rocks from the Dalradian of Scotland, with particular reference to the zonation in garnet. *Contrib. Mineral. Petrol.*, **18**, 347-371.
- Atkinson, B.K., & Meredith, P.G.** 1987. The theory of subcritical crack growth with applications to minerals and rocks. In: Atkinson, B.K. (eds.), *Fracture mechanics of rocks*. Academic Press, London,
- Atkinson, H.V.** 1988. Theories of normal grain growth in pure single phase systems. *Acta metall.*, **36**, No. 3, 469-491.
- Bailey, E.B., & Maufe, H.B.** 1960. "The Geology of Ben Nevis and Glen Coe" - Explanation of Sheet 53. *Mem. Geol. Surv. Scotland*,
- Ball, A., & White, S.H.** 1977. An etching technique for revealing dislocation structures in deformation structures in deformed quartz grains. *Tectonophysics*, **37**, T9-T14.
- Ballard, D.H., & Brown, C.M.** 1982. *Computer Vision*. Prentice-Hall,

Barber, D.J. 1990. Regimes of plastic deformation processes and microstructures: An overview. *In: Barber, D.J.a.M., P.G. (eds.), Deformation processes in minerals, ceramics and rocks.* Unwin Hyman, London, 169.

Barnicoat, A.B. 1982. Ph.D. Thesis, Edinburgh University.

Baxes, G.A. 1984. *Digital image processing.* Prentice-Hall, Englewood Cliffs.

Beck, P.A. 1954. *Philos. Mag. Suppl.* **3**, 245ff.

Blacic, J.D., & Christie, J.M. 1984. Plasticity and hydrolytic weakening of quartz single crystals. *J. Geophys. Res.*, **89**, 4223-4239.

Blenkinsop, T.G., & Dury, M.R. 1988. Stress estimates and fault history from quartz microstructures. *J. Struc. Geol.*, **10**, 673.

Boisen, M.B., & Gibbs, G.V. 1985. *Mathematical Crystallography: an introduction to the mathematical foundation of crystallography.* Mineralogical Society of America,

Bons, P.D., & Urai, J.L. 1992. Syndeformational grain growth: microstructures and kinetics. *J. Struct. Geol.*, **14**, 1101-1109.

Booker, G.R. 1970. Scanning electron microscopy: electron channelling effects. *In: Amelinck, S., Gevers, R., Remant, G. and Von Landuyt, J. (eds.), Modern diffraction and imaging techniques in Materials science.* North Holland, Amsterdam,

Brace, W.F., and Walsh, J.B. 1962. Some direct measurements of the surface energy of quartz and orthoclase. *Am. Mineralogist*, **47**, 1111-1122.

Brandon, D.G. 1966. The structure of high angle grain boundaries. *Acta Metall.*, **14**, 1479.

Brown, G.C. 1979. *Geochemical and geophysical constraints on the origin and evolution of Caledonian granites.* Spec. Publ. Geol. Soc. London, 645-651 pp.

Brown, P.E., Miller, J.A., Grasty, R.L. 1968. Isotopic ages of late Caledonian granitic intrusions in the British Isles. *Proc. Yorksh. Geol. Soc.*, **36**, 251-276.

Bunge, H.J. 1985. Representation of preferred orientation. *In: Wenk, H.-R. (eds.), Deformed metals and rocks: An introduction to modern texture analysis.* Academic Press, 73.

Bunge, H.J., & Weiland, H. 1988. Orientation correlation in grain and phase boundaries. *Textures and Microstructures*, **7**, 231-263.

Buntebarth, G., & Voll, G. 1991. Quartz grain coarsening by collective crystallisation in contact quartzites. *In: Voll, G., Topel, J., Pattison, D.R.M. and*

- Seifert, F. (eds.), *Equilibrium and kinetics in contact metamorphism: The Ballachulish igneous complex and its aureole*. Springer-Verlag.
- Buntebarth, G.** 1991. Thermal models of cooling. In: Voll, G., Topel, J., Pattison, D.R.M. and Seifert, F. (eds.), *Equilibrium and kinetics in contact metamorphism: The Ballachulish igneous complex and its aureole*. Springer-Verlag, Berlin, 484.
- Burke, J.E.** 1949. Some factors affecting the rate of grain growth in metals. *Am. Inst. Mining Metall. Engineers Trans.*, **180**, 73.
- Buseck, P.R.** 1992. *Minerals and reactions at the atomic scale: transmission electron microscopy*. Mineralogical Society of America, Washington, D.C., 508 pp.
- Byerlee, J.D.** 1968. Brittle-ductile transition in rocks. *J. Geophys. Res.*, **73**, 4741-4750.
- Carslaw, H.S., & Jaeger, J.C.** 1959. *Conduction of heat in solids*, 2nd ed., Clarendon Press, Oxford.
- Christie, J.M., Ord, A. and Koch, P.S.** 1980. Relationship between recrystallised grain size and flow stress in experimentally deformed quartzite. *EOS.*, **61**, 377.
- Coble, R.L.** 1963. A model for grain boundary diffusion controlled creep in polycrystalline materials. *J. Appl. Phys.*, **34**, 1679.
- Covey-Crump, S.J., & Rutter, E.H.** 1989. Thermally induced grain growth of calcite marbles on Naxos Island, Greece. *Contributions to Mineralogy and Petrology*, **101**, 69-86.
- Crane, A.** 1992. *Field guide for the Ballachulish and Glencoe region*. Aberdeen University.
- Danielsson, P.-E.** 1980. Euclidean Distance Mapping. *Computer Graphics and Image Processing*, **14**, 227-248.
- Dempster, T.J.** 1985. Uplift patterns and orogenic evolution in the Scottish Dalradian. *J. Geol. Soc. Lond.*, **142**, 111-128.
- Drury, M.R., Humphreys, F.J. and White, S.H.** 1985. Large strain deformation studies using polycrystalline magnesium as a rock analogue. Part II: dynamic recrystallisation mechanisms at high temperatures. *Phys. Earth Planet. Inters.*, **40**, 208-222.
- Elderton, W.P., & Johnson, N.L.** 1969. *Systems of frequency curves*. Cambridge University Press, London,

- Elliot, D.** 1973. Diffusion flow laws in metamorphic rocks. *Geol. Soc. Am. Bull.*, **84**, 2645.
- Etchecopar, A.** 1977. A plane kinematic model of progressive deformation in a polycrystalline aggregate. *Tectonophysics*, **39**, 121.
- Etheridge, M.A., Wall, V.J., Cox, S.F. and Vernon, R.H.** 1984. High fluid pressures during regional metamorphism and deformation: implications for mass transport and deformation mechanisms. *J. Geophys. Res.*, **89**, 4344-4358.
- Farmer, A.B.** 1992. *A microstructural investigation of natural deformation in quartz aggregates*. PhD., Leeds University,
- Feltham, P.** 1957. Grain growth in metals. *Acta. metall.*, **5**, 97-105.
- Ferry, J.M., & Spear, F.S.** 1978. Experimental calibration of the partitioning of Fe and Mg between biotite and garnet. *Contrib. Mineral. Petrol.*, **66**, 113-118.
- Fisher.** 1978. Rate laws in metamorphism. *Geochem. et Cosmochimica Acta*, **42**, 1035-50.
- Fliervoet, T.F., & White, S.H.** 1995. Quartz deformation in very fine grained quartzo-feldspathic mylonite. *J. Struc. Geol.*, **17**, 1096-1108.
- Flook, A.G.** 1978. Use of dilation logic on the Quantimet to achieve fractal dimension characterization of texture and structured profiles. *Powder Techn.*, **21**, 295-298.
- Friedel, J.** 1964. *Dislocations*. Pergamon Student Editions, Oxford, 491 pp.
- Gault, H.R.** 1949. The frequency of twin types in quartz crystals. *Am. Min.*, **34**, 147-159.
- Gilletti, B.J., & Yund, R.A.** 1984. Oxygen diffusion in quartz. *J. Geophys. Res.*, **89**, 4039-4056.
- Gleason, G.C.** 1990. The effects of annealing on lattice preferred orientations of deformed quartz aggregates. *Trans. AUG.*, **71**, 1657.
- Gonzalez, R.C., & Wintz, O.** 1987. *Digital image processing*. Addison-Wesley,
- Gordon, R.B.** 1965. Diffusion creep in the earth's mantle. *J. Geophys. Res.*, **70**, 2413.
- Grant, E., Porter A., & Ralph, B.** 1984. Grain boundary migration in single phase and particle-containing materials. *J. Mat. Sci.*, **19**, 3554-3573.
- Grimmer, H.** 1974. *Scripta Metall.*, **8**, 1221.

- Grimmer, H.** 1980. A unique description of the relative orientation of neighbouring grains. *Acta Cryst.*, **A36**, 382-389.
- Grimmer, H.** 1989. Coincidence orientations of grains in rhombohedral materials. *Acta Cryst.*, **A45**, 505-523.
- Grimmer, H.** 1989. A geometrical model of special grain boundaries in corundum. *Helvetica Physica Acta*, **62**, 231-234.
- Grimmer, H.** 1990. Special grain boundaries in rhombohedral materials. *J. Phys. Colloque*, **C1 51**, 155-160.
- Groshong, R.H.** 1988. Low temperature deformation mechanisms and their interpretation. *Bull. Geol. Soc. Am.*, **100**, No. 1329-1360,
- Hacker, B.R., Yin, A., Christie, J.M. and Snoke, A.W.** 1990. Differential stress, strain rate and temperatures of mylonitization in the Ruby Mountains, Nevada: Implications for the rate and duration of uplift. *J. Geophys. Res.*, **95**, 8569.
- Hacker, B.R., Yin, A., Christie, J.M. and Davis, G.A.** 1992. Stress magnitude, strain rate and rheology of extended middle continental crust inferred from quartz grain sizes in the Whipple Mountains, California. *Tectonics*, **11**, 36.
- Haessener, F., Pospiech, J. and Sztwiertna, K.** 1983. Spatial arrangement of orientation rolled copper. *Mat. Sci and Eng.*, **57**, 1.
- Haessener, F., & Hoffman, S.** 1978. *Migration of high angle grain boundaries*. Dr. Reider Verlag, Stuttgart, 63-95 pp.
- Handy, M.R.** 1989. The solid state flow of polymineralic rocks. *J. Geophys. Res.*, **95**, 8647-8661.
- Handy, M.R.** 1990. Deformation regimes and the rheological evolution of fault zones in the lithosphere: the effects of pressure, temperature, grainsize and time. *Tectonophysics*, **163**, 119-152.
- Handy, M.R.** 1991. Flow laws for composite viscous materials: a phenomenological approach. *Terra Abstracts*, **3**, 75.
- Harper, C.T.** 1967. The geological interpretation of potassium-argon ages of metamorphic rocks from the Scottish Caledonides. *Scott. J. Geol.*, **3**, 46-66.
- Harr, M.E.** 1977. *Mechanics of particulate media: a probabilistic approach*. McGraw-Hill, New York,
- Harris, A.L., & Pitcher, W.S.** 1975. The Dalradian supergroup. *In: Harris, A.L. et al. (eds.), A correlation of the Precambrian rocks in the British Isles*. Geol. Soc. Lond. Spec. Rep., **6**, 52-75.

- Harris, A.L., & Pitcher, W.S.** 1975. *The Dalradian Supergroup*. Geol. Soc. Lond.,
- Harte, B., & Voll, G.** 1991. The setting of the Ballachulish intrusive complex in the Scottish Highlands. In: Voll, G., Topel, J., Pattison, D.R.M. and Seifert, F. (eds.), *Equilibrium and kinetics in contact metamorphism: The Ballachulish igneous complex and its aureole*. Springer-Verlag, Berlin,
- Haslam, H.W., & Kimbell, G.S.** 1981. Disseminated copper-molybdenum mineralisation near Ballachulish, Highland Region. *Mineral. Recon. Progr. Rep.*, **43**, 45pp.
- Hay, R.S., & Evans, B.** 1988. Intergranular distribution of pore fluid and the nature of high-angle grain boundaries in limestone and marble. *J. Geophys. Res.*, **93**, 8959-8974.
- Heaney, P.J., & Verblen, D.R.** 1991. Observations of the α/β quartz transition in quartz: A review of imaging and diffraction studies and some new results. *Am. Min.*, **76**, 1018-1032.
- Hickman, A.H.** 1975. The stratigraphy of late Pre-Cambrian metasediments between Glen Roy and Lismore. *Scott. J. Geol.*, **11**, 117-142.
- Hillert, M.** 1965. On the theory of normal and abnormal grain growth. *Acta Metall.*, **13**, 227-238.
- Hirth, G., & Tullis, J.** 1992. Dislocation creep regimes in quartz aggregates. *J. Struc. Geol.*, **14**, 145-159.
- Hobbs, B.E.** 1968. Recrystallisation of single crystals of quartz. *Tectonophysics*, **6**, 353-401.
- Hodges, K.V., & Spear, F.S.** 1982. Geothermometry, geobarometry and the Al_2SiO_5 triple point at Mt. Moosilauke, New Hampshire. *Am. Mineral.*, **67**, 1118-1134.
- Hoernes, S., & Voll, G.** 1991. *Detrital quartz and K-feldspar in quartzites as indicators of oxygen isotope exchange kinetics*. Springer-Verlag, Berlin, 484 pp.
- Horn, B.K.P.** 1986. *Robot vision*. MIT Press,
- Hurford, A.J.** 1977. A preliminary fission track dating survey of Caledonian 'newer and last granites' from the Highlands of Scotland. *Scott. J. Geol.*, **13**, 271-284.
- Inoue, S.** 1986. *Video microscopy*. Plenum Press, New York,

- Jessel, M.W., & Lister, G.S.** 1990. A simulation of the temperature dependence of quartz fabrics. *In: Knipe, R.J. and Rutter, E.H. (eds.), Deformation mechanisms, rheology and tectonics.* **54**, The Geological Society, London, 353-362.
- Jessell, M.W.** 1986. Grain boundary migration and fabric development in experimentally deformed octachloropropane. *J. Struc. Geol.*, **8**, 527-542.
- Joesten, R.** 1983. Grain growth and grain boundary diffusion in quartz from the Christmas Mountain (Texas) contact aureole. *Amer. J. Sci.*, **283A**, 233-254.
- Joesten, R.L.** 1991. Kinetics of coarsening and diffusion-controlled mineral growth. *In: Kerrick, D.M. (eds.), Contact Metamorphism.* **Mineralogical Society of America, Reviews in Mineralogy**, **100**, 714-732.
- Joy, D.C., & Newbury, D.E.** 1977. A bibliography on the observation of crystalline materials by use of diffraction effects in the SEM. *Scanning Electron Microscopy*, 445.
- Joy, D.C., Newbury, D.E. and Davidson, D.L.** 1982. Electron channelling patterns in the SEM. *J. Appl. Phys.*, **53**, 81-122.
- Kamb, W.B.** 1959. Theory of preferred orientation development by crystallisation under stress. *J. Geology*, **67**, 153.
- Kasen, M.B.** 1983. Solute segregation and boundary structural change during grain growth. *Acta Metall.*, **31**, 489-497.
- Kaye, B.H.** 1988. Describing the structure of fine particle populations using the Korcak fractal dimension. *In: (eds.), Size characterisation.* Guilford, London,
- Kaye, B.H.** 1989. *A random walk through fractal dimensions.* Weinheim, VCH Verlagsgesellschaft,
- Kingery, W.D., Bowen, H.K., and Uhlmann, D.R.** 1976. *Introduction to ceramics.* John Wiley & Sons, New York, 1032 pp.
- Kirby, S.H.** 1985. Rock mechanics observations pertinent to the rheology of the continental lithosphere and the localisation of strain along shear zones. *Tectonophysics*, **119**, 1-27.
- Klapper, H.** 1980. Defects in non-metal crystals. *In: Tanner, B.K.a.B., D.K. (eds.), Characterisation of crystal growth defects by x-ray methods.* **130-166**, Plenum, New York,
- Knipe, R.J., & Wintsch, R.P.** 1985. Heterogeneous deformation foliation development and metamorphic processes in a polyphase mylonite. *In: Thompson, A.B., & Rubie, D.C. (eds.), Metamorphic reactions :kinetics, textures and deformation.* *Advances in Physical Geochemistry*, **4**, Springer, New York,

Knipe, R.J. 1989. Deformation mechanisms-recognition from natural tectonites. *J. Struc. Geol.*, **11**, No. No. 1/2, 127 to 146.

Knipe, R.J., & Rutter, E.H. 1990. *Deformation mechanisms, rheology and tectonics*. The Geological Society, London, 535 pp.

Knipe, R.J. and Lloyd, G.E. 1994. Deformation history during faulting: The Skiag Bridge backthrust, Assynt, NW Scotland. In: C.J. Maronne & M. Blanpied (eds.), *Faulting, Friction, and Earthquake Mechanics Part II, Pure and Applied Geophysics* . **142**, 229-254.

Kroll, H., Krause, C. and Voll, G. 1991. *Disordering, re-ordering and unmixing in alkali feldspars from contact metamorphosed quartzites*. Springer-Verlag, Berlin,

Lartique, S., & Priester. 1988. *J. Am. Ceram. Soc.*, **71**, 430.

Lasaga. 1986. Metamorphism reaction rate laws and development of isograds. *Min. Mag.*, **50**, 359-73.

Law, R.D., Knipe, R.J., & Dayan, H. 1984. Strain path partitioning within thrust sheets: microstructural and petrofabric evidence from the Moine Thrust Zone, Loch Eriboll. *J. Struc. Geol.*, **6**, 477-497.

Law, R.D., Casey, M. and Knipe, R.J. 1986. Kinematics and tectonic significance of microstructures and crystallographic fabrics within quartz mylonites from the Assynt and Eriboll regions of the Moine Thrust Zone. *Trans. R. Soc. Edin. Earth. Sci.*, **77**, 99-123.

Law, R.D. 1987. Heterogeneous deformation and quartz crystallographic fabric transitions: natural examples from the stack of Glencoul, northern Assynt. *Journal of Structural Geology*, **9**, 819-833.

Law, R.D. 1990. Crystallographic fabrics: a selective review of their applications to research in structural geology. In: Knipe, R.J. and Rutter, E.H. (eds.), *Deformation mechanisms, rheology and tectonics*. **54**, The Geology Society, London, 335-352.

Law, R.D., Schmid, S.M. and Wheeler, J. 1990. Simple shear deformation and quartz crystallographic fabrics: a possible example from the Torridon area of NW Scotland. *J. Struc. Geol.*, **12**, 29-46.

Lister, G.S., Paterson, M.S. and Hobbs, B.E. 1978. The simulation of fabric development during plastic deformation and its application to quartzite: The Model. *Tectonophysics*, **45**, 107-158.

Lister, G.S., & Hobbs, B.E. 1980. The simulation of fabric development during plastic deformation and its application to quartzite: The influence of deformation history. *J. Struc. Geol.*, **2**, 355.

Litherland, M. 1982. The structure of the Loch Creran Dalradian and a new model for the SW Highlands. *Scott. J. Geol.*, **18**, 205-225.

Lloyd, G.E. 1983. Strain analysis using the shape of expected and observed continuous frequency distributions. *J. Struc. Geol.*, **5**, No. No. 3/4, 225-231.

Lloyd, G.E. 1987. Atomic number an crystallographic contrast images with the SEM: a review of backscattered electron techniques. *Mineral. Mag.*, **51**, 3-19.

Lloyd, G.E., Law, R.D. and Schmid, S.M. 1987. A spherical electron channelling pattern map for use in quartz petrofabric analysis: correction and verification. *J. Struc. Geol.*, **9**, 251-261.

Lloyd, G.E., & Freeman, B. 1991a. SEM electron channelling analysis of dynamic recrystallisation a quartz grain. *J. Struc. Geol.*, **13**, 945-953.

Lloyd, G.E., Schmidt, N-H., Mainprice, D. and Prior, D.J. 1991b. Crystallographic textures. *Mineral. Mag.*, **55**, 331-345.

Lloyd, G.E., & Knipe, R.J. 1992. Deformation mechanisms accommodating faulting of quartzite under upper crustal conditions. *J. Struc. Geol.*, **9**, 251.

Lloyd, G.E., Law, R.D., Mainprice, D. and Wheeler, J. 1992. Microstructural and crystal fabric evolution during shear zone formation. *J. Struc. Geol.*, **14**, 1079-1100.

Lloyd, G.E., & Freeman, B. 1993. Dynamic recrystallisation of quartz under greenschist conditions. *J. Struc. Geol.*,

Louat, N.P. 1974. On the theory of normal grain growth. *Acta Metall.*, **22**, 721.

Lucke, K., & Stuwe, N.P. 1971. On the theory of impurity controlled grain boundary motion. *Acta Metall.*, **19**, 1087-1099.

Mackenzie, J.K. 1964. The distribution of rotation axes in a random aggregate of cubic crystals. *Acta Metall.*, **12**, 223.

Magennis. 1993. *Deformation processes and tectonics in the western Himalayas*. Ph.D., University of Leeds,

Mainprice, D., Lloyd, G.E., Casey, M. 1993. Individual orientation measurements in quartz polycrystals - advantages and limitations for texture and petrophysical property determinations. *J. Struc. Geol.*, **15**,

Mainprice, D., Lloyd, G.E. and Casey, M. 1993. Individual orientation measurements in quartz polycrystals: advantages and limitations for texture and petrophysical property determinations. *J. Struc. Geol.*, **15**, No. 9/10, 1169-1187.

- Mandelbrot, B.B.** 1975. *Stochastic models for the earth's relief, the shape and the fractal dimension of coastlines, and the number-area rule for islands*. National Academy of Science, USA,
- Mandelbrot, B.B.** 1982. *The fractal geometry of nature*. Freeman, New York,
- Marsh, B.D.** 1982. On the mechanics of igneous diapirism, stoping, and zone melting. *Am. J. Sci.*, **282**, 808-855.
- Masch, L., & Heuss-Abichler, S.** 1991. *Decarbonation reactions in siliceous dolomites and impure limestones*. Springer-Verlag, Berlin,
- McClay, K.R., & Atkinson, B.K.** 1977. Experimentally induced kinking and annealing of single crystals of galena. *Tectonophysics*, **39**, 175-193.
- McLaren, A.C.** 1986. *Some speculations on the nature of high-angle grain boundaries in quartz rocks*. AGU, Washington, D.C., 233-247 pp.
- Means, W.D.** 1983. Microstructure and micromotion in recrystallisation flow of octachloropropane: a first look. *Geol. Rundsch.*, **72**, 511-528.
- Means, W.D.** 1989. Synkinematic microscopy of transparent polycrystals. *J. Struct. Geol.*, **11**, 163-174.
- Means, W.D.** 1989. Synkinematic microscopy of transparent polycrystals. *J. Struct. Geol.*, **11**, 163-174.
- Meredith, P.G., & Atkinson, B.K.** 1983. Stress corrosion and acoustic emission during tensile crack propagation in Whin sill dolerite and other basic rocks. *Geophysical Journal of the Royal Astronomical Society*, **75**, 1-21.
- Miller, J.A., & Brown, P.E.** 1965. Potassium-argon age studies in Scotland. *Geol. Mag.*, **102**, 106-134.
- Minkowski, H.** 1901. Über die begriffe lange, oberfläche und volumen. *Jahresbericht der deutschen Mathematikervereinigung*, **9**, 115-121.
- Nicolas, A.** 1978. Stress estimates from structural studies in some mantle peridotites. *Trans. R. Soc. Lond.*, **A288**, 49.
- Olesen, N.O., & Schmidt, H-H.** 1990. The SEM/ECP technique applied on twinned quartz crystals. In: Knipe, R.J. and Rutter, E.H. (eds.), *Deformation mechanisms, Rheology and Tectonics*. **54**, Geol. Soc. Spec. Publ., London, 171-185.
- Olgaard, D.A., and Evans, B.** 1986. Effect of second phase particles on grain growth in calcite. *J. Am. Ceram. Soc.*, **69**, C272-C277.

- Ord, A., & Hobbs, B.E.** 1989. The strength of the continental crust, detachment zones and the development of plastic instabilities. *Tectonophysics*, **158**, 269-289.
- Pattison, D.R.M., & Harte, B.** 1985. A petrogenetic grid for pelites in the Ballachulish and other Scottish thermal aureoles. *J. Geol. Soc. Lond.*, **142**, 7-28.
- Pattison, D.R.M.** 1987. Variations in Mg/(Mg+Fe), F, and $(Fe,Mg) = 2Al$ in pelitic minerals in the Ballachulish thermal aureole, Scotland. *Am. Mineral.*, **72**, 255-272.
- Pattison, D.R.M., & Harte, B.** 1991. Petrography and mineral chemistry of pelites. In: Voll, G., Topel, J., Pattison, D.R.M. and Seifert, F. (eds.), *Equilibrium and kinetics in contact metamorphism: The Ballachulish igneous complex and its aureole*. Springer-Verlag.
- Pattison, D.R.M., & Harte, B.** 1988. Evolution of structurally contrasting anatectic migmatites in the 3-kbar Ballachulish aureole, Scotland. *J. Metam. Geol.*, **6**, 475-494.
- Perkins, D.I., & Chipera, S.J.** 1985. Garnet-orthopyroxene-plagioclase-quartz barometry: refinement and application to the English River subprovince and the Minnesota river valley. *Contrib. Min and Petrol.*, **89**, 69-80.
- Poirier, J.P., & Nicolas, A.** 1975. Deformation induced recrystallisation due to progressive misorientation of subgrains, with special reference to mantle peridotites. *J. Geol.*, **83**, 707-720.
- Poirier, J.P., & Guillope, M.** 1979. Deformation induced recrystallisation of minerals. *Bull. Mineral.*, **102**, 67-74.
- Poirier, J.P.** 1980. Shear localisation and shear instability in the ductile field. *J. Struct. Geol.*, **2**, 135-142.
- Poirier, J.P.** 1985. *Creep of crystals*. University Press, Cambridge,
- Pospiech, J., Sztwiertnia, K. and Haessener, F.** 1986. The misorientation distribution function. *textures and Microstructures*, **6**, 201-215.
- Pratt, W.K.** 1978. *Digital image processing*. John Wiley,
- Prior D, J.** 1988. *Deformation processes in the Alpine fault mylonites, South Island, New Zeland*. University of Leeds,
- Prior, D.P., Knipe, R.J. and Handy, M.R.** 1990. Estimates of the rates of microstructural change in mylonites. In: Knipe, R.J. and Rutter, E.H. (eds.), *Deformation mechanisms, rheology and tectonics*. **54**, The Geological Society, London, 309-320.

- Pryer, L.L., Robin, P-Y.F. and Lloyd, G.E.** 1995. An SEM electron channelling study of flame perthite from the Killarney Granite, Southwestern Grenville Front. Ontario. *Canadian Mineralogist*, **33**, 333-347.
- Randle, V., & Furley, J.** 1991. Experimental aspects of the use of electron back scattering for the characterisation of microtexture and mesotexture. *Textures and Microstructures*, **14-18**, Special issue, ICOTOM 9 Avignon,
- Randle, V.** 1992. *Microtexture determination and its applications*. Institute of Materials, London,
- Ransom, D.M.** 1971. Host control of recrystallised quartz grains. *Mineral. Mag.*, **38**, 83-88.
- Richardson, L.F.** 1961. The problem of contiguity: An appendix of statistics of deadly quarrels. *General Systems Yearbook*, **6**, 139-187.
- Roberts, J.L.** 1976. The structure of the Dalradian rocks in the North Ballachulish district of Scotland. *J. Geol. Soc. Lond.*, **132**, 139-154.
- Roberts, J.L., & Treagus, J.E.** 1977. The Dalradian of the Loch Leven area. *Scott. J. Geol.*, **13**, 165-184.
- Roberts, J.L., & Treagus, J.E.** 1977. The Dalradian rocks of the South West Highlands - an introduction. *Scott. J. Geol.*, **13**, 87-99.
- Roberts, J.L., & Treagus, J.E.** 1977. Polyphase generation of nappe structures in the Dalradian rocks of the SW Highlands of Scotland. *13*, **237-254**,
- Rosenfeld, A., & Kak, A.C.** 1982. *Digital picture processing*. Academic Press,
- Russ, J.C.** 1988. *Computer assisted microscopy, the measurement and analysis of images*. North Carolina State University,
- Russ, J.C.** 1992. Characterizing and modelling fractal surfaces. *Journal of Computer Assisted Microscopy*, **4**, 73-126.
- Russ, J.C.** 1994. *Fractal surfaces*. Plenum Press, New York and London,
- Rutter, E.H.** 1976. The kinetics of rock deformation by pressure solution. *Phil. Trans. R. Soc. Lond.*, **A283**, 319.
- Rutter, E.H.** 1983. Pressure solution in nature theory and experiment. *J. Geol. Soc. Lond.*, **140**, 725-740.
- Schmid, S.M., & Casey, M.** 1986. Complete fabric analysis of some commonly observed quartz C-axis patterns. In: Hobbs, B.E. and Hearsh, H.C. (eds.), *Mineral and*

rock deformation: Laboratory studies: The Paterson volume. Geophys. Monogr. 36, American Geophysical Union,

Schmidt, N.-H., & Olesen, N.O. 1989. Computer-aided determination of crystal lattice orientation from electron channelling patterns in the SEM. *Canad. Mineral.*, **27**, 15-22.

Schulson, E.M. 1977. Review of electron channelling patterns in the SEM. *J. Materials Sci.*, **12**, 1071.

Siamoto, H., H., Kempson, D. and Schulson, E.M. 1980. Electron channelling and its potential for petrofabric studies. *Can. Mineral.*, **18**, 251.

Simpson, C.J., Aust, K.T., & Winegard, W.C. 1971. The four stages of grain growth. *Metallurgical Transactions*, **2**, 987-991.

Smith, C.S. 1952. *Metal interfaces.* Cleveland, Ohio,

Thomas, L.A. 1945. Terminology of interpenetrating twins in alpha quartz. *Nature*, **155**, 424.

Thompson, A.W. 1972. Calculation of true volume grain diameter. *Metallog.*, **5**, 366-369.

Troll, G., & Weiss, S. 1991. *Structure, petrography and emplacement of plutonic rocks.* Springer-Verlag, Berlin, 484 pp.

Tullis J., C., J.M. and Griggs, D.T. 1973. Microstructures and preferred orientations of experimentally deformed quartzites. *Geol. Soc. Amer. Bull*, **84**, 297-314.

Turnbull, D. 1951. Theory of grain boundary migration rates. *Trans. AIME*, **191**, 661-665.

Twiss, R.J. 1977. Theory and applicability of a recrystallised grain size palaeopiezometer. *Pageoph.*, **115**, 227.

Twiss, R.J. 1986. Variable sensitivity piezometric equations for dislocation density and subgrain diameter and their relevance to olivine and quartz. *In: Hobbs, B.E. & Heard, H.C. (eds.), Mineral and rock deformation Laboratory studies-The Paterson Volume. 36,* Am. Geophys. Un. Geophys. Monogr, 247.

Urai, J.L. 1983. Water assisted dynamic recrystallisation and weakening in bischofite. *Tectonophysics*, **96**, 125-127.

Urai, J.L., Means, W.D. and Lister, G.S. 1986. *Dynamic recrystallisation of minerals.* AGU, Washington, D.C., 161-199 pp.

- Voll, G., Topel, J., Pattison, D.R.M. and Seifert, F.** 1991. *Equilibrium and kinetics in contact metamorphism. The Ballachulish igneous complex and its aureole.* Springer-Verlag.
- Weertman, J.** 1968. Dislocation climb theory of steady state creep. *Trans. ASM.*, **61**, 9.
- Weiss, S., & Troll, G.** 1989. The Ballachulish igneous complex, Scotland: petrography, mineral chemistry and order of crystallization in the monzodiorite - quartz diorite suite and in the granite. *J. Petrol.*, **30**, 1069-1115.
- Wenk, H.-J., & Christie, J.M.** 1991. Comments on the interpretation of deformation textures in rocks. *J. Struc. Geol.*, **13**, 1091-1110.
- Wheeler, J.** 1992. Importance of pressure solution and coble creep in the deformation of polymineralic rocks. *J. Geophys. Res.*, **97**, 4579-4586.
- White, J.C., & White, S.H.** 1981. On the structures of grain boundaries in tectonites. *Tectonophysics*, **78**, 613-628.
- White, S.H.** 1971. Dislocations in naturally deformed quartzite. *Nat. Phys. Sci.*, **231**, 85-86.
- White, S.H.** 1973. The dislocation structures responsible for the optical effects in naturally deformed quartzites. *J. Mat. Sci.*, **8**, 490.
- White, S.H.** 1975. Estimation of strain rate from microstructures. *J. Geol. Soc. Lond.*, **131**, 577.
- White, S.H.** 1976. The effects of strain on the microstructures, fabrics and deformation mechanisms in quartz. *Philos. Trans. R. Soc. London, Ser. A*, **283**, 69-86.
- White, S.H.** 1979. Palaeostress estimates in the Moine Thrust Zone, Eriboll, Scotland. *Nature*, **280**, 222.

APPENDIX A

THERMAL MODELLING

1.1 Introduction

Our Knowledge of the thermal framework of the Ballachulish aureole is limited to the constraints on the intrusion temperature, the initial country rock temperature and the peak temperatures attained during contact metamorphism at a variety of places within the aureole (i.e. distances from the contact where mineral data has been used to assess the temperature). At any one locality there is not enough evidence to ascertain the temperature history throughout the evolution of the contact metamorphic event. A knowledge of the evolution of temperature through time is crucial in order to investigate the kinetics of microstructural change during metamorphism (cf. chapter 7).

Temperature/time histories can be estimated throughout the thermal aureole by computer modelling of heat flow from the intrusion through the aureole rocks using an initial set of starting conditions (i.e. size and temperature of intrusion, the temperature of the country rocks prior to intrusion and the conductivity of the country rocks). The thermal model presented is calculated using heat flow equations for materials transferring heat by conduction, the equations for which were originally derived by Carslaw and Jaeger

(1954). The theoretical basis for thermal modelling will be presented, followed by the application of the methods to the Ballachulish aureole.

1.2 Theory of Thermal Modelling in an Igneous Aureole

This summary of the heat flow model used for this investigation is adapted from Barnicoat (1982). In a system transferring heat by conduction, the rate of heat transfer (q) across a distance (dx) can be described by the equation:

$$\frac{q}{a} = \frac{\partial T}{\partial x} \quad \text{Equation 1}$$

The above equation is an experimentally observed fact, however a constant is needed to describe the true relationship between heat flow and temperature gradient. This constant (K) is known as the conductivity. Conductivity varies from material to material, hence materials such as copper, which have a high conductivity transfer heat rapidly in comparison with rocks which have a low conductivity. The equation above can be rewritten with a conductivity term as:

$$q = -Ka \frac{\partial T}{\partial x} \quad \text{Equation 2}$$

Heat is conducted from high temperatures regions down gradient to low temperatures regions, hence accounting for the minus sign in Equation 2. In a 1-D system (i.e. one in which there is a temperature difference only in one direction), as illustrated in Figure A1, an energy balance equation may be constructed:

$$q_x + q_{gen} = q_{init} + q_{x+dx} \quad \text{Equation 3}$$

In English, the energy conducted into the left hand face (q_x) + heat generated within the element (q_{gen}) = change in internal energy (q_{init}) + energy conducted out from the right hand face (q_{x+dx}).

Each of these terms may be expanded as follows:

$$q = -Ka \frac{\partial T}{\partial x} \quad \text{Equation 4}$$

$$q_{\text{gen}} = q \cdot a \partial x \quad \text{Equation 5}$$

$$q_{\text{init}} = \rho c \partial \frac{\partial T}{\partial x} \quad \text{Equation 6}$$

$$q_{x+\partial x} = -Ka \frac{\partial T}{\partial x} = -a \left(\frac{K \partial T}{\partial x} + \frac{\partial}{\partial x} \left(\frac{K \partial T}{\partial x} \right) \cdot \partial x \right) \quad \text{Equation 7}$$

The last term is derived simply by expansion of $\frac{\partial T}{\partial x}$ using the chain rule of partial differentiation. Substitution of all the terms into the energy balance equation yields:

$$Ka \frac{\partial T}{\partial x} + q \cdot a \partial x = \rho c a \frac{\partial T}{\partial t} \cdot \partial x + a \left(\frac{K \partial T}{\partial x} + \frac{\partial}{\partial x} \left(\frac{K \partial T}{\partial x} \right) \right) \cdot \partial x \quad \text{Equation 8}$$

Collecting terms and eliminating gives:

$$\frac{\partial}{\partial x} \left(\frac{K \partial T}{\partial x} \right) + q = \rho c \frac{\partial T}{\partial t} \quad \text{Equation 9}$$

If K is independent of x, this reduces to

$$K \frac{\partial^2 T}{\partial x^2} + q = \rho c \frac{\partial T}{\partial t} = \text{The Heat Flow Equation} \quad \text{Equation 10}$$

Thus, the change in temperature with time of the element under consideration may be described by Equation 10. Potentially this equation may be integrated to produce an analytical solution for the temperature distribution throughout the body. However, such a solution requires starting and boundary conditions that are unrealistic for geological situations, hence numerical solutions are necessary to solve the heat flow equation in the Ballachulish setting. Finite difference methods have frequently been used by geologists to

model thermal evolution of rocks in a variety of tectonic regimes (e.g. England and Richardson, 1977; Richardson and England, 1979; Wells, 1980).

Finite difference methods are used to approximate the partial differentials in equation 10, and so provide a solution. The methods are approximate in that the derivatives at a point are approximated by difference quotients over a small interval. Therefore, $\frac{\partial T}{\partial t}$ is replaced by $(T(t+\delta t)-(T(t)))/\delta t$. This is an example of a forward difference approximation, backward differences of the form $(T(x)-(T(x-\delta t)))/\delta t$, or central differences of the form:

$$(T(t+\delta t)-(T(t))-(T(t)-T(t-\delta t)))/2\delta t \quad \text{Equation 11}$$

may also be used during modelling.

The temperatures in the Ballachulish aureole need to be calculated at a series of distances from the intrusion. Therefore it is convenient to construct a series of nodes of constant spacing through the aureole. Temperatures are calculated at constant time intervals which may also be thought of as nodes. Therefore, a two-dimensional grid is created with temperature values varying with distance from the aureole in the x-direction and with time in the y-direction (essentially the grid is a large matrix with increments of i corresponding to distance from the intrusion and j to increments of time).

The second order derivatives can also be approximated using finite difference methods, whereby

$$\frac{\partial^2 T}{\partial t^2} = \frac{\left(\frac{\partial T_{(t+\delta t)}}{\partial t} - \frac{\partial T_{(t)}}{\partial t} \right)}{\delta x} \quad \text{Equation 12}$$

To avoid bias in the results, the backward derivative is used in the first derivative and a backward derivative for the second derivative.

Finite difference methods are applied to Ballachulish by substituting the approximations into the heat flow equation. Solutions for times greater than zero may be obtained

directly from a given set of starting conditions. If time is varying along the j lines of the grid, the initial starting conditions are given along the $j=0$ line, and the boundary conditions along the $i=1$ and $i=n$ lines. An implicit method of solving the differential equations is used (i.e. one in which temperature is yielded from a set of simultaneous equations over the whole grid. The implicit method used is that due to Crank and Nicolson (1949). Explicit methods may be used, in which temperature is obtained directly for each grid point. However these solutions are often unstable, because errors related to the finite difference approximations are exaggerated through time.

The partial differential heat flow equation may be approximated explicitly as:

$$\frac{K \partial^2 T}{\partial x^2} = \rho c \frac{\partial T}{\partial t}$$

$$\frac{K}{\Delta x^2} (T(i+1, j) - 2T(i, j) + T(i-1, j)) = \rho c \frac{(T(i, j+1) - T(i, j))}{\Delta t} \quad \text{Equation 13}$$

This equation may be rearranged with temperature as the subject. One of these equations is constructed for each grid point, after substituting in the boundary conditions $(T_{i,j})$ and $T(n,j)$. The thermal evolution of the system is calculated for each time step, using the temperature framework of the last iteration as the starting conditions. For stable

solutions, $\frac{K \Delta T}{\rho c \Delta X^2}$ needs to be less than 0.5. Therefore, a large number of both time steps and distance steps is required, reducing the speed at which the models may be computed.

1.2.1 Implicit Methods

The restrictive criterion for stable solutions necessary when using explicit solutions may be avoided using Crank-Nicolson methods (Crank and Nicolson, 1949). Partial differentials are replaced by the averages of them at the beginning and the end of each time step. The average corresponds to the solution at the centre of each time step. The heat flow equation is approximated by:

$$\frac{K}{2} \left(\frac{T(i+1, j) - 2T(i, j) + T(i-1, j)}{\Delta X^2} + \frac{T(i+1, j+1) - 2T(i, j+1) + T(i-1, j+1)}{\Delta X^2} \right) = \frac{\rho c (T(i, j+1) - T(i, j))}{\Delta t}$$

This may be rearranged to obtain the Crank Nicolson formula:

$$-RT_{(i+1)} + (2 + 2R)T_{(i, j+1)} - RT_{(i-1, j+1)} = RT_{(i+1, j)} + (2 - 2R)T_{(i, j)} + RT_{(i-1, j)}$$

Equation 14

where $R = \frac{K\Delta t}{\rho c \cdot \Delta x}$

Obviously temperature is not given directly, however a series equations for each grid point must be constructed and solved simultaneously. Gaussian elimination being highly suited to computation is used to solve the Crank Nicolson equations.

1.2.2 Additions to thermal model in intrusive Settings

The evolution of the Ballachulish aureole has been modelled using a computer program CONTACT 8 adapted from Contact 1.0 (Barnicoat, 1982) which models heat flow in the crust. Contact8 consists of three main processes; data input, temperature calculation and data output. Data input allows the user to stipulate the starting and boundary conditions of the system to be modelled and, the values of constants used during the calculation (e.g. rock density) and the time over which the model is to run. The thermal evolution of the system is calculated using the methods outlined above for the relevant amount of time. Data is output both graphically and as text to a file.

Heat flow models described above form the basis of the thermal models of the Ballachulish intrusion. However the heat flow equations need to be adapted from Cartesian co-ordinates to cylindrical co-ordinates. The heat flow equation in cylindrical co-ordinates is modified to

$$\frac{\partial T}{\partial t} = \frac{\partial^2 T}{\partial r^2} + \frac{1}{r} \cdot \frac{\partial T}{\partial r} + \frac{1}{r^2} \cdot \frac{\partial^2 T}{\partial \theta^2} + \frac{\partial^2 T}{\partial z^2}$$

Equation 15

The later two terms can be ignored as the intrusion is modelled as an infinite cylinder that possessing circular symmetry. Hence $d^2T/dz^2=0$ (differences in temperature in the vertical plane) and $d^2T/d\theta^2=0$ (differences in temperature with respect to angle away from the plane of origin). Therefore Equation 15 may be reduced to

$$\frac{\partial T}{\partial t} = \frac{\partial^2 T}{\partial r^2} + \frac{1}{r} \cdot \frac{\partial T}{\partial r} \quad \text{Equation 16}$$

Equation 16 merely accounts for heat conducting away from the intrusion, in the shape of a pie slice, as opposed to the simpler Cartesian form where heat is conducting through a rectangular rock element (e.g. Figure A1). Heat flow within a cylindrical system may be approximated to a finite element Crank Nicolson formula:

$$-[\text{RT}_{(i+1,j+1)} - \text{ZT}_{(i+1,j+1)}] - [(2+2\text{R})\text{T}_{(i,j+1)}] - [\text{RT}_{(i-1,j+1)} + \text{ZT}_{(i-1,j+1)}] =$$

$$[\text{RT}_{(i+1,j)} - \text{ZT}_{(i+1,j)}] + [(2-2\text{R})\text{T}_{(i,j)}] + [\text{RT}_{(i-1,j)} + \text{ZT}_{(i-1,j)}]$$

where $\text{R} = \frac{K\Delta t}{\rho c \cdot \Delta x}$ Equation 17

Again a series of simultaneous equations are constructed, one for each node and solved by Gaussian elimination.

1.2.3 Latent Heat of Crystallisation

During cooling of an intrusion excess heat is produced due to latent heat of crystallisation. In geological situations it is common for crystals to melt when energy (usually heat energy) is input into the system, energy being the driving force for the morphological change. Latent heat of crystallisation is the opposite of this process, whereby energy is released as a liquid alters to a crystalline state (with a lower configurational energy). Obviously, latent heat of crystallisation only is a consideration at temperatures between the liquidus and the solidus, i.e. temperatures at which crystallisation occurs.

Wells (1980) described latent heat of crystallisation using a term $L \rho dV/dt$, where L is the latent heat of fusion and dV/dt is the derivative of the volume fraction of melt crystallised with respect to time. Assuming that the volume of melt crystals varies linearly with temperature between the liquidus and solidus :

$$V = bT + a \quad \text{Equation 18}$$

where a is a constant and b is given by $b = l/(T_l - T_s)$ where T_l is the liquidus temperature and T_s the solidus temperature. Under these circumstances

$\frac{\partial V}{\partial T} = \frac{1}{T_l - T_s} \cdot \frac{\partial T}{\partial t}$ which can be used in writing a finite difference representation of the now modified heat flow equation:

$$\rho c \cdot \frac{\partial T}{\partial t} = \frac{K \partial^2 T}{\partial x^2} + \frac{1}{r} \cdot \frac{\partial T}{\partial d} + q + L \rho \frac{\partial V}{\partial t} \quad \text{Equation 19}$$

It can be seen that the Crank Nicolson finite element equations are ideal for solving heat conduction in geological situations. The calculations are time consuming, however with modern computing facilities this does not pose much of a problem. Therefore, modelling the Ballachulish intrusion involves fixing the starting conditions and boundary conditions and iteratively solving the heat flow equation for a specified time period.

1.3 Intrusion Dimensions and Boundary Conditions

The thermal model described predicts the evolution of temperature in the Ballachulish aureole over a 500 000 year time period. The model itself is 2-dimensional, the intrusion and aureole are modelled as being cylinders of infinite length, hence there is not a need to account for changes in temperature in the vertical plane. Temperatures are calculated for a linear transect through the aureole.

There are two possible scenarios for intrusion, a ring dyke intrusion, or a cylindrical intrusion. The former intrusion mechanism involves intrusion of a diorite magma in a ring pattern, which was closely followed by a quartz diorite magma ring intruding between

the first intrusion and the country rock. The central core was later replaced by granite at 800°C, which had no effect on the country rock temperatures. The core of country rock is presumed to exist beneath the intrusion (geophysical data is not accurate enough to distinguish such a feature). The second intrusion mechanism considers a diorite cylindrical intrusion have intruded the country rock. This cylinder begins to assimilate country rock material and fractionate towards a quartz diorite composition. Eventually the centre of the intrusion is replaced by the granite diapir.

Although both styles of intrusion result in similar igneous features, their thermal affects on the surrounding country rocks are markedly different. The essential difference is in the amount of heat supplied to the aureole. A ring intrusion, being relatively thin will supply far less heat in comparison to the cylindrical model which is 5800km in diameter. Bunterbarth (1991) suggests that a cylindrical model is more appropriate because initial country rock temperatures would need to be anomalously high if aureole temperatures suggested by mineral data were to be attained within the aureole.

1.3.1 Thermal Properties of Country Rocks

Although a variety of rock types do occur within the Ballachulish aureole, this investigation concentrates only on the Appin Quartzite. The thermal models can be run with either a constant conductivity or a temperature dependant conductivity. Conductivity as a function of temperature has been measured by Buntebarth (1991) for the Appin quartzite. Values decrease from 7 W m⁻¹C⁻¹ at 40C to 3.5 W m⁻¹C⁻¹ at 300C. The variation in conductivity is linearly related to temperature by an equation of the form:

$$K = (0.17 + 5.39 \cdot 10^{-4}T) \quad \text{Equation 20}$$

Examples of anisotropy in the conductivity of deformed quartzites has been shown by Mainprice (1992). Anisotropy is a function of preferred crystallographic orientation. Full crystallographic orientation descriptions from samples of the Appin quartzite (see Chapter 5) have been used to predict variations in conductivity due to deformation. It is seen that anisotropy in the conductivity is poorly developed within the Appin Quartzite, hence it will be ignored during thermal modelling.

Water migration into the wall rocks is not considered. This is justified by the fact that the initial intrusion was relatively dry (water content of 0.5-1.5, Weiss and Troll, 1991), much of that water would rise vertically within the magma chamber rather than migrating radially and finally any water that did escape into the aureole would quickly be consumed by melt reactions within the pelites (Pattison and Harte, 1988).

1.3.2 Intrusion Geometry and Thermal Regime

A cylindrical intrusion of infinite height is considered as the closest approximation to the Ballachulish intrusion. Geophysical data (Rabbel and Meissner, 1991) indicates that the intrusion has a minimum depth range of 4km, thereby the assumption of an infinite cylinder is reasonable, since the aureole under consideration this study is only 1500m wide. The diorite intrusion has a radius of 2900m.

The initial intrusion temperatures were between 1050°C and 1100°C (Weiss and Troll, 1991), country rock temperatures are estimated to be in the range of 250°C and 350°C. The boundary of the aureole is 30km from the intrusion. This is one of the fixed boundaries for solving the heat flow equation, the temperature gradients disappearing, thus the country rock temperatures remain unchanged from the initial country rock temperature. Latent heat of crystallisation is calculated using a liquidus of the diorite is 1100°C and the solidus 760°C.

Temperatures are computed every 50m within the aureole and with 100 year time intervals. Each simulation is run for 500 000 years to ensure that peak temperatures have been reached within the area of interest (i.e. at distances less than 1500m from the igneous contact).

1.3.3 Summary of Input Data For Thermal Models

A series of starting conditions are fed into the computer which represent the geometry and thermal regime of the 'Ballachulish Granite' and country rocks at the instance of intrusion. The input data is in some cases fairly well constrained (e.g. radius of intrusion, liquidus temperature) and in other cases not so well constrained. The philosophy behind

thermal modelling is to run a series of thermal simulations; for each simulation one of the less well constrained variables is altered. Consequently it is possible to assess the effect of that variable on the thermal model. Each simulation is compared with the thermal framework of the igneous intrusion as defined by mineral data. The process of altering variables and rerunning the model is repeated until the predicted peak temperature variation within the aureole most closely matches the peak temperatures which have been ascertained from mineral data. It should be noted that the fact that the starting conditions a thermal model closely matches mineral data does not prove emphatically that they were the actual conditions experienced at Ballachulish during the intrusion. Notwithstanding this, the thermal model does adequately describe the thermal evolution of the aureole and indeed goes some way towards limiting range of possible starting conditions.

1.4 Results

Numerous thermal models have been calculated each with different initial conditions and boundary conditions. This investigation is not purely study into the effects of different variables on thermal evolution of an aureole. The thermal models produced are a means with which kinetics of microstructural evolution are to be examined. Therefore, the numerous models which have been produced will not be presented, but only the model which most closely fits mineral data, and hence is the model used for calculating rates of microstructural change. The starting conditions for the model were as follows: temperature of intrusion 1050°C, country rock temperatures 250°C, size of aureole 30km and an intrusion with a radius of 2900m.

Two graphs are presented, firstly a graph showing the temperature with respect to distance from the intrusion and secondly a graph indicating the peak temperatures attained in the aureole as a function of distance from the intrusion. The temperature history fro each node is output to a data file, from which it is possible to construct a graph showing the evolution of temperatures through time at a number of locations within the aureole (Figure A2). Peak temperatures are attained more rapidly close to the igneous contact. For example at 100m from the contact peak temperatures are attained within 10,000 years, whereas at 8km the temperatures are still rising even after 500 000 years. This is an important consideration for microstructural development, because not

only do peak temperatures vary throughout the aureole, but also the rate of change in temperature with respect to time. It is possible that this may have consequences for microstructural processes. The graph of temperature evolution through time for each node serves as a temperature framework employed to calculate the rates of microstructural change in the Ballachulish aureole.

Mineral equilibrium was maintained within the aureole (Harte and Pattison, 1985), hence mineral equilibrium data should reflect the peak temperatures attained at the distances from where the data has been taken. The peak temperatures within the aureole may be compared to mineral equilibrium data. Figure ? indicates that the fit between the thermal model and mineral equilibrium data is relatively good.

A distinct possibility, that has not been discussed, is that the intrusion was not instantaneous. The flow of magma to the surface to supply volcanic eruptions could potentially pump magma through the intrusion over a period of time. This situation is modelled by resetting the intrusion temperature after each finite element calculation, thereby maintaining the intrusion temperature at 1050°C for a specified number of time steps. These models tended to have a great effect on the country rock close to the intrusion, but relatively little effect further away. Continuous intrusion models do not compare particularly well with the mineral data. Therefore, non-instantaneous models were discounted.

APPENDIX B

ANALYTICAL TECHNIQUES

The methods of data collection used in the research program are outlined in this Appendix with particular attention being paid to electron microscopy which has been the fundamental tool employed to obtain much of the geological data.

1.1 Optical Microscopy

The light microscope has been used primarily for specimen reconnaissance and microstructural characterisation, calculation of grain sizes (using linear intercept methods), and to aid identification of deformation mechanisms and mechanisms of annealing. Photomicrographs presented within this thesis were obtained on a Leitz Ortholux II^R polarising light microscope with a Wild Photoautomat MPS 50 camera and daylight 100 ASA colour print film.

1.2 Scanning Electron Microscopy (SEM)

A Camscan Series 4 SEM utilises a variety of material properties to image different microstructural and microtextural aspects of a material. Much of the data collected

during this study has been acquired using BackScattered Electron mode (BSE) or BSE related techniques which utilise mineral composition and crystallographic properties. Many examples of these techniques are well-documented in the geological literature (Lloyd 1987; Lloyd et al. 1987; Olesen and Schmidt 1990; Prior et al. 1990; Lloyd and Freeman 1991; Lloyd and Knipe 1992; Lloyd and Freeman 1993; Pryer et al. 1995).

1.2.1 Basic Principles

In this section a very brief outline of SEM the physical processes involved in image generation when an electron beam is scanned across the surface of the specimen are discussed. The actual images are produced by interaction of electrons, emitted from the sample, with a detector. The sensitivity of the detector may be controlled to amplify the signal and thereby alter the brightness of the image displayed on the screen. The variation in the emitted signal across the surface of the specimen determines the contrast level seen on the CRT display. The types of signal generated reflects the beam energy, resolution, the working distance and the diameter of the beam, and each requires a specialised detector for the collection and generation of their specific visual representation of the surface. Three types of imaging mode are available on the **Camscan Series 4** secondary electron, backscattered electron, cathodo-luminescence mode, together with X-ray mode.

Secondary Electrons (SEI) are capable of imaging surface topography.

Backscattered electron signal where the bulk of the intensity reflects the atomic mass of the atoms with which they interacted:- **BSE** atomic (**Z-**) contrast mode images mineral composition. Backscattered electrons, where a small portion of the intensity of the overall signal reflects the inelastic scatter of diffracted electrons (dependant on crystal orientation) produces images of Orientation Contrast (**OC**) and images of diffraction patterns which relate to the precise crystallographic orientation (Electron Channelling Patterns - **ECP** and Electron BackScattered Diffraction **EBSD**).

Cathodoluminescence (CL) induced light rays are generated by electron specimen interaction.

X-rays are primarily for chemical analysis.

1.2.2 Image Generation and Detection

The generation of an SEM image is dependant upon the emission of electrons from the electron gun, usually a tungsten or lanthanum hexaboride (LaB_6) filament. The electrons are directed into the column as a divergent beam through an anode, where beam deflecting coils direct the beam on to the optic axis of the column. The beam passes through a double condenser lens system, where 'C1' (spot size) demagnifies the cross-over of the divergent beam by 80% and 'C2' demagnifies it by a further 15%, and focuses the second, smallest point of cross-over on to the plane of the specimen surface.

The size of the beam between C2 and the surface is controlled in part by the size of the condenser aperture (CA), which immediately follows C2; the condenser aperture (CA) varies in size from $100\mu\text{m}$ for SEI and BSE Z-contrast images to $70\mu\text{m}$ for BSE/EC images. The aperture controls the number of electrons reaching the specimen: the smaller the aperture, the fewer the number of electrons. The diameter of the beam as it hits the specimen controls the resolution of the machine, and is a function of the size of the condenser aperture, the location of the specimen with respect to the condenser aperture (i.e. working distance, WD), and, most importantly, the spot-size (C1). The complex affect of the working-distance on the resolution is such that to raise or lower the specimen with respect to the condenser aperture will change the setting for C2 (i.e. moving the focus point of the finer beam cross-over with respect to the specimen surface) and in turn this will affect the demagnification of the beam and thus its diameter. In short, the smaller the working distance, the smaller the spot size, and therefore the greater the resolution.

As mentioned, the condenser aperture controls the number of electrons reaching the specimen surface, but it also controls the depth of field seen in the image: the smaller the aperture for a given focused beam, the more parallel are the electron paths within the beam, and thus a greater depth of field is created within the image. Against this however, diffraction at this aperture increases beam diameter (spot size), reducing effective resolution. (figure). Additionally, a focused beam at C2 with a small aperture means a

low convergence angle (and a large depth of field value) but a reduction in the number of electrons. Choice of final aperture size is therefore a compromise between beam strength (kV), depth of field and resolution. For Z-contrast a large aperture and lower kV is preferred; in EC mode a smaller aperture and a more powerful beam current is used.

The SEM image is generated by one of four scanning procedures:

1. the rectangular raster, for 2-dimensional images;
2. the line scan, for study of the variation in the signal intensity along a 1-dimensional track.
3. the stationary spot, for x-ray microanalysis.
4. the rocked spot, for crystallographic analysis through the generation of ECPs.

The difference between (1-3) and (4) is that the pivot point of the beam (P), as it passes through the second and final set of beam deflector coils, lies within the objective lens in modes (1-3); in the rocking technique (4), the P-point lies on the specimen surface, allowing the user to sample the changeable intensity of the backscattered electrons with respect to the beam angle. It is by this method that the user is able to distinguish area of different crystallographic orientation according to the variation in image contrast.

1.2.3 Electron Beam - Specimen Interaction

The beam interacts with the specimen in two ways:

1. elastic scattering events, where no significant amount of energy is imparted from the electron beam to specimen;
2. inelastic scattering event, where energy is absorbed by the specimen and dissipated as heat, light, x-rays secondary electrons or as backscattered electrons.

The latter type show a range of intensities which reflect the number and type (angularity) of the scattering events they have endured. In any specimen under bombardment by an electron beam, each electron has an equal chance of colliding with an atomic target within the specimen, and thereby being scattered. Such collision and scattering generates atomic z-contrast images in the SEM, where collision and interaction between incident electrons and constituent atoms leads to energy absorption on the part of the latter, electron excitation and then energy dissipation in the form of backscattered electrons, i.e. electrons discharged from the specimen surface back towards the original source, where they are collected by a suitable detector. For geologists interested in polymineralic specimen, or in the variation in composition within individual minerals, these Z-contrast images are the best way to visualise the nature of physical variations in composition. The intensity of the backscattered signal increases as the atomic density of the specimen increases, because there is an increased number of target atoms for the electrons to interact with.

1.2.4 Detection of Signal

Detection of the desired signal is largely dependant on the availability of a suitable detector. Most SEMs can be equipped with detectors that can receive light, secondary or backscattered electrons. The important point in all cases is that the detectors are positioned as close to the specimen as possible so that each detector can receive as much of its required signal as possible without incurring misalignment of the detector with respect to the deflected electron path. The latter point is especially important in the case of the less easily deflected X-rays. To counteract this, specimens may be moved and tilted to facilitate the collection of signals should the need arise, requiring the user to be aware of the internal geometry of the specimen chamber. To ease the congestion in the chamber the SEI detector can be positively biased, encouraging the easily deflected secondary electrons to follow curved paths to the detector; the BSE detector is usually negatively-biased for preferential collection of backscattered electrons. This combination allows a closer positioning of the X-ray and light detectors.

1.2.5 Principles of Electron Channelling in the SEM

Images relating to crystallographic orientation are created from two types of related BSE/EC signals in the SEM:

1. Orientation or crystallographic contrast (**OC**): areas of the crystalline material with uniform crystallographic orientation possess uniform contrast levels, but relative variation of the contrast level becomes apparent where areas of non-matching crystallographic orientation (grains/subgrains) coincide (Lloyd 1987; Lloyd and Knipe 1992; Lloyd et al. 1992). The "grey-level" of the contrast in the image is non-quantitative;

2. Electron channelling patterns (**ECPs**) (Booker 1970; Joy and Newbury 1977; Joy et al 1982; Schulson 1977; Saimoto et al. 1980; Lloyd 1987). These SEM images are analogous in appearance to the Kikuchi patterns obtained in the TEM.

1.2.6 Generation of Electron Channelling (OC and ECPs)

For a comprehensive account of the mechanics approach to the generation of BSEs from the surface of a crystalline material bombarded by an electron beam, see review by Farmer (Farmer 1993, chapter 3) and references therein. See also the review of SEM techniques and their application to geological materials by Lloyd (1987).

The Camscan Series 4 SEM at the University of Leeds (Electron Optics Units) possesses the ability to generate and collect OC images and ECPs. It is fundamentally important in the generation of these patterns to use as large a scanning angle as possible, and this may be achieved in one of two ways.

1. mechanical rocking of the surface of the specimen under a stationary beam (Coates 1967);

2. rocking of the electron beam about a fixed point on the surface of the specimen (Van Essen and Schulsen 1969).

The Camscan Series 4 used for the generation of the ECPs reported in this thesis utilises the latter technique. As outlined earlier, rocking of the beam requires the replacement of the final lens aperture with a divergence lens aperture, and the turning off of the lower set of scan deflection coils. This moves the final cross-over point (P) from the objective lens on to the surface of the specimen, where a correctly focused beam will rock through a sufficiently large scanning angle on a chosen point on the sample surface, allowing the generation of ECPs from area of uniform OC as small as $10\mu\text{m}$.

The Z-contrast BSE signal is a combination of the atomic mass of the material and, to a significantly lesser extent, the crystallographic orientation of the individual crystalline components of each mineral in the aggregate. To generate the orientation-contrast (OC) images in EC mode particular conditions of SEM operation are required:-

1. *High Contrast*:- as the OC component of the overall BSE signal is swamped by the Z-contrast signal, the SEM set-up must be altered to detect these extremely high intensity frequencies. Possible solutions are to either increase the magnification so that the field of view contains as little high density material as possible, or to induce bias in the analysis by examination of only those area which are monomineralic.

2. *Working Distance*:- BSE emissions from the specimen are directional by their nature. By lowering the working distance, and thereby bringing the BSE detectors closer to the source of emission, the reception of the signal is enhanced. This has the added value of increasing the rocking angle during the generation of the ECP. Reducing the working distance also has the advantage of reducing the spherical aberration of the final lens which can cause a distortion of the beam diameter.

3. *Beam Current*:- it is usual to increase the beam current from 20kV to 25-30 kV during EC operation. This has the effect of raising the EC signal above the background noise.

4. *Beam Diameter*:- the beam diameter determines the size of the area from which the ECP is taken, and so it is preferable to have as small a beam as possible in order to achieve precision in the location of the sample site. A reduction of beam diameter may be achieved at the expense of the size of the convergent angle, thereby reducing the number

of electrons in the beam. To counteract this limitation the beam current is increased in order to raise the brightness of the electron source.

5. *Beam Collimation*:- both OC images and ECPs are generated as a function of the variation of the angle of incidence of the electron beam upon the specimen surface. The angular divergence of the beam is therefore an important factor in the operational conditions used during observation of a specimen by the EC technique. With a large angle of divergence, the Bragg Law for specific atomic planes is not met at a specific point, resulting in the generation of a blurred "ECP" of equal contrast throughout and which covers a broad area of the specimen: this is an OC image. For ECPs, the angle of divergence is much smaller, as low as 0.3-3 medians in order to achieve the greatest resolution.

6. *Dynamic Focus*:- the presence of such a facility permits a further reduction in beam diameter, without any associated reduction in the convergence angle or source brightness. The benefits of the dynamic focus are the increased precision of ECP location, from points as small as 5-7 μ m.

1.2.7 Cathodoluminescence

Cathodoluminescence (CL) textures were examined using the Camscan Series 4 SEM. The identification of metamorphic/deformation-induced or modified luminescence has been a largely neglected topic, and when incorporated with the observations made by the other techniques the results indicate the important potential for this technique in the clarification of rock evolution. The SEM detects light intensities reflected from a specimen, a variety of microstructural aspects may be responsible for differing luminescence: e.g. chemical composition, defect densities and the temperature/pressure conditions under which a material formed.

1.2.8 Chemical Analysis on the Electron Microprobe

Quantitative mineral micro-analyses were obtained using the CamecaTM cambex SX-50 electron microprobe at the University of Leeds, employing wavelength dispersive X-ray analysis. Element peak and background count times varied between 10-30 seconds and

5-15 seconds respectively, dependant upon the relative abundance within the mineral for analysis. ZAF corrections were performed “on-line. The analyses were made using a beam current of 10nA and an accelerating voltage of 15 kV. An analysis was performed across two grains of quartz which had contrasting CL-signatures in order to investigate the cause of variations in luminescence intensity.

1.3 Preparation of Specimens for BSE Observation

As important as machine set-up, the preparation of specimens requires particular care and quite often the “standard” procedure must be adapted to suit the requirements of individual specimens. An extra 10 minutes at a particular stage in the polishing process can mean the difference between getting a good quality image and a “noisy” one (Lloyd 1987). The principle aim of polishing is to reduce the surface topography to at least 0.5µm.

The procedure begins with cutting an oriented chip, where the face for observation is 1 cm². This chip is mounted in resin; the surface for observation on the hardened resin block is ground flat, using 600 and 500µm corundum powders for approximately 10 and 15 minutes respectively. The surface is then polished on a “dialap”-lubricated, nylon-coated lap using four decreasing sizes of diamond paste (10, 3, 1 and 0.25µm). Each stage of diamond polishing takes about 5-15 minutes, depending on the range of minerals present. The specimen is washed in a sonic bath between each stage in the polishing procedure.

For observation in EC mode, the specimen requires an additional polishing procedure, referred to as “Syton-polishing”. This involves an ultrafine sodium hydroxide silica slurry (Syton) on a Malvern Instruments Multipol polisher for an absolute minimum of 8 hours, to give a mechano-chemical etch polish.

1.4 Transmission Electron Microscopy (TEM)

Detailed microscopic examination of certain aspects of particular specimens was performed using Transmission Electron Microscopy (TEM). TEM research has

frequently been used by geologists to analyse both the chemistry and microstructures of rocks (see Buseck 1992 and references therein). Within this investigation TEM research has been limited to using the machinery as a high magnification/high resolution optical microscope. Images are acquired by transmitting electrons through a ultrafine section of sample ($<0.5\mu\text{m}$), the microstructural details of the images are revealed as a consequence of electron diffraction. The TEM provides an ideal tool with which one can examine fine scale microstructures such as subgrains and dislocations (White and White 1981).

APPENDIX I

EDS ANALYSIS

The energy-dispersive X-ray (EDS) analysis was performed using a JEOL JXA-8000 scanning electron microscope (SEM) equipped with an EDAX 9900 EDS system. The analysis was conducted on a polished and etched surface of the sample. The results are presented in the following table.

The EDS analysis shows the presence of the following elements in the sample:

Elemental analysis results (wt%):

Element	Weight %
Al	10.5
Si	68.2
O	18.8
Fe	0.5

The above results are consistent with the expected composition of the sample.

The EDS analysis was performed on a JEOL JXA-8000 SEM equipped with an EDAX 9900 EDS system.

APPENDIX C

KONTRON MACROS

The microstructural shape and size parameters employed to characterise microstructures in this investigation are measured using macros for a Kontron Vidas21 image analyser. Many of the macros are system macros supplied by the manufacturers. The relevant macros are defined here using the descriptions from the user manual.

Area: measures the area of an object; the number of pixels is multiplied by the scaled pixel area.

Maximum Diameter (kontron macro:DMAX): the longest diameter of an object, obtained by selecting the largest of the feret diameters (fig. ??) measured in 32 different directions (i.e. angular resolution of 5.7 degrees).

Min Diameter (kontron macro:DMIN): is similar to DMAX, but taking the shortest among the feret diameters.

Diameter of Circle (kontron macro:DCIRCLE): the equivalent circle diameter (Figure C1) as defined by $DCIRCLE = 2\sqrt{AREA/\pi}$.

Aspect Ratio (*kontron macro:FSHAPE*): defined as $FSHAPE = DMAX/DMIN$.

Perimeter (*kontron macro:PERIM*): defined as the boundary length of an object; holes within an object will contribute to the perimeter.

Circularity Factor (*kontron macro:FCIRCLE*): The area of a shape is compared to the perimeter via $FCIRCLE = 4 \times \pi \times AREA / PERIM^2$; values of this parameter range between close to 0 for very elongated or rough objects to 1 for circular objects.

APPENDIX D

CHANNEL-EULER CONVERSIONS

This appendix describes the format of channel data files (measurements are in euler angles) and how the data is converted into an orientation matrix which is necessary to compute misorientations.

Data output from channel programs compares the crystal axes (a,b,c) to the specimen reference axes (x,y,z). Two mathematical techniques have been used to describe the relationship of the reference frames: direction cosines are used in early versions of CHANNEL and euler angles in more recent versions.

Three direction cosines relate a crystallographic axis in the crystal reference frame (e.g. a-axis) to a reference axis in the specimen co-ordinate reference frame. Nine direction cosines are necessary to adequately describe the relationship of all three crystal axis (a,b,c) to the three specimen reference axis (x,y,z).

$$[G] = \begin{bmatrix} g_{11} & g_{12} & g_{13} \\ g_{21} & g_{22} & g_{23} \\ g_{31} & g_{32} & g_{33} \end{bmatrix} = \begin{bmatrix} \cos\theta_a & \cos\theta_b & \cos\theta_c \\ \cos\psi_a & \cos\psi_b & \cos\psi_c \\ \cos\phi_a & \cos\phi_b & \cos\phi_c \end{bmatrix}$$

where θ are the angles between the crystal axes and the x specimen axis

ψ are the angles between the crystal axes and the y specimen axis

ϕ are the angles between the crystal axes and the z specimen axis.

[G] is the basic transformation matrix needed to manipulate data in order to calculate grain misorientation and produce pole figures and inverse pole figures.

More recent versions of CHANNEL relate the specimen axes to the crystal axes in the form of euler angles. The two reference frames (x,y,z and a,b,c) are brought into coincidence by a series of rotation of the crystal reference frame around the x and z axis of the specimen reference frame (Bunge, 1985):

1st rotation of ϕ_1 about the crystal c axis (001) until 100 is in the plane of the specimen x axis.

2nd rotation of ψ about the crystal a axis (100) until 010=the specimen y axis.

3rd rotation of ϕ_2 about the crystal c axis (100) until all three specimen and crystal axes are aligned.

The rotations quoted above are Bunge's specification (Bunge 1985), other notations are often used, for example Roe's specification chooses the second rotation to be around the crystal b axis (010) rather than the 100 axis for the Bunge's notation. Figure ? illustrates the effect of performing the three rotations in succession. The relationship between the elements of the orientation matrix and the Euler angles are:

$$\begin{aligned}g_{11} &= \cos \psi_1 \cos \psi_2 - \sin \psi_1 \sin \psi_2 \cos \Phi \\g_{12} &= \sin \psi_1 \cos \psi_2 + \cos \psi_1 \sin \psi_2 \cos \Phi \\g_{13} &= \sin \psi_2 \sin \Phi \\g_{21} &= -\cos \psi_1 \sin \psi_2 - \sin \psi_1 \cos \psi_2 \cos \Phi \\g_{22} &= \sin \psi_1 \sin \psi_2 + \cos \psi_1 \cos \psi_2 \cos \Phi \\g_{23} &= \cos \psi_2 \sin \Phi \\g_{31} &= \sin \psi_1 \sin \Phi \\g_{32} &= -\cos \psi_1 \sin \Phi \\g_{33} &= \cos \Phi\end{aligned}$$

APPENDIX E

PROGRAM LISTINGS

Introduction

This appendix contains listings of four programs, two of which are macros written for a Vidas 21 image analysis system. The programs are as follows,

- 1) A Vidas macro to separate feldspar impurities from quartz grains and measure size and shape parameters.
- 2) A program to calculate moment ratio factors from the output of the Vidas macro above.
- 3) A vidas macro to measure the fractal dimension of individual grains in an aggregate.
- 4) A program that calculates CSL for rhombohedral lattices.

PROGRAM 1 (Vidas Macro)

This is a macro written for a Kontron Vidas21 system. The macro language is similar to 'C'. Many of the commands are system macros written by the manufacturers (e.g. getim - is a macro to load an image file).

{First part of program downloads the image and separates quartz grains from feldspar impurities}

```
fname="51"  
fname2="51g"  
bin="binary"  
getim fname,1  
scalgeom 1,"1:1-scale",_ON,_ON  
dis2lev 1,2,211,255,_ON,_ON,1
```

```

dilate 2,3,7,255,1
fill 3,3
drawline 2,2,0
ovlgrey 2,2,2,0fill 3,3
erode 3,3,7,255,1
scrap 3,3,_OFF,0,100,_ON,_ON
dis2lev 1,2,168,241,_ON,_ON,1
storim bin,3
notim 3,3
xorim 2,3,1

```

{Second part of the program performs the measurement of grains and outputs the data to a file, measurements are listed two lines below as part of the 'initObj' macro}

```

resetpar
InitObj ANGLEELL,AREA,DCIRCLE,ELLIPSEA,ELLIPSEB,FCIRCLE,FSHAPE,OBJLABEL,PERIM
dilate 1,2,7,0,1
identframe 2,2,_ON,1,256,256,0,0,_ON,_ON,_ON
erode 2,2,7,0,1
copy 2,3
measobj 2,fname,_OFF
resetpar

```

{the image co-ordinates of the Centres of Gravity of each object are recorded for use in FRLABEL2 macro}

```

InitObj ACPY,CGRAVX,CGRAVY
measobj 3,fname2,_OFF
greygr 3,3,3,1,255,255
storim fname,3
clearallof

```

PROGRAM 2 (Turbo Pascal)

```

program betaOne_betaTwoDistribution;

```

{ Program to calculate the beta 1 and beta 2 variables which describe a distribution - Harr, 1977, see also chapter 4. Grain sizes are read in from output files from grainsmeas macro written for the Kontron Vidas21 image analyser. The measurements are input into an array (dataarray) for }

```

uses

```

```

  crt,dos,mathfunc;

```

```

type

```

```

  dataarray=array[1..600] of single;

```

```

  grain=

```

```

    record

```

```

      count:array[1..600] of integer; objlabel:dataarray; area:dataarray;

```

```

      perim:dataarray; dcircle:dataarray; fcircle:dataarray; fshape:dataarray; ellipsea:dataarray;

```

```

      ellipseb:dataarray; angelli:dataarray;

```

```

    end;

```

```

  workfiles=array[1..11] of integer; measurements=array[1..8] of string;

```

```

  Mean = OBJECT

```

```

    average:real;

```

```

    sum:real;

```

```

        procedure init (x:dataarray;maxelement:integer);
    end;
    statistic = OBJECT(mean)
        variance:real;
        skewness:real;
        kurtosis:real;
        procedure init(x:dataarray;maxelement:integer);

    end;

    beta = OBJECT(statistic)
        beta1:real;
        beta2:real;
        procedure init (x:dataarray;maxelement:integer);

    end;

Procedure mean.init (x:dataarray;maxelement:integer);
var
    i:integer;
begin
    sum:=0;
    average:=0;
    for i := 1 to maxelement do
        sum:=sum+x[i];
        average:=sum/maxelement;
    end;

Procedure statistic.init (x:dataarray;maxelement:integer);
var
    i: integer;
    partialskew,partialkurt,partialvar:single;
begin
    mean.init(x,maxelement);
    variance:=0;
    skewness:=0;
    kurtosis:=0;
    for i := 1 to maxelement do
        begin
            partialvar:= raise ((x[i]-average),2); partialskew:=raise ((x[i]-average),3); partialkurt:=raise
            ((x[i]-average),4); variance:=variance+partialvar; skewness:=skewness+partialskew;
            kurtosis:=kurtosis+partialkurt;
        end;
        variance:=variance/maxelement; skewness:=skewness/maxelement;
        kurtosis:=kurtosis/maxelement;
    end;

Procedure Beta.init (x:dataarray;maxelement:integer);
begin
    statistic.init(x,maxelement); beta1:=(raise(skewness,2))/(raise (variance,3));
    beta2:=kurtosis/(raise(variance,2));
end;

{*****End of Object Methods*****}

```

```
{*****Program constants and variables*****  
*****}
```

```
const filenumber:workfiles=(71,79,80,54,55,57,60,69,77,78,48);  
  fvector:measurements=('area','perim','dcircle','fcircle'  
, 'fshape','ellipsea','ellipseb','angell');
```

```
var  
maxelement,i,j:integer;  
fin,fout:text;  
data:grain;  
feature:beta;  
fileout:string;
```

```
{*****FILE I/O PROCEDURES*****}
```

```
procedure filein(j:integer);
```

```
var  
  i:integer;  
  name:string;
```

```
begin
```

```
  str(filenumber[j],name);  
  name:=name+'.fre';  
  assign(fin,name);  
  reset (fin);  
  readln(fin);  
  readln(fin);  
  maxelement:=0;  
  i:=1;  
  while not eof(fin) do  
    begin  
      read (fin,data.count[i]);  
      read (fin,data.objlabel[i]);  
      read (fin,data.area[i]);  
      read (fin,data.perim[i]);  
      read (fin,data.dcircle[i]);  
      read (fin,data.fcircle[i]);  
      read (fin,data.fshape[i]);  
      read (fin,data.ellipsea[i]); read (fin,data.ellipseb[i]); read (fin,data.angelli[i]); readln (fin);  
      maxelement:=maxelement+1; i:=i+1;
```

```
    end;
```

```
  close(fin);
```

```
end;
```

```
procedure fileoutopen(fileout:string);
```

```
begin
```

```
  assign (fout,fileout); rewrite(fout);
```

```
end;
```

```
procedure outfile;
```

```
begin
```



```
write(fout,fvector[i]:12); write(fout,filename[j]:5); write(fout,feature.beta1:7:2);  
writeln(fout,feature.beta2:7:2);  
end;
```

```
{*****END OF I/O PROCEDURES*****}
```

```
{*****MAIN PROGRAM CONTROL LOOP*****}
```

```
begin {main program}  
  for i := 1 to 8 do  
    begin  
      fileout := fvector[i] + '.bta';  
      fileoutopen(fileout);  
      case i of  
        1:begin  
          for j := 1 to 3 do  
            begin  
              filein(j); feature.init(data.area,maxelement); outfile;  
            end;  
          close(fout);  
        end;  
        2:begin  
          for j := 1 to 3 do  
            begin  
              filein(j); feature.init(data.perim,maxelement); outfile;  
            end;  
          close(fout);  
        end;  
        3:begin  
          for j := 1 to 3 do  
            begin  
              filein(j); feature.init(data.dcircle,maxelement); outfile;  
            end;  
          close(fout);  
        end;  
        4:begin  
          for j := 1 to 3 do  
            begin  
              filein(j); feature.init(data.fcircle,maxelement); outfile;  
            end;  
          close(fout);  
        end;  
        5:begin  
          for j := 1 to 3 do  
            begin  
              filein(j); feature.init(data.fshape,maxelement); outfile;  
            end;  
          close(fout);  
        end;  
        6:begin  
          for j := 1 to 3 do  
            begin
```

```

        filein(j); feature.init(data.ellipsea,maxelement); outfile;
    end;
    close(fout);
end;
7:begin
    for j :=1 to 3 do
        begin
            filein(j); feature.init(data.ellipseb,maxelement); outfile;
        end;
        close(fout);
    end;
8:begin
    for j :=1 to 3 do
        begin
            filein(j); feature.init(data.angelli,maxelement); outfile;
        end;
        close(fout);
    end;
end;{of case }
end;

```

end.

PROGRAM 3 (Vidas Macro)

This is a macro written for a Kontron Vidas21 system. The macro language is similar to 'C'. Many of the commands are system macros written by the manufacturers (e.g. getim

```

##### #Macro to
automatically calculate fractal dimension of a grain # #The grains are picked automatically and
the fractal dimension of each # #grain labelled on the image. This image is outputted with the name
# #*****f.img. Version 2 - calculates fractals for numerous binary images# #defined in array images in
the first line #
#####
images[8]:=80,78,77,60,49,55,57,54
z=1
for z=1,z<9,z=z+1
imagestring=string(images[z])
clearall 0
fname=imagestring
fout=imagestring+"f"
write fout
getim fname,1
scrap 1,1,_OFF,0,500,_ON,_ON
resetpar
copy 1,2
InitObj AREA
identframe 1,2,_OFF,1,512,512,0,0,_ON,_OFF,_ON
measobj 3,fout,_OFF
resetpar
InitObj ACPX,ACPY,CGRAVX,CGRAVY
measobj 2,"acpoints",_OFF
identify 2,2,_OFF,_OFF

n=1
control=1
while(1)
j=0

```

```

DBopen "acpoints", "acpx,acpy"
for j,j<n,j=j+1
  DBread "acpoints"
  if _STATUS:break
endfor
if _STATUS:break
n=n+1
clear 3,0
GWpixel 3,ACPX,ACPY,255
markobj 2,3,1,_ON,_OFF,_ON
fill 1,1
resetpar
InitObj DCIRCLE
identify 1,1,_ON,_OFF
Measo 1
iterations=int(DCIRCLE)
greygr 1,1,1,1,255,255
clear 3,0
contour 1,3,3,5,255,_OFF,_ON
i=1
resetpar
DBopen fout,"area"
AREA=-999
InitObj AREA
identify 3,3,_ON,_OFF
measobj 3,fout,_OFF element[16]:=1,5,9,14,18,22,26,30,35,39,43,47,52,56,1025
while 1
  erode 3,3,7,0,1
  identify 3,3,_OFF,_OFF
  measobj 3,fout,_ON
  i=i+1
  write i
  if iterations<element[i]:break
endwhile
AREA=-999
DBopen fout,"area"
DBappend fout #####
#Calculate Fractal Dimension
DBopen fout,"area"
control=0
dilatedarea[15]:=0.0 eldiameter[15]:=1.12,5.17,9.37,13.58,17.80,22.02,26.24,30.46,34.68,38.90,43.13,47.35,51.57
check=1
while 1
  control=control+1
  DBread fout
  dilatedarea[control]=AREA
  check=int(dilatedarea[control])
  if check== -998 or control==15: break
  numofmeas=control
endwhile
if numofmeas>8
  control=1
  normeldiameter[15]:=0.0
  for control=1,control<=numofmeas,control=control+1 perimestim[control]=dilatedarea[control]/eldiameter[control]
  perimestim[control]=perimestim[control]/DCIRCLE normeldiameter[control]=eldiameter[control]/DCIRCLE
  perimestim[control]=log(perimestim[control]) normeldiameter[control]=log(normeldiameter[control])
endfor
numofmeas=numofmeas-2
fd=0.0 fd=(perimestim[numofmeas]-perimestim[6])/(normeldiameter[numofmeas]-normeldiameter[6]) fd=1-fd
num=fd*100

```

```
degrees:=(180*radians)/pi;
end;
```

```
procedure primenos; {inputs prime numbers into array}
begin
  prime[1]:=1; {crap programming, but can't be bothered to calc them}
  prime[2]:=2;
  prime[3]:=3;
  prime[4]:=5;
  prime[5]:=7;
  prime[6]:=11;
  prime[7]:=13;
  prime[8]:=17;
  prime[9]:=19;
  prime[10]:=23;
  prime[11]:=29;
  prime[12]:=31;
  prime[13]:=37;
  prime[14]:=41;
  prime[15]:=43;
  prime[16]:=47;
end;
```

```
{-----
*****File Handling*****}
-----}
```

```
procedure openfile;
begin
  assign(fin,path+fname);
  reset(fin);
  fnameout:='276.plt';
  assign(fout,fnameout);
  rewrite(fout);
  writeln(fout,'mu=',mu, 'rho=',p);
  writeln(fout);
  writeln(fout,'    m    u    v    w    angle    sigma'); writeln(fout,'-----
-----');
end;
```

```
procedure infile;
var
  u,v,w:real;
begin
  repeat
    read(fin,rot_vector);
  until (frac((rot_vector.uvw[1]*2+rot_vector.uvw[2]+rot_vector.uvw[3])/3)=0)
  or (eof(fin));
end;
```

```
procedure outfile;
begin
  if sigma<50 then
  begin
    with rot_vector do
    begin
      write(fout,m:10:2);
      write(fout,uvw[1]:10);
```

```

        write(fout,uvw[2]:10);
        write(fout,uvw[3]:10);
        write(fout,angle:10:2);
    end;
    writeln(fout,sigma:10:2);
end;
end;

{-----End of File Handling-----}

```

```

{-----CALCULATION PROCEDURES-----}

```

```

procedure ef1;
var
check1,check2:real;
begin
    f1:=1;
    repeat
        check1:=comp/i;
        check2:=(m+rot_vector.uvw[3])/i;
        if (frac(check1) = 0) and (frac(check2) = 0) then
            f1:=i;
        i:=i+1;
    until i=mu;
end;

procedure ef2;
var
check1,check2,check3,check4:real;
begin
    i:=1;
    f2:=1;
    check1:=0;
    check2:=0;
    check3:=0;
    check4:=0;
    repeat
        check1:=comp/i;
        if m+rot_vector.uvw[3] <> 0 then check2:=(m+rot_vector.uvw[3])/i;
        if rot_vector.uvw[1] <> 0 then check3:=rot_vector.uvw[1]/i;
        if rot_vector.uvw[2] <> 0 then check4:=rot_vector.uvw[2]/i;
        if (((frac(check1) = 0) and (frac(check2) = 0)) and (frac(check3)=0)) and (frac(check4)=0) then f2:=i;
        i:=i+1;
    until i=mu;
end;

procedure ef3;
var
check1,check2,check3,check4:real;
begin
    i:=1;
    f3:=1;
    repeat
        check1:=mu/i;
        check2:=((2*(1/f1))*rot_vector.uvw[1])/i;
        check3:=((2*(1/f1))*rot_vector.uvw[2])/i;
        check4:=rot_vector.uvw[2]/i;

```

```

nominatora:=mu*sqr(rot_vector.uvw[3]); nominatorb:=(2*p)*(sqr(rot_vector.uvw[1])+(rot_vector.uvw[1]*rot_v
nominator:=nominatora+nominatorb;
nominator:=nominator/(denom*(3*mu));
m:=sqr(nominator);
coincidence:=false;
if (frac(m)<0.0001) or (frac(m)>0.9999)then
begin
    coincidence:=true;
    m:=round(m);
end;

```

```
end;
```

```
{-----}
```

{Next two to functions check rotation axis to choose the lowest angle rotation from the equivalent rotations in quartz}

```
{-----}
```

```

function checkSST(A:crystalvector):boolean;
var
    check:array[1..5] of boolean;
    i:integer;
begin
    for i:=1 to 5 do
        check[i]:=false;
    with A do
        begin
            if m>=uvw[3] then check[1]:=true;
            if m>=sqr(p/(2*mu)*(uvw[1]+uvw[2])) then check[2]:=true; if uvw[3]=0 then
                begin
                    if uvw[2]>=uvw[1] then check[3]:=true;
                end;
            if (uvw[3]>0) and (m=sqr(p/(2*mu)*(uvw[1]+uvw[2]))) then begin
                if uvw[2]>uvw[1] then check[4]:=true;
            end;
            if check[3] or check[4] =true then check[5]:=true;
            if ((check[1] and check[2]) and (check[5]))=true then
                checkSST:=true;
        end;
    end;
end;

```

```

function IsLowerBound(A:crystalvector):boolean;
var
    c,b:real;
begin
    IslowerBound:=false;
    c:=frac(mu/2);
    b:=frac(p/2);
    if (c>0) and (b>0) then
        begin
            if sigma>=sqr(8*mu*p)/3 then
                islowerBound:=true;
        end
    else
        begin
            if sigma>=sqr(2*mu*p)/3 then
                IsLowerBound:=true;
        end;
    end;
end;

```

```

end;
end;

```

```

{-----
-----MAIN CONTROL PROGRAM-----
}
begin
  fname:='rotaxis.';
  openfile;
  primenos;
  t:=1;
  repeat
    infile;
    {rot_vector.uvw[1]:=0;
    rot_vector.uvw[2]:=2;
    rot_vector.uvw[3]:=1;
    rot_vector.angle:=85.9;}
    t:=t+1;
    theta:=rot_vector.angle;
    comp:=2;
    i:=1;
    findemm;
    if coincidence then
      begin
        checkm(rot_vector.uvw[1],rot_vector.uvw[2],rot_vector.uvw[3]);
        ef1;
        ef2;
        ef3;
        ef4;
        with rot_vector do
          begin f:=mu*(3*(trunc(m)*trunc(m))+(uvw[3]*uvw[3]))+(2*p*((uvw[1]*uvw[1])+(uvw[1]*uvw[2])+(uv
          end;
          sigma:=f/((3*f1*f2*f3*f4));
          if ((rot_vector.uvw[1]<>0) or (rot_vector.uvw[2]<>0)) or (rot_vector.uvw[3]<>0) then
            begin
              if (checkSST(rot_vector)) and (IsLowerBound(rot_vector)) then
                outfile;
            end;
          end;
        until eof(fin);
        close(fin);
        close(fout);
      end.

```